Polarimetry of planetary systems

by

William George King McLean

Thesis

Submitted to the University of Warwick

for the degree of

Doctor of Philosophy

Department of Physics

June 2017

Contents

List of Tables

List of Figures

Acknowledgments

I'd like to extend my gratitude to Dr Stefano Bagnulo, firstly for taking me on as his student, and for all of his help and inspiration during my PhD. I'd also like to thank Dr Daphne Stam, who worked with me throughout my PhD, for all of her help. I would like to thank the Science and Technologies Facilities Council for the award of a studentship that enabled me to carry out my research. This thesis would not have been possible without funding from the COST Action grant MP1104 "Polarisation as a tool to study the Solar System and beyond." Funding from this grant enabled me to take part in two conferences, and two visits with Dr Daphne Stam. I'd like to also extend my thanks to the C2PU observing team, for their kind invitation to their observing team, and for training me as a remote observer. I'm very grateful to all of the colleagues who made the effort to take the observations, from all four telescopes, and for all the valuable assistance I have had from many of them in reducing and analysing the data.

Declarations

Chapter 4 contains the following original contributions: twelve Earthshine spectropolarimetry datasets, theoretical models of flux and polarisation signals from Earth-like planets, three Mars spectropolarimetry datasets, and five Mars imaging polarimetry datasets. The Earthshine observations were obtained by Michael Sterzik and Daphne Stam, and were pre-reduced by Stefano Bagnulo. With the aid of Stefano Bagnulo's *FORTRAN* code and *sm* script, I have finalised the reduction and created the plots, along with carrying out preliminary modelling with the help and supervision of Daphne Stam, who wrote the modelling code. The Mars data were taken by Galin Borisov (Rozhen), Stefano Bagnulo, myself, Aaron Stinson (WHT), Alberto Cellino, Maxime Devogèle, and David Vernet (Calern). I have reduced and analysed all of the Mars data with my own *iraf* and *MATLAB* scripts.

Chapter 5 is based on McLean et al. [2017], with figures reproduced with permission © ESO. The original contributions are: eight imaging polarimetry datasets and two spectropolarimetry datasets of Jupiter, along with model interpretations of the data and models of the expected flux and polarisation signals from Jupiter-like exoplanets. The Jupiter observations were carried out by Galin Borisov (Rozhen), Stefano Bagnulo, Alberto Cellino, Maxime Devogèle, and David Vernet (Calern). I have reduced and analysed all Jupiter data with my own *IDL*, *iraf*, and *MATLAB* scripts, partially in collaboration with Galin Borisov. I carried out modelling with the help and supervision of Daphne Stam.

Chapter 6 presents the following original results: eight spectropolarimetry datasets of Saturn, its rings, and Titan, in addition to model interpretations of the results

and model computations of the flux and polarisation of Saturn-like exoplanets. The observations were carried out by Galin Borisov (Rozhen), Stefano Bagnulo, Alex Martin, myself, and Aaron Stinson (WHT), and I have reduced and analysed the data with my own *IDL*, *iraf*, and *MATLAB* scripts. I have carried out the modelling with the help and supervision of Daphne Stam.

Chapter 7 presents the following original contributions: three spectropolarimetry and three imaging polarimetry datasets of Uranus, one set of spectropolarimetry and seven sets of imaging polarimetry of Neptune, model interpretations of the Uranus data and models of the flux and polarisation signals of Uranus and Neptune-like exoplanets. The observations were taken by Stefano Bagnulo (WHT), Galin Borisov (Rozhen), Alberto Cellino, Maxime Devogèle, myself, and Jean-Pierre Rivet (Calern). I have reduced and analysed all data with my own *iraf* and *MATLAB* scripts, and I have carried out the modelling with the help and supervision of Daphne Stam.

Abstract

Light reflected by planetary atmospheres and/or surfaces is polarised, and the degree and direction of polarisation can yield information that cannot always be gleaned from flux measurements alone. Polarimetric studies of solar system planets can reveal more details about the seasonal variations in their atmospheres, and the variation with orbital geometry can place constraints on the properties of cloud particles. With the advent of extremely large telescopes, and potentially the most accurate instruments ever realised thus far, polarimetry has great potential for both detecting and characterising exoplanets. A key difference when observing exoplanets with respect to the planets of our solar system is that despite the much lower signal-to-noise than solar system planets, we can access them at wider phase angle ranges, thus enabling us to probe their scattering properties more extensively, especially at geometries where the degree of polarisation is highest. This can result in an easier interpretation of the atmospheric characteristics through theoretical modelling.

My original contribution to the field that is presented in this thesis is the observation, data reduction and analysis of polarimetric data along with model interpretation of the six most outer solar system planets and Titan. In addition, model results for exoplanets of varying types are shown and discussed. The overall goal is to show that polarimetry is necessary for giving a full description of light reflected by planetary atmospheres and surfaces, and to demonstrate its worth as a diagnostic tool for atmospheric characterisation, from both ground-based observations of solar system and exoplanets, and from in-situ missions to the outer planets, such as a potential atmospheric probe into any of the outer planets.

Chapter 1

Introduction

With the exception of nearby objects in the solar system, most information gleaned about the objects in the Universe is in the form of light, whether in the form of emission or scattering. Electromagnetic waves are collected on Earth, or in Earth-orbit, by telescopes, and are recorded onto detectors. The evolution of the detectors used over the last few decades, namely, the transition from photographic plates to sophisticated charge-coupled device (CCD) cameras has enabled us to greatly advance our knowledge and understanding of the Universe. With the construction of large aperture telescopes in the last twenty years or so (such as the Very Large Telescope (VLT) 4× 8.2 metre telescopes in Chile), and the advent of future Extremely-Large Telescope class facilities (such as ESO's E-ELT, set to be constructed in the 2020s), our means for probing the Universe, both local and afar, have never been as advanced and full of such potential.

Electromagnetic radiation (or simply "light" as we refer to it in the optical regime), is characterised by three properties: the propagation direction, the frequency (or wavelength) and amplitude of the oscillation, and the oscillation direction - the polarisation. The propagation direction, and the amplitude as a function of wavelength, are the most commonly used information in determining the properties of objects in the Universe. Polarisation is often neglected, even though a complete description of light is not possible without considering it. The oscillation direction of the electric field is, by convention, described when talking about the polarisation of light, since one also has the information pertaining to the magnetic field direction since the electric field oscillates perpendicular to the magnetic field.

Polarisation of light is something that is observed in everyday life. Light reflected from any surface is polarised, and sunglasses with polarised filters are very commonly

used to suppress part of this reflected sunlight, such as when driving, or looking at the surface of a body of water. Figure 1.1 shows the surface of a pond containing fish, viewed with and without a polarising filter. Note how the polarising filter reduces the glare from the surface, enabling the user to see the fish much more clearly.

Figure 1.1: Left: image of fish in water without a polarising filter. Right: same image but with a polarising filter. Image credit: https://www.fashioneyewear.co.uk/blog/eye-health-info/what-are-polarized-sunglasses.

As of June 2017, there are 2950 total confirmed exoplanet detections, through various means[1], with almost as many unconfirmed discoveries. The increasing number of ground and space-based missions dedicated to exoplanet study along with the advancement of telescope and instrument technologies suggests that this number will continue increasing. We should also see more and more details regarding the physical properties of exoplanets revealed in the coming years and decades, such as the shape, size, and composition.

Light that is scattered in and reflected by planetary atmospheres is usually polarised, and the value of polarisation is governed by the local atmospheric conditions, the wavelength, and the phase angle. The phase angle is the angle between the Sun (or the parent star(s) of the planet when observing exoplanets), the target, and the observer. The accessible phase angle range from Earth for the inner planets Mercury and Venus spans the full range from 0° to 180°, whilst for the planets outside of Earth's orbit it is limited to values decreasing as the distance from Earth to the

[1] http://exoplanets.org/

planet increases.

The variation of the degree of linear polarisation with wavelength and the phase angle can provide a wealth of information including cloud-top altitudes and cloud composition, and can also reveal the presence of atmospheric absorbers such as methane. Studying the variation of the degree of linear polarisation of light reflected by Venus enabled the composition of the clouds of Venus to be deduced; see Section 4.2 for a detailed review of this. Polarimetric measurements promise to be a crucial tool for characterising the atmospheres of exoplanets, and this is discussed in Section 1.4.

Polarimetry is the general term used to describe the technique of studying the polarisation of light. *Spectropolarimetry* is the term used when considering the variation of the polarisation with wavelength. The studies presented in this thesis are a mixture of both imaging polarimetry (so the consideration of polarisation at one wavelength, and seeing how it varies with spatial direction and/or orbital geometry) and spectropolarimetry. The objects of study are the six outermost planets of the solar system, Titan, and also exoplanets.

This chapter is structured as follows: Section 1.1 gives a summary of the history and development of astronomical polarimetry, from its genesis in the early 19th century, right up until the modern era. Section 1.2 reviews how the observed radiation from planets, stars, and other objects is described. Section 1.3 then gives an overview of polarimetric studies of reflected light in the solar system from small bodies, with the planets each treated as specific cases in the following chapters. Section 1.4 presents a review of polarimetric studies conducted on exoplanet systems, both from observations and theory. Section 1.5 then lays out the aims of this thesis, and what will be presented in each chapter.

1.1 History and development of polarimetry

Etienne-Louis Malus is generally accredited as being the first to study and quantify the polarisation of light in the early 19th century, with the first use of the word "polarize/polarise" being attributed to him. Malus showed that linearly polarised light can be created through reflection and refraction by the surfaces of what are now known as dielectric bodies, such as water and glass [Malus, 1809]. Augustin Fresnel continued Malus's work on quantitatively analysing the polarisation properties of light, publishing a set of now famous laws which govern the polarisation properties of light reflected and refracted at the surfaces of dielectric media [Fresnel,

1819]. George Gabriel Stokes then further quantified the way in which polarisation is measured and represented, through his development of the Stokes parameters: a set of four quantities providing a full description of electromagnetic radiation, which are operationally connected with intensity measurements [Stokes, 1852].

The first occurrence of polarimetry in astronomy was circa 1811, by Francois Arago. He pointed a telescope at the Moon to see if the reflected sunlight had any polarimetric properties similar to those observed by Malus in reflections from glass surfaces. The equipment used by Arago was rather simple by today's standards, but sophisticated for the time. It consisted of a quartz plate, and a Wollaston prism used as a beam splitter. Arago was the first to discover that light reflected by the Moon is polarised [Dougherty & Dollfus, 1989]. It was found by de la Provostaye & Desains [1850] that the degree of polarisation of light scattered from the surface of solids is dependent on the incidence and emergence angles of the light, and on the composition of the substance. It was also found that darker materials give a larger degree of polarisation that lighter ones. Brewster [1863] carried out further research into the polarisation of light reflected by different surfaces, and found that rough surfaces give different polarisation than smoother surfaces. Brewster established the connection between the refractive index and the polarising angle. Brewster's angle, also known as the angle of polarisation, is the angle at which reflected light is fully polarised. At all other angles the reflected light is only partially polarised.

There were further polarimetric observations conducted during the 19th century, but these were restricted to the brightest bodies, with the Moon being the main target. The polarisation of sunlight reflected by comets was first observed in 1819 by Arago from the tail of the Great Comet of 1819 (Comet Tralles) [Arago, 1858]. Light from Capella, which was the closest star system to the comet on the sky during the observations, was observed to be unpolarised. This confirmed that the polarisation of the light from the comet was not due to Earth's atmosphere.

These first astronomical applications of polarimetry were difficult to interpret, due to the complexity of the physics governing the processes taking place. It was found that the polarisation of sunlight reflected by the Moon varied strongly with the lunar phase, and polarisation of light reflected by darker regions of the Moon (maria) was greater than that reflected by bright regions of the Moon (highlands). This effect is referred to as Umov's law, and was formally established in 1905 [Umov, 1905]. It was first observed by de la Provostaye & Desains [1852] from their laboratory studies of the polarisation of light scattered from light and dark materials. Umov's law states that the polarisation, P, of the light reflected by a solid astronomical

body, such as the Moon, is related to the albedo, a, through

$$P \approx \frac{1}{a}. \tag{1.1}$$

The Umov effect has been important throughout the history and development of observational astronomy for establishing the dimensions of asteroids from measurements of their luminosity. On the surface of the Moon, along with planets, asteroids and other solid bodies, the light is reflected by means of diffuse reflection as opposed to specular reflection. Diffuse reflection is where incident light is reflected at many different angles, scattering the light, and specular reflection is where the light is only reflected at one angle. Diffuse reflection is caused by microscopic inhomogeneities on the surface of materials, such as on paper and rocky surfaces. Specular reflection results when the surface is much smoother, such as as the polished surface of a mirror, or a clear body of water.

In the early 20th century, Bernard Lyot conducted observations of the planets and moons of the solar system. Lyot [1929] found that light reflected from the polar regions of Jupiter was polarised, and also observed polarisation from light reflected by Saturn and its rings. Lyot also took measurements of the atmosphere of Venus. To try and interpret his observations of linear polarisation of these objects, Lyot carried out laboratory experiments with particulate surfaces [Lyot, 1929, 1934]. A major discovery from Lyot's work was the change in direction of polarisation observed at phase angles below $\sim 20^\circ$ for atmosphere-less objects. This is referred to as "negative polarisation" due to the directional value imprinted in the sign. This arises due to the type of material that the surface is composed of, and it has been observed that most atmosphere-less bodies of the solar system exhibit negative polarisation at low phase angles.

Audouin Dollfus followed up these observations of Lyot, making further polarimetric investigations of the planets and moons of the solar system. Dollfus was one of the leading contributors to solar system polarimetry in the 20th century, and specific results are discussed throughout this work.

A major result for planetary polarimetry came in the 1970s, when Hansen & Hovenier [1974] successfully characterised the clouds of Venus by comparing ground-based imaging polarimetry with radiative transfer models. More recent results are discussed in this work, including the application to extrasolar planets.

The current state of polarimetry, as of early 2017, is that many telescopes around the world are now equipped with sophisticated polarimeters. New measurements

are being made more and more often, and in fact the field of polarimetry is undergoing somewhat of a resurgence, with its importance in the potential detection and characterisation of exoplanets often emphasised. Most polarimetric measurements are circular polarisation studies of stellar magnetic fields, however this is outside the scope of this work. This thesis, along with providing an original contribution, gives an overview of what has been observed polarimetrically in the solar system throughout the past two centuries, and the application of polarimetry to exoplanets is discussed.

1.2 Description of planetary radiation

This section gives the definitions of the various parameters used when measuring the reflected light from a planet or other smaller body. Chapter 2 gives a more mathematical description of the radiation.

As a function of wavelength, λ, sunlight (or starlight, in the case of exoplanets) reflected by an orbiting planet can be fully described by the Stokes parameters, which are given in the form of a 4-component column vector,

$$\mathbf{F}(\lambda, \alpha) = \begin{pmatrix} F(\lambda, \alpha) \\ Q(\lambda, \alpha) \\ U(\lambda, \alpha) \\ V(\lambda, \alpha) \end{pmatrix}, \tag{1.2}$$

where α is the planetary phase angle, that is, the angle subtended by the Sun (or star, in the case of an exoplanet) and the observer, as seen from the planetary centre. Figure 1.2 illustrates this, and the phase angle is related to the single scattering angle, Θ, through the equation $\alpha = 180^\circ - \Theta$. F represents the reflectance of the planet - when deriving this quantity from observations of solar system objects, one must divide by the solar spectrum to cancel out the variation in wavelength of the flux generated by the Sun. Q and U represent the total linearly polarised flux, and V represents the total circularly polarised flux. Q and U are, by definition, quantities that are defined with respect to a specific reference system, usually this is with respect to the plane containing the Sun, planet, and observer. In the case of this work the direction perpendicular to the planetary scattering plane is used as the zero point, with positive polarisation in this direction, and negative polarisation perpendicular to this (so parallel to the scattering plane). The sign is merely a convention, and is used solely to indicate the direction of polarisation, with the degree

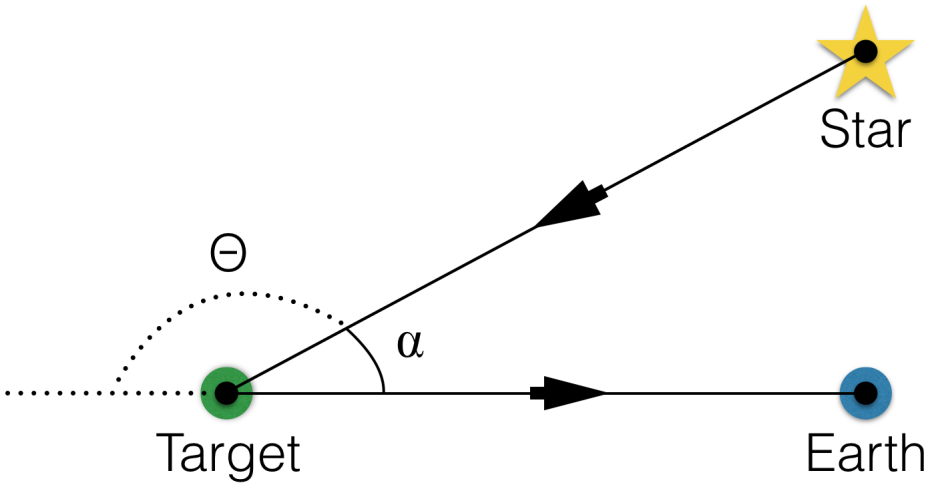

Figure 1.2: Simple illustration showing the phase angle, α, the angle between the star, the observed target, and Earth. The scattering angle, Θ, is also shown.

of polarisation always positive. This is explained in more detail in Section 1.2.1. The transformation between reference planes, such as from the optical plane of a polarimeter, is achieved through use of the following rotation matrix [see Hovenier & van der Mee, 1983]:

$$\begin{pmatrix} 1 & 0 & 0 & 0 \\ 0 & \cos 2\beta & \sin 2\beta & 0 \\ 0 & -\sin 2\beta & \cos 2\beta & 0 \\ 0 & 0 & 0 & 1 \end{pmatrix}, \tag{1.3}$$

where β is the angle between the two reference planes, and is measured in an anti-clockwise direction from the old to the new reference plane when looking towards the observer. In the work presented here, the reduced Stokes parameters are used to describe the reflected planetary radiation in both the observations and models, and are given by

$$P_Q = \frac{Q}{F} \tag{1.4}$$

$$P_U = \frac{U}{F} \tag{1.5}$$

$$P_{\mathrm{L}} = \frac{\sqrt{Q^2 + U^2}}{F}, \tag{1.6}$$

where P_{L} is the total degree of linear polarisation of reflected starlight, and is independent of the choice of reference plane. If P_{L} is used to describe the linear polarisation, the direction of polarisation is given by the position angle, χ, which can be obtained from Q and U by[Hansen & Travis, 1974]

$$\chi = \frac{1}{2} \arctan\left(\frac{U}{Q}\right). \tag{1.7}$$

The details of how the reduced Stokes parameters were calculated from the telescope data are described in Chapter 3. For most planets, the degree of circular polarisation can be considered to be very small, so it will therefore not be considered in the work presented here. This can be done without introducing any errors into the calculated values of F, Q, and U [Stam & Hovenier, 2005]. Also, the sunlight that is incident on a planet is considered unpolarised, since this is the case to a very small error when integrated over the solar disk [Kemp et al., 1987]. For the exoplanet calculations, the incident stellar light is also assumed to be unpolarised.

Signals that are spatially resolved, such as light reflected from individual parts of a planet, can be described using the same formalisms, but replacing the phase angle α with the local illumination and viewing angles (so at each given location on the planet) θ_0, ϕ_0, θ, and ϕ, respectively. This is explained more clearly in Section 2.3.2.

1.2.1 Polarisation of light reflected by smaller bodies

Light reflected by asteroids and other small rocky bodies at visible wavelengths is incident light from the Sun scattered by their surfaces, thus it is expected to be partially linearly polarised. The degree of linear polarisation, P_{L} can be measured by means of a polarising filter as

$$P_{\mathrm{L}} = \frac{F_{\max} - F_{\min}}{F_{\max} + F_{\min}}, \tag{1.8}$$

with $F_{\max}$ and $F_{\min}$ the maximum and minimum flux counts, respectively, measured when rotating the polarising filter around its optical axis. If one considers only Fresnel reflection and Rayleigh scattering, it could be expected that the maximum flux coincides with the point where the optical axis of the polarising filter is aligned perpendicular to the scattering plane, but this is not what is in fact observed with polarimetric measurements. Observations show the direction of maximum flux to be coincident with the scattering plane when the objects are observed in a phase angle range from zero to the inversion angle, α_{inv}, which is usually around 20° for most

asteroids [Cellino et al., 2015]. At larger phase angles the maximum flux, and thus the plane of polarisation, changes by 90°, becoming perpendicular to the scattering plane which is predicted from elementary physics. If we call $F_\perp$ and $F_\parallel$ the fluxes measured through a polarising filter orientated perpendicular and parallel to the scattering plane, respectively, $F_\perp$ and $F_\parallel$ correspond to $F_{\max}$ and $F_{\min}$ in Eqn. 1.8, but in some phase angle ranges $F_\perp$ corresponds to $F_{\max}$, and in others $F_{\min}$. Thus, the following parameter is always used when measuring the linear polarisation of asteroids and other atmosphereless bodies of the solar system [Cellino et al., 2015]:

$$P_{\mathrm{r}} = \frac{F_\perp - F_\parallel}{F_\perp + F_\parallel}. \tag{1.9}$$

The absolute value of P_{r}, usually expressed as a percentage, gives the value of the degree of linear polarisation, with the sign indicating whether $F_\perp$ corresponds to $F_{\max}$ or $F_{\min}$. If $F_\perp$ corresponds to $F_{\min}$, P_{r} is negative, and this situation is referred to as negative polarisation, but as mentioned previously in Section 1.2 this is of course a conventional definition, with linear polarisation of course always being positive. The phase angle range in which P_{r} exhibits negative values is known as the negative branch of polarisation.

Figure 1.3 shows a plot of the linear polarisation as a function of phase angle for asteroid (7) Iris. The negative polarisation branch can be seen to extend up to a value of around $\alpha \sim 22°$. The most extreme value of negative polarisation, $P_{\min}$ occurs in the phase angle range 10-12°, with a value of around 0.7% for Iris. Upon reaching $P_{\min}$, P_{r} shows a linear trend with progressing phase angle. The slope of this linear growth is measured at the inversion angle, α_{inv}, around 22° in the case of Iris, and is denoted as h, with units of percentage of linear polarisation per degree [Cellino et al., 2015].

Due to the limitations in the range of phase angles that can be observed from Earth, Figure 1.3 cannot show that P_r continues to increase with phase angle. This has been seen from laboratory experiments and in observations of near-Earth objects, which can be observed across greater phase angle ranges than those for the main-belt asteroids. The increase in the degree of linear polarisation is observed to continue up to a value $P_{\max}$, which is usually reached at phase angles of around 100° [see Belskaya et al., 2009].

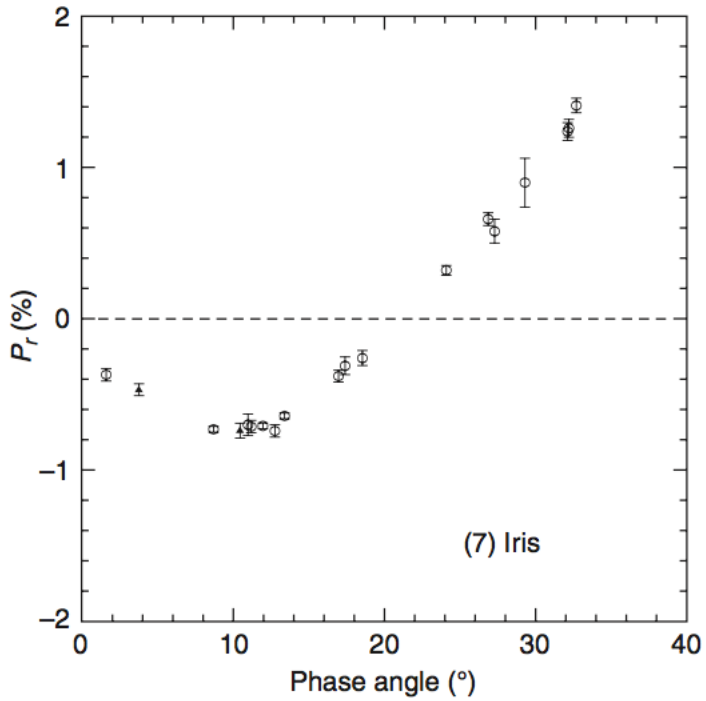

Figure 1.3: Plot of linear polarisation as a function of phase angle for the asteroid (7) Iris. Image credit: Cellino et al. [2015].

1.3 Polarimetry of the solar system (overview)

The Sun, planets, moons, and smaller bodies of the solar system have been the subject of many polarimetric studies. Since we are studying the objects orbiting around the Sun, we do not need to consider the mechanisms that produce polarisation in the process of emission. All of the planets of the solar system have been the subject of polarimetric studies, with some a lot more than others. As well as enabling us to find out more about the planets, these studies provide a benchmark for future polarimetric investigations of extrasolar planets. For the minor bodies of the solar system, most of which have not been visited by dedicated space missions, polarimetry is an important remote sensing tool for determining their albedo and composition. The advent of large telescopes (a telescope is generally referred to as being "large" if the primary mirror size is $\geq$ 6 m) since the late 1990s has extended the range of objects with which polarimetric studies can be carried out [Bagnulo et al., 2011]. Fainter objects such as Centaurs, trans-Neptunian objects (TNOs) and cometary nuclei have been the subject of polarimetric observations in the past two decades or so. Future instruments at ESO's Very Large Telescope (VLT) and the planned E-ELT should increase the likelihood of a detection of an extrasolar

planet through polarimetric means.

Clouds present in the atmospheres of solar system planets have a variety of compositions. Earth of course has water clouds (both in liquid and ice form depending on the altitude at which the clouds are formed). On the giant planets, the clouds are composed of water vapour, ammonia, hydrogen sulphide, and methane. On Mars, the clouds forming in its tenuous atmosphere are made up of carbon dioxide. Venus is enshrouded in a thick layer of clouds made of sulphuric acid droplets. No matter what their composition, clouds influence the climate conditions on any planet. Clouds (both from the top and bottom) are highly reflective, and they reduce the amount of incoming sunlight, and outgoing thermal radiation from the planet. Clouds also play a significant role in the formation of storm systems. To fully account for the effect of clouds on the climate of a planet, (and thus elucidate on whether the planet is habitable or not), detailed information regarding the cloud coverage, cloud particle sizes, and cloud altitude is required.

Measuring the polarisation of reflected sunlight provides a means of studying a planet's atmosphere, and enables a determination of whether the atmosphere is clear, hazy or has an optically dense cloud coverage. The shape of the cloud particles can also be determined (i.e., whether they are spherical or irregularly shaped). The refractive index of the cloud constituents and the particle size distribution can also be determined. Polarimetry can be used to distinguish between the contribution to the atmosphere of the gas molecules (which follow a Rayleigh scattering law, varying with wavelength as λ^{-4}) and the cloud particles, which according to Mie theory, have scattering properties which depend a lot less on wavelength [Woszczyk et al., 1974]. It has been demonstrated that polarimetric observations are more sensitive to the characteristics of cloud particles than intensity measurements, therefore the technique of polarimetry is a powerful tool for investigating the properties of clouds and surfaces on planets [Hansen, 1971a].

Each of the planets of our solar system have very different features, and cannot be treated collectively. The individual planets are specific cases, treated in detail in the various chapters of this thesis with new contributions presented for most. The rest of this chapter is dedicated to categories of objects that can be described collectively, i.e., asteroids, comets, and TNOs, followed by a discussion on the application of polarimetry to exoplanets.

Ranging from Ganymede, the largest moon in the solar system, to small dust particles, the solar system contains a vast number of objects other than the Sun including, by the current classification, eight planets. Carrying out polarimetric studies of the

satellites of the outer planets from Earth is challenging because these bodies are close to their much brighter parent planets, thus the surface is difficult to resolve from ground-based observations. As for any object in the outer solar system, the phase angle range observable from Earth is narrow: the moons of Jupiter can be observed at phase angles of 0 to 12°, Saturn's moons from 0 to 6°, Uranus's moons from 0 to 3°, and Neptune's moons from 0 to 2°. Beginning with the Moon, the rest of this section gives an overview of key polarimetric studies carried out on the smaller bodies of the solar system. Figure 1.4 shows plots of the linear polarisation as a function of phase angle for many of the small objects that will be discussed in this section.

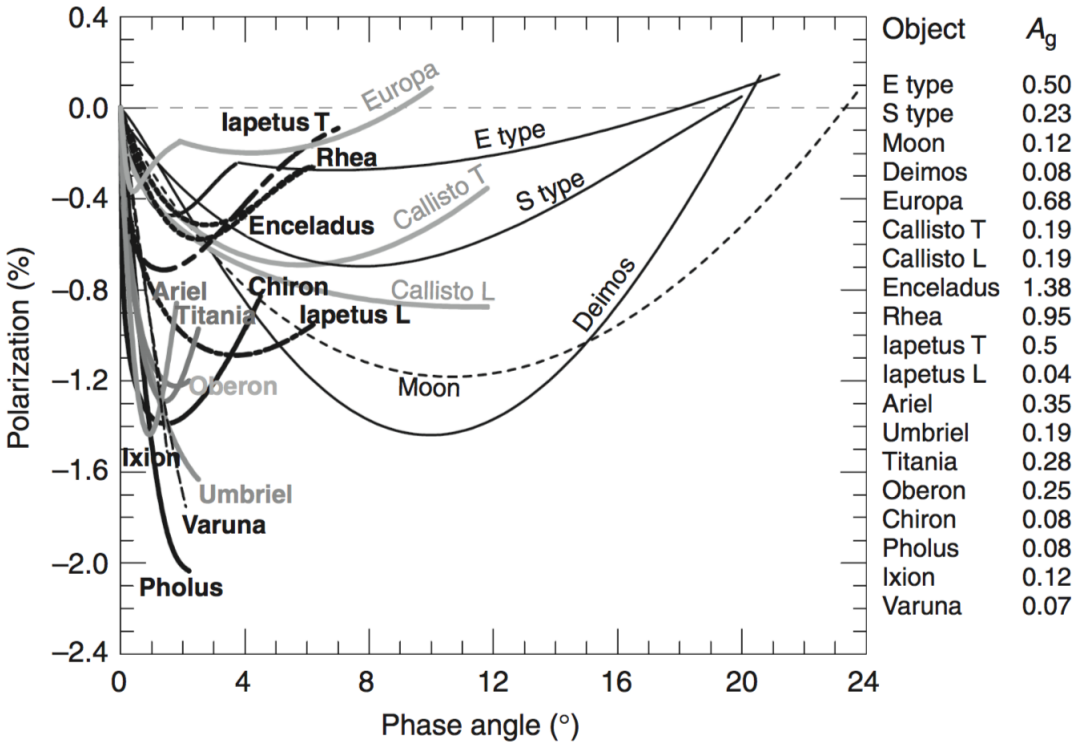

Figure 1.4: Polarisation phase curves for different small bodies: the Moon, Deimos, Europa, Callisto, Enceladus, Rhea, Iapetus, Ariel, Titania, Oberon, Umbriel, E and S-type asteroids, the Centaurs Chiron and Pholus, and the TNOs Ixion and Varuna. The geometric albedos are given on the right-hand side. Figure taken from Rosenbush et al. [2015], see references therein for the data.

.

1.3.1 The Moon

The Moon was the subject of the first astronomical polarimetric studies, for the obvious reason of its proximity to Earth, and thus contrasts between different regions could be observed. Much work has been carried out on trying to understand the polarisation of light reflected by the lunar surface. As mentioned in Section 1.1, Arago [1858] was the first to observe the lunar polarisation, with many followup measurements carried out throughout the 19th century. The Moon has a relatively large polarimetric signal, but early studies of lunar polarisation revealed little diagnostic information with polarimetry still a relatively underexploited technique in optical studies of the Moon. Polarimetry has never been carried out from the lunar surface or in lunar orbit. Interpretations of lunar polarimetric measurements suffer from the same problems as for Mercury, Mars, and other bodies populated with irregular regolith particles.

As mentioned in Section 1.1, Lyot was the first to discover that the direction of polarisation of light reflected by the Moon varies with phase angle. Audouin Dollfus carried out much work on lunar polarisation [see Dollfus, 1962, 1998, 1999, 2000; Dollfus & Bowell, 1971; Dollfus et al., 1971].

Two types of polarimetric measurements are possible for the Moon: discrete and imaging. Discrete polarimetry means polarimetry that has been conducted on specific regions of the Moon, whereas imaging polarimetry presents maps of the polarimetric parameters [Shkuratov et al., 2015]. Key studies that have carried out a sizeable number of discrete polarimetric measurements of the Moon are those by Dollfus & Bowell [1971], Shkuratov et al. [1992], Shkuratov & Opanasenko [1992], and Opanasenko & Shkuratov [1994]. Lunar polarisation can reach levels of almost 20% at phase angles near 100°, as shown in Figure 1.5.

Imaging polarimetry of the lunar surface was carried out by Bowell & Zellner [1974]; Dzhapiashvili & Korol' [1982]. A key result from this was that the degree of linear polarisation at large phase angles correlated with the albedo, demonstrating the Umov effect [Umov, 1905; Hapke, 2005]. Laboratory measurements of lunar samples are crucial for understanding the discrete measurements of lunar polarisation, and have been conducted by Dollfus & Bowell [1971]; Bowell et al. [1972]. Shkuratov et al. [2015] give a more complete overview of polarimetric studies of the Moon.

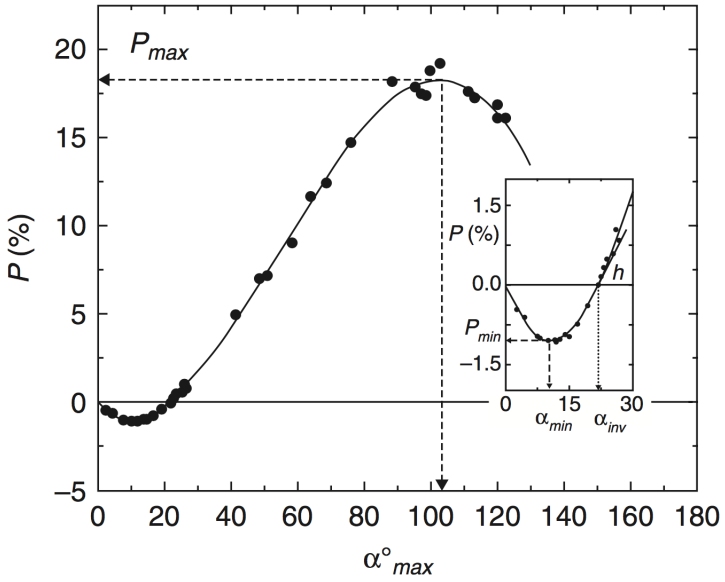

Figure 1.5: Polarisation of the Luna-16 landing site as a function of phase angle, at a wavelength of λ=0.43 μm. Figure from Shkuratov et al. [2015], with original data from Kvaratskhelia [1988].

1.3.2 Moons of Jupiter

The Galilean moons of Jupiter: Io, Europa, Ganymede and Callisto, are the four largest moons of Jupiter, and were discovered in 1610 by Galileo Galilei. The earliest polarimetric studies of these bodies showed that the polarisation is different for the eastern and western elongations [Veverka, 1977]. Due to the synchronisation of the axial and orbital periods of rotation, these satellites always keep the same face to Jupiter, similar to the Moon and Earth. So when observed from Earth a different hemisphere is shown at eastern and western elongations. These hemispheres are expected to have differing regolith microstructures and chemical compositions, and this would cause a difference in the properties of the observed reflected light [Rosenbush et al., 2015].

Rosenbush & Kiselev [2005] carried out imaging polarimetry of the four moons at phase angles from 0.19° to 2.22°. The observed polarisation was compared with laboratory measurements of polarisation of certain materials, and the results were found to be consistent with a surface containing regions with different types of surface layers, with both very bright and relatively dark materials present. The high albedo material (most likely ice) causes a narrow negative polarisation branch, whereas the dark absorbing material (such as dirty ices or silicate materials) causes

a wide branch of negative polarisation. All of the satellites apart from Callisto were observed to have bright materials present, as inferred by a secondary minimum on the negative polarisation branch. This study shows the use of polarimetry as a technique for characterising the surface layer types of solar system objects.

1.3.3 Moons of Saturn

The study of the degree of linear polarisation of light reflected by Titan is the subject of original work presented in this thesis (see Section 6.2.5).

Iapetus is Saturn's third largest moon. Its bulk density of 1.150 ± 0.004 g/cm^3 indicates that it is mostly composed of ice material. The rotation of Iapetus is synchronised to the orbital period of Saturn, hence the moon is tidally locked to its parent planet. An interesting observation of Iapetus is that the leading and trailing hemispheres have an albedo contrast from 0.04 on the dark leading hemisphere to 0.39 on the trailing hemisphere [Spencer & Denk, 2010]. There are several theories as to how this albedo difference has arisen. Spencer & Denk [2010] suggest that deposition of material from Saturn's outer retrograde satellites has resulted in the leading hemisphere having a darker albedo, hence increasing its temperature and sublimation rates of water-ice.

Ejeta et al. [2012] observed the bright side of Iapetus at five different phase angles, carrying out spectropolarimetry over the wavelength range 400-800 nm, in order to assess the light scattering behaviour of any potential surface water-ice present on Iapetus. The degree of linear polarisation was found to increase with phase angle, from -0.9% at 0.77° to -0.3% at 5.2°. The polarimetric phase function was found to be in agreement with previous studies, and with other solar system bodies with a high albedo, such as the icy Galilean satellites and certain types of asteroid. The study provides an additional line of evidence for the way small solar system bodies with high surface albedos and/or surfaces rich in water ice scatter light.

Enceladus is the sixth-largest moon of Saturn. It has the highest albedo of any object in the solar system, reflecting almost 100% of sunlight incident upon it. This was measured by the Voyager missions in 1981, which established that the high geometric albedo is consistent with snow or ice. In 2005, the Cassini spacecraft completed three close flybys of the moon, and the onboard instruments gathered data indicating that Enceladus is geologically active [Spencer et al., 2006].

The only record of polarimetric study of Enceladus, Rhea, and Dione is from observations carried out from 2010 in the R filter. The data are presented in Rosenbush et al.

[2015]. The phase curves for Enceladus and Rhea can be seen in Figure 1.4, with each body displaying a negative polarisation branch fairly typical for atmosphere-less bodies at small phase angles. The phase curve of Dione is limited to phase angles of less than 2°, and displays a steeper branch of negative polarisation [see Rosenbush et al., 2015]. Polarimetric studies of Enceladus at higher phase angles would be especially interesting due to the possibility of detecting polarised light resulting from scattering by cryovolcanic ejecta.

Titan is the largest moon of Saturn, and a unique moon of our solar system, because it is the only one with a sizeable atmosphere. When observed polarimetrically from Earth-based telescopes (and thus at small phase angles like for Saturn) the polarisation is positive, whereas other low albedo solid bodies have a negative polarisation in the same phase angle range [West et al., 2015]. This is due to the atmosphere of Titan, inferred by Kuiper [1944] who concluded that Titan must have an atmosphere based on finding gaseous methane in its spectra.

Veverka [1973] found positive polarisation from Titan, and from this result also inferred the presence of an atmosphere, consisting of a thin molecular layer overlying an absorptive cloud deck. The high polarisation was attributed to the overlying molecular layer, which would cause incident light to undergo Rayleigh scattering, resulting in a relatively high degree of linear polarisation. Measurements from space missions have also confirmed these findings from data taken at higher phase angles, but the strong polarisation is thought to be caused by scattering from cloud and haze particles rather than molecules. HST polarimetric observations from 220 nm to 2000 nm have been shown to be consistent with those polarimetric measurements taken at higher phase angles by space instruments [Bazzon et al., 2014].

Pioneer 11 was the first spacecraft to observe Titan's strong linear polarisation near a phase angle of 90° first reported by Tomasko [1980], followed with a detailed analysis by Tomasko & Smith [1982]. It was found that to account for the observed results the polarisation of the haze particles resulting from single scattering had to be 95% or higher at 90° phase angle at red wavelengths, including photons that were multiply-scattered (which would usually lower overall polarisation). It was noted by Tomasko & Smith [1982] that a vertically homogenous atmosphere consisting of spherical aerosol particles of any refractive index could not account for the high polarisation at any of the observed wavelengths. Attempts were made over the few years that followed to model the optical properties of the haze, but a close enough solution could not be found. Tomasko & Smith [1982] proposed that the differences between red and blue wavelengths could be due to particle sizes increasing with

atmospheric depth.

Following Pioneer 11, the cameras on the two Voyager missions took data for larger phase angles than for Pioneer 11, near 160°. The intensity at these phase angles was found to be too high (known as forward scattering) to be explained by particles of a small enough size to be able to produce high polarisation [Rages & Pollack, 1981]. At these phase angles the intensity is most sensitive to the uppermost layer of aerosol particles, thus photons scattered by particles residing in deeper layers are not registered. Tomasko & Smith [1982] considered this and proposed a model that had larger haze particles at the very top of the haze layer, with radius 0.25 μm, overlying smaller particles that produced high polarisation at smaller phase angles. This model atmosphere configuration was found to account for both the high polarisation and high forward scattering, but a microphysical process producing such a particle distribution is thought to be unlikely [West et al., 2015].

West et al. [1983] found the same problem of matching strong polarisation near a 90° phase angle and strong forward scattering when computing models. A more detailed look into possible types of non-spherical particles was made, but none of the non-spherical particle types described in the literature at the time provided a means to account for the observations. Various laboratory experiments were conducted to try and simulate the haze particles of Titan, and these suggested that the particles could be aggregates of small spheres [Bar-Nun et al., 1988].

West & Smith [1991] carried out further models to calculate the optical properties of these types of particles, with a code utilising a method known as the discrete dipole approximation [see Draine, 1988]. A model fit of the Pioneer 11 and Voyager 2 disk-integrated polarisation data was found, with two models of differing aggregate structures. Data were fitted reasonably well with a model atmosphere containing aggregate particles of monomer radius 0.06 μm, with smaller particles located near the top of the haze layer. This model fitted the polarisation from the small monomer size and the open structure of the particles, with the strong forward scattering produced by coherent scattering in the forward direction, which was found to be sensitive to the overall size of the aggregate particle [West et al., 2015].

Further models of the aggregated haze considering the microphysical processes involved and the particle structure and optical properties were carried out [Cabane et al., 1992, 1993; Rannou et al., 2003; Bar-Nun et al., 2008; Lavvas et al., 2009], with the models evolving in sophistication over the years. Data acquired with the Huygens lander helped to further advance this modelling effort.

The Cassini-Huygens mission entered Saturn orbit in 2004, and consisted of an or-

biter to study the Saturn system (Cassini) and a probe designed to descend into the atmosphere of Titan (Huygens). As the Huygens probe travelled through the atmosphere, polarisation (Stokes F and Q) data were acquired between 160 and 30 km from the surface. The photometric, spectroscopic, and polarimetric measurements that were conducted by the Huygens probe provided a major advancement for the study of the haze on Titan [West et al., 2015]. It was found by Tomasko et al. [2009] that the average haze particle over the probe landing site was made of around 4000 individual monomers with mean radius 0.04 ± 0.01 μm at a range of altitudes from 150 km all the way down to the surface.

1.3.4 Asteroids

Cellino et al. [2015] and references therein give a detailed review of asteroid polarimetry, and since this thesis is devoted mainly to planetary polarimetry there is only a short summary presented here, with some general results from asteroid polarimetry.

Asteroids are bodies orbiting the Sun that are primarily composed of various rocks and minerals, and do not have an atmosphere. There are millions of asteroids in the solar system, ranging in size with the largest, Ceres, having a diameter of almost 1000 km. Some asteroids could be remnants of planetesimals that never grew large enough to become planets. Most asteroids orbit the Sun in the main asteroid belt, with some located in other smaller groups such as the Jupiter trojan asteroids orbiting around the fourth and fifth Lagrangian points of Jupiter, and also bodies closer to Earth's orbit, known as near-Earth objects.

Main belt asteroids orbit the Sun between the orbits of Jupiter and Mars and thus observations are restricted to a phase angle range from approximately 0° to 30°. For near-Earth objects the largest attainable phase angle can often be greater than 40°. A key result from asteroid polarimetric observations is that the plane of linear polarisation at small phase angles is usually parallel to the scattering plane, referred to as negative polarisation and with a change in polarisation direction at the inversion angle, as mentioned in Section 1.2.1.

The phenomenon of the negative polarisation (i.e., the change in direction of the polarisation) may be explained in terms of coherent backscattering [Muinonen et al., 2002], and coherent backscattering is likely the cause of two optical phenomena observed from atmosphere-less solar system bodies at opposition (zero phase angle). One of these phenomena is a narrow peak of brightness that is centred at the exact

direction of backscattering. The other phenomenon is the negative polarisation branch observed at small phase angles, which can be accompanied by a very narrow sharp minimum that is centred at phase angles near zero. The modelling of light scattering through the coherent backscattering mechanism is very complex to carry out [see Muinonen et al., 2012, and references therein], thus interpretation of such observations can be challenging.

Polarimetry of asteroids involves measuring the linear polarisation of sunlight scattered by the surfaces of asteroids at visible wavelengths. Most polarimetric measurement of asteroids has been focussed on the variation of the broadband linear polarisation in the V filter (wavelengths between 500-580 nm) as a function of the phase angle. The observed curves of the polarisation plotted against the phase angle can be used to calculate the geometric albedo of the asteroids. This is made possible due to the fact that there are empirical relations between surface albedo and features of the polarisation curve [Cellino et al., 2012], but, as for planets and other small bodies, data points at as many phase angles as possible are required in order to maximise the accuracy of such calculations. The geometric albedo is related to the optical properties of an object's surface, and to the way in which the incident sunlight is scattered. The albedo can be used to deduce macroscopic properties of an asteroid as well, such as the mineralogical composition. Knowledge of the albedo combined with photometric measurements at visible wavelengths can enable good estimates of the size of objects to be made.

Bagnulo et al. [2015] investigated the use of spectropolarimetry as a tool for asteroid characterisation. Spectropolarimetric measurements of asteroids with different albedos and taxonomic classes were analysed, and it was found that asteroids with slight variations in their reflectance spectra may have stark differences in their polarisation spectra. This finding was suggested as a reason to use spectropolarimetry to refine the classification of asteroids. Bagnulo et al. [2015] also found that the Umov law was violated in some cases, so that the degree of linear polarisation and the value of reflectance may have a positive correlation.

1.3.5 Comets

Kiselev et al. [2015] give a detailed overview of comet polarimetry, with a brief summary presented here.

A comet is a low density body in an elongated orbit around the Sun that is made primarily of ices (mainly water, carbon dioxide, and carbon monoxide) and dust (sil-

icates, carbon, and organics). The nuclei of comets have not warmed significantly, thus their compositions are thought to resemble that of the protoplanetary cloud that the solar system was created from. Upon approaching the Sun on their elongated orbits, comets develop a tenuous atmosphere known as a coma that consists of sublimated ices and dust particles lifted from the surface by the flow of gas. Spectroscopy of comets has indicated emission of gases, absorption of solid species, and a continuum value caused by radiation from the Sun undergoing scattering mainly from dust particles. Dust and gas leave the comet nucleus from jets on the side facing the Sun, and then stream away under the Sun's influence. This dust and gas aligns itself with the magnetic field of the solar wind and forms a tail. Variations in the solar wind cause structures to form in these tails.

Sunlight that is scattered by cometary dust can be polarised, thus polarimetry is a powerful diagnostic tool for characterising the properties of the dust, such as: the shape and structure of the particles, the size distribution of the particles, and the complex refractive index of the material. Like for planets and other minor bodies, observations in a broad phase angle of comets are required for a full characterisation of the particles that compose them. Models of observational data with the assistance of data from laboratory experiments have shown cometary dust to be composed of an ensemble of particles with a complex structure and composition, with predominantly large aggregates of particles of sub-micron size.

Since the 1970s, results from various ground-based and space-based missions have provided measurements of the degree of linear polarisation for comets in a phase angle range from 0-157°. The negative polarisation branch has also been characterised, with trends in the phase angle dependence of the degree of linear polarisation revealing several different polarimetric classes of comet. The polarisation of comets as a function of wavelength has also been studied, along with variations in the polarisation between the coma and tail, with polarisation of jets of material emanating from the surface carried out along with the study of other features in the coma [see Kiselev et al., 2015, and references therein].

1.3.6 Trans-Neptunian Objects and Centaurs

Belskaya & Bagnulo [2015] give an overview of the polarimetric studies that have been undertaken on these objects, with a summary presented here.

The Kuiper Belt is believed to be a remnant of the protoplanetary disk from which the solar system was formed. It is composed of a number of icy objects, which lie

beyond the orbit of Neptune, and some of the objects present are larger than Pluto, such as the dwarf planet Eris, discovered in 2003. A trans-Neptunian object (TNO), is any solar system object that lies beyond the orbit of Neptune in the Kupiter Belt. Pluto was the first TNO to be discovered, in 1930, and the second one not discovered until 1992 (with the exception of Pluto's moon Charon, discovered in 1978). There are over 1200 of these objects now known to exist. The largest known TNOs are Eris and Pluto, followed by Makemake and Haumea. Centaurs are minor planets of the solar system, with a semi-major axis lying between the orbits of Jupiter and Neptune. TNOs, Centaurs and comets contain the most primordial material left over from the formation of the Sun and the planets, and polarimetry can be used for characterising their surface properties.

Polarimetry has been used to try and characterise several TNOs. TNOs can only be observed from Earth at very small phase angles, due to their distance. At these small phase angles, small solar system objects (ranging from moons to small asteroids) exhibit negative polarisation. The variation of the negative polarisation with phase angle is dependent on the size and composition of the scattering particles, and the way in which they are packed together.

Bagnulo et al. [2008] used polarimetry to characterise the surfaces of nine TNOs, four of which were observed in previous works with five new ones observed. Two classes of objects exhibiting different polarimetric behaviour were found. Objects with a diameter > 1000 km, such as Pluto and Eris, were observed to have a small polarisation in the scattering plane (0.5%), which slowly changes with the variation in phase angle. Smaller objects were found to have a rapidly changing linear polarisation with phase angle, reaching 1% at a phase angle of 1°. The larger objects have a higher albedo than the smaller ones, as determined by the slope of the polarimetric curve.

Centaurs are objects which have escaped from the Kuiper Belt through gravitational interaction with Neptune and the other giant planets. They may eventually become members of the Jupiter family of comets, or could be ejected from the region through close encounters with the giant planets. Chiron was the first Centaur which was observed with polarimetry [Bagnulo et al., 2006]. Polarimetry was obtained with FORS1 at the VLT at phase angles ranging from 1.4° to 4.2°. A pronounced branch of negative polarisation was found, and modelling showed that a way to explain this negative polarisation was a two component surface consisting both of dark and bright scattering material.

Belskaya et al. [2010] carried out further polarimetry on Centaurs. Chiron was

again observed, along with Chariklo and Pholus. The first definite conclusions on polarisation properties of Centaurs were found. Observed Centaurs all had surfaces which gave a negative value of polarisation. All three objects were found to display diverse behaviour of polarisation with phase angle, each different to that found from trans-Neptunian objects. This implies that the physical properties of the topmost surface layers of these objects are different. Another feature found was a shift of negative polarisation minima toward lower phase angles, for all three observed Centaurs. For Chiron, the minimum polarisation was found to occur at a phase angle of 1.5°, which is the smallest angle of any solar system body observed so far at which a polarisation minimum occurs. A possible explanation of this was suggested to be a small amount of water frost on a dark surface.

1.4 Polarimetry of extrasolar planets

The first extrasolar planet was detected in 1992, orbiting a pulsar [Wolszczan & Frail, 1992], and in 1995 the first planet orbiting a main sequence star was discovered [Mayor & Queloz, 1995]. Since then, almost 3000 have been discovered, with almost as many awaiting confirmation, as mentioned earlier in the chapter (an online catalogue is maintained at exoplanet.eu, and exoplanets.org, with the known physical properties of detected and unconfirmed exoplanets). Over 20 years after these first exoplanets were detected, the rate of detections has increased almost exponentially year after year. Many instruments dedicated to exoplanet detection and characterisation have been successfully installed at telescopes all over the world, with several space missions as well. NASA's Kepler mission is arguably the most noteworthy mission in the relatively nascent field of exoplanet detection and characterisation, with the telescope having led to the discovery of thousands of exoplanets and exoplanet candidates [Borucki et al., 2003, 2010].

Most of the presently known exoplanets have been detected via indirect methods, where one does not actually detect radiation reflected or emitted by the planet, but the effect of the planet on its parent star is observed. The two main detection methods that have yielded the majority of discoveries thus far are the radial velocity technique (also known as the Doppler method), and the transit method. The radial velocity method works by detecting the effect of the gravitational pull of an orbiting planet on the line-of-sight velocity (the radial velocity) of the star. This is achieved by measuring the shift in spectral lines of light emitted by the star from known positions of lines measured in laboratories here on Earth. The second technique is

the transit method, where the flux of the star is monitored, and planets are deemed to be orbiting the star if the flux is observed to dip periodically for short amounts of time. It takes three observations of a planet transiting a star for a detection to be confirmed. The disadvantage of these techniques is that the planet must be orbiting its star near edge-on in order for a transit to be detected, or for radial velocity changes to be measured.

It has been found that combinations of the indirect methods can yield properties of exoplanets including the orbital period, the radius, and the minimum mass. The spectrum of incident starlight on the upper atmosphere of an exoplanet can provide information on the atmospheric composition [Charbonneau et al., 2002], and so can monitoring how the combined flux spectrum of the planet and star change with time [Queloz et al., 2000]. Such observations of the flux spectrum can yield information on temperature and atmospheric dynamics.

There are other techniques that have, or have the potential, to yield exoplanet discoveries; these include pulsar timing (how Wolszczan & Frail [1992] detected the first exoplanet), astrometry, and direct imaging. Bozza et al. [2016] give a complete overview of the various methods, and how to fully exploit them.

Direct imaging is a method where light from the planet itself is measured. This can either be the stellar light reflected by the exoplanet's atmosphere or surface, or the infrared radiation that the planet emits. A major problem with directly imaging exoplanets is that the angular separation of the planet and star is usually far too small for the objects to be resolved, especially with ground-based telescopes which have the additional limitation imposed by Earth's atmosphere. All directly imaged exoplanets thus far published in the literature have angular separations between the planet and star that are of the order of $\sim$100 AU or more, so at the distance of the Kuiper belt if one were to use the solar system as an analogy.

As well as the separation problem, there is the fact that the stellar flux has a signal much greater than the relatively weak signal of the reflected or emitted radiation from the planet. In the case of a terrestrial sized exoplanet orbiting a solar-type star at 1 AU, the contrast is 10^{-10} [Crossfield, 2015]. However, this is an instance where polarimetry can prove to be advantageous. Integrated over the stellar disk, light from most stars can be considered unpolarised [see Kemp et al., 1987], while it can become polarised upon interaction with a planet. The degree of polarisation is dependent, of course, on the composition of the planet, the phase angle at which the observation is carried out, and the wavelength of the light. In a planetary system containing a hot Jupiter (a Jupiter-like exoplanet that orbits very close to its parent

star, usually within the orbit of Mercury when compared to the solar system), the polarisation of the combined flux from the unresolved star and planet is expected to be between $10^{-5} - 10^{-6}$ [Seager et al., 2000], and this will vary with the planet's orbit around the star, and the changing phase angle.

A key advantage of polarimetry over flux observations is that the degree of polarisation is a relative measure, which helps to characterise planetary atmospheres. The polarisation is independent of the distance between the planet and the star, the distance from the observer to the planet, the radii of the planet and star, and the incoming flux from the star. Therefore, when these parameters are not accurately known - which will often be the case with observed exoplanets - atmospheric information from the polarisation measurements can still be derived. To obtain atmospheric measurements using the observed flux is more complicated, since the absolute flux must be known as well. Also, the degree of polarisation is unaffected by its journey through Earth's atmosphere. So the polarisation features present at certain wavelengths are preserved without the need for atmospheric corrections to be applied.

Wiktorowicz & Stam [2015] give a detailed review of the application of polarimetry to exoplanets, with the following sections summarising the work that has so far been carried out, and also laying out what the future holds for this field. The exo-analogues of solar system planets will be discussed in the appropriate chapters of this thesis.

1.4.1 Studies to date

Currently, the literature pertaining to polarimetric observations of exoplanets is composed of five publications detailing observations of four spatially unresolved exoplanet systems studied by three different groups: HD 189733, τ Boötes, 55 Cancri, and υ Andromedae.

Berdyugina et al. [2008] was the first study to announce the detection of polarised, scattered light from the spatially unresolved exoplanet system HD 189733, with the planet HD 189733b known to be the closest transiting hot Jupiter planet to Earth [Bouchy et al., 2005]. The authors took B-band data over the course of 93 nights, with the DIPol instrument attached on to the 0.6 m KVA telescope in La Palma, Spain. A signal with amplitude $\Delta P \approx 2{\times}10^{-4}$ was detected in phase with the transit of the planet across the star. This was a relatively high signal of linear polarisation which would normally require a high sensitivity for a ground-based instrument.

Berdyugina et al. [2008] interpreted these observations using a model with the most favourable polarisation properties: one with a Lambertian sphere, with geometric albedo A_g=2/3, a polarisation dependence close to that of Rayleigh scattering, with any multiple scattering neglected (multiple scattering lowers the degree of polarisation of reflected light; see Chapter 2 for further elaboration). However, the reported polarisation amplitude would have necessitated the scattering surface of the planet to have a radius of $R = 1.5 \pm 0.2\,R_{\rm Jup}$, whereas Torres et al. [2008] found that the planet's radius was $R = 1.138 \pm 0.027\,R_{\rm Jup}$ in the optical regime from transit photometry measurements.

A follow-up study was made by Wiktorowicz [2009], who carried out six nights of observations of HD 189733 with the POLISH polarimeter on the Palomar 5 m telescope in California, USA. Wiktorowicz [2009] was unable to verify the detection of the scattered light from the planet by Berdyugina et al. [2008], and found an upper limit to the modulation of the polarimetric signal to be $\Delta P \approx 7.9 \times 10^{-5}$, with 99% confidence. However, these observations were made with a broader, redder filter than that used by Berdyugina et al. [2008], and the λ^{-4} dependence of Rayleigh scattering makes it challenging when comparing observations made in different filters.

The HD 189733 system was observed again by Berdyugina et al. [2011a] for nine nights with the TurPol polarimeter, attached to the 2.5 m Nordic Optical Telescope (NOT) in La Palma. Data were obtained in the U, B, and V bands, and a polarimetric signal was observed that was concurrent with the planet's transit across the star. However, the amplitude was refined downwards from the previous study [Berdyugina et al., 2008] from $\Delta P \approx 2 \times 10^{-4}$ to $\Delta P \approx 1 \times 10^{-4}$, thus resolving the previous discrepancy of the different value of planetary radius derived from transit photometry.

A Rayleigh scattering haze composed of small particles has been noted to enshroud HD 189733b through transmission spectroscopy studies [Pont et al., 2008, 2013], so a relatively high polarisation would be expected, but the amplitudes reported are too high to be explained very easily [Bailey, 2014].

A non-detection of scattered light from the τ Boötes and 55 Cancri systems was reported by Lucas et al. [2009], with the PlanetPol instrument at the 4.2 m WHT, La Palma. Upper limits on the polarisation of the two systems were given in a broad red filter (between 590 nm - 920 nm) and an upper limit on the geometric albedos of the planets were derived from Rayleigh scattering models.

Berdyugina et al. [2011b] reported the detection of the non-transiting hot Jupiter planet υ Andromedae b from ten nights of TurPol observations at the NOT. How-

ever, the amplitude of the polarimetric signal was found to be degenerate between planetary radius and albedo, and the fact that the planet is non-transiting (it was discovered via the radial velocity technique) precludes direct measurement of the radius.

Much theoretical work has been carried out on the study of what could potentially be detected from exoplanets using polarimetry. Stam et al. [2004] carried out a study of light reflected by Jupiter-like exoplanets, demonstrating that different atmospheric configurations containing mixtures of molecules, cloud, and haze particles can all leave different imprints on the flux and polarisation spectra. Stam [2008] describes models of the reflected flux and polarisation from Earth-like exoplanets. The study demonstrates that polarimetry can be a useful tool for deriving cloud-top altitudes, and oxygen mixing ratios in planetary atmospheres.

Karalidi et al. [2012a] present a numerical study that assesses the potential of polarimetry as a diagnostic tool for detecting features arising due to the presence of water clouds on exoplanets. Polarisation is more sensitive to detecting rainbow features, and the scattering angle of the rainbow features are sensitive to the refractive index and the effective radius of the scattering particles. Karalidi et al. [2012a] investigate the influence of ice clouds on the rainbow feature, since such clouds can mask the rainbow signature. Karalidi et al. [2012a] found that the total flux only shows a weak signal arising from the rainbow feature, with the introduction of ice clouds dampening the signal. The degree of linear polarisation was found to be more sensitive to the rainbow feature, and Karalidi et al. [2012a] demonstrate that liquid water clouds covering a fraction of 10-20% of a planetary surface, with half of these clouds also covered by ice clouds, still produces a feature in the polarisation due to the rainbow.

Karalidi & Stam [2012] show disk-integrated model flux and linear polarisation signals of reflected starlight from spatially unresolved exoplanets with horizontal inhomogeneities. It was found that the introduction of variations in surface and cloud coverage in the integrated signal left different traces in the flux and polarisation signals, with the shape of the polarisation phase function sensitive to the introduction of significant horizontal inhomogeneities.

Fossati et al. [2012] reports that polarimetry could be used to detect rocky planets orbiting close ($\sim$0.01AU) to the parent star in the habitable zone of white dwarfs because the polarimetric signal is 10^2 to 10^4 times larger than it would be for a planet in the habitable zone of a typical Sun-like star.

Karalidi et al. [2013] present numerical models of disk-integrated spectropolarimetric

signals of reflected starlight from gaseous exoplanets with horizontal and vertical inhomogeneities. Features present on the gaseous planets of the solar system such as belt and zonal regions, cyclonic spots (such as Jupiter's GRS), and polar hazes were included to see if these features left an imprint on the disk-integrated flux and linear polarisation signals. It was found that a planet including a feature similar to Jupiter's GRS covering a few percent of the visible disk would introduce a noticeable variation in the measured flux and polarisation signals. The disk-integrated signals of planets containing polar haze caps were found to have an increased degree of linear polarisation, but a negligible change in the flux signal.

1.4.2 What the future holds

The ability to detect or characterise exoplanets that are spatially unresolved is currently at the limit of the telescopes and instruments available presently. As Wiktorowicz & Stam [2015] and Snik & Keller [2013] highlight, special attention must be given to systematic effects, which are especially apparent when observing from ground-based telescopes. Systematic effects can arise from the telescope and instrument, the sky, the interstellar medium, and the host star of the exoplanet. Atmospheric effects also have to be considered as, for example, it has been noted that observations from telescopes in La Palma can be affected by spurious polarisation signals resulting from Saharan dust blown into the atmosphere [see Hough et al., 2006; Bailey et al., 2008].

For spatially resolved exoplanets, polarised light from long-period exoplanets may be resolved with the Gemini Planet Imager (GPI; Macintosh et al. [2006, 2014]), and the Spectro-Polarimetric High-contrast Exoplanet REsearch instrument of the VLT (SPHERE; Beuzit et al. [2008]). Telescopes planned for the future, such as ESO's European Extremely Large Telescope (the E-ELT), will further enable the study of polarised light scattered from exoplanets.

1.5 Rationale and aim of this thesis

The aim of this thesis is to apply the technique of polarimetry, both in an observational and theoretical capacity, to some of the planets and moons of the solar system, and to extrasolar planets. Imaging polarimetric and spectropolarimetric data for Earth, Mars, Jupiter, Saturn, Uranus, Neptune, and Titan are presented, and have all been fully reduced mostly using my own data reduction scripts. Some

of this work has been published or submitted for publication, and will be indicated when appropriate. The overall goals of the thesis are to present new results for the planets and moons of the solar system, and explain what these results show in terms of theoretical models. As well as this, the application to exoplanets is strongly emphasised, and model results for exoplanets of varying configurations are presented. Polarimetry is often an underexploited technique in astronomy, and a major aim of this thesis is to convince the reader that it is both necessary, and not over complicated (and doesn't have to be financially expensive, which is a major factor for the inclusion of polarimeters in telescopes and space missions).

The largest contribution to this thesis is the many observations of Jupiter, obtained mostly with the Torino Polarimeter at Calern (see Section 3.2.4 for a description). I was given a fantastic opportunity to be trained as an observer on this telescope, ultimately aiding in obtaining the large volume of data presented in this thesis. Working with these data occupied the majority of the time that was spent on the PhD, on developing the reduction technique and on modelling the results.

The remainder of this work is structured as follows: Chapter 2 presents the framework for describing light and its polarisation properties, and discusses physical mechanisms from which polarised light can arise. The radiative transfer code used to model some of the observations, and model light reflected by exoplanets, is also presented in this chapter. Chapter 3 describes the various instruments and telescopes used for gathering the data presented in this thesis, along with the data reduction techniques that were developed and applied.

Chapter 4 presents a review of polarimetric studies of the terrestrial planets of our solar system, along with spectropolarimetric observations of Earthshine, and models of light reflected from Earth-like exoplanets. Variations in the continuum flux and polarisation arising from changes in the surface and atmospheric composition are explored. Imaging polarimetric and spectropolarimetric observations of Mars are also presented, along with models of light reflected by planets with dusty surfaces and tenuous atmospheres. Chapter 5 presents polarimetric maps and spectropolarimetry of Jupiter, along with model interpretations. Models of light reflected by Jupiter-like exoplanets are also presented and discussed. Chapter 6 shows several sets of spectropolarimetric results for Saturn, its rings, and Titan, along with imaging polarimetry of Saturn in the continuum and in prominent methane bands. A model interpretation of the spectropolarimetric data is also presented, along with modelled flux from Saturn-like exoplanets. Chapter 7 then presents imaging polarimetric and spectropolarimetric observations of Uranus and Neptune. Chapter 8

finally summarises the work presented in this thesis, its implications, and discusses what future work could be carried out.

Chapter 2

Theory

Electromagnetic waves consist of both electric and magnetic field components oscillating in perpendicular planes, both of which are perpendicular to the direction of propagation. Electromagnetic waves contain information about the source from which they were emitted. This information can be deduced from analysing the direction of propagation, the amplitude and frequency of the oscillations and the direction of oscillation - also known as the polarisation. Polarimetry measures how the electric field vector oscillates in the plane perpendicular to the direction of propagation. There are several mathematical formalisms used to describe polarisation. The Jones formalism describes light in terms of the amplitude and phase of an electric field vector, and in astronomy this formalism is used to describe waves in the sub-millimetre and radio parts of the spectrum. The Stokes formalism applies to measurements of the intensity of photon fluxes in the optical regime, and can describe partially polarised and unpolarised light. This is useful for astronomical polarimetry since the degree of polarisation of most sources tends to only be of the order of a few percent.

There are many processes that can lead to radiation becoming polarised in astrophysical situations. Polarimetric mechanisms relate to the emission or absorption of atoms when a magnetic field is present, or to the scattering of light by particles such as free electrons, or grains of dust. In planetary atmospheres, unpolarised stellar light can interact with the constituent particles, which impart a certain level of polarisation on the scattered photons.

This chapter is structured as follows: Section 2.1 gives an overview of the methods by which light can become polarised, then Section 2.2 presents a mathematical description of light and explains how the polarisation is described. Section 2.3 then

describes the radiative transfer code used when carrying out the various models that are presented in this study.

2.1 Physical Mechanisms of Polarisation

Polarised light can result from two types of physical interactions: emission, predominantly in stars, and scattering, such as from interstellar dust and particles in the atmospheres of planets like Jupiter. This work only considers light that is polarised due to interaction with planetary bodies, i.e. polarisation that results from scattering. This section outlines the means by which polarised light results: firstly from emission, in stars, and then from scattering, with an emphasis on scattering in planetary atmospheres and light scattered by biological material.

2.1.1 Polarisation Resulting from Magnetic Fields

Whilst this work does not consider polarisation of light that is emitted from stars, a brief overview is given here for completeness. More details on this subject can be found in Landi Degl'Innocenti & Landolfi [2004] and Bagnulo & Landstreet [2015]. The Zeeman effect is used for the detection and study of magnetic fields in stars. The classical interpretation of the cause of the Zeeman effect is outlined below.

Line formation at a star can occur due to the emission of an electric charge in the presence of a magnetic field, oscillating at a frequency ν_0 under the action of an elastic force. When observed along the direction perpendicular to the vector of the magnetic field, the motion of the charge can be split into three components. One of these is at a frequency equal to the natural frequency of the oscillator (called the π component), one equal to the natural frequency plus the Larmor frequency and the final equal to the natural frequency minus the Larmor frequency. These components are called the σ components, with the Larmor frequency designated by ν_{L}. The π component of the harmonic oscillation is parallel to the direction of the magnetic field vector, and the σ components are perpendicular to the magnetic field. If the electric charge is observed along the direction parallel to the magnetic field vector, then the motion of the charge can be described by two circular oscillations in opposing directions (σ components), at the frequencies $\nu_0 \pm \nu_{\mathrm{L}}$. These components are shown in Figure 2.1.

If an emission line is formed in the presence of a magnetic field, and is observed perpendicular to the line of sight, then it will appear to be split into three compo-

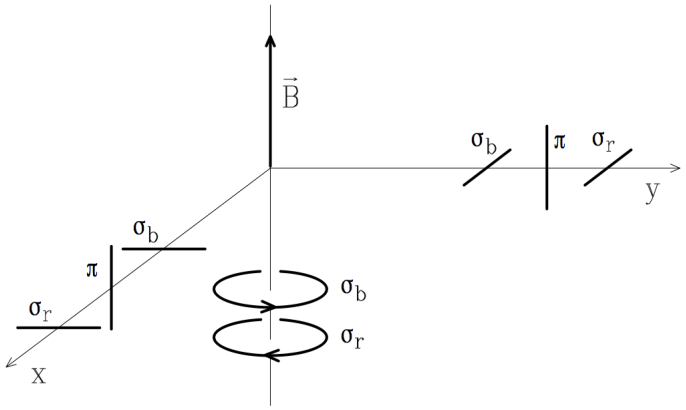

Figure 2.1: This shows the components of the light interacting with the magnetic field. Figure from Bagnulo & Landstreet [2015].

nents: a π component and two σ components. The π component is polarised in the direction parallel to the magnetic field, at frequency ν_0, and the two σ components with frequencies $\nu_0 \pm \nu_L$ are both linearly polarised in the direction perpendicular to the magnetic field. If the spectral line observed is an absorption line, then this line will have its π component polarised in the direction perpendicular to the magnetic field, and the two σ components will be linearly polarised in the direction parallel to the magnetic field. If the magnetic field is directed along the line of sight, then the spectral line will appear to be split into two σ components at $\nu_0 \pm \nu_L$, which are circularly polarised in opposite directions. If the magnetic field vector is orientated at an arbitrary angle, then the spectral line components of this 'Zeeman triplet' are elliptically polarised.

2.1.2 Polarisation resulting from scattering

A detailed review of the concepts and the theory involved in light scattering from planetary atmospheres can be found in Hansen & Travis [1974], and also in Hovenier et al. [2004], with the following providing a brief overview sufficient for the work presented in this thesis.

If light is incident on a particle much smaller than the wavelength of the light, this light will undergo a process known as Rayleigh scattering. The cross-section (i.e. the probability) for Rayleigh scattering varies as λ^{-4} so it is much stronger for smaller wavelengths. Since blue wavelengths have a much higher scattering cross section, this is the reason for the blue appearance of the sky. At sunrise and sunset, the

reason for the reddish appearance of the sky is that the light has to travel through a larger amount of atmosphere, so most of the blue light is scattered before it reaches our eyes, meaning colours towards the red end of the spectrum dominate. Water and ice molecules in clouds are much larger than the molecules that make up the air, so they scatter all wavelengths of light equally, hence appearing white [Greenler, 1980].

Rayleigh scattering from haze particles can produce light with a strong degree of linear polarisation, from 20% to 90%, depending on the structure of the particle from which the light is scattered. Haze particles lie suspended in the atmosphere, and obscure visibility. Examples of haze particles are water vapour, smoke, and dust. Light reflected from planetary atmospheres is generally polarised, thus polarimetry is a strong tool for the detection and characterisation of these atmospheres, and potentially the inference of life on other planets.

In clouds, liquid droplets cause linear polarisation through reflection and refraction, which can cause degrees of polarisation $> 50\%$ for scattering angles of around 140°, the angle at which the primary rainbow is produced (depending on the refractive index and effective radius of the scattering particles). Ice crystals in clouds reflect and refract light in different ways, and no distinct polarisation features such as rainbows are produced, except locally. As mentioned in Section 1.4.1, Karalidi et al. [2012a] carried out a numerical study showing that polarimetry can detect the rainbow feature arising from the presence of liquid water on exoplanets, even when there are ice clouds present above the liquid water clouds.

Multiple scattering in planetary atmospheres can randomise the direction of polarisation caused by the previous single scatterings, and cause an overall significant lowering of the observed polarisation degree. So the net polarisation of reflected light is dependent on the scattering angle, the properties of the scattering particles, and on the general structure of the atmosphere [Buenzli & Schmid, 2009]. Section 2.3 gives a more detailed account of light reflection in planetary atmospheres, with an emphasis on how to model such events.

2.1.2.1 Polarisation Induced by Organic Molecules

Biological molecules are chiral, that is, two forms of the molecule can exist with both forms mirror images of each other. These two different forms are known as left and right handed, and are not superimposable on each other. An everyday example would be scissors: a pair of left-handed scissors is not superimposable on a pair of

right-handed scissors. Homochirality is a term used when a molecule can potentially exist in both mirror image forms, but only one is known to exist. Sugars and nucleic acids exist only in their right-handed form, whilst amino acids and proteins exist only in their left-handed form. The reasons for the phenomenon of homochirality in living material are unknown, but are potentially related to the origin of life.

Chirality induces optical activity, with each form, left or right handed, rotating the reflected or transmitted light in opposite directions. Homochirality guarantees an excess of circularly polarised light in one direction. Therefore, biosignatures could be sensed remotely by means of polarimetry. Deciduous plants on Earth have a sharp increase in their leaf reflectance at wavelengths between 700-750 nm [Seager et al., 2005]. This is known as the vegetation red-edge, caused by the presence of chlorophyll, and is an example of a biosignature.

Woolf et al. [2002] were the first to detect the vegetation red-edge in the spectrum of Earthshine. Sterzik et al. [2012] reports on the detection of the vegetation red-edge caused by the presence of chlorophyll on Earth, from spectropolarimetric observations of Earthshine.

2.2 Measurement and Description of Polarisation

Section 1.2 gave an overview of how to describe planetary radiation, and the equations and methods detailed there are sufficient for the applications considered in this work. However, a PhD thesis on polarimetry would not be complete without an exploration of the various formalisms that light and its polarisation can be described with. Equally as important is the mathematical representation of the various optical devices that are used in astronomical polarimeters, and the various components of a polarimeter are described in Section 3.1.

2.2.1 Stokes Formalism

The Stokes formalism was introduced by Stokes [1852], and it applies to intensity measurements of photon fluxes as performed by detectors in the optical regime. It can describe partial polarisation, which is useful for astronomical polarimetry because most sources have a degree of polarisation of at most a few percent. Interference phenomena however cannot be described by the Stokes formalism. The Stokes parameters are illustrated in Figure 2.2.

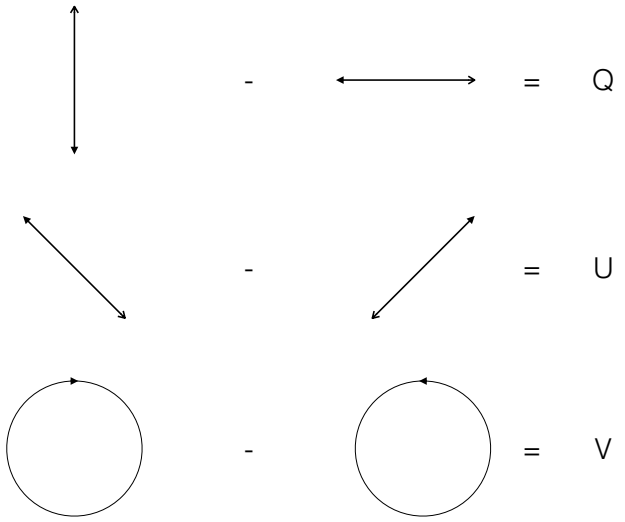

Figure 2.2: A basic diagram showing how the Stokes parameters are defined in terms of the light oscillating in various planes.

The Stokes vector is expressed as:

$$\mathbf{S} = \begin{pmatrix} F \\ Q \\ U \\ V \end{pmatrix} = \begin{pmatrix} F'_{0^\circ} + F'_{90^\circ} \\ F'_{0^\circ} - F'_{90^\circ} \\ F'_{45^\circ} - F'_{-45^\circ} \\ F'_{RHC} - F'_{LHC} \end{pmatrix} \tag{2.1}$$

which spans the space of all the polarisation states of light (namely unpolarised, partially polarised, and fully polarised). The F component represents the incoherent sum of the signal (there are no interference effects), Q and U are the differences in linear polarisation states at two perpendicular planes and the V component represents the circular polarisation. F can also be expressed as $F'_{45^\circ} + F'_{-45^\circ}$ or $F'_{RHC} + F'_{LHC}$. So, for example, light with a Stokes vector of $\mathbf{S}$ = (1,0,0,0) would be completely unpolarised, and a Stokes vector of $\mathbf{S}$ = (1,1,0,0) describes light with a linear polarisation in the 0° direction. A Stokes vector of $\mathbf{S}$ = (1,0,0,1) would imply right-handed, circularly polarised light (clockwise as seen by the observer), and (1,0,0,-1) would imply left-handed, circularly polarised light (anti-clockwise as seen by the observer).

In the case of fully polarised light, the total flux is given by:

$$F = \sqrt{(Q^2 + U^2 + V^2)} \tag{2.2}$$

and for partially polarised light the flux is given by:

$$F \geq \sqrt{(Q^2 + U^2 + V^2)} \tag{2.3}$$

The degree of polarisation, P, is the ratio of the flux of polarised light to the flux of the unpolarised light. This quantity can be represented in terms of the Stokes parameters by:

$$P = \frac{\sqrt{Q^2 + U^2 + V^2}}{F} \tag{2.4}$$

which in the case of only linear polarisation ($V = 0$), we add an L subscript to P to indicate that only linear polarisation is present:

$$P_{\mathrm{L}} = \frac{\sqrt{Q^2 + U^2}}{F}. \tag{2.5}$$

2.2.2 Mueller Calculus

The Mueller calculus employs matrix algebra to compute the signal of a beam of light propagating through one or more optical elements, usually polarisers and retarders (more details on the optics are given in Section 3.1). Conventional algebraic and trigonometric methods are cumbersome when the number of polarisers or retarders is large, fundamentally due to the complicated nature of light and its interaction with matter. The incident light is described by several parameters: amplitude, degree of polarisation, and form of polarisation (linear or circular). The Mueller calculus simplifies the calculations by condensing all of the necessary parameters describing the light into one single vector. Each optical element can also be represented by a single matrix, and the result of introducing any number of optical combinations can be found simply by multiplying the matrices of each component together. Then this matrix is multiplied by the vector specifying the incoming light, to produce the vector describing the light exiting the optical setup.

The incoming light is described by the Stokes vector (see Eqn. 2.1) and the elements present are described using the Mueller matrices, so the Stokes vector of the light

upon exiting the optical setup is given by:

$$\mathbf{S_{out}} = \mathbf{M} \cdot \mathbf{S_{in}} \tag{2.6}$$

where $\mathbf{M}$ represents a Mueller matrix of an arbitrary single optical device. $\mathbf{S_{in}}$ and $\mathbf{S_{out}}$ are the Stokes vectors describing the light upon entry to and exit from the optical device, respectively. For a system consisting of several different optical devices, the outgoing Stokes vector is given by:

$$\mathbf{S_{out}} = \mathbf{M_n}... \cdot \mathbf{M_2} \cdot \mathbf{M_1} \cdot \mathbf{S_{in}} \tag{2.7}$$

where $\mathbf{M_n}...\mathbf{M_1}$ are the Mueller matrices of the n elements present in the optical system, with $\mathbf{M_1}$ representing the first element and $\mathbf{M_n}$ representing the last element.

The Mueller matrix is what is used to describe each optical element, e.g., a polariser, a retarder or a scatterer. These matrices are 4×4, containing 16 elements. Most of the elements are zero for certain ideal devices.

The Mueller matrix of an individual device indicates the composition of the device along with its azimuthal orientation. For example, the Mueller matrix of a linear polariser with a horizontal transmission axis is different from the matrix describing a similar polariser which has been turned so that its transmission axis is at 45°. Turning an optical device around such that a different face serves as the entrance face for the light may also mean a different Mueller matrix is required. Tilting a device so that light is incident at an oblique angle may also necessitate the use of a different matrix.

A Mueller matrix only describes the optical device with respect to one beam emerging. For the case of a Wollaston prism, which has two emerging beams, a single Mueller matrix can only describe one of these beams. So if both beams are of interest, then two Mueller matrices must be used and two separate calculations must be carried out.

The standard rules of vector and matrix algebra apply for the Mueller calculus, but the following convention must also be observed: the vector which represents the incident beam must be written furthest to the right, and the matrices representing successive devices encountered must be arranged in order, so the last device to be encountered by the light would have its matrix written at the far left [Shurcliff, 1962].

2.2.3 Jones Calculus

The Jones calculus, developed by Jones [1941], is another formalism which may be used to describe the interaction of light with an optical system. The Jones formalism of polarisation describes light in terms of an electric field vector, with an initial amplitude and phase. In the context of astronomical polarimetry, this formalism applies to the submillimetre/radio regime, where the detectors are antennae which directly measure the electric field vector. This treatment is derived directly from electromagnetic theory, and employs a vector to describe the incident light, with the optical device represented by a matrix, and the outgoing light ray is obtained by multiplying the vector of the incoming light with the matrix of the optical device. It is most suited for solving problems in which the phase is of importance. The Jones vector describes an incoming beam of light's state of polarisation and amplitude components at a given position along the beam. In a right-handed Cartesian coordinate system, if the beam of light is travelling along the z-axis, then the Jones vector has the general form:

$$\mathbf{E} = \begin{pmatrix} E_x(t) \\ E_y(t) \end{pmatrix} = \begin{pmatrix} A_x e^{i(kz-\omega t+\phi_x)} \\ A_y e^{i(kz-\omega t+\phi_y)} \end{pmatrix} \tag{2.8}$$

where E_x and E_y are the scalar components of the instantaneous electric field vector along the x and y axes, respectively. A_x is the maximum value of E_x, and A_y is the maximum value of E_y. The wavenumber is represented by k $(= 2\pi/\lambda)$, z is the position along the z (propagation) axis at $t = 0$, ω is the angular frequency $(\omega = 2\pi\nu)$ and t the time. ϕ_x and ϕ_y represent the initial phases of the waves.

The intensity of a beam of light in the Jones calculus is proportional to the sum of the squares of the magnitudes of the individual elements of the vector. The units of intensity or amplitude can be chosen such the constant of proportionality is unity, giving:

$$F = A_x^2 + A_y^2 \tag{2.9}$$

Shurcliff [1962] gives a more detailed description of both the Jones and Mueller calculi, and provides several examples.

2.2.4 Comparison of Mueller Calculus and Jones Calculus

The Jones and Mueller calculi have much in common; each formalism describes the incoming and outgoing light with a vector, and employs matrix algebra in order to compute the final vector. Each type of calculus can be performed simply by looking up the matrices describing the various types of optical device and carrying out the calculations.

However, the Jones calculus differs from the Mueller calculus in several ways:

- The Mueller calculus is based on experimental studies, whereas the Jones formalism is derived from the classical theory of electromagnetism.
- The optical devices are described by a 2×2 matrix instead of a 4×4 in the Jones calculus. The elements of these matrices can be complex, whereas all matrix elements are real for the Mueller calculus.
- The Jones calculus is useful for describing problems in which phase information must be preserved, whereas the Mueller calculus pays no attention to phase.
- The Jones calculus is suitable for handling problems which involve combining two coherent beams. The Mueller calculus is not designed to handle such scenarios.
- The Mueller calculus utilises the Stokes vector in its calculations, with the first component of the Stokes vector being the intensity. The intensity is not directly given in the Jones calculus, the sum of the squares of each element must be computed in order to find it.

2.3 Radiative transfer modelling

In order to interpret some of the observational data presented in this thesis, numerical models of flux and polarisation of the reflected light were carried out via an adding-doubling algorithm. The modelling was achieved by considering the planetary atmospheres to be constructed from locally plane parallel, horizontally homogeneous layers with pressure profiles specific to the individual planet. Each atmospheric layer consisted of a mixture of molecules, and optionally cloud and/or haze particles, relatively larger than the molecular species, of varying optical thickness. Cloud and haze particles with different microphysical properties were trialled when comparing data with models, and the height in the atmosphere along with optical

thickness was varied in order to try and reproduce the observed values of polarisation, whether as a function of planetary latitude, wavelength, or phase angle. The models in this study only consider spherical particles, described by Mie theory, with fractal aggregates also considered in the case of Jupiter models (see Chapter 5). Firstly a description of radiative transfer in a planetary atmosphere is presented in Section 2.3.1, then Section 2.3.2 explains how the model works. Section 2.3.3 then demonstrates the sensitivity of the code to changes in the input parameters.

2.3.1 Radiative transfer in a planetary atmosphere

A review of basic concepts is presented here, Chandrasekhar [1950]; Hansen & Travis [1974]; Hovenier & van der Mee [1983] give a more detailed treatment of radiative transfer, and of the inclusion of polarisation in such calculations.

All media such as planetary atmospheres, oceans, and stellar environments contain electromagnetic radiation. Where there is radiation present in such a medium, it is said that a radiation field exists. It is assumed here that radiative (energy) transfer follows the classical theory that energy is transported across surface elements along pencils of rays. A key concept in describing a radiation field is the intensity at a specific point in a certain direction, and can be defined thusly: the amount of radiant energy $\mathrm{d}E$, in the frequency interval ν to $\nu + \mathrm{d}\nu$ which is transported in the time interval $\mathrm{d}t$ through the surface area element $\mathrm{d}\sigma$ in directions confined to the element of solid angle $\mathrm{d}\Omega$ and with an axis parallel to the surface element can be written as:

$$\mathrm{d}E = I \,\mathrm{d}\nu \,\mathrm{d}\sigma \,\mathrm{d}\Omega \,\mathrm{d}t, \tag{2.10}$$

where I is the specific intensity; see Fig. 2.3 for an illustration. The intensity I of a radiation field at point O in the direction r of a unit vector $\mathbf{r}$ is the energy that flows at O in the direction of r, per unit of frequency interval, surface area perpendicular to r, solid angle and time. In SI units the intensity is given in $\mathrm{W\,Hz^{-1}\,m^{-2}\,sr^{-1}}$. The energy flowing in the direction of r through an element of surface area $\mathrm{d}\sigma'$ that makes an angle of ϵ with $\mathrm{d}\sigma$ per unit of frequency, solid angle, and time is $I \cos\epsilon \,\mathrm{d}\sigma'$ where I is the intensity at O in direction r.

The net flux, F, is also an important quantity in radiative transfer calculations. This is defined as the amount of energy at point O flowing in all directions per unit

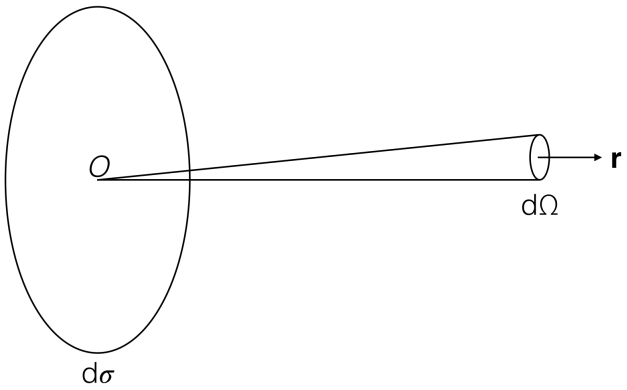

Figure 2.3: Illustration showing the surface area element $\mathrm{d}\sigma$ and the element of solid angle $\mathrm{d}\Omega$, used to define the intensity at a point O in the direction r of unit vector $\mathbf{r}$.

of frequency interval, surface area, and time:

$$F = \int \mathrm{d}\Omega \, I \, \cos \epsilon \tag{2.11}$$

where the integral is performed over all solid angles with I generally a function of direction. The SI units of flux are $\mathrm{W\,Hz^{-1}\,m^{-2}}$. The integral can also be performed over all frequency ranges (a bolometric flux), where the units would be then in $\mathrm{W\,m^{-2}}$.

A various range of terms exist for describing the concepts of intensity and flux. Intensity can also be called specific intensity or radiance, and from the point of view of an observer it can be known as surface brightness. Flux is often called irradiance, or flux density in the case where it is per unit frequency. However, the most fundamental quantity for describing the energy flow from a specific point in a radiation field is intensity, which is always per unit solid angle. For light propagating in a planetary atmosphere, it is useful to consider a parallel beam of light in one direction, which serves as a good approximation for sunlight entering a planetary atmosphere [Hansen & Travis, 1974]. In this approximation, the radiation field can be described via the net flux related to a unit area in the direction perpendicular to that of the propagating light. The following subsection describes the various angles and terms used when performing the local calculations of reflected light.

2.3.2 The radiative transfer code

The radiative transfer model that is used in this thesis for the interpretation of observations and modelling of exoplanetary signals is an adding-doubling algorithm similar to that used in the study of Karalidi et al. [2013]. The code is based on the description by de Haan et al. [1987] and includes polarisation for all orders of scattering. For a model atmosphere composed of stacked, vertical layers with scattering and/or absorbing gaseous molecules, cloud, and/or haze particles, with a lower bound of either a black or reflecting surface, the code calculates the Stokes vector (see Section 1.2) of the reflected sunlight (starlight in the case of an exoplanet) for pre-defined illumination and viewing angles.

The user defined illumination (incidence) and viewing (emergence) angles are defined as follows: θ_0 represents the angle between the incident flux and the local vertical direction (also known as the solar zenith angle); θ represents the angle between the reflected flux and local vertical direction; and $\phi - \phi_0$ represents the azimuthal angle between the propagation direction of the incident flux and the reflected flux, which is measured in the local horizontal plane. The atmospheric layers considered in this thesis are horizontally homogeneous, thus only the differential azimuthal angle is relevant. Given a pixel on the planet and a specific phase angle, the local values for θ_0, θ, and $\phi - \phi_0$ are computed. The locally reflected flux vector (defined with respect to the local meridian plane, containing the local zenith and the direction towards the observer, $\mathbf{F}$, is calculated by [see Hansen & Travis, 1974]:

$$\mathbf{F}(\mu, \mu_0, \phi - \phi_0) = \mu_0 \mathbf{R}(\mu, \mu_0, \phi - \phi_0)\mathbf{F}_0, \tag{2.12}$$

where $\mathbf{F}_0$ represents the vector of the incident (unpolarised) stellar or solar flux, and $\mathbf{R}$ represents the 4×4 local planetary scattering matrix. The parameters $\mu_0 = \cos\theta_0$ ($0° \leq \theta_0 \leq 90°$), and $\mu = \cos\theta$ ($0° \leq \theta \leq 90°$). All of the models used assume incident unpolarised light from the star or the Sun, meaning that the incident flux vector is always $\mathbf{F}_0 = [F_0, 0, 0, 0]$, where F_0 is the total incident solar or stellar flux measured perpendicular to the direction of incidence divided by π [see Hansen & Travis, 1974]. Only the first column of the 4×4 planetary reflection matrix $\mathbf{R}$ is required, since the incident light is unpolarised, meaning Eq. 2.12 becomes

$$\mathbf{F}(\mu, \mu_0, \phi - \phi_0) = \mu_0 \mathbf{R}_1(\mu, \mu_0, \phi - \phi_0)\mathbf{F}_0, \tag{2.13}$$

where $\mathbf{R}_1$ represents the first column of the planetary reflection matrix. Given a (local) model atmosphere, $\mathbf{R}_1$ is calculated for the given local illumination and

viewing geometries with the adding-doubling algorithm. The circular polarisation is ignored in the computations, which can be done without introducing a significant error [Stam & Hovenier, 2005]. As was mentioned before, the reference plane for the locally computed Stokes parameters Q and U is the local meridian plane. The degree of linear polarisation of the reflected flux is independent of the chosen reference plane. Since only the normalised reflected fluxes and degree of linear polarisation are considered, the solar spectrum and the solar flux incident on the objects considered do not have to be taken into account. Also, the distance between the objects and the parent star is irrelevant for the modelling carried out in this work.

2.3.2.1 The model atmospheres

The numerical simulations were carried out for atmospheres composed of stacked plane-parallel layers, all horizontally homogeneous. All layers contain gas molecules and optionally have in addition cloud and/or haze particles. A black or reflecting homogeneous surface bounds the model from below; for atmospheres with high optical thickness, such as that of Jupiter, the extent of the atmosphere precludes an influence of the surface albedo. An atmospheric profile consisting of 20 layers, a tropospheric cloud layer, and up to two haze layers residing above was used in all of the atmospheric models. A basic representation of the model atmospheric layers are shown in Figure 2.4a and Figure 2.4b for atmospheres with both one and two haze types, respectively.

The radiative transfer calculations require knowledge of the optical thickness, b, the single scattering albedo, a, and the single scattering matrix, $\mathbf{S}_{\mathrm{sca}}$, of the mixture of molecules, cloud, and/or haze particles for each atmospheric layer. The optical thickness of an atmospheric layer, b, is given by the sum of the molecular, cloud, and/or haze extinction optical thicknesses as described in Stam [2008].

The Rayleigh scattering optical thickness is higher at shorter wavelengths, decreasing with approximately λ^{-4} toward longer wavelengths. The molecular scattering optical thicknesses of the individual atmospheric layers, $b^{\mathrm{m}}_{\mathrm{sca}}$, are dependent on the molecular column density (i.e. the number of molecules per m^2), the gas refractive index, and the depolarisation factor of the molecular mixture, for which the typical values of the specific atmosphere are used [see Hansen & Travis, 1974]. The molecular column density varies as a function of ambient temperature and pressure. The model results presented in this thesis were all calculated using a 20 layer model atmosphere, with pressures and molecular mixing ratios dependent on the body that the light was reflected from. The atmospheric layers are assumed to be in

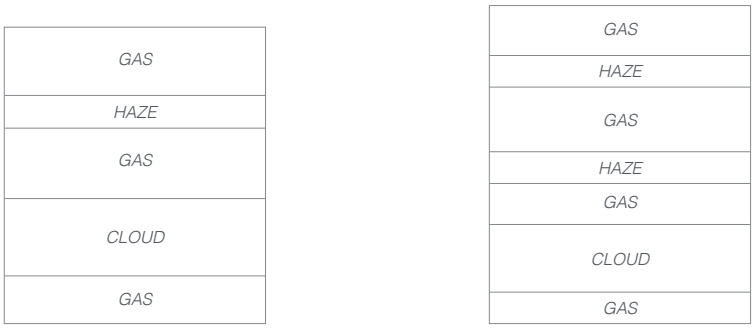

(a) (b)

Figure 2.4: Basic schematic of the model atmospheric layers: left is for an atmosphere with a cloud and one haze layer, right is for an atmosphere with one cloud layer and two haze layers. Gas layers consist of gaseous molecules, the scattering properties of which are described by Rayleigh scattering theory. The cloud and haze layers contain gaseous molecules and larger particles that fall under the Mie scattering regime. Pressure increases with decreasing height, so the clouds are at a higher pressure (lower altitude) than the haze layers(s).

hydrostatic equilibrium. The wavelength region considered depends on the observations, and is specified in each chapter, but is always between 0.35 μm and 1.0 μm. The measured CH_4 absorption cross sections of Karkoschka [1994] were used for the modelling of gas and ice giants.

The cloud and haze particle properties (except those of the fractal particles used only in Jupiter models) used are calculated via a Mie algorithm, described by de Rooij & van der Stap [1984], with a standard size distribution defined by Hansen & Travis [1974], as follows:

$$n(r) = Cr^{(1-3v_{\rm eff})/v_{\rm eff}} {\rm e}^{-r/v_{\rm eff}r_{\rm eff}}, \tag{2.14}$$

where C is a normalisation constant, $n(r){\rm d}r$ is the number of particles per unit volume with radii between r and $r + {\rm d}r$, $r_{\rm eff}$ is the effective radius, and $v_{\rm eff}$ is the effective variance [see Hansen & Travis, 1974, for the definitions]. The units of $r_{\rm eff}$ are microns, whilst $v_{\rm eff}$ is dimensionless.

The single scattering albedo of the mixture of gas molecules, and either cloud or haze particles, is given by

$$a(\lambda) = \frac{b^{\rm m}_{\rm sca}(\lambda) + b^{\rm a}_{\rm sca}(\lambda)}{b^m(\lambda) + b^a(\lambda)}, \tag{2.15}$$

and the scattering matrix of the mixture [see Hovenier et al., 2004] is calculated as

$$\mathbf{S}_{\rm sca}(\lambda) = \frac{b^{\rm m}_{\rm sca}(\lambda)\mathbf{S}^{\rm m}_{\rm sca}(\lambda) + b^{\rm a}_{\rm sca}(\lambda)\mathbf{S}^{\rm a}_{\rm sca}(\lambda)}{b^{\rm m}_{\rm sca}(\lambda) + b^{\rm a}_{\rm sca}(\lambda)}, \tag{2.16}$$

where $\mathbf{S}^{\rm m}_{\rm sca}$ and $\mathbf{S}^{\rm a}_{\rm sca}$ are the scattering matrices of the molecules and either the cloud or haze particles, respectively. All of the scattering matrices depend on the wavelength λ, but are also functions of the scattering angle, Θ (with $\Theta = 180^\circ - \alpha$, where α is the planetary phase angle).

Model computations are of course tailored specifically to the planet in question, and each chapter will outline the properties used in the modelling, such as the number of atmospheric layers, and the particle properties and cloud/haze layer optical thickness.

2.3.3 Sensitivity of the code to the input parameters

This section aims to demonstrate the effects of changing the various input parameters to the doubling-adding code. The input file can be modified to change values specific to the planet, and specify the files containing the coefficients representing the aerosol particles used in the atmosphere. Since gaseous planets are the main subject of this work, all model simulations use a Jupiter-like atmospheric profile (as in Chapter 5) with the inclusion of a single aerosol layer of cloud particles in the troposphere. The effective radius, effective variance, and complex refractive index of the particles are all varied to demonstrate the influence these values have on the disk-integrated flux and polarisation signals, both as a function of wavelength and phase angle.

Table 2.1: Properties of the model cloud particles.

Cloud model	$r_{\rm eff}$ (μm)	$v_{\rm eff}$	$n_{\rm i}$
1	0.5	0.05	1.42+0.05i
2	1.0	0.05	1.42+0.05i
3	0.5	0.1	1.42+0.05i
4	0.5	0.05	1.50+0.05i
5	0.5	0.05	1.42+0.001i

Table 2.1 shows the parameters for each of the five model cloud particles. Plots of the flux and degree of linear polarisation as a function of wavelength for each of the five models are shown in Fig. 2.5, and as a function of phase angle in Fig. 2.6. Model 6 is the same as model 1 but with a cloud deck at slightly higher altitude,

thus with less overlying gas molecules.

Clear differences can be seen between all six model atmospheres in both the flux and polarisation, demonstrating the effect that particle size, particle size distribution, and both the real and complex parts of the refractive index can have on the signal received from a Jupiter-like exoplanet. This is not only the case for Jupiter-like exoplanets of course, but for exoplanets of any configuration. Often the model particles used in computations take the values of refractive index from laboratory measurements; the differences in the plots shown here due to refractive index, especially in the absorptive (imaginary) part, clearly emphasise the necessity of accurate laboratory measurements in order to interpret observational data.

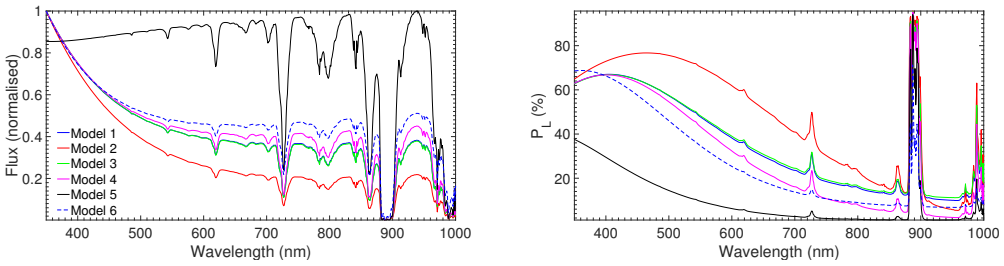

Figure 2.5: Plots of the flux and polarisation for the five model atmospheres as function of wavelength, with the individual cloud properties for each model given in Table 2.1. Model 6 is the same as for model 1, but with a slightly higher cloud deck.

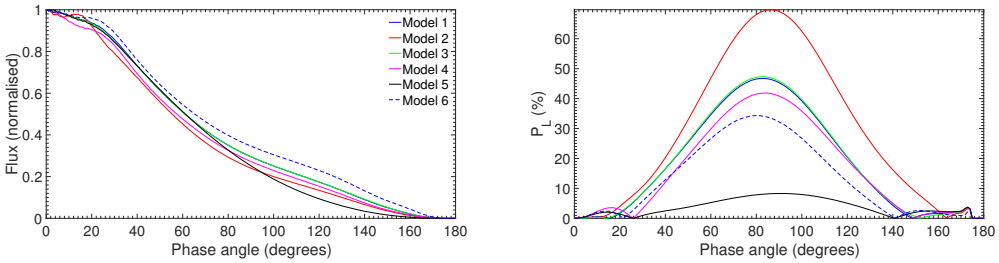

Figure 2.6: Plots of the flux and polarisation for the five model atmospheres as a function of phase angle, with the individual cloud properties for each model given in Table 2.1. Model 6 is the same as for model 1, but with a slightly higher cloud deck.

Chapter 3

Instrumentation and data reduction

The data presented in this thesis have been obtained with four instruments all mounted at different telescopes, namely: ISIS at the WHT, FoReRo2 at NAO Rozhen, ToPol at Calern, and FORS2 at the VLT, thus the data reduction methods used for each dataset have been optimised for the relevant instrument. Additionally, both spectropolarimetry and imaging polarimetry data involve different steps in the data reduction in order to extract the final data, fully corrected for any instrumental effects. This chapter begins with Section 3.1, which describes the various optical components that are used when constructing polarimetric instruments. The instruments and the telescopes used for collecting the data presented in this work are described in Section 3.2, with Section 3.3 detailing the data reduction methods, in both a general sense and how it was tailored for each instrument. For all observations of the planets and moons, the S/N was generally high as these are bright objects, and the spectral resolution was always 2 nm after rebinning.

3.1 Polarimetric optics

To produce light that is polarised for study here on Earth, a lamp would be used along with a polariser. A polariser receives natural unpolarised light and produces light with a polarisation of some sort. Different forms of polarisers are described in this section. Regardless of what process produces the polarisation, there must be some form of asymmetry involved, since polarisation by definition is caused by the breaking of symmetry. The polariser must select a particular polarisation state and

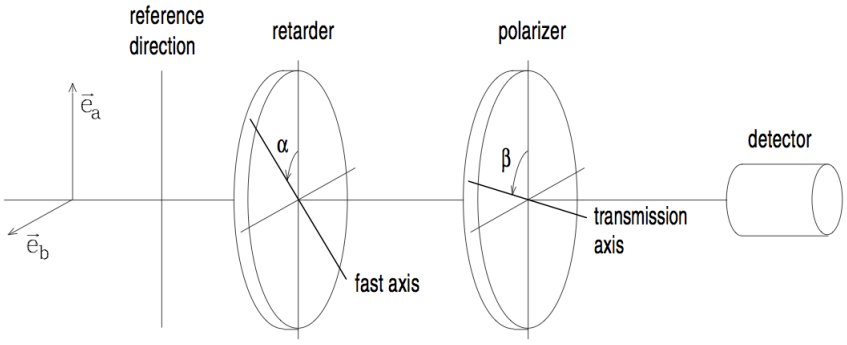

Figure 3.1: The components of an ideal polariser, from Landi Degl'Innocenti & Landolfi [2004]

remove all of the others.

This chapter will discuss the various optical comments required in order to realise a polarimeter. A schematic of an ideal polariser is shown in Figure 3.1.

3.1.1 Polarisers

A perfect polariser is a device which results in the emerging beam having complete linear polarisation, regardless of the initial state of polarisation before passing through the polariser. It can operate either by transmission or reflection. The vibrational direction of the emergent linearly polarised radiation is a property inherent to the polariser, related to the polariser's principal axis. Most polarisers operate via transmission, so the principal axis is known as the transmission axis.

For a single beam polariser, any component of the incident light with a direction of vibration perpendicular to the principal axis is rejected. A perfect polariser is never physically realisable, since the orthogonal component to the principal axis is never perfectly rejected. Therefore, unpolarised light incident on a polariser will only emerge partially polarised. The degree of polarisation of this light gives a measurement of the efficiency of the polariser, and is known as the polarisance [Clarke, 2010].

Many polarisers use birefringence (where the refractive index of the material depends on the polarisation and direction of propagation of the light) and two refracted beams can sometimes be produced as output. These beams are linearly polarised in perpendicular directions. Their directions of vibration define the axes of the

polariser. Several types of polariser are discussed below.

3.1.1.1 Dichroic Polarisers

Dichroism is a phenomenon which occurs in crystals, where a beam of white light travelling through the crystal emerges as two beams with two distinct colours (therefore, two differing wavelengths). Crystals which show several colours are said to exhibit pleochroism. The phenomenon of dichroism was found to be due to different dependencies of absorption on wavelength for the two directions of vibration in the crystal. The two vibration axes became known as the extraordinary and ordinary axes in a doubly refracting crystal. Substances are known for which 100 percent of the light across all wavelengths is absorbed for one direction of vibration, whilst along the other axis the absorption is non-zero but relatively constant. White light viewed through such a material and then a doubly refracting crystal will have two beams, with non-zero and zero wavelength independent intensities. This phenomenon is still referred to as dichroism, and is used in manufacturing sheet polarisers. Tourmaline is one such crystal which exhibits dichroism, and this was used to make polarisers in the 19th century.

3.1.1.2 Birefringent Polarisers

Two different forms of birefringent polarisers are used in astronomical polarimeters. One form separates the beams using the differences in the amount of refraction in the orthogonal axes. The other involves total internal reflection (TIR) of one of the components at a boundary. Two simple forms of refracting polariser are the Rochon and Wollaston prism. Each of these is made by cementing two components together, such as quartz or calcite. Light first enters perpendicular to the rear surface of the first prism, where the ordinary and extraordinary beams travel collinearly, although with different refractive indices. At the angled interface between the two prism components, the beams are interchanged, such that the beam along the ordinary axis enters a medium with a higher refractive index and is refracted towards the normal. The beam along the extraordinary axis experiences a lower refractive index and is refracted away from the normal. The angle of divergence between the two beams is then increased further upon exiting the prism. So, diverging ordinary and extraordinary beams exit the Wollaston prism. Figure 3.2 gives an illustration of a Wollaston prism.

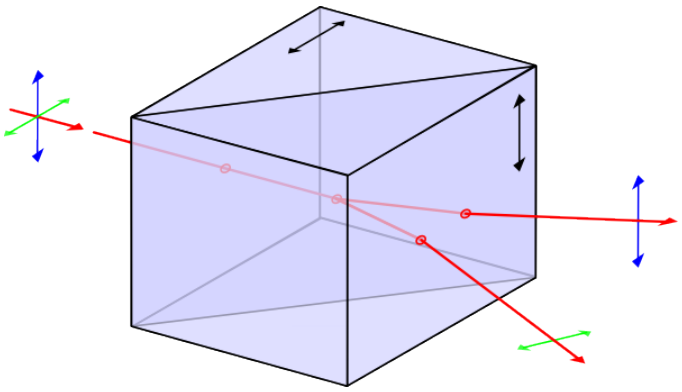

Figure 3.2: A schematic of light entering, passing through, and exiting a Wollaston prism. Both of the amalgamated prisms have perpendicular optical axes. Image from Wikipedia.

3.1.1.3 Reflection Polarisers

Unpolarised light incident on a surface will have some of its light transmitted (refracted) and some of it reflected. If the angle between the reflected light and the refracted light paths is 90°, then the reflected light will be completely linearly polarised. The angle between the incident light and the surface normal at which this occurs is known as Brewster's angle. A dielectric plate can thus act as a perfect polariser. However, the reflected beam also traces out a cone as the polariser is rotated, so a reflecting plate is not often used as a polariser. The transmitted light is partially polarised, and by using successive plates set at Brewster's angle, the transmitted light becomes more and more polarised. This type of setup is known as a pile-of-plates polariser. It is not often used in the optical regime, but is used in the infrared.

3.1.2 Retarders

A retarder, or retarder wave plate, is an optical device that introduces a phase shift between orthogonal components of a ray of light. The most common types of retarder wave plate induce a phase delay of either π or $\pi/2$, known respectively as half wave plates and quarter wave plates. The differential retardation is produced between two components of the light resolved along two perpendicular directions fixed into the device. These directions are known as the fast and the slow axes, and the amount of retardation produced is known as the retardance.

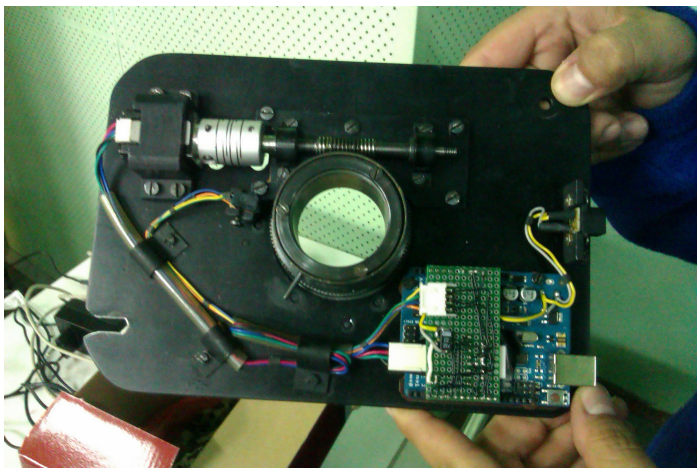

Figure 3.3: Retarder waveplate, along with motor control electronics to remotely rotate it.

Quarter wave plates are most often used to convert circular into linearly polarised light. Half wave plates are used to produce linearly polarised light from light which is already linearly polarised, but rotates the direction of vibration.

Figure 3.3 shows a retarder half-wave plate, used in FoReRo2 (more details given in Section 3.2.3). The retarder is mounted in a motorised wheel so that it can be rotated remotely during the observations.

3.2 Instruments

3.2.1 FORS2@VLT

FORS2 is the visual and near ultraviolet FOcal Reducer and low dispersion Spectrograph, version 2, and is an instrument available for use at the Very Large Telescope (VLT), of the European Southern Observatory (ESO), Chile, a group of four individual telescopes, each with a primary mirror of 8.2 m diameter. FORS2 is designed to operate in the wavelength range 330-1100 nm, and is fully described by Appenzeller et al. [1998]. FORS2 can operate in several modes: imaging, polarimetry, long-slit, and multi-object spectroscopy. The polarimetric modes of FORS2 allow the measurement of either linear and circular polarisation, for both imaging polarimetry and spectropolarimetry. The instrument enables one to measure the position angle and degree of either linear or circular polarisation through use of a rotatable $\lambda/2$ or $\lambda/4$ waveplate placed in front of the beam-splitting Wollaston prism. Figure 3.4

shows the instrument mounted at the Cassegrain focus. FORS2 data is presented only in Section 4.3 of this thesis, thus only the data reduction method specifically tailored to this dataset is described here.

Figure 3.4: FORS2, mounted at the Cassegrain focus of the telescope. Image credit: ESO.

3.2.2 ISIS@WHT

ISIS[1] is the Intermediate dispersion Spectrograph and Imaging System, mounted at the 4.2 m William Herschel Telescope (WHT), of the Isaac Newton Group of telescopes on the island of La Palma, Spain. ISIS is capable of both imaging polarimetry and spectropolarimetry, and can image in blue and red regions of the spectrum simultaneously, through the use of dichroic filters that split the incoming light and send it through two different grisms, and the final signal is then recorded on two CCDs. Both arms of the instrument are optimised for their respective wavelength ranges. Similarly to FORS2, ISIS is capable of carrying out both linear and circular polarisation measurements, with the use of a rotatable $\lambda/2$ or $\lambda/4$ waveplate placed in front of the beam-splitting device, which in the case of ISIS is a Savart plate, made of calcite. Several sets of data in this thesis were taken with ISIS: see Section 4.4, Chapter 6, and Chapter 7.

[1] http://www.ing.iac.es/astronomy/instruments/isis/

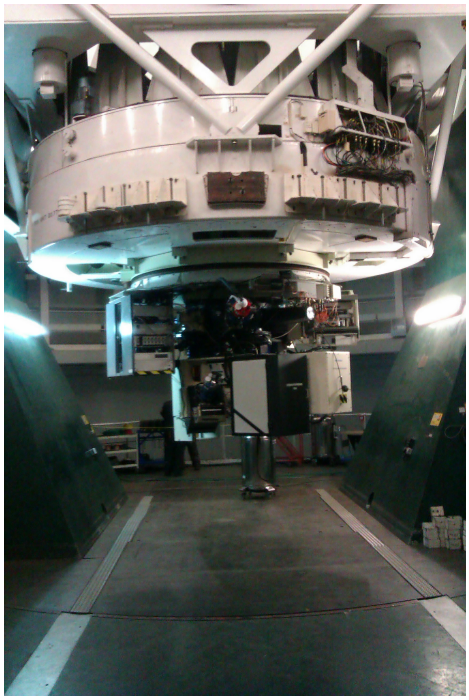

Figure 3.5: ISIS, attached to the Cassegrain focus of the 4.2 m WHT.

3.2.3 FoReRo2@Rozhen

FoReRo2 is the 2-Channel-Focal-Reducer instrument (version 2), equipped with polarimetric optics, at the two-metre telescope of the Bulgarian National Astronomical Observatory, Rozhen, Bulgaria. The instrument is described in detail by Jockers et al. [2000] and it utilises a retarder Super-Achromatic (in the range 380–790 nm) True Zero-Order Waveplate 5 (APSAW-5)[2] and a Wollaston prism to measure either $F + Q$ and $F - Q$ or $F + U$ and $F - U$ on the CCD. The retarder waveplate is a recent addition to the instrumental setup and it is not described in the original paper by Jockers et al. [2000]. Figure 3.6 shows the instrument (unattached to the telescope).

3.2.4 ToPol@Calern

ToPol is the Torino Polarimeter, mounted at the one-metre "Omicron" (West) telescope of the C2PU (Centre Pédagogique Planète et Univers) facility (Calern plateau, Observatoire de la Côte d'Azur, France). The instrument consists of a double wedge Wollaston prism configuration, which is described in detail in Oliva [1997], and the

[2]http://astropribor.com/content/view/25/33/

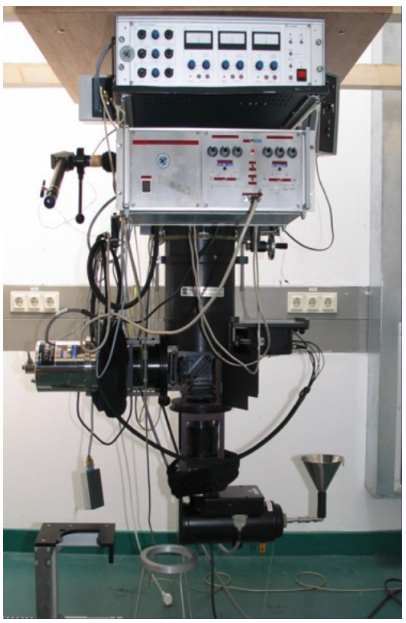

Figure 3.6: FoReRo2, unmounted from the telescope.

instrument itself is described in Pernechele et al. [2012]. Commissioning data are presented in Devogèle et al. [2017]. The instrument is shown in Figure 3.7.

3.3 Data reduction methods

3.3.1 CCDs

All modern astronomical data are recorded on Charged Coupled Devices (CCDs), the invention of which in the 1970s ensured a major revolution in astronomical data acquisition. Previous to the invention of the CCD, astronomical data were usually recorded on photographic plates, far less efficient devices. CCDs come in a range of sizes, and over time their efficiency has continued to improve; modern telescopes have their CCDs replaced every few years as the technology further advances. On a CCD, each collecting element is a light sensitive silicon capacitor referred to as a "pixel", and each pixel acts as an individual part of the silicon array, capable of collecting incoming photons, that then register their presence through interaction with the pixel material, via the photoelectric effect. Most pixels on a CCD have a saturation point, usually around 10^5 photoelectrons, so the exposure time of an astronomical object must be chosen carefully, such that not only to get sufficient photons, but also not to overfill the pixel well.

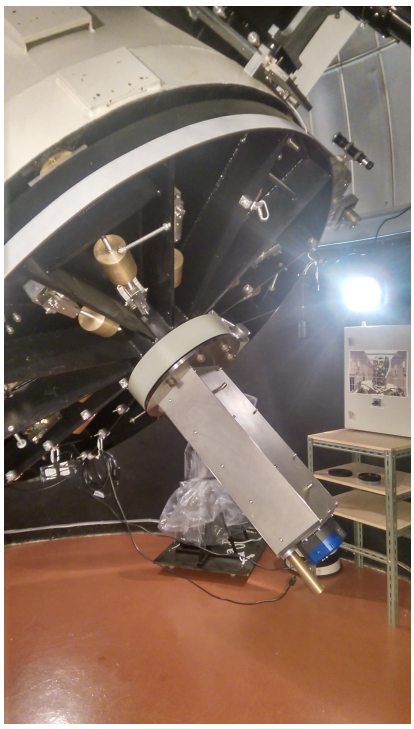

Figure 3.7: ToPol, encased and mounted at the Cassegrain focus of the one-metre telescope at C2PU.

After the CCD is exposed to the object, the CCD is then read out to a computer, with the number of photoelectrons in each pixel represented by a digital number. Every CCD has a value associated with it that converts the number of electrons to Analogue-to-Digital Units (ADU), or counts. This quantity is known as the gain, and most modern astronomical observing facilities would have this value listed in the header file of an observation. Howell [2000] gives a detailed description of CCDs and their use in astronomy. Once the CCD image is read out to the computer, it is then saved in a certain format, which in this thesis is always as a FITS (Flexible Image Transport System) file, which is a standard digital file format, and is the most common one used in astronomy.

3.3.2 Bias and flat fielding

A bias level is added to the CCD to avoid having negative counts, since this is an unphysical phenomenon. This bias level is removed from the images before extracting the scientific information. To do this, a series of bias frames must be taken on the night of observing, which are zero second exposures taken with the

shutter closed. The bias frames are then median averaged together, and subtracted from the science frames, as well as from the other calibration images.

Each pixel on the CCD has a slightly different gain than the neighbouring pixels, so the response to incoming photons is slightly different. In order to smooth this effect out for incoming radiation, the science images are divided by the flat field. Flat fields are images taken of a uniformly illuminated area, usually the inside of a telescope dome or the twilight sky (with median filtering applied to ensure no stars are present in these images). These images have the same exposure time as the science frames. Since the pixels on the CCD have a different response to light of different wavelengths, flat fields for each filter used have to be taken. Many observatories have a flat field screen on the inside of each dome, and usually have a method specified in their observing manuals for obtaining flat fields specifically tailored to work best for their CCDs [Howell, 2000]. Flat fields are normalised before the science data is corrected, so as not to unintentionally reduce the pixel counts in the science frames. Another reason for using flat field images is to correct for artefacts that may be present on the CCD, such as scratches or dust. Dividing the science images by a flat field removes these artefacts, whilst preserving the scientific content. Several images are taken, and are usually median averaged. Median averaging is best used in case of cosmic rays and background stars, which are discarded in the averaging process.

In this thesis it is always the reduced Stokes parameters that are calculated (see later in the chapter for how these are calculated from observations for each instrument). These are a ratio of the polarised to unpolarised flux, therefore any flat field correction would mathematically cancel. Most data presented in this thesis are thus not flat field corrected, but when a correction has been performed the reason is explained in the appropriate section.

3.3.3 Spectropolarimetry

3.3.3.1 FORS2

The first step in the data reduction, like for most of the data presented in this thesis, was to subtract the bias frames. Several bias frames were median averaged, with the *iraf* task *zerocombine*, and then the task *ccdproc* was used to subtract the bias frames from the science data. Then, the flatfielding was performed, using the *iraf* task *imarith* to divide the science images by the flatfield frames. The next step was to extract the flux counts from the CCD images. The CCD of FORS2 is divided into

strips, as illustrated in Figure 3.8, with adjacent strips contained fluxes for ordinary and extraordinary beams.

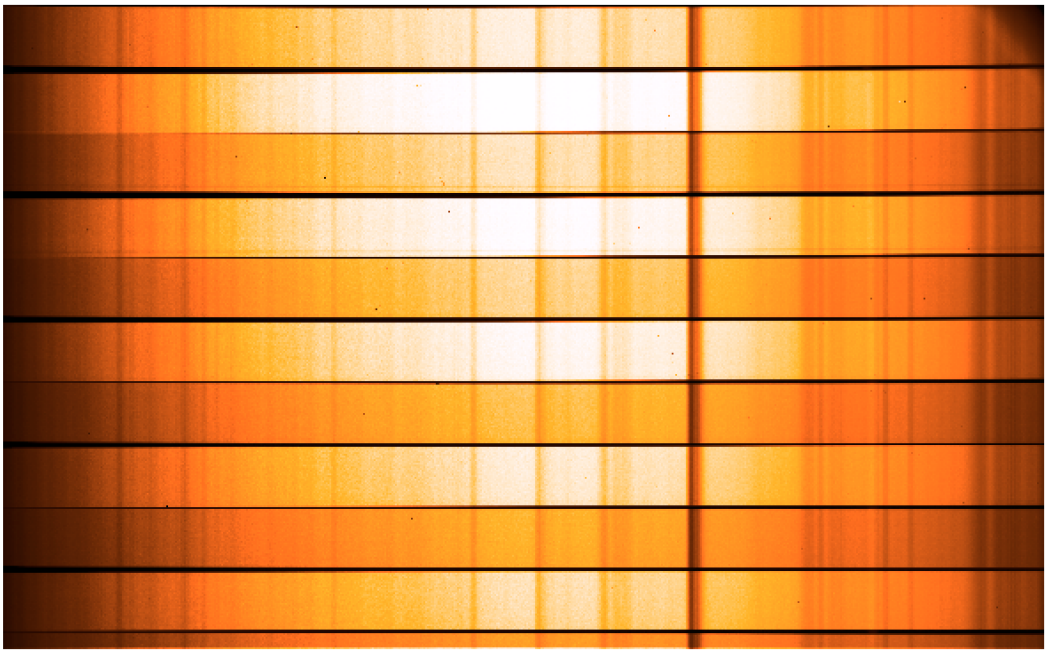

Figure 3.8: An image of earthshine data on the FORS2 CCD.

A dedicated *FORTRAN* script was then used to carry out the remainder of the data reduction, namely: wavelength calibration, defining of apertures around the individual strips, summing of fluxes, and spectrum extraction.

FORS2 has a polarimetric module that allows the use of the beam-swapping technique, which is fully described in Bagnulo et al. [2009], with the key concepts and equations given here. The beam-swapping technique minimises the errors that can be introduced through instrumental polarisation, with any value of instrumental polarisation less than 0.1% [Cikota et al., 2017], which is less than the size of the error due to photon noise. The flux combinations to calculate the Stokes parameters were carried out in *MATLAB*. After the fluxes of the ordinary and extraordinary beams were extracted and written to ASCII files, the beam-swapping technique was applied to calculate the Stokes parameters:

$$P_X = \frac{1}{2N} \sum_{j=1}^{N} \left[\left(\frac{f^{\parallel} - f^{\perp}}{f^{\parallel} + f^{\perp}} \right)_{\alpha_j} - \left(\frac{f^{\parallel} - f^{\perp}}{f^{\parallel} + f^{\perp}} \right)_{\alpha_j + \Delta\alpha} \right] \tag{3.1}$$

where X stands for either Q or U, N represents the number of pairs of retarder

angles, $f^{\perp}$ is the flux in the perpendicular beam, $f^{\parallel}$ is the flux in the parallel beam, α is the retarder angle with respect to its zero point in degrees, and $\Delta\alpha$ is 45°. The sum is over all pairs of retarder angles which the observations have been obtained over; in our case, $N = 4$, since 8 different retarder waveplate angles were used for measuring each Stokes parameter (thus 16 angles in total: 0 - 337° in steps of 22.5°).

The uncertainties are calculated as in Bagnulo et al. [2009]. The error on P_X is given by

$$\sigma_{P_X} = \frac{1}{2\sqrt{N}F}, \tag{3.2}$$

where N is the number of pairs of exposures, and F is the flux accumulated in both ordinary and extraordinary beams from all exposures. The error on the position angle, χ, is given by

$$\sigma_{\chi} = \frac{1}{2}\frac{\sigma_{P_L}}{P_{\mathrm{L}}}, \tag{3.3}$$

with $\sigma_{P_L} = \sigma_{P_X}$.

3.3.3.2 FoReRo2

As for the FORS2 data reduction, the beam swapping technique was used, thus any instrumental polarisation is negligible. An image of the CCD of Uranus spectropolarimetry is shown in Figure 3.9. The data reduction for the FoReRo2 spectropolarimetry was carried out in *iraf*, with the flux combinations to calculate the Stokes parameters carried out in *MATLAB*. The science frames were bias subtracted, and then collapsed into 1D spectra with a wavelength calibration then performed using arc-lamp spectra taken just after the observations. The fluxes of the ordinary and extraordinary beams were then extracted, and the beam-swapping technique was applied to calculate the Stokes parameters.

Observations were taken at either four or eight individual retarder waveplate angles. The reduced Stokes parameters were calculated with Eqn. 3.3.3.1. The spectrum of a solar analogue was also obtained. The solar analogue was used to derive the reflectance spectrum of the objects: since the light reflected by the planet or moon is from the Sun, the spectral energy distribution will be mostly composed of that of the Sun's, so this must be divided out in order to extract the true reflectance spectrum. As is shown in the following chapters, the solar analogue is not entirely an exact match of the Sun's spectrum, therefore some features or remnants of the solar flux

Figure 3.9: Left: spectrum of Uranus as shown on the CCD of FoReRo2, both ordinary and extraordinary beams.

remain in the reflectance spectra of the object. Polarised standard stars were also observed in order to characterise the instrumental position angle offset, and these are shown in Table 3.1 along with the solar analogue star. The position angle of polarisation that is obtained from the data is one that is an instrumental angle, θ_{inst}, and in order to obtain the real value the following calculation is performed:

$$\Delta = \theta_{\text{inst}} + \theta_{\text{cat}} \tag{3.4}$$

$$\theta_{\text{actual}} = \Delta - \theta_{\text{inst}} \tag{3.5}$$

with θ_{cat} the catalogue values of θ, taken from Schmidt et al. [1992]. This calculation was performed for all spectropolarimetry datasets that had a polarised standard star taken along with the data.

An unpolarised standard star was also observed by Galin Borisov in April 2017, details of which are given in Table 3.1 and the result of which is shown in Figure 3.10. The non-zero value of linear polarisation increasing with wavelength is most likely due to the slit [Keller, 2002], since the instrumental polarisation for imaging polarimetry measurements has been found to be virtually zero. This is the subject of an ongoing investigation at the time of writing.

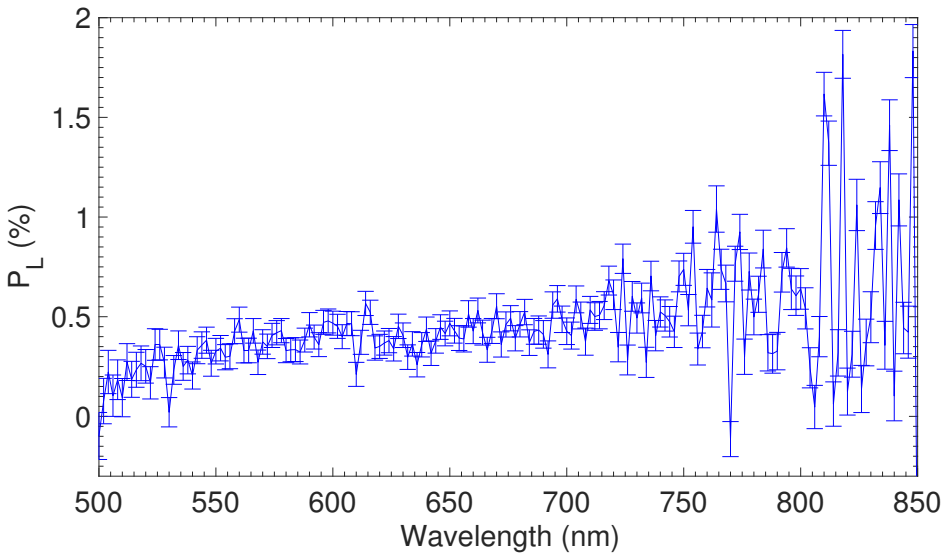

Figure 3.10: P_L of an unpolarised standard star taken with FoReRo2.

Table 3.1: Standard stars observed with FoReRo2.

Object	Type	Date	UT	Exp. Time (s)	Filter/Grism
HD1835	Solar analogue	19/09/2014	21:38	1	GrismW
HD204827	Polarised	06/11/2015	18:02	60	GrismW
HD161056	Polarised	10/07/2016	23:13	60	GrismW
HD161056	Polarised	11/07/2016	23:12	12	IF642
HD161056	Polarised	11/07/2016	23:28	10	IF620
HD161056	Polarised	11/07/2016	23:49	18	IF590
HD154892	Unpolarised	25/04/2017	22:40	60	GrismW

3.3.3.3 ISIS

The blue and red arms were effectively treated as separate instruments in the data reduction process, since different bias frames were required, as well as different wavelength calibration images from arc-lamps. Additionally, the positions of the ordinary and extraordinary beams on the CCD are swapped between the red and blue arms (the difference between ordinary and extraordinary beams was determined by measuring the Stokes parameters of a standard star, and comparing against known values).

The data reduction procedure for both arms involved the same steps. The first step was to subtract the bias. This was done in the standard way, with several bias frames median averaged, with the *iraf* task *zerocombine*, and then the task *ccdproc* was used to subtract the bias frames from the science data. Depending on the dataset, either a one dimensional or a two dimensional wavelength calibration was carried out. The 1D calibration is the standard method for reducing observations of point sources, such as stars or most asteroids. In the case of this thesis, the only point sources observed were the ice giant planets (depending on the resolution of the instrument), Titan, and standard stars.

The 1D reduction method firstly involves collapsing the spectra for each retarder angle in the *iraf* ask *apall*. This task takes the average of a certain number of lines, and then adds these together, producing a 1D spectrum. This was done interactively for one image, and then the rest of the images are collapsed using the first image as a reference, using the same aperture sizes and polynomial fit. The next step was to combine the images taken for each individual retarder angle, to increase the signal-to-noise ratio. So for example, if ten exposures were taken for each retarder position, then the ten images would be combined to form one master image, with a higher pixel intensity value for the science data. The *iraf* task *speccombine* was used for this, which added the 1D images together.

Spectra of arc-lamp emissions were also taken several times on the night of observing. This is in order to fit a wavelength scale to the CCD images. Arc-lamp spectra were taken either before or just after the observations, so that all of the instrumental setup and observing conditions were preserved. As with the science images, the arc images were collapsed and combined in the same way, so that one master arc-lamp image was produced. Each arc-lamp spectrum only pertained to a single observation. The *iraf* task *identify* was used to identify the emission lines of the lamp recorded by the CCD. This was done separately for each aperture, since the line positions

could be slightly different for each part of the CCD. Once a good fit was performed between the data and the known lines, the wavelength identification was written to the database. After this, the calibration was applied to the science images using the task *dispcor*. It is in this task where rebinning was also carried out. After this, the task *wspectext* was used to convert the images to text files, with a list of the intensity value per pixel.

Since most of the data presented in this thesis are of extended objects, such as Jupiter and Saturn, the images recorded on the CCD are quite different to those from stars, thus cannot be treated in the same way when attempting to extract the scientific content. Figure 3.11 shows on the CCD the line spread function of the raw spectrum of a standard star, along with the size of the apertures. Figure 3.12 show the corresponding images for Saturn. It is clear that the apertures are larger for Saturn, and also the figure shows that they are extended, and clearly not similar to those from a point source. Collapsing the spectrum of an extended object could potentially lead to a less accurate wavelength calibration, thus a 2D data reduction method was attempted for some of the observations of extended objects presented in this work.

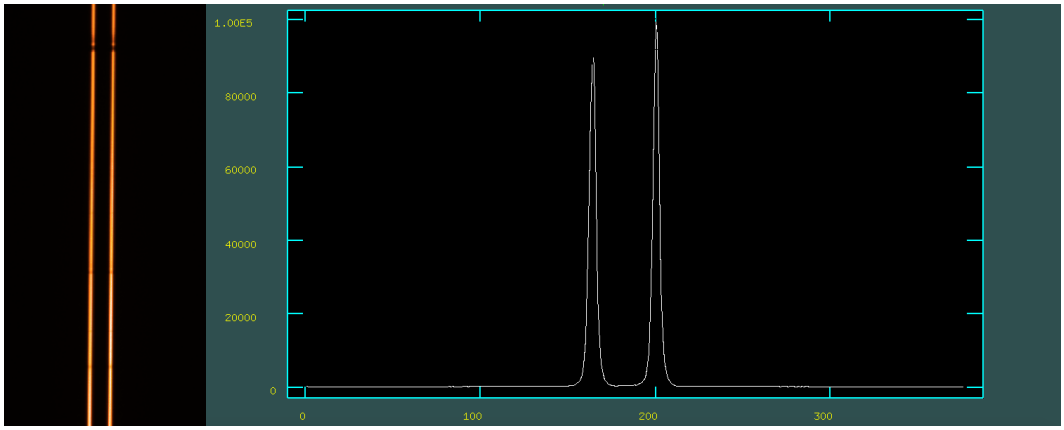

Figure 3.11: Left: spectrum of a polarised standard star as shown on the red CCD of ISIS, both ordinary and extraordinary beams. Right: both beams shown in *iraf*, for definition of apertures for 1D spectrum extraction.

The 2D reduction method produced the same end result, with some different intermediate steps. The first difference is that neither the science images nor the arc-lamp images are collapsed into 1D spectra before wavelength calibration. The CCD image is first mapped in wavelength, and then the distortion is corrected for. The *iraf* task *identify* was used firstly to define arc-lamp emission lines for a section of the 2D image, then *reidentify* was used to do this for sections across the entire

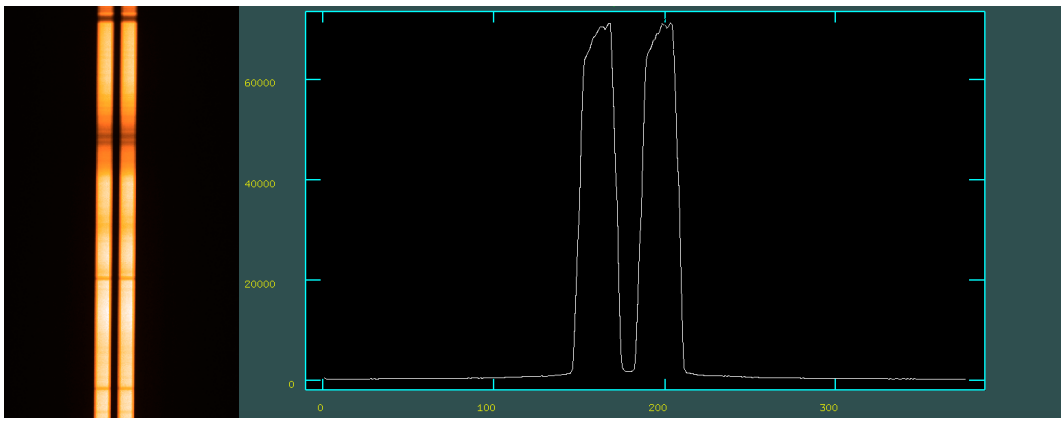

Figure 3.12: Left: spectrum of Saturn as shown on the red CCD of ISIS, both ordinary and extraordinary beams. Right: both beams shown in *iraf*, for definition of apertures for 1D spectrum extraction. Note that the apertures are much wider than those in Figure 3.11.

image. The task *fitcoord* was then used to fit a 2D function to the arc-lamp images, with *transform* finally applied to fit the 2D calibration to the science images.

Unfortunately, the 2D reduction method often failed. The reason for this is still unclear. However, this was not a significant issue, because the 1D reduction method provided very similar results to the 2D method, for the objects that the 2D reduction method proved to be successful. Figure 3.13 shows the reduced linear polarisation spectrum of Saturn data taken on the 03/02/2015, with the red arm of ISIS. The results of both the 2D reduction and the 1D reduction are shown. For clarity, error bars are included for the 2D reduction, but not the 1D, and it can be seen that the results are virtually the same, with any variations contained entirely within the error bars.

Whether a 1D or 2D reduction was used, the final output files containing the flux values in the ordinary and extraordinary beams for each wavelength were combined with the beam-swapping technique (see Eqn. 3.3.3.1).

The use of the beam-swapping technique ensured a minimisation of instrumental polarisation. To demonstrate this, two unpolarised standard stars were observed by Stefano Bagnulo with ISIS in spectropolarimetric mode in January 2015. The observing log of these stars is shown in Table 3.2. Polarised standard stars were also observed at each epoch to characterise the instrumental position angle offset, and these are also shown in Table 3.2, along with solar analogues that were used to divide out the solar spectrum and obtain the reflectance of the objects. The correction for the position angle of polarisation was carried out as in Section 3.3.3.2.

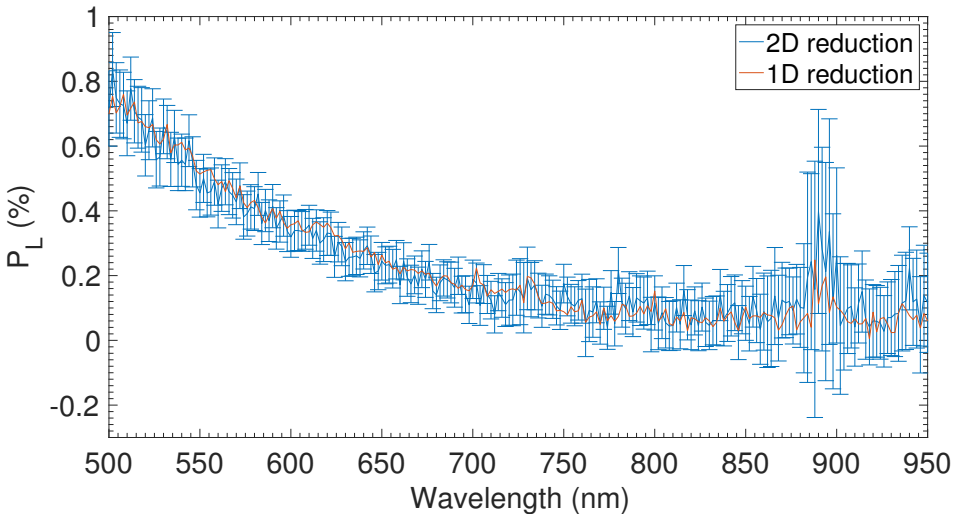

Figure 3.13: Comparison of the 2D and 1D reduction methods for Saturn data.

Figures 3.14 and 3.15 show the degree of linear polarisation of two unpolarised standard stars as a function of wavelength, observed with ISIS. The figures show that the instrumental polarisation is zero within the error bars.

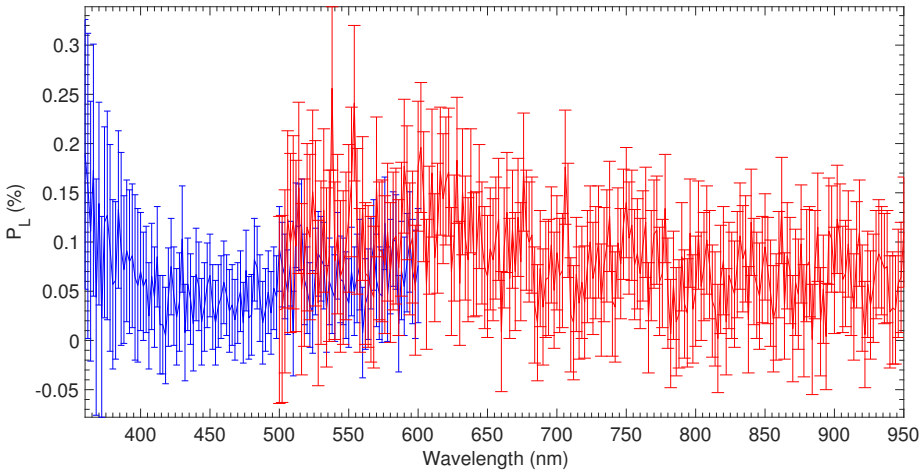

Figure 3.14: Polarisation as a function of wavelength in both blue and red arms of ISIS for unpolarised standard star HD103095.

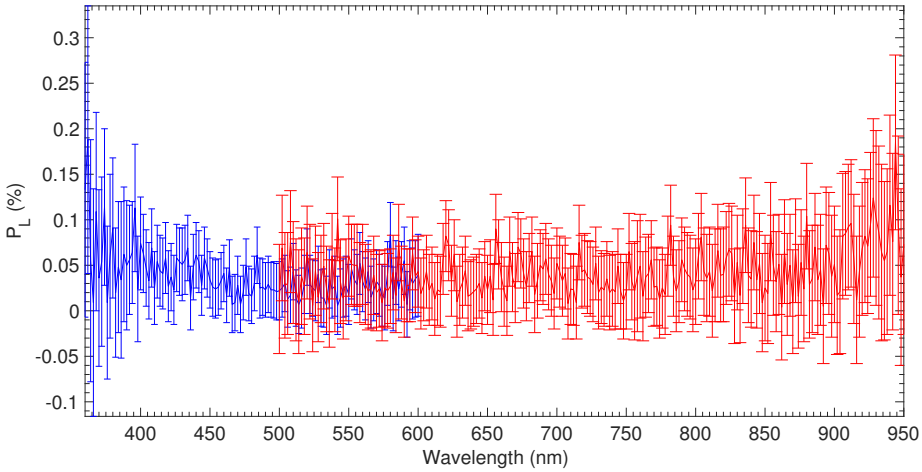

Figure 3.15: Polarisation as a function of wavelength in both blue and red arms of ISIS for unpolarised standard star HD125184.

Table 3.2: Solar analogues along with polarised and unpolarised standard stars observed over the three epochs of ISIS observations.

Object	Type	Date	UT	Exp. Time (s)	Grism
HD25443	Polarised	11/03/2014	20:30	30	R300B
HD25443	Polarised	11/03/2014	21:03	10	R158R
HD159222	Solar analogue	12/03/2014	07:04	10	R158R
HD159222	Solar analogue	12/03/2014	07:05	20	R300B
HD204827	Polarised	05/01/2015	19:24	10	R158R
HD204827	Polarised	05/01/2015	19:31	60	R300B
HD28099	Solar analogue	06/01/2015	01:12	20	R158R
HD28099	Solar analogue	06/01/2015	01:16	30	R300B
HD103095	Unpolarised	07/01/2015	06:10	5	R158R
HD103095	Unpolarised	07/01/2015	06:13	10	R300B
HD125184	Unpolarised	07/01/2015	06:20	5	R158R
HD125184	Unpolarised	07/01/2015	06:24	20	R300B
HD28099	Solar analogue	02/02/2015	23:09	60	R158R
HD28099	Solar analogue	02/02/2015	23:13	180	R600B
HD154445	Polarised	04/02/2015	06:30	2	R158R
HD154445	Polarised	04/02/2015	06:35	20	R600B

3.3.4 Imaging polarimetry: disk-integrated

3.3.4.1 FoReRo2 and ToPol

Data for the standard stars, Uranus, Neptune, and some of the Mars data were reduced by using aperture polarimetry, which essentially sums up all the flux in a defined annulus around the object, and then computes the Stokes parameters from these summed fluxes. After the data were dark subtracted, the next step was to cut out the individual strips. Then the object was shifted to a common centre in each strip, for each CCD read-out. Many images were combined to form the final image for each strip, in order to increase the signal-to-noise ratio.

Following the shifting and adding, the next step was to actually perform the aperture polarimetry. This was done using the *iraf* task *phot*, which was also used to find the centre of the images for shifting. Each of the images was input, and a magnitude file was produced. This file contained the total flux counts summed up in the user defined annulus. The aperture size was determined by looking at the curve of growth of the flux and polarisation with increasing aperture size. An example of this is shown in Fig. 3.16, for December 2015 observations of Uranus with ToPol in the V filter, showing the flux in arbitrary units for all four apertures stabilising around the aperture with a pixel value of 18, along with a plot of $P_{\rm L}$ as a function of aperture size.

This analysis was performed for each aperture polarimetry data set, with an appropriate aperture size chosen that gave a value stabilising at a particular aperture size for all four fluxes and the polarisation. The fluxes have all been multiplied by the CCD gain, which is the conversion factor from analogue-to-digital units to electron counts. When calculating fluxes and magnitudes of an object, it is crucial to get the absolute flux calibration. However, when considering the polarised flux, we take ratios to obtain the Stokes parameters, so any conversion factors inevitably divide out when combining the fluxes.

The next step is to calculate the Stokes parameters and the associated errors. The beam-swapping technique was used for FoReRo2, and for ToPol the following equations give the reduced Stokes parameters:

$$P_Q = \frac{Q}{F} = \frac{S_1 - S_2}{S_1 + S_2}, \tag{3.6}$$

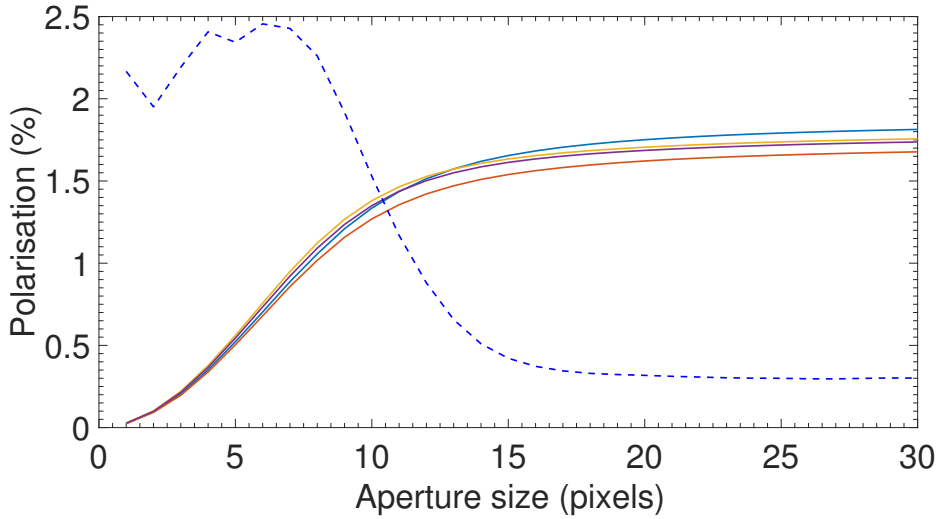

Figure 3.16: Growth curves of the flux in all four strips shown as solid lines, from ToPol observations of Uranus. The dashed curve is the value of P_{L} calculated from the fluxes in all four strips.

$$P_U = \frac{U}{F} = \frac{S_3 - S_4}{S_3 + S_4}, \tag{3.7}$$

where $S_1 = F + Q$, $S_2 = F - Q$, $S_3 = F + U$, and $S_4 = F - U$. The errors in these values vary with the signal-to-noise ratio of the data, and are given by:

$$\sigma_Q = \frac{1}{\sqrt{S_1^2 + S_2^2}}, \tag{3.8}$$

$$\sigma_U = \frac{1}{\sqrt{S_3^2 + S_4^2}}, \tag{3.9}$$

and

$$\sigma_P = \sigma_Q = \sigma_\chi \tag{3.10}$$

since $\sigma_Q \approx \sigma_U$ [Bagnulo et al., 2009]. These errors account only for photon noise.

Unpolarised and polarised standard stars were also observed at each epoch, with the observing log shown in Table 3.3. Table 3.4 gives the values of instrumental polarisation derived from the unpolarised standard stars. As in Devogèle et al. [2017], the offset of the position angle was not found to vary greatly between each epoch, with the instrumental polarisation also remaining stable.

Table 3.3: Unpolarised and polarised standard stars observed with ToPol.

Object	Type	Date	UT	Exp. Time (s)	Filter
HD43384	Polarised	17/10/2015	03:01	0.3	V
HD43384	Polarised	09/12/2015	23:30	1.0	V
HD154445	Polarised	11/04/2016	02:35	1.0	V
HD154445	Polarised	11/04/2016	02:39	1.0	R
HD154445	Polarised	11/04/2016	02:45	3.0	B
HD154445	Polarised	07/06/2016	22:36	0.2	V
HD154445	Polarised	09/06/2016	00:05	0.5	V
HD18803	Unpolarised	10/12/2016	18:46	0.2	V
HD18803	Unpolarised	10/12/2016	18:50	0.2	R
HD18803	Unpolarised	10/12/2016	18:55	0.5	I
HD18803	Unpolarised	10/12/2016	19:01	2.00	B
HD18803	Unpolarised	10/12/2016	19:08	20.00	U
HD10476	Unpolarised	10/12/2016	20:48	0.05	V
HD10476	Unpolarised	10/12/2016	20:53	0.05	R
HD10476	Unpolarised	10/12/2016	20:58	0.05	I
HD10476	Unpolarised	10/12/2016	21:04	2.00	B
HD10476	Unpolarised	10/12/2016	21:12	10.00	U

3.3.5 Imaging polarimetry: disk resolved (maps)

Flux and polarimetric maps were produced using this method with both FoReRo2 and ToPol. The final product is the same for each instrument (flux and polarimetric maps), but the data reduction methods are different, with each described in detail in this section.

3.3.5.1 Polarimetric maps with FoReRo2

The data reduction again firstly involved the subtraction of a master bias frame. The imaging polarimetry was taken using the same instrumental setup as the spectropolarimetry, except with the respective filters in place of the grism, so the beam-swapping technique was again used to calculate the Stokes parameters from the individual flux images, via Eqn. 3.3.3.1. However, the individual images had to be aligned, as for the ToPol data. As Fig. 3.17 shows, there are two images taken for each retarder angle: the ordinary and extraordinary beams, meaning that for each of the eight retarder angles two images had to be aligned, therefore 16 images in total were aligned. This was achieved using the task *daophot* in *iraf*, something that unfortunately did not work for the ToPol data, perhaps due to the increased spatial resolution and larger distortion between beams in the ToPol data. The FoReRo2

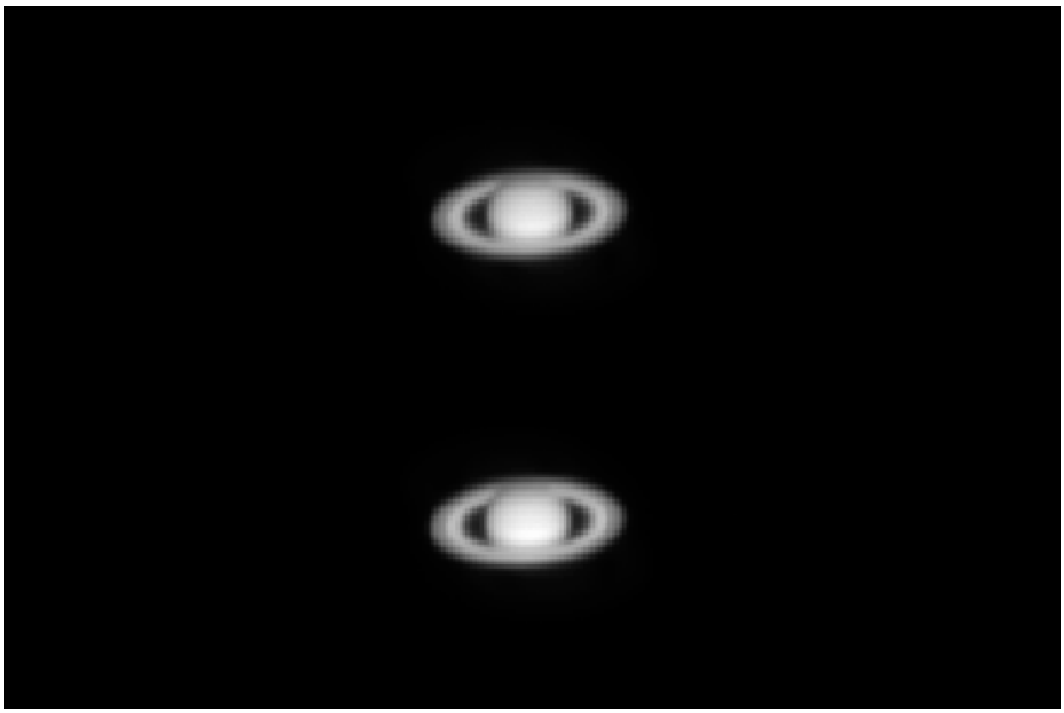

Figure 3.17: FoReRo2 CCD image of Saturn in the 620 nm filter. From the top down, the two beams are proportional to: $F + Q$, $F - Q$.

images were aligned to sub-pixel precision using this method.

3.3.5.2 Polarimetric maps with ToPol

The ToPol data reduction required special attention when combining the images on a pixel-to-pixel level, because the individual Stokes parameters can only be derived from combining the images from each of the four beams (see Fig. 3.18). The incoming light to the telescope splits into four beams when travelling through the double Wollaston prism in the optical setup of the instrument. The CCD is partitioned into four horizontal strips, and each beam of light is projected onto one of the strips. The labels S_1, S_2, S_3, and S_4, correspond to the signals (on a pixel level) in each strip from top to bottom respectively. The reduced Stokes parameters, that is Q and U normalised to the total flux of light, were then calculated from these values, as in Section 3.3.4. Additional uncertainties arising from the image alignment and/or distortions can increase the total error bar; these issues and their effects are discussed later in this section.

The different optical path of each beam of light gives rise to two effects which must

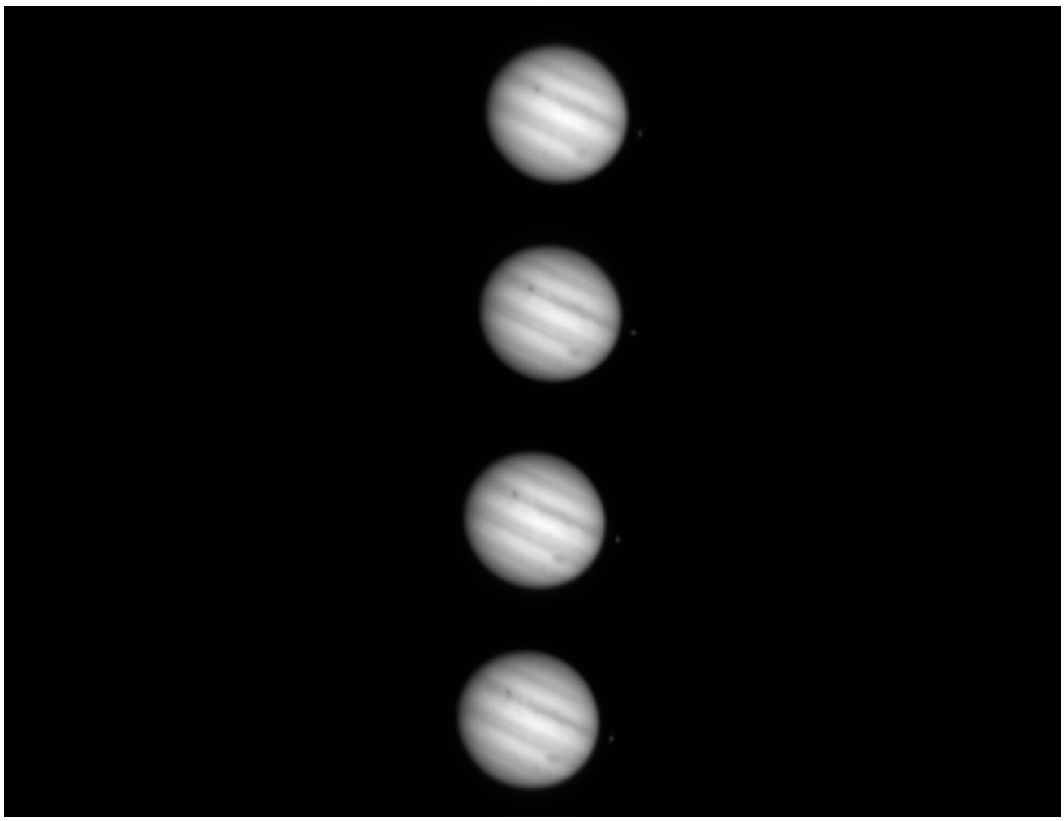

Figure 3.18: ToPol CCD image of Jupiter in the V filter. From the top down, the four beams are each proportional to $F + Q$, $F - Q$, $F + U$, and $F - U$.

be accounted for: firstly, the different images in each strip of the CCD have to be aligned in order to be superimposed. Secondly, the different images on the CCD have a different sharpness, even when taken at the same time, arising from distortion caused by the beam path taken through the instrument. These issues are discussed after the instrumental polarisation is first considered.

When considering CCD images of extended sources it is important to quantify the instrumental polarisation and how it varies across the field of view of the polarimeter. The variation of the instrumental polarisation across the field of view was characterised by the observation of known unpolarised standard stars at different locations in the field of view. Figure 3.19 shows a map of the variation of the instrumental polarisation around the location of the centre of one of the strips on the CCD. This was constructed from observations of the unpolarised star HD90508, and the observations were taken during February and March of 2015 with ToPol, by Maxime Devogèle, in the V filter. Each point corresponds to the average of ten individual measurements of one second on the star taken at the same location on

the CCD field. The map is a binning of all of the points within 2 arcseconds of a specific location on the CCD field.

The observed variation in P_Q and P_U is of the order 10^{-3} at the very most. This variation is rather negligible when compared with the other sources of error, such as the photon noise and the error from image alignment (discussed later in this section), and thus these small variations in the instrumental polarisation across the CCD were able to be safely ignored.

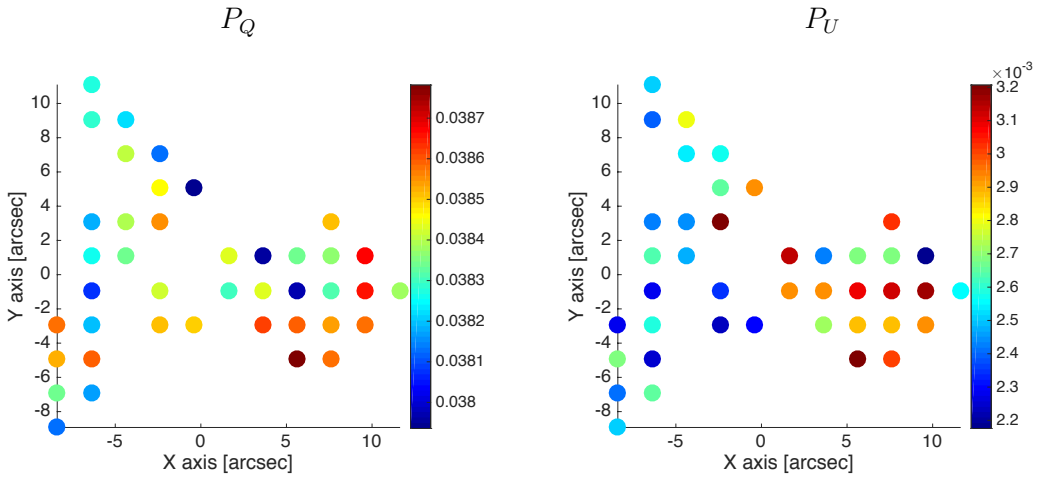

Figure 3.19: Left: map of the variation on the CCD of P_Q. Right: corresponding variation of P_U.

As a function of time, the instrumental polarisation was fairly stable, varying only by several hundredths of a percent over the period that the data from ToPol used in this thesis were acquired (February 2015 - January 2017). The instrumental polarisation in each filter is given in Table 3.4, along with the effective central wavelength in nanometres (nm)[3]. These values were calculated from observations of unpolarised standard stars HD10476 and HD18803, taken with ToPol by the author in December 2016 (see Table 3.3).

[3]http://www.aip.de/en/research/facilities/stella/instruments/data/johnson-ubvri-filter-curves

Table 3.4: ToPol instrumental polarisation in each of the five filters.

Filter	Filter λ_c (nm)	Instrumental P_Q (%)	Instrumental P_U (%)	Instrumental P_L (%)
U	365.6	5.78±0.02	0.67±0.02	5.82±0.02
B	435.3	5.97±0.06	0.62±0.06	6.01±0.06
V	547.7	3.82±0.01	0.27±0.01	3.83±0.01
R	634.9	3.59±0.01	0.39±0.01	3.61±0.01
I	879.7	3.65±0.02	0.55±0.02	3.69±0.02

In each individual image, the images in the four strips were all misaligned to some extent because of the different optical path the four beams take. Successive images taken were misaligned perhaps because of slightly inaccurate guiding of the telescope, or because of seeing variations shifting the images for the short exposure times used. Conventional algorithms used for image alignment, such as those available in *iraf*, seem to be optimised for the use with point sources and not extended objects with undefined shapes. A major part of the time spent on the work presented in this thesis went into devising the best image alignment method for this data; with all methods trialled multiple times by different people and using different software. All of the alignment methods were first trialled for Jupiter, and it was found that Saturn images were too distorted to be successfully aligned. The Mars data were successfully aligned, most likely because it is of a similar shape when projected onto the CCD as Jupiter.

The first attempt at aligning the images was done by using the *phot* task in the *iraf daophot* package, but this was proven to be unrelaible, most likely since Jupiter is an extended source with no obvious centre, and is not perfectly circular, so the software was unable to successfully locate the centre to a sub-pixel level of accuracy. The second method that was tried again involved using *iraf* for a Jupiter dataset with two of the Galilean moons visible. This also did not yield success, most likely because the S/N ratio of the moons is very small, with their images changing shape too much between strips. A third method involved taking the best alignment from the first *iraf* method and then making slight adjustments by eye, but this was obviously not a reliable method that could have a quantifiable error. The results of this method are illustrated in Fig. 3.20, which shows latitudinal cuts of the linear polarisation along the central meridian of Jupiter, from three CCD images taken successfully in the B filter. Each of the three plots show a slight variation across the centre of Jupiter with a significant variation at the polar regions. The differences between each of the images cannot be accounted for just by the error on the flux counts from the photon noise, and the different polarisation values cannot be real because the images were only taken several seconds apart. The difference in P_{L} at the polar regions must be due to errors in the alignment of the images on the strips on each CCD image.

Ultimately, no success was found with aligning the ToPol images using any known image alignment or fitting techniques. Thus, a new alignment technique using IDL was devised. This operated through defining an annulus to the outermost region of Jupiter (where the signal is lowest) and fitting an ellipse with the centre and radius

returned by the algorithm. The next stage was to shift each image to a common centre and then cut out and combine to produce the intensity and polarimetric maps. Each image was normalised to its maximum value before being input to the centring algorithm to ensure the same intensity range was always used for each strip. These modified images were only temporary and created solely for the purpose of aligning the original images to a common centre; the original images were the ones used when calculating the reduced Stokes parameters.

Figure 3.21 shows latitudinal profiles in the B filter, produced from the same images used to create the plots shown in Fig. 3.20. Unlike the plots in Fig. 3.20, the polarisation at the poles is much more consistent between the successive images and the features shown across the centre of the disk are also aligned much better. Each method gives consistent results for the north pole, but with the new method the polarisation is actually significantly lower. It is not at all obvious how to asses the reliability of the alignment or to decide which method produces the best results. Given that the differences are all within the error bars due to the photon noise for this new IDL alignment method, it was deemed to be the most reliable alignment method and this was the one used for the data analysis. The intensity images were also checked, and it was found that there was no clear variation in the sharpness of any features between the alignment methods.

In order to quantify the remaining sub-pixel errors arising from the alignment method, maps of $P_Q, P_U, P_{\rm L}$, and χ for each image were constructed, and then the difference between successive images was calculated (a "null" map). The final error used is the combined error from both the photon noise and the image alignment.

The minimum resolvable detail on the disk of a planet is determined by the seeing at the time of observation, which is calculated through measuring the width of the PSF of a standard star. The plate scale of the ToPol images was 0.2379 arcseconds/pixel, so to account for the seeing limitation, a 5×5 box-car smoothing (floating average) was applied to each flux image before combination to create the Stokes parameters.

The analyser used in ToPol consists of two Wollaston prisms sealed together, and this splits the incoming light from the telescope into the four beams. These four beams then all travel along a slightly different optical path towards the CCD and are then focussed at different distances from the CCD. A technique that attempted to quantify and correct for the distortion was devised, and involved taking an observation of a globular cluster and measuring the distances between some of the individual stars in each strip. This method was applied by master's student Giovanni Paolini.

One strip was always used as a reference point, with the correction applied to the

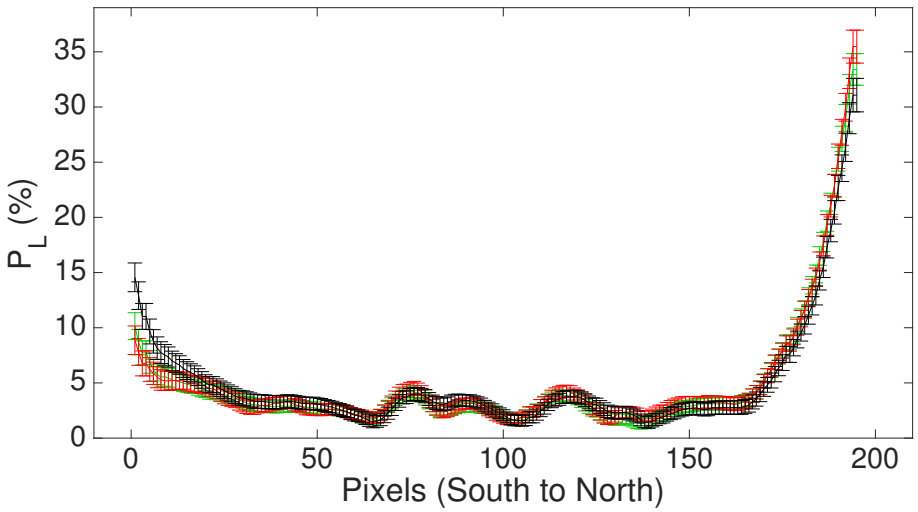

Figure 3.20: Plots of $P_{\rm L}$ vs. distance along the central meridian of Jupiter, as derived from three different CCD images that were read out successively in the B filter, represented by different colours, along with the error bars.

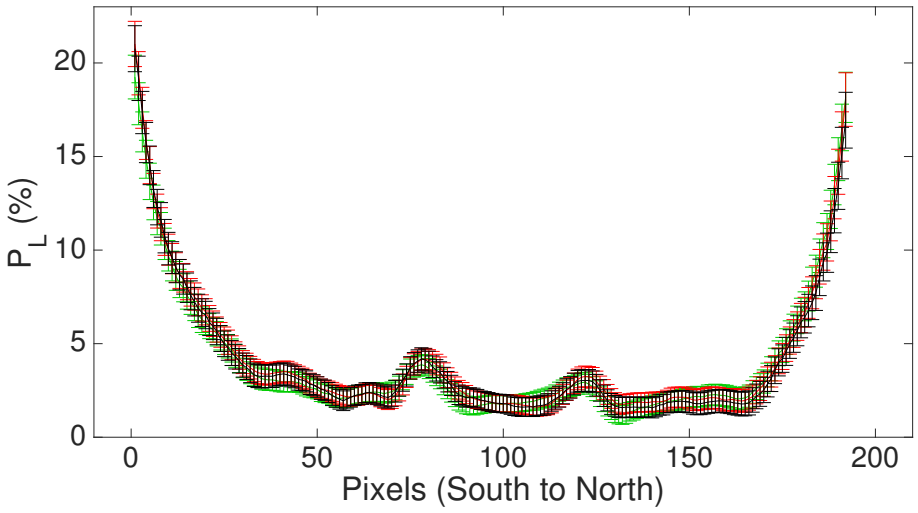

Figure 3.21: Same as for Fig. 3.20, but with the new alignment method.

other three strips. A large number of distances were extracted from the cluster image, and these were used to create a map of the distortion across the CCD. An assumption here is that the aberrations are not time dependent. After calculating the relative distance of the stars between each other, the residuals of these data were used to produce a fit across the whole CCD to obtain error values for each pixel in the two spatial coordinates of the CCD. The residuals were then created by comparing the distances in three strips with respect to one reference frame. The fitting was performed with a 5^{th} order two-dimensional polynomial and a weighting matrix was also used to give more reliability to data close to the frame centre for the production of more accurate results in that area. The order of the polynomial fit maintained the dispersion of the correction at the 0.1 pixel level in both the x and y coordinates, and thus using a higher order of polynomial was deemed to be unnecessary. The distortion corrections obtained were then applied to the Jupiter data on the three strips other than the reference strip.

Unfortunately, the method seemed to introduce more errors than it corrected for, which is shown by Fig. 3.22. This figure shows a map produced with the distortion correction method, compared with a map produced with the final alignment method described previously. These maps are differences between polarimetric maps that were produced with successive images, taken a matter of seconds apart, thus any variations in the polarisation outside of the photon noise error would be due to the alignment method. The residuals shown in the maps are clearly higher for the distortion correction method, so it was therefore decided to not use this distortion correction and to produce the polarimetric maps with the previous shifting and alignment method.

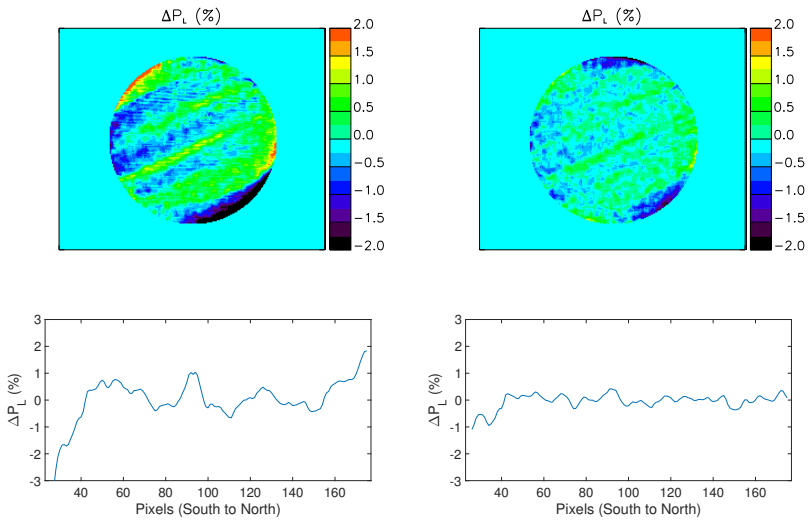

Figure 3.22: Top left: difference between polarimetric maps, denoted ΔP_{L} (i.e., "null maps") created from images that were taken several seconds apart, using the distortion correction method. Top right: Difference between maps created from the same images as for the top left, but with no distortion correction. Bottom left: difference across the central meridian of Jupiter of the maps produced with distortion correction. Bottom right: difference across the central meridian of the maps made with no distortion correction.

Chapter 4

The terrestrial planets

Abstract

Section 4.1 and Section 4.2 give an overview of polarimetric studies of Mercury and Venus, respectively. No results for these planets are presented here, but the review of literature for each is included for completeness, and because important results have been obtained for them, especially Venus. Section 4.3 then presents a study of Earthshine. This follows on from Sterzik et al. [2012], who obtained spectropolarimetry of Earthshine, and later obtained more data for monitoring purposes, with some of these datasets used to produce the results presented in this chapter. Some routines were applied to finalise the data reduction, and the illuminated part of Earth as seen from the Moon during the observations was obtained[1]. Variations caused by surface albedo, cloud height and optical thickness are discussed, along with the influence of the lunar surface on the data. A preliminary rough modelling has been performed, with disk-integrated model signals from Earth-like exoplanets presented showing differences in signal caused by variations in the cloud parameters. Section 4.4 then presents imaging polarimetry and spectropolarimetry of Mars, with one set of the imaging polarimetry data taken when the angular diameter of Mars was sufficiently large for disk-resolved polarimetric maps to be constructed. Changes with time in the flux and polarisation of Mars are likely due to seasonal variations in the Martian atmosphere, potentially caused by dust storms ejecting particulate material from the surface into the tenuous atmosphere.

[1] https://www.fourmilab.ch/cgi-bin/Earth/action?opt=-m

4.1 Mercury

The closest planet to the Sun has been the subject of very few polarimetric studies. Observations of Mercury are usually compared with lunar data, since each body is covered with regolith which is thought to have formed through meteoroid impacts. Additionally, the Moon and Mercury have similar photometric properties, and both have spectra typical for bodies that have iron-bearing silicates [Kaydash et al., 2015].

Observing Mercury from Earth is rather challenging, since the largest elongation that Mercury is seen from the Sun is only around 25°, meaning that all observations have to be made just after sunset or just before sunrise. Mercury has actually been observed during the day by Dollfus & Auriere [1974]. Data were collected from different areas of the surface, and for the whole disk at six wavelengths for small phase angles. It was found that the degree of linear polarisation varied with phase angle, wavelength, and also with the region observed. The dependence on planetary coordinates was found to be more prominent when observed at large phase angles [Kaydash et al., 2015]. Polarisation curves were compared with observations of the lunar surface, and laboratory studies of samples from the lunar surface. It was found from comparison with the lunar data that the surface of Mercury is covered by a layer of regolith similar to that of the Moon, made of dark and absorbing material.

Figure 4.1 shows plots of the linear polarisation of light reflected by Mercury at six different wavelengths as a function of phase angle, obtained by Dollfus & Auriere [1974]. The albedo of Mercury increases with wavelength, and these plots show that the degree of polarisation at large phase angles decreases as the wavelength increases. This is a manifestation of the Umov effect mentioned previously in Section 1.1.

Observations of the surface of Mercury were taken over a planetocentric longitudinal range of 265-330° by Kiselev & Lupishko [2004]. It was found that the degree of linear polarisation varied by 1.5%, even over such a narrow longitudinal range. Variation in polarisation had been noted for other longitude ranges before by Dollfus & Auriere [1974]. The observed variations of polarisation with longitude is thought to be caused by differences in the type of terrain at different locations on Mercury [Kiselev & Lupishko, 2004].

Ground-based imaging polarimetry of Mercury was carried out by Ksanfomality et al. [2007], with maps of the intensity and polarisation produced of the planetary disk. However, problems with filtering out the Earth's atmosphere posed questions regarding the reliability of these maps and, as will be discussed in later chapters of this thesis, emphasises the need for caution and extra-high prescision when con-

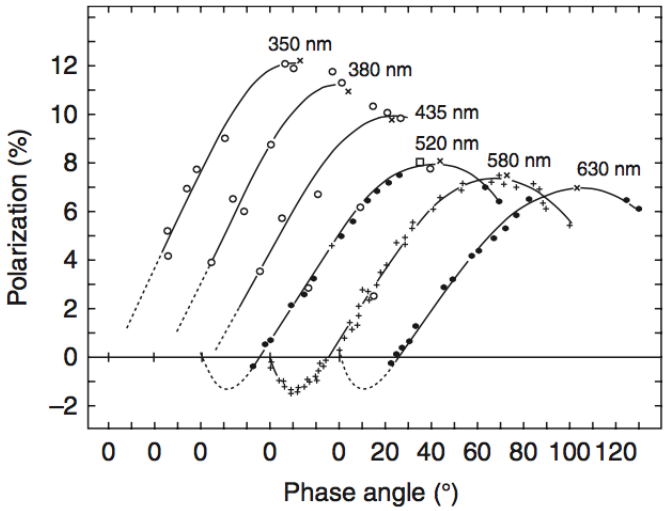

Figure 4.1: Polarisation of light reflected by the whole disk of mercury in six filters. The curves are shifted along the x axis for clarity. Figure reproduced from Kaydash et al. [2015], with original from Dollfus & Auriere [1974].

structing intensity or polarimetric maps. As Figure 4.2 shows, the maps do however show that there are details present in the polarisation map that are not found in the intensity image, which implied that the surface of Mercury exhibited properties not conforming to the Umov effect [Kaydash et al., 2015]. These observations

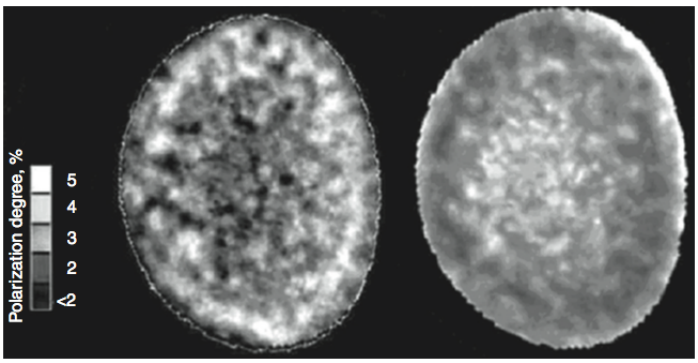

Figure 4.2: Left: degree of linear polarisation of Mercury. Right: corresponding intensity map. Both images were taken at a phase angle of 63° in a red filter. Figure reproduced from Kaydash et al. [2015], with original from Ksanfomality et al. [2007].

were carried out at a phase angle of 63°, far from the angular position where the maximum of polarisation is observed ($\sim 110°$), but this is not a possible reason for the discrepancies between intensity and polarisation [Kaydash et al., 2015]. It is known from polarimetry of the lunar surface and from laboratory experiments that

the slope of polarisation as a function of phase angle near the inversion angle also correlates quite closely with the degree of polarisation at larger phase angles.

López Ariste et al. [2012] performed spectropolarimetry of the Na D emission lines emitted in the exosphere of Mercury in two different phase angle ranges. Scattered solar light causes the emission of Na D lines from the exosphere, and like every scattering process, this emission is polarised. Polarisation was found in the D_2 line but not in the D_1 line. Broadband polarimetry at certain phase angles were found to be roughly a factor of two less than what would be expected from an isolated sodium atom. Depolarisation caused by the high optical depth is stated as the most probable cause of this factor of two discrepancy. The possibility of using these types of measurements to infer physical conditions in the exosphere of Mercury and as a tool for for studying the magnetic field of Mercury and its variability was emphasised by López Ariste et al. [2012].

Mercury has been visited by only two spacecraft: NASA's Mariner 10 mission, launched in 1974, and NASA's MESSENGER mission, launched in 2004. None of these spacecraft conducted polarimetric measurements of Mercury, but of course future spacecraft containing polarimeters could vastly increase our knowledge of the composition of the surface of Mercury.

4.2 Venus

This section reviewing polarimetric studies of Venus is extensive (although by no means exhaustive), and whilst this work does not include new polarimetric studies of Venus, many of the concepts and findings resonate with those for other planets, such as Jupiter and Saturn. In particular, the spherical nature of the cloud particles of Venus allows a model fit with particles generated using Mie theory, whereas for the gas giants the particles are known to be complex in shape, precluding the use of Mie theory for an accurate particle characterisation. Later sections and chapters will discuss this in more detail.

Unlike for Mercury, there are a vast number of polarimetric studies of Venus in the literature. This is partly because Venus is more favourable to observe polarimetrically from Earth than the outer planets, because Venus can be observed at a wide range of phase angles, including quadrature. The outer planets can only be observed at small phase angles, where the observed light is mostly backscattered light with a low degree of polarisation.

Venus is enshrouded by a thick atmosphere, with the rocky surface below hidden beneath thick cloud layers. Polarimetry has thus often been used for remote sensing of these aerosol particles contained in the clouds.

The first measurements of the polarisation of sunlight reflected from Venus were carried out in the 1920s by Lyot [1929]. Lyot also carried out laboratory measurements and showed that multiple scattering had the effect of reducing the amount of polarisation, without altering the general shape of the polarisation curve. Lyot's analysis of the observational data led him to conclude that the clouds of Venus contained small transparent droplets, which he assumed to be water vapour. Other ground-based polarimetric studies were carried out after this [see Hansen & Hovenier, 1974; Gehrels et al., 1979; Dollfus et al., 1979; Konnen et al., 1993], with some of the key results discussed in this section, but more recently the majority of polarimetric studies of Venus are based on the analysis of spacecraft polarimetric data [Kaydash et al., 2015].

Hansen [1971b] carried out a computational study on the polarisation of sunlight reflected from Venusian clouds, and demonstrated that polarisation observations are more sensitive to the cloud particle characteristics then intensity measurements. The polarisation of reflected sunlight was found to decrease with increasing optical thickness, due to the multiple scattering of the photons. Even if the intensity of the reflected sunlight is low, the polarisation can still be high. If multiple scattering occurs, then polarisation features caused by previous scatterings will still be present.

Hansen & Hovenier [1974] used ground based aperture polarimetry to determine that the clouds of Venus are composed of sulphuric acid droplets around one micron in size. Intensity spectra could only establish the presence of clouds, but did not contain enough information to deduce the composition of the clouds. Observing the variation in brightness across the planetary disk, and with phase angle, constrained the size of the cloud particles slightly, but polarimetry was required to fully characterise the particles.

Hansen & Hovenier [1974] determined the refractive indices, the shape and size distribution of the particles, and also the cloud-top pressure of the visible clouds on Venus. To deduce these parameters, observations taken by several authors (see Hansen & Hovenier [1974] and references therein) were compared with models for different sizes of particles and refractive indices at different wavelengths. Figure 4.3 shows the variation in the polarisation of Venus with phase angle, with several models fitted for different particle sizes. The modelling was carried out by Hansen & Hovenier [1974], and were computed for the wavelength $\lambda = 550\,\mathrm{nm}$. The refractive

index for each curve is 1.44, with the variation in polarisation between curves due to the different particles sizes. A close fit is obtained for particles with a radius of 1.05 microns. The phase curve of Venus is very different to that of Mercury or the Moon, due to the influence of the dense atmosphere. Also measured in green light, the polarisation of Venus is negative at large phase angles, and can have two maxima and two minima. This behaviour is typical of small spherical particles [see Lyot, 1929; Hansen & Arking, 1971; Young, 1973; Coffeen & Hansen, 1974; Hansen & Hovenier, 1974; Coffeen, 1979]. The spike in polarisation at a phase angle near 18° could be from the primary rainbow feature occurring in scattering of spherical particles, at a refractive index of 1.44.

Hansen & Hovenier [1974] found that the size, shape and refractive indices of the particles are very uniform over most of the illuminated part of Venus, at least for the clouds visible down to an optical depth of around one, where the pressure was found to be 50 mb. The analysis was based on disk-integrated observations, so the properties of the particles are average values. Before this study was carried out there were many theories as to what the atmosphere of Venus was composed of. Models were computed for observations taken at different wavelengths from the near UV to the IR; it was found that the refractive index of the cloud particles ranged from 1.46 ± 0.015 at $\lambda = 365$ nm to 1.43 ± 0.015 at $\lambda = 990$ nm, which matches with a concentrated sulphuric acid solution [see Young, 1973]. The cloud particles were found to have a narrow size distribution with a mean effective radius of $r_{\text{eff}} \sim 1050 \pm 100$ nm, and effective variance $v_{\text{eff}} = 0.07 \pm 0.02$. Later work by Kawabata & Hansen [1975] presented further models of the Venusian clouds, but were found to be only slightly different to the findings of Hansen & Hovenier [1974]. The study by Hansen & Hovenier [1974] clearly demonstrated the power of polarimetry, compared with standard intensity measurements. Intensity spectra can reveal much about planets, but polarisation spectra and phase angle curves can yield extra information.

Dollfus et al. [1979] compiled polarimetric images from measurements of several parts of the disk of Venus. The findings of Dollfus et al. [1979] agreed with those from disk-integrated polarisation of Hansen & Hovenier [1974]. The direction of polarisation was found to not always remain parallel or perpendicular to the plane of scattering in all regions observed. It was suggested by Dollfus et al. [1979] that this may be due to the filamentary structure in the clouds. The orientation of the polarisation angle was also found to differ in the polar regions, most likely due to local variations in cloud coverage. It was also found that at phase angles near α_{inv} the direction of polarisation can vary. At wavelengths of $\lambda = 364$ nm and phase

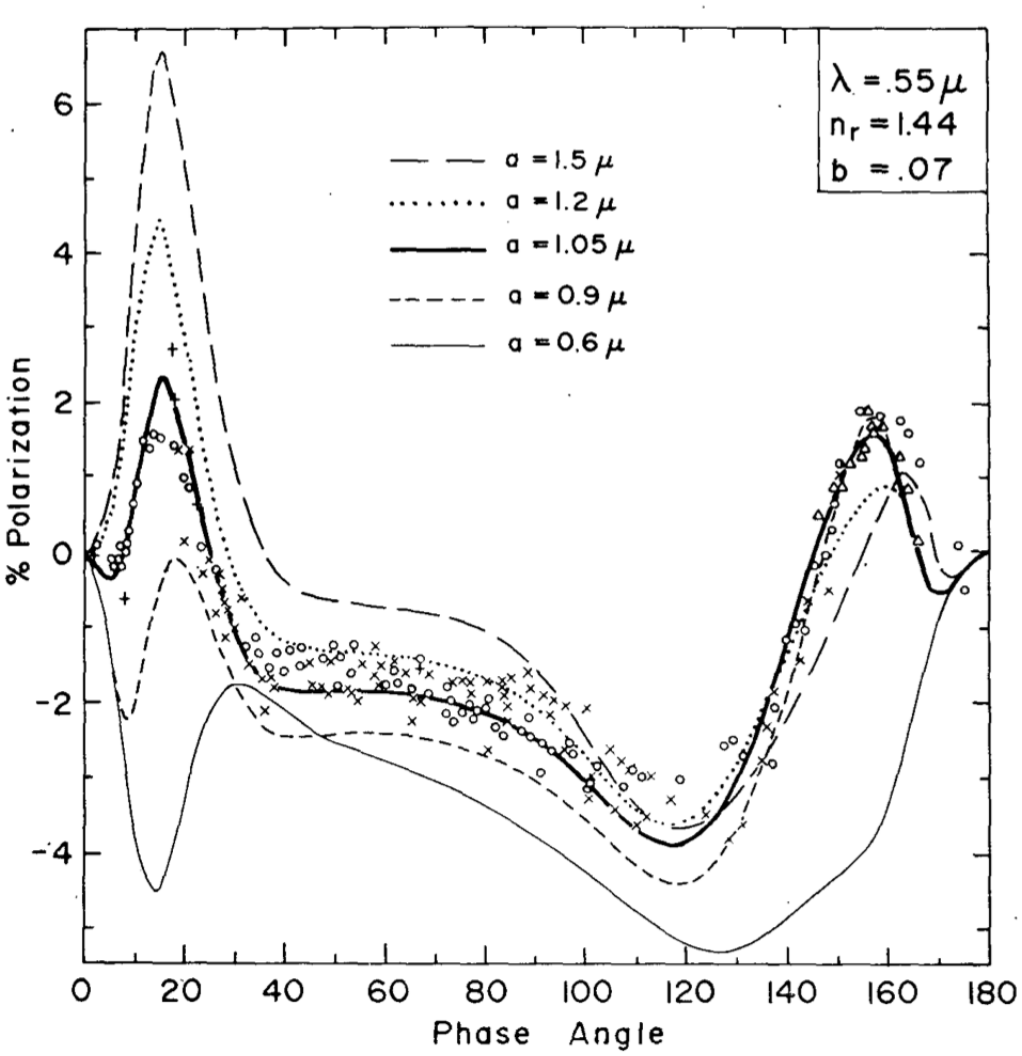

Figure 4.3: Observations of the polarisation of the sunlight reflected by Venus in the visual wavelength region, along with polynomials generated from models. The observations are indicated by the different points - each type of point refers to a different study (see Hansen & Hovenier [1974] and references therein). Image from Hansen & Hovenier [1974].

angles near 100°, Dollfus et al. [1979] found that the polarisation was negative in the northern hemisphere and the equatorial regions, but positive at southern latitudes. This can cause disk-integrated polarisation to vanish.

Several studies of linear polarisation with phase angle and wavelength have revealed certain variations across the disk of Venus. Starodubtseva [1987] found that for a wavelength range of 360-630 nm and at phase angles from 69-104° the regional polarisation of Venus changes with time, including differences in polarisation in the spring and autumn elongations. A haze of small particles with a size of 200 nm was put forward as potential cause of these variations. Periodical variations occurring around every 4.5 days were also observed from the same data set [Starodubtseva, 1991]. An inverse correlation between intensity and polarisation was also found from this study, which demonstrates the Umov effect in action. Variations in the polarisation with wavelength, phase angle, and planetary location were also observed by the Pioneer Venus orbiter [Limaye, 1984].

The demonstration of Hansen & Arking [1971], Young [1973], and Hansen & Hovenier [1974] that the size and composition of Venusian cloud particles could be deduced from ground-based observations was hailed as a major breakthrough in polarimetric remote sensing for planetary science. The analysis and interpretation of polarimetric measurements taken of objects lacking a sizeable atmosphere are however much more challenging tasks, occasionally leading to ambiguous results [Kaydash et al., 2015].

Measurements of the atmosphere of Venus have been conducted with the NASA Pioneer Venus spacecraft, launched in 1978, and ESA's Venus Express orbiter, launched in 2005. The photopolarimeter onboard Pioneer Venus mapped the intensity, degree of linear polarisation, and direction of polarisation across the visible disk of Venus at a spatial resolution of around 500 km. Data were taken at four wavelengths, and the results are presented in Kawabata et al. [1980]. The results of the Pioneer Venus mission are consistent with the presence of sulphuric acid droplets of around $\sim$1 μm radius found with Earth-based polarimetry [Hansen & Hovenier, 1974].

Analysis of the Pioneer Venus data showed a large value of positive polarisation near the day-night terminator and the cusps of the disk at 935 nm, which is quite different from the large negative values of polarisation found at this wavelength and phase angle by the 1 μm sulphuric acid droplets. Another region of positive polarisation, but with smaller magnitude, was found at the terminator and cusps at 550 nm [Travis et al., 1979]. These variations in polarisation magnitude and direction are consistent with a thin layer of sub-micron aerosol particles across the

entire planet residing in the lower stratosphere, at an altitude much higher than the main sulphuric acid cloud deck [Travis et al., 1979]. Through comparison of the phase angle dependence of the polarisation in the polar regions with theoretical single scattering models at different wavelengths, Kawabata et al. [1980] provided estimates of the haze particle properties: an effective radius $r_{\text{eff}} = 0.23 \pm 0.04\,\mu$m, effective variance of the distribution $v_{\text{eff}} \sim 0.18 \pm 0.1$, and a refractive index of $n = 1.45 \pm 0.04$.

The submicron haze particles have been shown to be present at different levels in the atmosphere of Venus: in the cloud deck, above the clouds, and below the clouds [Ragent et al., 1985]. Their exact nature is presently unknown, and is likely to vary with atmospheric altitude and planetary location. The need to include these submicron particles in models to fit the polarisation was shown by Knibbe et al. [1997], where models are presented that attempt to fit polarisation measurements with a haze layer above the clouds, and submicron and micron sized particles mixed in with the sulphuric acid cloud layer. If there are haze particles mixed with the clouds, and the effective radii of the cloud particles are in the range 850-1150 nm, with the effective radii of the haze particles between 200-300 nm, the haze particles can contribute a fraction of up to 70% of the total atmospheric scattering coefficient at a wavelength of 550 nm [Kaydash et al., 2015].

The Venus Express orbiter had a polarimeter that operated in the spectral range 650-1700 nm, which studied the aerosols on the dayside of Venus [Korablev et al., 2012].

Rossi et al. [2013] studied the polarisation data from Venus Express for data taken in the northern hemisphere at a wavelength of $\lambda = 1553$ nm. This was the first time polarisation of Venus was studied at this wavelength. Measurements taken at low and high latitudes (less than and more than 50°, respectively) show differences at large phase angles. The findings of Rossi et al. [2013] confirm previous estimates of upper cloud-particle properties of Venus. A wide minimum in polarisation was observed at a phase angle of 18°, and Rossi et al. [2013] note this could be a glory corresponding to sulphuric acid particles of radius 1 μm. A glory is a ringed phenomenon that is observed at the point diametrically opposite the light source, and the glory phenomenon is a source of much debate, with its understanding quite incomplete [see Bohren & Huffman, 1998; Laven, 2004; Greenler, 1980]. Interestingly, glory-like phenomena have been repeatedly observed in images taken by a camera on the Venus Express spacecraft [Petrova et al., 2013].

Rossi et al. [2015] present further analysis of polarimetric data from Venus Express,

with a retrieval of the cloud parameters. The data were again mainly for the northern hemisphere, in the full spectral range of the instrument. Temporal variations in the latitudinal and longitudinal distributions of the Venusian clouds and hazes are examined. The results are all in agreement with previous ground-based observations and those from the Pioneer Venus mission. Mean values of the cloud and haze particles are derived from fitting numerical models: the cloud were found to have an effective radius $r_{\text{eff}} \sim 1\,\mu\text{m}$, and effective variance $v_{\text{eff}} \sim 0.07$, and a refractive index of $n_r = 1.42 \pm 0.02$ at a wavelength of $\lambda = 1.101\,\mu\text{m}$. An upper limit on the haze optical thickness at high latitudes was found to be $\tau_{\text{h}} = 0.17$.

The Soviet spacecraft Venera 8 and Venera 10 landed on Venus, both of which contained a nephelometer, a device that can measure the properties of particles suspended in a fluid. Each of these probes carried out studies of the aerosols beneath the visible cloud deck of Venus [Ragent & Blamont, 1980]. However, the nephelometers did not take measurements of polarisation as a function of phase angle.

Other studies of Venusian polarimetry include a search for ice crystals in the upper atmosphere of Venus with polarimetry [Konnen et al., 1993]. Additionally, Sato et al. [1996] analysed polarisation measurements of the polar regions taken by Pioneer Venus. This work analysed the radii and refractive indices of haze particles in the northern and southern polar regions. A major finding that is noteworthy of Venusian polarimetry is the excellent concurrency between results obtained with ground-based telescopes and those obtained from Venusian orbiter missions. In particular, the agreement in the estimated properties of the particles in the clouds and hazes of Venus is remarkable [see Ragent et al., 1985; Grinspoon et al., 1993; Taylor, 2006].

4.3 Earth

4.3.1 Introduction

Sources of the polarisation in light reflected and scattered by Earth come from a combination of scattering in the atmosphere, and reflection and scattering at the surface. Contributions to the atmospheric scattering come from Rayleigh scattering in the clear air, and scattering by aerosols, such as cloud particles. Particles scattered off water droplets in clouds will show a rainbow polarisation feature at a scattering angle of 140°, a feature which does not show for ice crystals. The surface scattering can arise from reflections or scattering from the canopies of forests, desert

and the glint of sunlight from smooth ocean surfaces, snow and ice [Wolstencroft & Breon, 2005].

Currently, the best way with which to observe polarised light of the entire Earth is by means of Earthshine observations. Earthshine is sunlight first reflected by Earth, and then reflected back to Earth by the Moon. For example, if we observe a crescent moon, then the Earthshine is the light from the rest of the lunar disk not illuminated by the Sun. Leonardo da Vinci noted the phenomenon of the Earthshine in the Codex Leicester, published in 1510, when he realised that Earth and the Moon both reflect sunlight at the same time.

The lunar surface acts as a diffuse reflector, and spatially integrates the light coming from the sunlit part of Earth. Since the Sun-Earth-Moon viewing geometry changes as Earth rotates, different parts of Earth can be sampled. Earthshine is thus a powerful remote sensing tool, allowing us to perform ground-based observations of the disk-integrated signal from Earth as seen from space. Thus, measurements of Earthshine can provide an approximation for observations of the disk-integrated signal from an exoplanet, which can be used as a benchmark for developing observational techniques for finding exoplanets with properties similar to Earth. As will be elaborated on later in this section, polarimetric observations of Earthshine can potentially be used even to infer the presence of biosignatures that could be attributed to life. A major challenge in the interpretation of observations of Earthshine is trying to distinguish whether changes in polarisation are due to light that is reflected from different parts of Earth, and/or changes in cloud coverage. Additionally, it is difficult to quantify changes in polarisation that are due to the inhomogeneous lunar surface and its variable depolarising effect.

Dollfus [1957] made pioneering observations of Earthshine at a wavelength of $\lambda = 550\,\mathrm{nm}$. The degree of linear polarisation was found to vary sinusoidally with phase angle, and was observed to have a maximum polarisation of around 10% near a phase angle of 90°. However, the light from Earth scattered by the lunar surface is partially depolarised, with the cause thought to be the lunar regolith having a negative branch of polarisation [see Shkuratov et al., 2015]. Dollfus [1957] observed that Earthshine from darker, lower albedo regions of the Moon (maria) had a higher degree of polarisation, whereas that from brighter, high albedo (highland) regions of the Moon had a lower degree of polarisation. The depolarisation factor was estimated by Dollfus [1957] to be a factor of ∼3.3, thus the true value of the disk-integrated linear polarisation of the sunlight reflected by Earth at a phase angle of 90° was estimated to be around 30-35%. Later estimates of the linear

polarisation of sunlight reflected from Earth were made from measurements taken with the orbital POLDER instrument in three filters: 443 nm, 670 nm, and 865 nm. These measurements showed that polarisation is strongly dependent on variations in cloud coverage and on wavelength [Wolstencroft & Breon, 2005].

Bazzon et al. [2013] also observed the difference in lunar depolarisation first noted by Dollfus [1957] through Earthshine measurements from different regions of the lunar surface in BVRI passpands, finding that Earthshine from the darker maria region had a degree of polarisation 1.30 ± 0.01 times higher than that from the brighter highland regions. The location on the Moon at which the Earthshine was observed is therefore a crucial factor when analysing such data.

Spectropolarimetry of Earthshine [Sterzik et al., 2012; Takahashi et al., 2013; Miles-Páez et al., 2014] all show a decrease in the polarisation in the optical from blue to red wavelengths. To the first order, this is caused by Rayleigh scattering from small particles in the atmosphere of Earth. To accurately determine the polarisation of light scattered by Earth, the depolarisation of the Moon must first be understood and estimated correctly [Wiktorowicz & Stam, 2015].

Figure 4.4 shows plots from Sterzik et al. [2012], who carried out spectropolarimetry of Earthshine at two different epochs. These plots are for one epoch, with the red lines showing P_Q, and black lines showing model spectra. The continuum polarisation and residual polarisation (calculated by subtracting a polynomial fit from the continuum spectrum) are plotted with different scale units shown on the right-hand y axis, in order to show more clearly the fine structure in the spectrum. The model spectra were reduced in amplitude to correct for the lunar depolarisation effect. Different line styles represent models with different parameters (see Sterzik et al. [2012] for details). The green line represents P_U, with the same scale as the right-hand side. The open triangles are POLDER-based estimates of the disk-integrated Earth polarisation at the corresponding wavelengths, with different cloud coverage levels. The open diamond shows the estimate of Dollfus [1957] after correction for lunar depolarisation.

Observing the disk-integrated light reflected by Earth is challenging because it is necessary to manoeuvre a spacecraft at a distance great enough to capture the entire illuminated disk. A disk-integrated signal of light from Earth contains information on all of the features visible at the time, namely: clouds, hazes, and contributions from surface features such as water, ice, sand and soil. Earth is the only planet in the Universe currently known to harbour life, therefore studies of the disk-integrated signature of the reflected light from Earth can be used as a benchmark to search

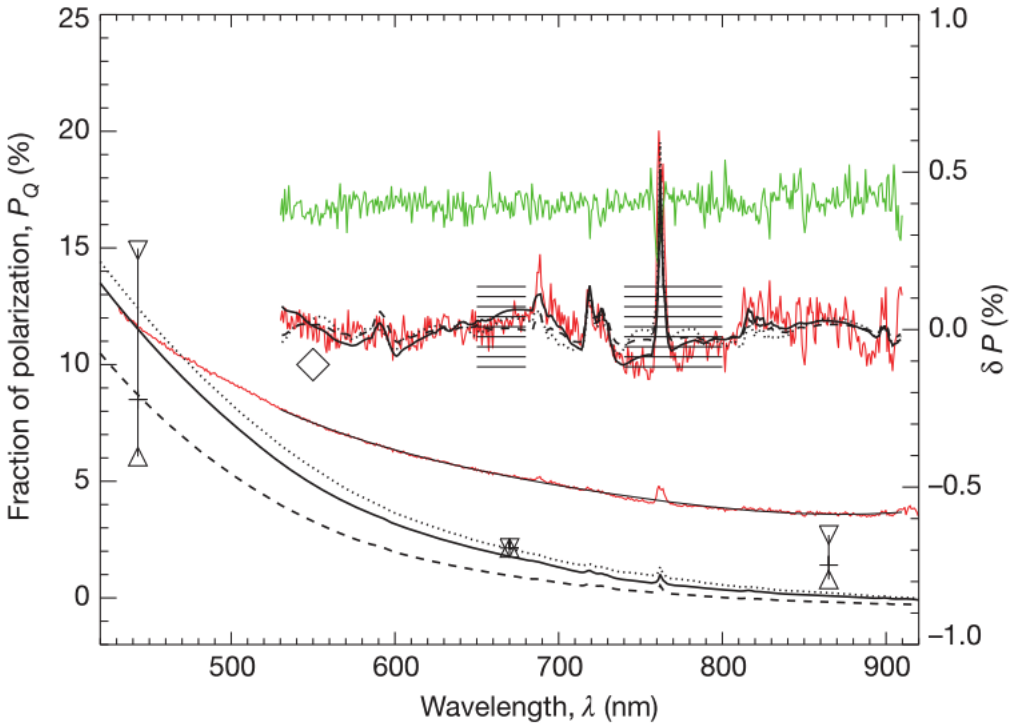

Figure 4.4: Polarisation of Earthshine, see the text for figure explanation. Figure from Sterzik et al. [2012].

for life on exoplanets. The spectral energy distribution of such a signal from Earth would yield features such as molecular oxygen, water, and ozone (O_3) absorption lines. Polarimetry of disk-integrated light from Earth would serve as an excellent benchmark for studies of exoplanets that may be similar to Earth. There is at present only one satellite monitoring the disk-integrated signal of Earth (the NASA DSCOVR satellite), but this satellite unfortunately does not have polarimetric optics onboard. Proposals for missions to be placed on the lunar surface with polarimetric optics to observe the disk of Earth have been mooted [Karalidi et al., 2012b], but until this materialises the best method to observe Earth in polarised light is through the study of Earthshine.

The clouds in the atmosphere of Earth are found at a broad range of altitudes. Most of the clouds are formed in the lowest region of the atmosphere, the troposphere, where the temperature generally decreases with increasing altitude. On average, the upper boundary of the troposphere with the next layer, the stratosphere, decreases with increasing latitude, thus the maximum cloud-top altitude also decreases with increasing latitude. This ranges from $\sim$20 km in equatorial regions of Earth to $\sim$10 km in the polar regions. The highest clouds usually have ice particles present in their upper layers. The reason that most clouds form in the troposphere is due to the relative lack of water vapour in other layers of the atmosphere, but some cloud types can be found in upper layers. Noctilucent clouds are tenuous cloud formations composed of ice crystals that can occur in the mesosphere, the layer above the stratosphere, at certain latitudes and are season dependent. Other cloud types can form, but the predominant ones that are seen from space are likely to reside in the troposphere, and thus the same might be expected for exoplanets.

This section presents Earthshine observations taken with the FORS2 instrument at the VLT, Chile. The observations were taken by Daphne Stam and Michael Sterzik (programme ID 090.C-0096(A)). Data for twelve individual epochs are presented, along with models of the flux and polarisation reflected by Earth-like planets, as a function of wavelength and phase angle. As mentioned before, a major problem with the interpretation of such data is the influence of the lunar surface, which is known to cause a depolarising effect on the incident light from Earth that is then reflected back. This is discussed later on when the data are presented.

The rest of this section is structured as follows: Section 4.3.2 gives the details of the observations and then presents the results of the observations, with Section 4.3.3 following this with models of Earth-like exoplanets. Section 4.3.4 then discusses and summarises the findings from this section.

4.3.2 Observations and results

A total of twelve datasets are presented, and all were taken with FORS2 at the VLT. The instrument and the data reduction are described in Section 3.2.1 and Section 3.3.3.1, respectively. Figure 4.5 shows the image of Earth and what is visible on the illuminated, visible surface at the time each dataset was taken. Table 4.1 gives the log of the observations, and is structured as follows: column one assigns a name to each dataset, column two lists the date of observations, and column three gives the corresponding universal time (UT). Column four states the exposure time of each frame in seconds. Column five gives the phase angle (that is, the angle Sun-Earth-Moon, as if the Earth was observed from the Moon). Column six gives the name of the grism used, and column seven gives the name of the filter, if used.

Table 4.1: Details of the Earthshine observations, with the column meanings explained in the text.

Dataset	Date	Time (UT)	Exp. Time (s)	STO (°)	Grism	Filter
ES1	06/10/2012	07:42	150	111.54	300V	GG435
ES2	07/12/2012	07:46	60	81.25	300V	GG435
ES3	17/12/2012	00:36	60	50.07	300V	GG435
ES4	18/12/2012	00:22	60	62.86	300V	GG435
ES5	19/12/2012	00:33	60	75.40	300V	GG435
ES6	19/12/2012	01:59	60	75.96	300V	GG435
ES7	02/02/2013	06:10	120	106.37	300V	GG435
ES8	03/02/2013	07:05	120	93.11	300V	none
ES9	03/02/2013	08:02	120	92.74	300V	GG435
ES10	03/02/2013	09:03	120	92.38	300V	none
ES11	04/02/2013	07:43	120	79.73	300V	none
ES12	05/02/2013	07:49	120	66.39	300V	none

Plots of P_{L} as a function of wavelength are shown in Figure 4.6 and Figure 4.7 for datasets when the African continent and the Pacific Ocean are the predominant features, respectively. The datasets and phase angles are labelled on the graphs.

Differences in the polarisation between each of the datasets must be due to combinations of a variation in phase angle, surface area coverage, and cloud coverage at the time of observation. Additionally, the region of the Moon from which the disk-integrated data is observed from also influences the final result, because of the depolarising effect of the lunar surface. The lunar surface has two main distinguishing features: the dark planes known as maria, and the lighter highland areas. The maria are composed of basaltic rocks, formed by ancient volcanic eruptions. They

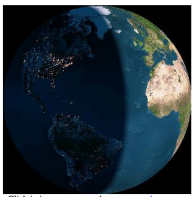

(a) Dataset ES1, $\alpha = 111.54°$.

(b) Dataset ES2, $\alpha = 81.25°$.

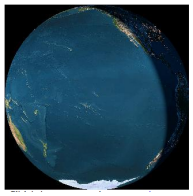

(c) Dataset ES3, $\alpha = 50.07°$.

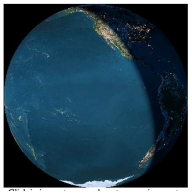

(d) Dataset ES4, $\alpha = 62.86°$.

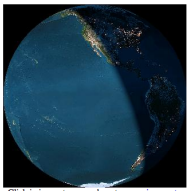

(e) Dataset ES5, $\alpha = 75.40°$.

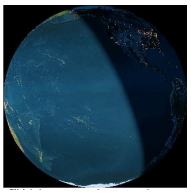

(f) Dataset ES6, $\alpha = 75.96°$.

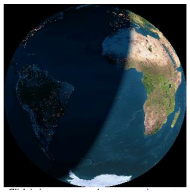

(g) Dataset ES7, $\alpha = 106.37°$.

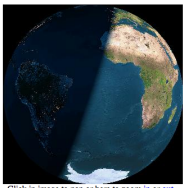

(h) Dataset ES8, $\alpha = 93.11°$.

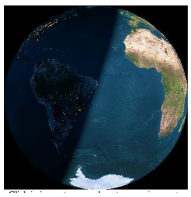

(i) Dataset ES9, $\alpha = 92.74°$.

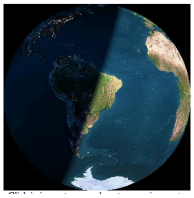

(j) Dataset ES10, $\alpha = 92.38°$.

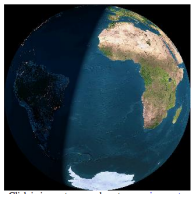

(k) Dataset ES11, $\alpha = 79.73°$.

(l) Dataset ES12, $\alpha = 66.39°$.

Figure 4.5: Different parts of Earth visible from the Moon in each dataset.

reflect less light than the highland regions since they are rich in iron, so appear dark to the naked eye, and by the Umov law have a higher polarisation than the highland regions.

The differences in the four Pacific Ocean datasets will be due to a combination in the phase angle difference, from 50° to 76°, and the change in the cloud fraction, cloud altitude, optical thickness, and particle types at the time of observation. Additionally, the surface features can also greatly affect the polarisation; it can be seen in Figure 4.5 that, whilst the Pacific Ocean is the dominant feature in all four datasets, different fractions of North and South America, Oceania, and Antarctica are all visible. The different surface properties of these landmasses will all influence the total disk-integrated signal.

Interpretation of the eight datasets showing the African continent and Atlantic Ocean as the dominant features suffers from the same problem of differing landmasses contributing to the signal. As well as large parts of Africa and the South Atlantic, parts of Europe, South America, the Arabian Peninsula, and both polar regions are visible. Unknown cloud information again makes it further problematic to characterise the cause of differences in these datasets. The phase angle variation will be partly due to these changes, ranging from 66.39° to 111.54°.

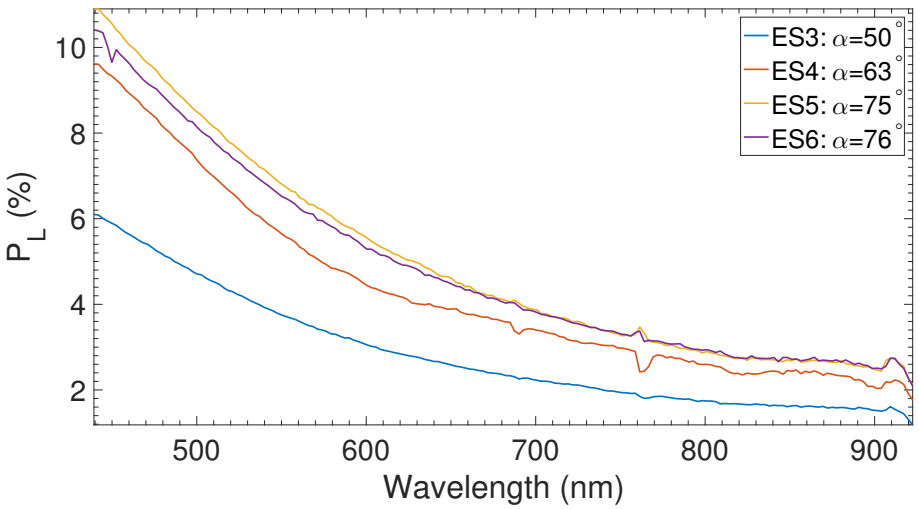

Figure 4.6: P_{L} versus wavelength for the four datasets with the Pacific Ocean the dominant feature.

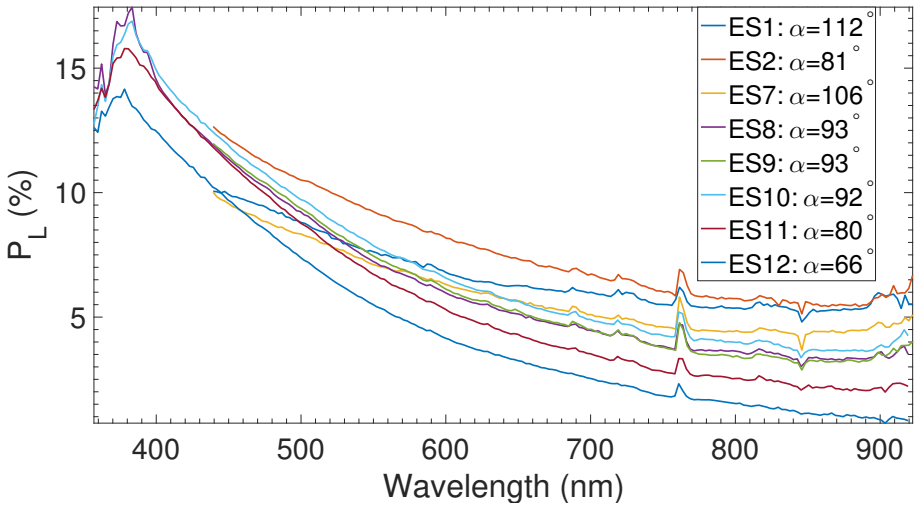

Figure 4.7: $P_{\rm L}$ versus wavelength for the eight datasets with the African continent in view.

4.3.3 Models of Earth-like exoplanets

Models of the flux and polarisation of the light reflected by Earth-like exoplanets were computed using the radiative transfer algorithm described in Section 2.3. The models use particle parameters similar to Karalidi et al. [2011], assuming a constant refractive index of 1.335+0.00001i; the authors of Karalidi et al. [2011] remark that their results are unaffected by assuming a constant refractive index. The size parameter of clouds on Earth is known to vary from values as small as a few microns, to several tens of microns, as has been reported from some satellite measurements [Minnis et al., 1992; Goloub et al., 2000]. Different cloud particle properties are used to demonstrate the sensitivity of the degree of linear polarisation to the cloud type. The first cloud particle type used has an effective radius, $r_{\rm eff} = 6\,\mu$m, with $v_{\rm eff} = 0.4$. The second cloud type has an effective radius, $r_{\rm eff} = 2\,\mu$m, with $v_{\rm eff} = 0.1$. Both cloud types have a refractive index 1.335+0.00001i.

Figure 4.8 shows the spectral variation of linear polarisation for clouds of $r_{\rm eff} = 6\,\mu$m for different altitudes in the atmosphere, and optical thicknesses, at a phase angle of 90°. Figure 4.9 shows the same models but with clouds of $r_{\rm eff} = 2\,\mu$m. Model 1 shows a clear atmosphere, with an albedo of 0.3. Model 2 has a cloud with optical thickness b^c=0.5 at a height of 3 km from the surface. Models 3, 4, and 5 have clouds with b^c=1.0, 2.0, and 10.0, respectively, all at a height of 3 km. Model 6 has a cloud of b^c=10.0 at a height of 2 km, and model 7 has a cloud of b^c=10.0 at a

height of 4 km. The models clearly indicate that introducing clouds has the effect of reducing the polarisation, and increasing the atmospheric height of the cloud reduces it even further. This is due to the fact that light has to penetrate more into the atmosphere to scatter off the lower height clouds, thus fewer photons actually make it both through, and back up. The clouds higher up have more photons interact with them, therefore more multiple scattering takes place in the cloud layer, and a lower polarisation is found. The higher polarisation at bluer wavelengths is due to the increased contribution of Rayleigh scattering, which varies as $\sim \lambda^{-4}$. Figure 4.10 show phase curves for clouds of $r_{\text{eff}} = 6\,\mu$m for different altitudes in the atmosphere, with Figure 4.11 showing plots for clouds of $r_{\text{eff}} = 2\,\mu$m. All models were ran with phase angle intervals of 2°, at a wavelength of 550 nm.

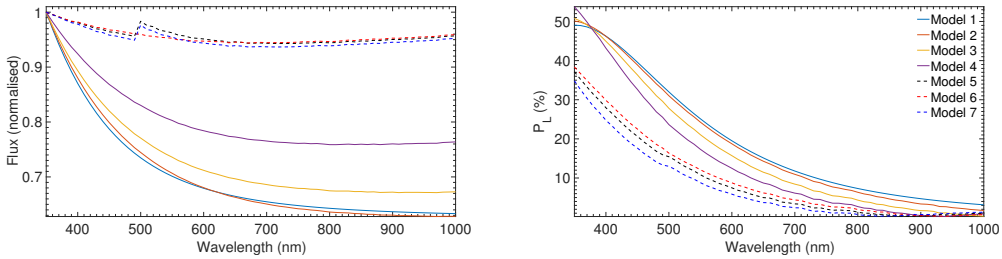

Figure 4.8: Models of the normalised flux and P_{L} showing the effects of cloud height and optical thickness in the atmosphere of an Earth-like planet, for cloud particle type 1.

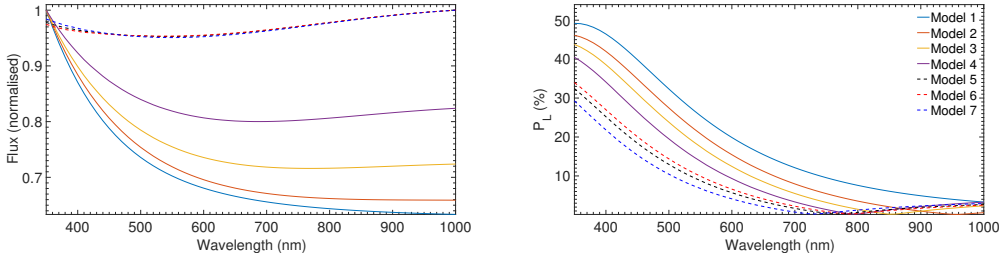

Figure 4.9: Models of the normalised flux and P_{L} showing the effects of cloud height and optical thickness in the atmosphere of an Earth-like planet, for cloud particle type 2.

4.3.3.1 Biosignatures

Biological molecules are chiral, that is, two forms of the molecule can exist, both of which are mirror images of each other. These two different forms, known as left and right handed, are not superimposable on each other. Homochirality is a term

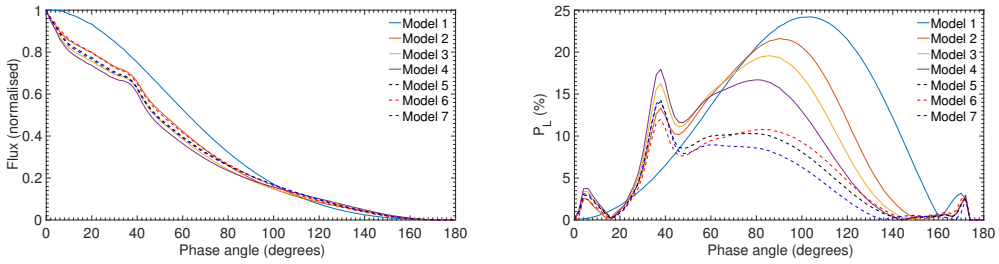

Figure 4.10: Normalised flux and P_{L} as a function of phase angle for the seven model atmospheres, for cloud particle type 1.

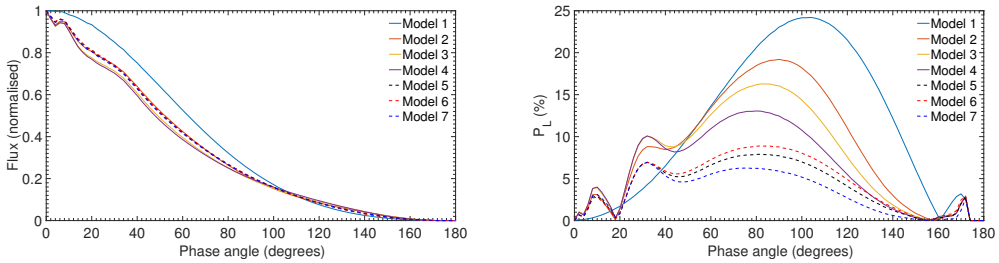

Figure 4.11: Normalised flux and P_{L} as a function of phase angle for the seven model atmospheres, for cloud particle type 2.

used when a molecule can potentially exist in both mirror image forms, but only one is known to exist. Sugars and nucleic acids exist only in their right-handed form, whilst amino acids and proteins exist only in their left handed form. The reasons for homochirality in living material are unknown, but are surely related to the origin of life.

Chirality induces optical activity, with each form (left or right handed) rotating the reflected or transmitted light in opposite directions, thus, biosignatures can potentially be detected through means of observing the circular polarisation of light. An excess of circular polarisation in either its left or right-handed form can indicate the presence of biological materials. Whereas the presence of atmospheric water vapour can provide the evidence for the conditions to support life, circular polarisation measurements from exoplanets could give us further indications that life on these planets exists.

Sterzik et al. [2010] used the EFOSC2 instrument on the ESO New Technology Telescope (NTT), to observe samples of biological materials, taking both linear and circular polarisation spectra. A bacterial species residing in the Atacama desert (an extreme environment on Earth) was one of the targets observed. These were the first and highest precision measurements of circular polarisation of living material

taken with an astronomical instrument.

The experiment found chiral signatures of pigments which are involved in photosynthetic chain reactions in living molecules. The paper states that more accurate measurements of the polarised signal amplitudes requires experiments to be undertaken under better controlled laboratory conditions. Observing the polarimetric signatures of the bacteria considered in the study in their natural habitat beneath translucent rock surfaces will allow the feasibility of detecting this type of bacteria on other solar system bodies with future extremely large telescopes.

4.3.4 Discussion and summary

Earthshine observations were carried out on several nights, for Sun-Earth-Moon phase angles ranging from 51 - 111.5°. The spectral variation in the linear polarisation is quite obvious in each dataset. However, there are not enough data to infer whether these changes are in fact purely due to different surface and cloud features of Earth, or due to the depolarising lunar surface. The difficulty in obtaining Earthshine data from high-accuracy instruments makes further study challenging. A model fit to these data is also difficult to achieve, without knowledge of all of the atmospheric and surface properties at the time, as well as the lunar depolarising effect.

Model fits have been computed for the signal that would be received by exoplanets that are similar to Earth, showing differences in the continuum flux and the degree of linear polarisation due to different cloud-particle types, optical thickness, and atmospheric height. Models both as a function of phase angle and of wavelength are presented. It is shown that the degree of linear polarisation decreases smoothly with wavelength; this is likely due to the dominance of Rayleigh scattering towards bluer wavelengths, with Mie scattering dominating at longer wavelengths resulting in a lower polarisation.

The surface and atmospheric properties of terrestrial-type exoplanets are expected to be varied, and it is thus difficult to know exactly what signal would be detected. However, the models presented here should hopefully give an indication of the spectral features that should be looked for, the filters that one should be conducting observations in, and the phase angle variation that should be achieved in order to make affirmed discoveries. For example, if one is seeking to confirm the presence of water vapour in the atmosphere (or in the surface water) of an exoplanet, then the primary rainbow feature in the polarisation phase-angle curve can provide evidence

of this. However, the signal-to-noise ratio required to make this detection would be rather ambitious, but with the advent of even larger telescopes and high-precision instrumentation, it is not completely unfathomable that such discoveries can be made in the future.

There is a great deal of potential in the Earthshine data presented in this work, and the analysis presented is only of a preliminary nature. To further quantify the differences in the signal between all of the datasets, cloud data obtained from satellite measurements could be used to further constrain model fits. If the sky was relatively clear over the illuminated region of Earth at the time of observation, then detailed information on the surface coverage could be used. However, model fits of the degree of linear polarisation using different cloud types and surface types were attempted, but did not fit the value nor the slope of the data with wavelength. As mentioned several times before, the main cause of this could be the influence of the lunar surface on the reflected light. Using the lunar surface essentially as a mirror to observe Earth as an exoplanet is far from an ideal scenario, and dedicated instruments should be used for this in order to further reduce errors.

Future work in this area should include observations of the disk-integrated Earthshine, in both flux and polarised flux, using dedicated instruments, such as from the lunar surface. A proposed instrument that would do this is called LOUPE; see Karalidi et al. [2012b] for further details.

4.4 Mars

4.4.1 Introduction

Since Mars is outside of Earth's orbit, the phase angle range at which it can be observed is limited to angles within the interval 0–47°. Mars has a tenuous atmosphere, thus polarimetric observations of Mars yield information about the surface along with the atmosphere. There is a larger volume of polarimetric data obtained with Earth-based telescopes for Mars than for Mercury, but the interpretation of the surface properties suffers from the same issues as that for Mercury, thus polarimetry has proved more fruitful in studying the atmosphere of Mars [Kaydash et al., 2015].

The first polarimetric study of Mars was carried out by Lyot [1929], who identified the negative polarisation branch for the Moon, Mars, and asteroids. Since the study by Lyot, there have been several polarimetric investigations of Mars, with the work of A. Dollfus the most well-known [see Dollfus, 1961; Dollfus & Focas, 1969; Dollfus

et al., 1983, 1984, 1996; Ebisawa & Dollfus, 1993].

The scatterers on the Martian surfaces are aggregates of small irregular shaped grains of soil of differing size. The atmosphere contains molecules and small particles composed of mists and clouds made of ice crystals, and often relatively large particles blown up from the ground from dust storms [Kaydash et al., 2015]. Figure 4.12 shows polarimetric data of the surface of Mars with white ice clouds and yellow dust clouds. The range of behaviour in polarisation with phase angle resulting from differing cloud coverage can be clearly seen. The typical parameters of the negative polarisation branch of Mars can be seen from Figure 4.12, and these have been observed to change with time and varying cloud coverage [Ebisawa & Dollfus, 1993]. The minimum value of polarisation has been known to increase for darker albedo features on the surface of Mars than for brighter highland regions.

The polar regions have the lowest absolute value of minimum polarisation. The negative polarisation branch varies due to changes in atmospheric haze: when a relatively strong dust storm takes place, the branch becomes shallower with a smaller inversion angle. This was first noticed by Lyot [1929] and later confirmed several times [e.g. Dollfus et al., 1984].

The negative polarisation characteristics have a strong variation with wavelength, such as the inversion angle increasing from 14° at blue wavelengths to 26° in the near-IR. This is thought to be due to the effect of changes in the gas and aerosols of the atmosphere. Laboratory measurements of light reflected from Martian soil analogues [Shkuratov, 1987; Shkuratov et al., 2002] have demonstrated that the polarisation of light scattered by the Martian surface can also have a significant dependence on wavelength.

Fox [1997] presents ground-based spectropolarimetric observations of Mars near the polarisation inversion angle, in a wavelength range from 320-1050 nm. Two significant changes in the slope of the polarisation curve were observed at wavelengths around 460 and 830 nm. The feature at 460 nm was attributed to the more significant contribution of the atmosphere in the UV. Around 400 nm, as the atmosphere becomes transparent towards longer wavelengths, the polarisation would be expected to reverse as the surface contribution begins to dominate. The feature at 830 nm was thought to be due to both contributions from the atmosphere and the surface being small at this wavelength, since it is close to the inversion angle.

Measuring the circular polarisation of light reflected from solar system (and potentially extrasolar) objects can provide a powerful remote sensing tool for the detection of organic molecules [see Sparks et al., 2015]. Imaging polarimetric measurements

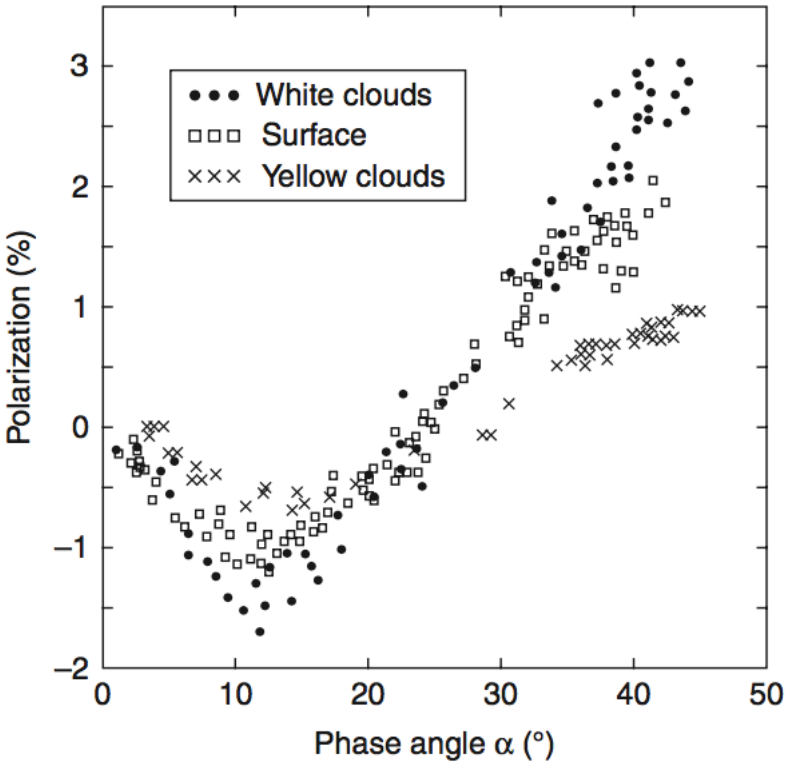

Figure 4.12: P_Q of light reflected from Mars as a function of phase angle of the surface, white clouds, and yellow clouds at a wavelength of 600 nm. Figure from Kaydash et al. [2015] with the data based on plots from Lee et al. [1990] and Ebisawa & Dollfus [1993].

of Mars were taken by Sparks et al. [2005], to search for any anomalous optical activity. Two narrow-band filters covering 43% of the Martian surface were used. A small non-zero value of circular polarisation was detected, but it was at the limit of the instrumental capability, so there was no clear indication of any chiral signatures on Mars.

Several studies have been made to try and further understand the properties of light scattered by Mars and its atmosphere. Early modelling attempts used spherical particles to represent the aerosols [Tishkovets & Shkuratov, 1982]. Later work established that the shape of the aerosol particles is a crucial factor when computing models [Petrova, 1999], and that ignoring the particle shape when interpreting photometric data can introduce an error of up to 100% when estimating the optical thickness of aerosols [Mishchenko et al., 1995]. It was later found by Dlugach & Petrova [2003] that observations taken with the limited phase angle range attainable from Earth, and also in specific wavelength bands, precluded an unambiguous characterisation of the aerosol particles.

The Soviet Mars 5 mission was the first to carry out polarimetry of Mars in-situ, in 1974. This mission provided data on regional variations of the polarisation at phase angles of 62° and 90° [Kaydash et al., 2015].

The space shuttle Endeavour carried a spectropolarimeter that was used to study Mars, with a spectral coverage of 210-1020 nm and a spectral resolution of 4 nm [Fox et al., 1997]. All measurements were taken at a phase angle of 21°, close to the Martian inversion angle of polarisation. In the visual region of the spectrum, the negative polarisation characteristics were observed to vary slightly with wavelength, with the polarisation in the UV positive, and significantly different, with an abrupt 90° shift in polarisation angle occurring around 460 nm. The increase in polarisation in the UV from the visual was due to larger scattering of photons in the atmosphere. Assuming a CO_2 atmosphere, a surface pressure of 6 mbar was determined [Fox et al., 1997].

Imaging linear polarimetry of Mars was obtained for the first time with the Hubble Space Telescope, taken during the 2003 opposition when Mars was at its closest approach to Earth for 60,000 years, 0.372 AU [Shkuratov et al., 2005; Kaydash et al., 2006]. Five series of images were taken at different phase angles, all below 16°, and in three spectral channels in the blue and UV. Various regions on the surface were observed in the southern hemisphere, where it was Martian summer. The atmosphere of Mars was relatively clear of both dust and water ice clouds at this time. The only polarimetric contrast observed on the surface was in the polar

caps, perhaps because of dusty haze and faint clouds obscuring the surface. At the relatively short wavelengths of the observations, these factors have even more influence because the aerosol scattering optical thickness is higher [Kaydash et al., 2015]. Disk-integrated results showed a good agreement with the general trends observed with Earth-based polarimetry. High negative polarisation values at UV wavelengths were found, and the suggested cause was water-ice condensation in the atmosphere.

An interesting phenomenon observed in the HST datasets are semi-transparent clouds giving transient high polarisation, often with magnitudes up to 3%, usually seen in the western part of the Martian disk. Studying the movements of these features allowed a verification of global circulation models of the atmosphere of Mars [Kaydash et al., 2006]. The surface albedo variation remained visible through these clouds. There are similar clouds in the same region of the Martian disk that did not give such high polarisation phenomena. This has been observed before from Earth-based observations in the visible spectral range [Ebisawa & Dollfus, 1993], and can be explained as clouds consisting of different aerosol particles with varying scattering properties.

Irregularly shaped micron-sized particles could cause high polarisation from optically thin clouds on Mars. Clancy et al. [2003] and Wolff & Clancy [2003] showed that such particles are present in hazes at high altitudes at various locations on the planet, and in different seasons. Nucleation of water-ice crystals on sub-micron dust can form highly polarising clouds. Polarimetric studies of particulate surfaces is difficult, and there are currently no means to accurately calculate the scattering matrix for densely packed particles of arbitrary shapes and sizes [Kaydash et al., 2015]. The same problem is faced for planetary atmospheres with non-spherical constituents, such as for Jupiter. Interpreting observations of polarised light reflected from planetary surfaces is challenging, due to the complex nature of modelling the underlying physics in the coherent backscattering mechanism, as mentioned in Section 1.3.4.

This section presents observations of Mars taken with ISIS in spectropolarimetric mode, at two epochs. Additionally, one spectropolarimetric dataset taken with FoReRo2 is presented. Two sets of disk-integrated imaging polarimetry from FoReRo2 were also observed, along with two sets of disk-integrated imaging polarimetry from ToPol, all in different filters in the optical. One set of disk-resolved imaging polarimetry was obtained with ToPol, and from these polarimetric maps were constructed. All of the datasets show differences that can be attributed to combinations of different phase angle, Martian season, and diurnal variations in the surface and

atmospheric properties of Mars, such as dust storms.

The rest of this section is structured thusly: Section 4.4.2 give details of the observations taken with all three instruments, along with the presentation of the results, with Section 4.4.3 discussing and summarising this section.

4.4.2 Observations and results

Three spectropolarimetric datasets are presented: two were observed with the ISIS at the WHT, and one with FoReRo2 at NAO Rozhen. Additionally, five imaging polarimetry datasets are presented: three taken with ToPol at Calern, and two taken with FoReRo2, in various filters. One set of the ISIS data was taken by Stefano Bagnulo, Will McLean, and Aaron Stinson (programme ID W/2014A/5), and the other by Stefano Bagnulo (programme ID W/2014B/30). All of the FoReRo2 observations were carried out by Galin Borisov. The ToPol observations were taken by Alberto Cellino, Maxime Devogèle, and David Vernet. The data were reduced in the same way as described in Section 3.3. This section is divided into two parts: firstly the spectropolarimetric observations are discussed and presented, and secondly the imaging polarimetry.

4.4.2.1 Spectropolarimetry

The observing log of the three spectropolarimetry datasets is shown in Table 4.2, with the table organised as follows: column one assigns a name to the dataset, with columns two and three giving the date of observation and the Universal Time (UT) in the middle of each run respectively. Column four lists the exposure time, column five gives the instrument with which the data were taken, and column six lists the grism used. Column seven gives the phase angle, and column eight the angular diameter of Mars at the time of observation. Columns nine and ten then give the north pole angle and the distance of the north pole from the centre of the planetary disk, respectively. The slit width for dataset IP1 was $1''$, and for dataset SP2 the slit was chosen to be narrower, at $0.5''$, due to the smaller angular diameter of Mars in this epoch. The slit width for dataset SP3 was $1''$.

In addition to the Mars data, several calibration objects were also observed. The spectrum of a solar analogue was taken in order to obtain the reflectance spectrum of Mars, since light reflected from any solar system body will be dominated by the solar spectrum. The spectrum of the solar analogue is similar to that of the Sun, thus the solar features are partly cancelled out when the two are divided. In addition to

solar analogues, both unpolarised and polarised standard stars were observed. The purpose of taking these observations was to quantify the instrumental polarisation, and to establish the offset of the position angle of the instrument; details of how this correction was performed are given in Section 3.3.

Table 4.2: Observing log of the Mars spectropolarimetry, with the column meanings explained in the text.

Dataset	Date	UT	ET (s)	Instrument	Grism	α (°)	Ang. D. (″)	NP Ang. (°)	NP Dist.(″)
SP1	12/03/2014	02:40	1.00	ISIS	R300B	20.56	12.83	36.33	+6.02
SP1	12/03/2014	02:50	0.26	ISIS	R158R	20.56	12.83	36.33	+6.02
SP2	06/01/2015	19:20	0.50	ISIS	R158R	26.80	4.69	353.21	-2.15
SP2	06/01/2015	19:32	8.00	ISIS	R300B	26.80	4.69	353.21	-2.15
SP3	11/07/2016	20:07	0.50	FoReRo2	GrismW	35.31	15.10	38.57	+7.24

The reflectance spectrum for each of the three spectropolarimetric datasets are shown in Figure 4.13a, Figure 4.13d, and Figure 4.13g. Each of the three datasets show very similar trends in the variation of the reflectance with wavelength, with a smooth increase from lower to higher wavelengths. The two ISIS datasets, which have a longer wavelength coverage than the FoReRo2 dataset, show the reflectance starting to decrease slightly after 800 nm. The patterns observed in the data here are consistent with previous studies showing reflectance spectra of Mars [Mustard & Bell, 1994]. Features above and below the continuum appear to be due to Earth's atmosphere and remnant lines from the solar spectrum, perhaps due to differences between the spectrum of the Sun and the solar analogue stars.

Figure 4.13b, Figure 4.13e, and Figure 4.13h show the total linear polarisation P_{L} for the three spectropolarimetric datasets, with Figure 4.13c, Figure 4.13f, and Figure 4.13i showing the corresponding variation of position angle with wavelength.

Figure 4.13b shows a dip in the polarisation around 410 nm, with a corresponding feature in the position angle spectrum in Figure 4.13c. This has been noted previously: Fox [1997] observed this from spectropolarimetric observations, occurring at a wavelength between 460-486 nm, depending on time, and the feature was also observed to broaden. The data in Fox [1997] are from observations taken in the phase angle range 20-23°, and SP1 in this study was taken at phase angle 20.56°.

The polarisation dip was attributed to the atmosphere of Mars becoming more transparent towards longer wavelengths, which may cause a major change in polarisation as the contribution from the surface begins to dominate. Fox [1997] also observed another polarisation dip at 830 nm, but it is not observed in any of the data presented here. This could be due to different amounts of aerosol particles in the atmosphere, but to fully understand these phenomena further observations must be taken closer in time, as well as of different regions of the Martian disk and at a wide range of phase angles.

Dataset SP2 was taken at a slightly larger phase angle than that of SP1, 26.80°, which is higher than the polarisation inversion angle for Mars. A minimum in polarisation in Figure 4.13e is observed around 570 nm, where the transition between the data taken in the blue arm and the red arm occurs. It was tested whether this could be due to errors in the data reduction process, but any discrepancies could not be identified. This could also potentially be attributed to changes in the amount of dominance that the atmosphere has on the degree of polarisation.

Dataset SP3 was taken when Mars was at a phase angle of 35.31°, much higher than that for datasets SP1 and SP2. As would be expected for this phase angle difference,

the value of the degree of linear polarisation is correspondingly higher. This dataset was taken with FoReRo2, and thus only has values spanning the wavelength range 500-850 nm. The value of linear polarisation decreases from its peak at 500 nm of 3.5%, to its lowest value at 850 nm, of 2.5%. The slope appears to change slightly towards shorter wavelengths, but without data obtained at bluer wavelengths it is difficult to characterise this change.

Interestingly, there appears to be little correlation between the degree of linear polarisation and the reflectance in each dataset, demonstrating that polarimetry provides a different facet to the behaviour of atmospheric and surface properties of planets.

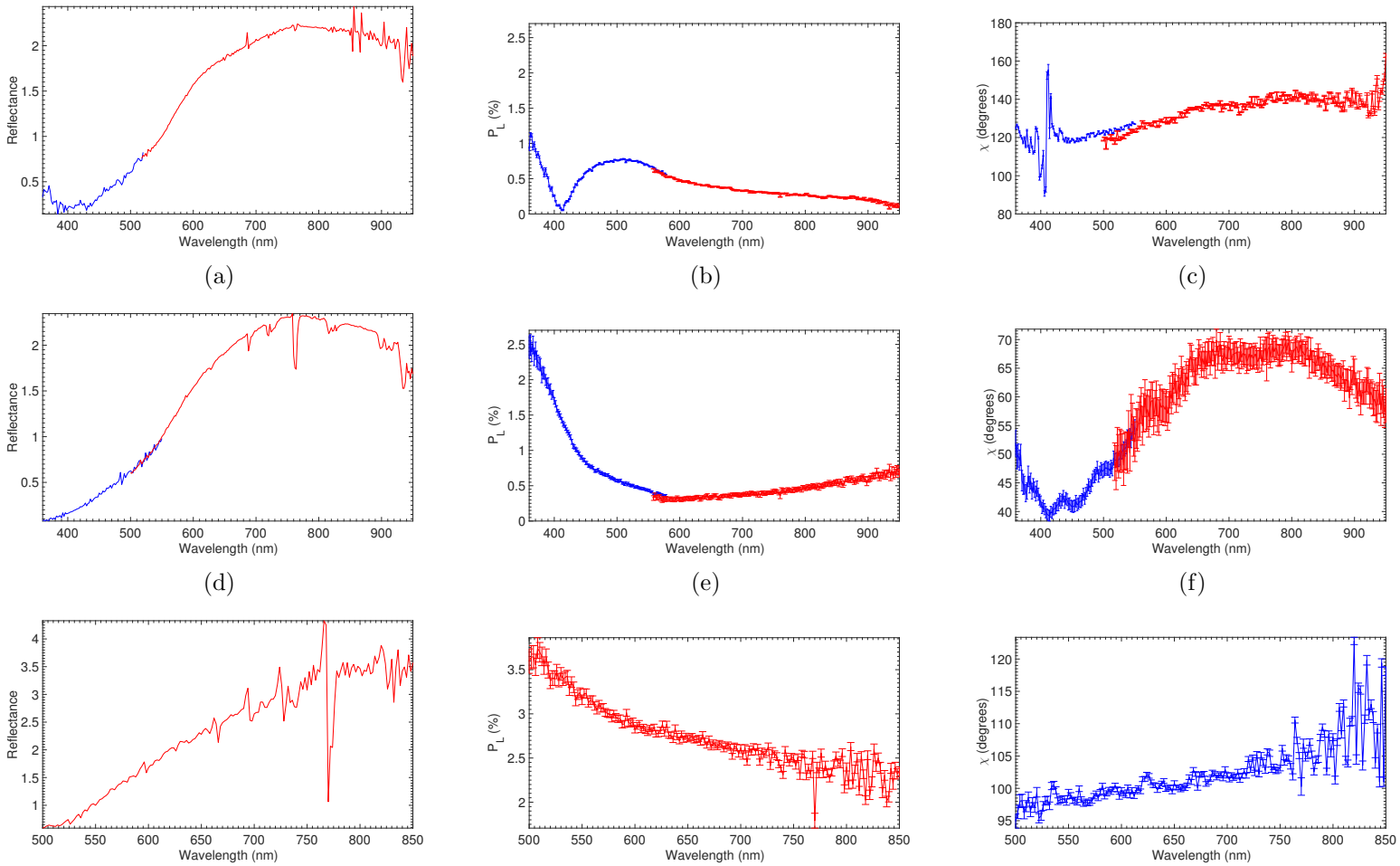

Figure 4.13: Plots of reflectance, degree of linear polarisation, and position angle for all three Mars spectropolarimetry datasets. The top row shows the results for dataset SP1, the middle row SP2, and the bottom row SP3.

4.4.2.2 Imaging polarimetry

The observing log for the five imaging polarimetry datasets is given in Table 4.3 with columns much the same as for Table 4.2, except with the filter listed instead of the grism. The disk-integrated degree of linear polarisation is given by column eleven, and the position angle of polarisation by column twelve. Figure 4.14 shows a CCD image of Mars taken with ToPol for dataset IP3 in the R filter. The angular diameter of Mars in this dataset proved to be sufficiently large that polarimetric maps could be produced in three filters, since Mars was at its closest approach to Earth for some 15 years or so. For the rest of the ToPol and FoReRo2 imaging polarimetry datasets, only disk-integrated values are given.

Table 4.3: Observing log of the Mars imaging polarimetry, with the column meanings explained in the text.

Dataset	Date	UT	ET (s)	Inst.	Filter	$\alpha\,(^\circ)$	Ang. D. ($''$)	NP Ang. ($^\circ$)	NP Dist.($''$)	$P_{\rm L}$ (%)	$\theta\,(^\circ)$
IP1	26/02/2015	17:36	0.1	ToPol	V	18.69	4.21	330.67	-1.88	0.75±0.02	22.32 ±0.90
IP1	26/02/2015	17:42	0.05	ToPol	R	18.69	4.21	330.67	-1.88	0.66±0.02	50.45 ±0.98
IP2	10/12/2015	05:55	0.8	ToPol	B	31.39	4.96	33.58	+2.27	3.00±0.02	130.37 ±0.18
IP2	10/12/2015	05:39	0.05	ToPol	V	31.39	4.96	33.58	+2.27	1.02±0.01	151.12 ±0.12
IP2	10/12/2015	05:55	0.8	ToPol	R	31.39	4.96	33.58	+2.27	0.97±0.01	146.02 ±0.12
IP3	06/06/2016	21:45	0.3	ToPol	V	13.40	18.46	38.01	+8.92	1.09±0.01	165.65±0.23
IP3	06/06/2016	21:43	0.1	ToPol	R	13.40	18.46	38.01	+8.92	0.76±0.01	154.43±0.40
IP3	06/06/2016	21:52	2	ToPol	B	13.40	18.46	38.01	+8.92	1.23±0.01	177.46±0.18
IP4	10/07/2016	20:17	0.14	FoReRo2	IF620	34.90	15.09	38.58	+7.29	2.05±0.02	46.23±0.31
IP5	11/07/2016	20:59	0.2	FoReRo2	IF590	35.33	15.09	38.56	+7.24	2.37±0.03	46.84±0.41
IP5	11/07/2016	20:47	0.1	FoReRo2	IF620	35.33	15.09	38.56	+7.24	2.09±0.02	44.83±0.32
IP5	11/07/2016	20:35	0.1	FoReRo2	IF642	35.33	15.09	38.56	+7.24	2.06±0.03	47.19±0.37

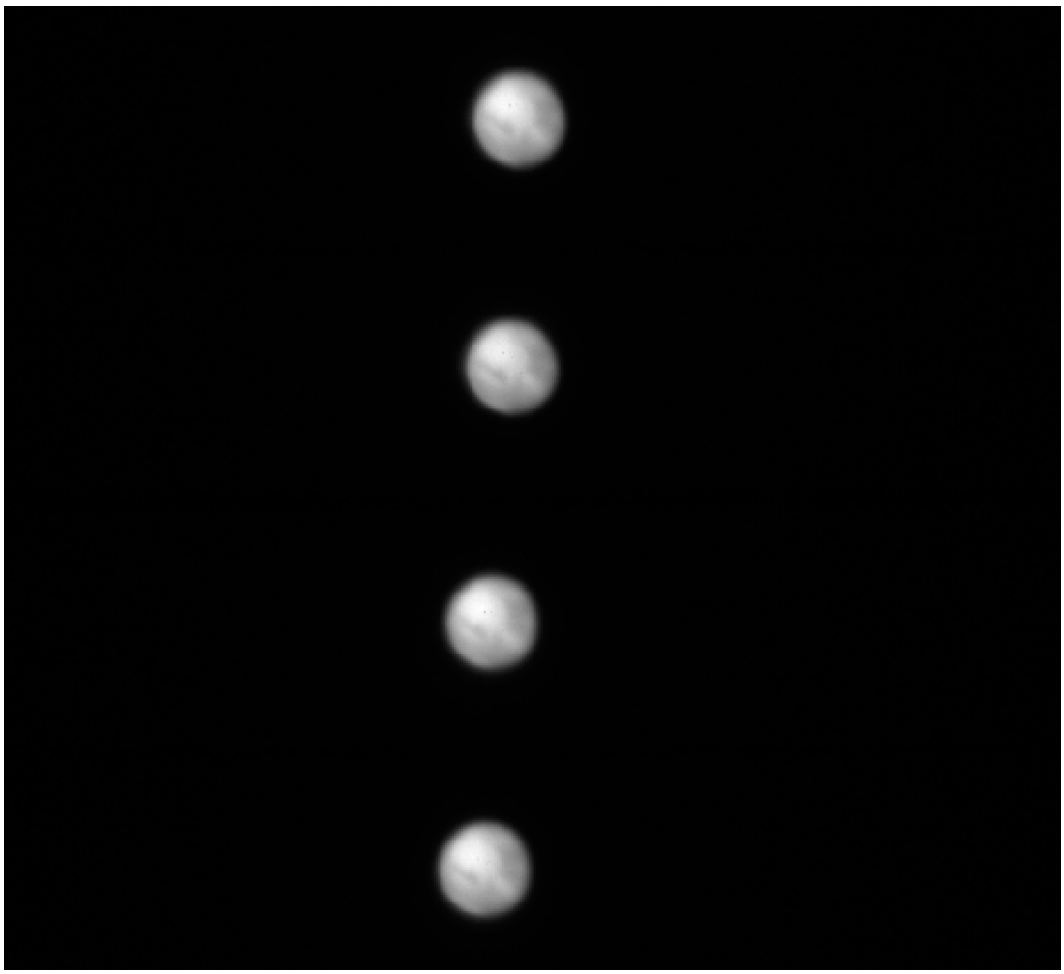

Figure 4.14: ToPol CCD image of Mars in the R filter, from 06/06/16, when Mars had an angular diameter of 18.46".

Dataset IP1 has a degree of polarisation that appears to slightly decrease from 0.75% to 0.66% from the V to the R filters, with the position angle jumping from 22.32° to 50.45°. Dataset IP2 was taken ten months after 1P1, and for a larger phase angle, showing correspondingly higher degrees of polarisation in each of the B, V, and R filters. The degree of polarisation drops sharply from 3.00% in B to 1.02% in V, with another slight decrease in the R filter, for which the degree of polarisation is 0.97%. The position angle increases from 130.37° in B to 151.12° in V, and dropping slightly to 146.02° in R.

Dataset IP3 is the one for which polarimetric maps were constructed. The disk integrated values of polarisation are smaller than those for IP2, due perhaps in large part to the smaller phase angle of Mars at the time of observation. The polarisation is at its highest in the B filter, with a value of 1.23%. This decreases slightly to

1.09 % in V, with another slight drop going to the R filter, for which the degree of polarisation is 0.76%. The position angle decreases with increasing wavelength in this dataset from 177.46° in B to 165.65° in V, and dropping slightly to 154.43° in R.

Datasets IP4 and IP5 were both taken with FoReRo2. The filters used were ones that were actually in place for the purpose of carrying out observations of Saturn, since they are filters with one being in a known strong methane band (at around 620 nm) and two in the continuum either side of this band (590 nm and 642 nm). IP4 has data taken only in the 620 nm filter, with a disk-integrated value of the degree of linear polarisation of 2.05%.

Dataset IP5 has data for both the methane filter and the two continuum filters: showing a slight falloff in polarisation with increasing wavelength in the range 590-642 nm, from 2.37% at 590 nm to 2.06% at 642 nm. These polarisation values are relatively high for the phase angle at which these observations were taken, since dataset IP2 was taken at a phase angle not much lower than for these ones (both phase angles are in the range 31-36°), but of course such variations are possible, and cannot be fully understood without further knowledge of the behaviour of the polarisation as a function of phase angle in a greater range. The angles of polarisation do not show any significant variations in this short wavelength range. The values of polarisation are consistent with that observed with dataset SP3, taken at the same epoch.

The disk-resolved polarimetric maps produced with dataset IP3 are shown in Figure 4.15, Figure 4.16, and Figure 4.17, for the B, V, and R filters, respectively. All of the flux maps are normalised, and are not calibrated with a solar analogue star, so any features and differences are only relative measures. The flux maps show more features in the V and R filters, with regions of brighter and darker contrast more obvious than in the B filter.

The P_{L} maps all have the scale saturated at 4%, in order to more clearly show the variations in polarisation across the disk. Direction arrows are superposed to the P_{L} maps representing the position angle. The arrows do not have an arrowhead because the direction of polarisation only varies between 0° to 180° and angle 0 (180)° is taken to be the vertical direction.

Features that can be seen in the polarisation maps include that of the polarisation at the northern polar region, which can be seen to be slightly higher than the rest of the disk in the B filter, with this observed also in the V filter, but less prominently, and it is not seen at all in R. This could be due to an aerosol layer of small particles

concentrated in this region, so would show more obviously at bluer wavelengths. In the B filter, various patches of slightly higher and lower polarisation can be seen across the equatorial and mid-latitude regions, along with higher polarisation values in the southern polar regions, with the indication of a souther polar hood perhaps composed of small aerosol particles.

The polarisation across the disk of Mars in the V filter is starkly different to that of the B and R filters, with the variation in regions of higher and lower polarisation quite obvious. The polarisation angle is observed to change across the disk, with some slight changes between the filters as well. The changes in polarisation and position angle must be due to the combined effect of the aerosol particles resident in the Martian atmosphere, and the irregular particles that compose the surface. The Martian atmosphere is perhaps the largest contributor to the B filter data, with the behaviour in polarisation in the V filter perhaps due to a mixed contribution from both the atmosphere and the surface, with the surface then perhaps being the main contributor in the R filter.

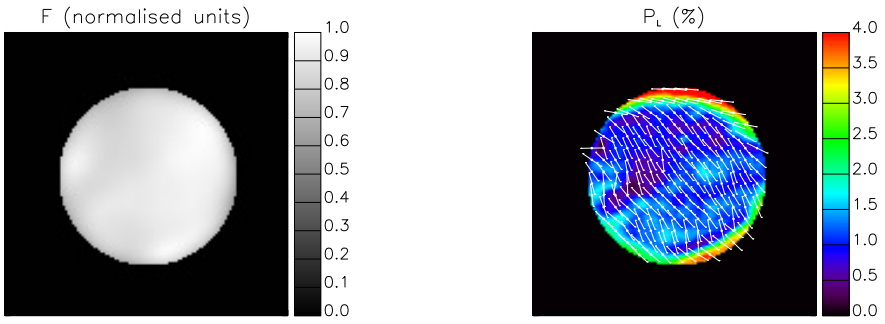

Figure 4.15: Left: intensity, right: linear polarisation with position angle for the B filter.

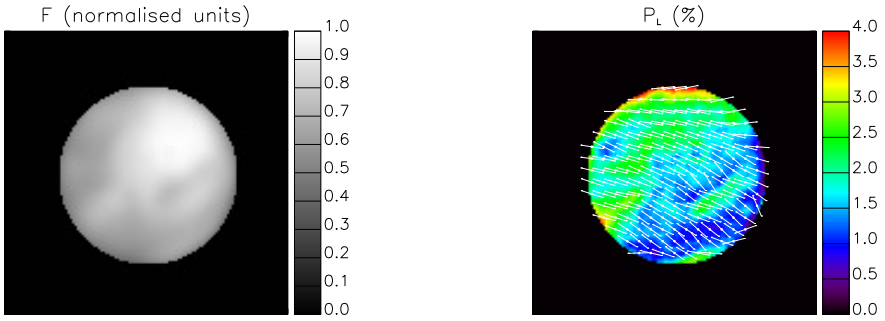

Figure 4.16: Left: intensity, right: linear polarisation with position angle for the V filter.

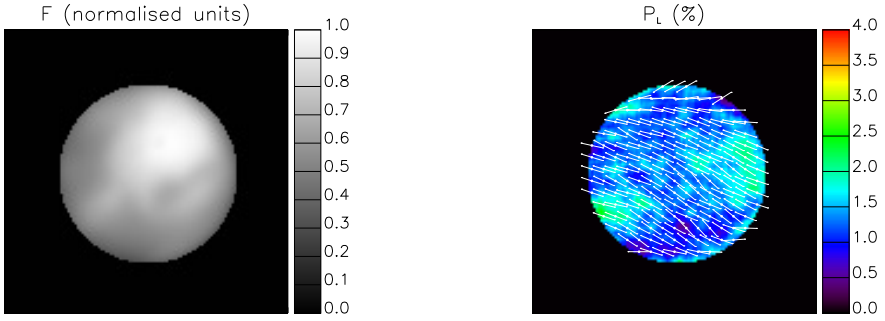

Figure 4.17: Left: intensity, right: linear polarisation with position angle for the R filter.

4.4.3 Discussion and summary

Three spectropolarimetric datasets of Mars have been presented, along with five imaging polarimetry datasets. All datasets were taken at different phase angles, and likely for different planetary conditions on Mars. Dataset SP1 shows a dip in polarisation around 410 nm, similar to a feature observed in previous studies in the blue wavelength region. This has been attributed to the atmosphere becoming less of an influence on the observed degree of linear polarisation. Dataset SP2 shows a different polarisation dip at a longer wavelength, of around 570 nm, which could be due to changes in the dominance of the atmosphere towards longer wavelengths, but it is not fully known. Dataset SP3 shows a steady decrease in linear polarisation from 500-850 nm.

Ground-based imaging polarimetry taken for a range of phase angles was also presented and discussed. The values are somewhat consistent with the change in phase angle, with the FoReRo2 data showing a larger degree of linear polarisation than that taken with ToPol. These values are however consistent with the values observed in dataset SP3. The polarimetric maps produced from dataset IP3 show variations in polarisation across the disk of Mars, and with wavelength, perhaps due to changes in the aerosol composition of the atmosphere and/or the surface composition as a function of distance. The aerosol particle type could influence the behaviour of the polarisation as a function of wavelength.

The data presented here have corroborated findings of previous studies, such as changes in polarisation gradient with wavelength that could be due to the change of the atmospheric influence towards higher wavelengths. As with previous studies, the disk-integrated values of broadband linear polarisation have shown to increase with phase angle in all filters, with the polarisation higher in the B filter.

Future work aimed at understanding the polarimetric behaviour of Mars should include observations of different regions of the Martian disk, for the full phase angle range and observations should ideally be taken on a diurnal, or even hourly, basis to try and understand how much aerosols in the tenuous atmosphere contribute to the total signal. Space missions are essential for gaining a full understanding of the scatterers present in the Martian atmosphere and on the surface, because a full phase angle characterisation of the flux and degree of linear polarisation is necessary in order to compute accurate models.

Chapter 5

Jupiter

Abstract

Disk-resolved imaging polarimetry of Jupiter in the U, B, V, and R filters is presented over the phase angle range $\alpha = 4$–$10.74°$, showing the contrast between the belts and zones, along with the sharp increase in polarisation at the polar regions. Additionally, spectropolarimetry of Jupiter in the wavelength range 500–850 nm is presented, showing a decrease in the degree of linear polarisation with increasing wavelength, and changes in polarisation across strong methane bands. Model fits to the data were attempted by varying the cloud height and optical thickness, and this can approximately reproduce the variation in polarisation with planetary latitude in the V and R filters, but not for the B filter. A model fit to the spectropolarimetric datasets was also achieved with similar model atmospheres. The potential application that polarimetry has to the study of Jupiter-like exoplanets is also investigated. The work in this chapter is based on McLean et al. [2017], and most figures are from this work with accreditation where appropriate.

5.1 Introduction

The atmosphere of Jupiter is known to be composed of distinct belt and zone regions with varying aerosol compositions and altitudes. The zones are seen as bright bands that encircle Jupiter, with the belts appearing as darker bands. It is thought that the clouds are mainly composed of ammonia, with the zones containing dense clouds at higher altitudes, with the belts having thinner clouds lower down in altitude [Ingersoll et al., 2004]. A diffuse haze layer is present above the ammonia cloud

deck, and a thicker haze covers the polar regions of Jupiter. The particles in the belts and zones are to this day enshrouded in mystery; their chemical composition is still a subject of much debate. It is thought that the particles could be complex compounds made up of sulphur, phosphorous, and carbon [Ingersoll, 1976; West et al., 2004].

There is a vast catalogue of observational study of Jupiter, from ground-based telescopes and from Earth-orbiting telescopes. Additionally, there have been concentrated bursts of information from the space missions that have observed Jupiter and its moons: NASA's Pioneer 10 and 11, Voyager, Galileo, and Cassini missions. Observational results from the Pioneer and Voyager missions are reviewed by West et al. [1986], along with ground-based studies of Jupiter carried out up to 1986, and also theoretical studies. A more recent review of the Jovian cloud microphysics taking the more recent space missions into consideration is given by West et al. [2004]. These studies also show images of Jupiter that were taken with the Cassini probe when it flew by en-route to Saturn in 2000 for a gravity assist. Images were taken in the strongest methane absorption bands: 619 nm, 727 nm, and 750 nm. These data were acquired in the second half of summer in the northern hemisphere of Jupiter (summer solstice took place in May 2000), and therefore the second half of winter in the southern hemisphere.

The images showed the brightness increasing in the equatorial band and at the southern polar hood of Jupiter. A high-latitude stratospheric haze layer at a pressure level of 3 mbar caused this increase in brightness of the southern polar hood. The north pole was also shown to have a bright polar hood, but was more diffuse and spread over a greater area than the southern polar hood at the time of the Cassini fly-by. A tropospheric haze layer at a pressure level of around 200 mbar was found in the equatorial region, appearing to be denser than haze in midlatitude regions. These Cassini data showed that the bright equatorial band is asymmetric around the equator, which is perhaps a seasonal effect. The Great Red Spot (GRS), a storm region located in the souther hemisphere with the centre located 22° south of the equator, is known to be so prominent in images because it is a region with high-altitude tropospheric haze. [West et al., 2004].

Light reflected by Jupiter is polarised, due to scattering taking place in its dense atmosphere. The variation in degree of polarisation as a function of location on the disk of Jupiter can constrain the particle properties, along with observations across different wavelength and phase angle ranges. As for all of the outer planets, Earth-based observations of Jupiter are limited by the phase angle range that Jupiter is

accessible in, thus precluding a full characterisation of the properties of the particles in the atmosphere from such observations. Space-based observations have been taken on several occasions, for specific regions of the planet at certain phase angles.

Lyot [1929] was the first to conduct polarimetric observations of Jupiter. Lyot's results showed a positive value of linear polarisation at the poles of Jupiter with a value of $\approx$ 5-8%, and a direction of polarisation perpendicular to the limb. Near the equator, Lyot observed the value of polarisation to be almost zero when Jupiter was near opposition, and noted a polarisation of $\approx$ 0.4% directed parallel to the equator for higher phase angles near 10°. Different parts of Jupiter's disk were often observed by Lyot polarimetrically from 1922 to 1926, with the polarisation at the polar regions always larger than that observed in the centre of the Jovian disk. The equatorial polarisation was observed to have a varying direction with the distance from the centre of the disk, with the absolute value of polarisation always remaining small. In the last half century or so, other studies of polarised light reflected by Jupiter have verified Lyot's measurement of larger values of polarisation at the poles, attaining values of around 7-8% in blue light [Dollfus, 1957; Gehrels et al., 1969; Morozhenko & Yanovitskii, 1973; Hall & Riley, 1976; Carlson & Lutz, 1989; Starodubtseva et al., 2002; Shalygina et al., 2008].

Schmid et al. [2011] carried out imaging polarimetry and spectropolarimetry of Jupiter, and observed a relatively high value of polarisation in the polar regions at a phase angle near 10.4°, with a maximum of around 11.5% in the southern region and 10% in the north, where Jovian spring had just commenced. Figure 5.1 shows maps of the polarisation of Jupiter from Schmid et al. [2011], where differences between the poles and the limbs at the equator are apparent. This chapter is based on McLean et al. [2017], which is the most recent ground-based polarimetric study of Jupiter.

Observations made of Jupiter carried out from Earth or in Earth-orbit are limited to a low phase angle range ($0° \lesssim \alpha \lesssim 12°$), where generally only low degrees of polarisation are observed, due to the near backward scattering direction [Dlugach & Mishchenko, 2008]. The higher than expected polarisation that has been observed at the limbs of Jupiter is caused by a larger contribution of second order scattered light, which has a higher polarisation [Schmid et al., 2011]. To gain a wider phase angle coverage for Jupiter, and thus enable a full phase characterisation, space missions are needed.

Pioneer 10 and 11 carried out polarimetric observations of Jupiter in the 1970s, with a photopolarimeter onboard each spacecraft. At a phase angle of $\approx$ 90°, the

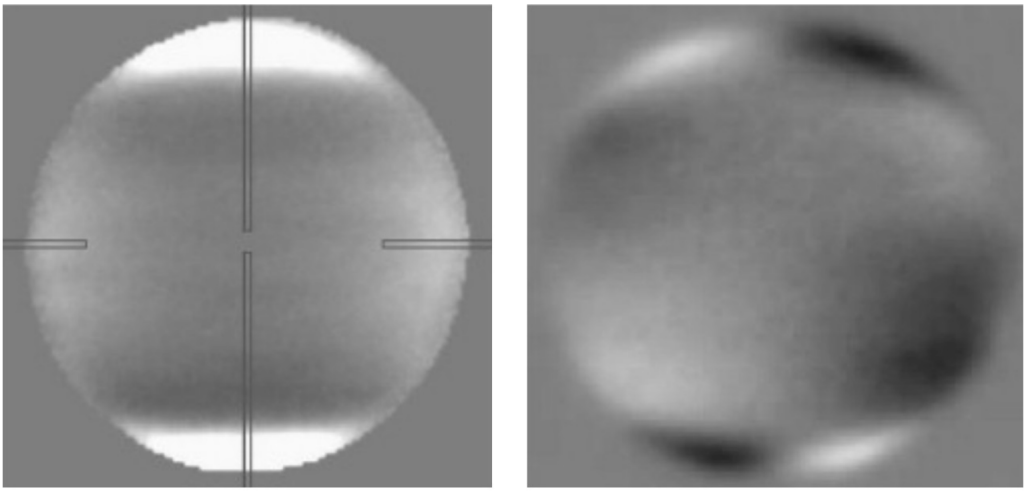

Figure 5.1: Polarimetric maps of Jupiter in a filter centred on 730 nm, taken from Schmid et al. [2011]. Q is shown on the left and U on the right. North is up and East is left. The grey scale is normalised to the intensity at the centre of the disk and spans the range from -1.0% (black) to +1.0% (white). The lines on the Q image represent the slit positions for spectropolarimetric observations presented in the same study.

polarisation in the B and R filters reached values as high as $\approx 50\%$ at the polar regions with relatively smaller values ($< 10\%$) at equatorial latitudes [Smith & Tomasko, 1984]. West et al. [2015] presents a more complete review of polarimetric studies of Jupiter taken with space missions.

Modelling of polarised light reflected by Jupiter has been attempted by Morozhenko & Yanovitskii [1973]; Mishchenko [1990]; Dlugach & Mishchenko [2008]. These studies aimed to interpret measurements of the degree of linear polarisation taken of the centre of the Jovian disk, in terms of the refractive index and size distribution of the particles. Mie theory for spheres was used, along with various non-spherical particles in the study by Dlugach & Mishchenko [2008]. The conclusion was that some or all of the aerosols must be non-spherical in shape, and it was emphasised that observations across the full phase range (unobtainable from Earth) were required in order to provide a full characterisation. Even with observations taken by the Pioneer and Galileo missions (the latter covered a much broader phase angle range, but had a more limited coverage in wavelength), an accurate particle size distribution has not yet been obtained for Jupiter. It is thought that the main scattering particles in Jupiter's atmosphere are ice crystals composed of ammonia, possibly coated with organic hazes condensing down from the stratosphere, but these cannot be modelled with spherical or ellipsoidal particles, especially when trying to fit polarimetric data.

This chapter presents polarimetric maps of Jupiter along with spectropolarimetry for ten different epochs. The imaging polarimetry data used for creating the polarimetric maps was obtained in the period February 2015–June 2016 with ToPol in the four broadband U, B, V, and R filters. These observations were carried out by Alberto Cellino, Maxime Devogèle, and David Vernet. The polarimetric maps were constructed with a spatial resolution on the planet, at an equatorial diameter of the 1 bar pressure level of about 140,000 km, of approximately 774,000 km^2 (around 880 km x 880 km) per pixel at the centre of the disk. The spectropolarimetric datasets were obtained in December 2014 and November 2015 with FoReRo2 by Galin Borisov.

The rest of this chapter is structured as follows: Section 5.2 gives details of the observations and presents the results. Section 5.3 describes and presents the atmospheric models that were used to interpret the observations, along with sample results showing what could be observed from Jupiter-like exoplanets. Finally, Section 5.4 summarises and concludes the work presented in this chapter.

5.2 Observations and results

5.2.1 Observing log

Table 5.1 shows the log of the observations and is organised as follows: column one assigns a name to each dataset, column two gives the dates of observation, and column three states the Universal Time (UT) for the middle of each observing block. Column four gives the exposure time of each frame, in seconds. Column five states the filter used, with both of the spectropolarimetric observations taken in the wavelength range 500-850 nm. Column six gives the planetary phase angle, α, at the time of observation. Columns seven through nine give other planetary parameters at the time of observation, namely, the angular diameter at the equator in arcseconds, the planetary north-pole position angle relative to the north celestial meridian in degrees, and the distance to Jupiter's north pole from the centre of the disk in arcseconds on the sky[1].

[1]Planetary parameters have been calculated using JPL HORIZONS: http://ssd.jpl.nasa.gov/?horizons

Table 5.1: Observing log of the Jupiter imaging polarimetry and spectropolarimetry observations, with the column meanings explained in the text.

Dataset	Date	UT	Exp.Time (s)	Filter/Grism	α (°)	Ang.Diam. (")	NP Ang (°)	NP Dist. (")
SP1	20/12/2014	03:30	3.00	GrismW	8.64	42.11	+21.16	-19.69
IP1	25/02/2015	21:57	0.05	R	3.94	44.74	+19.23	-20.92
IP1	25/02/2015	22:03	0.05	V	3.94	44.74	+19.23	-20.92
IP1	25/02/2015	22:14	0.40	B	3.94	44.74	+19.23	-20.92
IP2	26/02/2015	00:03	0.05	R	3.96	44.74	+19.23	-20.92
IP2	26/02/2015	00:13	0.05	V	3.96	44.74	+19.23	-20.92
IP3	26/02/2015	21:13	0.05	V	4.13	44.68	+19.19	-20.89
IP3	26/02/2015	21:24	0.05	R	4.13	44.68	+19.19	-20.89
IP3	26/02/2015	21:35	0.20	B	4.13	44.68	+19.19	-20.89
IP4	17/10/2015	04:40	0.05	V	6.73	32.15	+24.87	-15.03
SP2	06/11/2015	03:29	3.00	GrismW	8.73	33.42	+25.17	-15.62
IP5	10/12/2015	04:56	0.08	V	10.46	36.56	+25.41	-17.08
IP5	10/12/2015	05:06	0.50	B	10.46	36.56	+25.41	-17.08
IP5	10/12/2015	05:15	0.07	R	10.46	36.56	+25.41	-17.08
IP6	10/04/2016	21:37	0.30	B	6.37	42.87	+24.94	-20.03
IP6	10/04/2016	21:22	0.05	V	6.37	42.87	+24.94	-20.03
IP6	10/04/2016	21:29	0.05	R	6.37	42.87	+24.94	-20.03
IP7	06/06/2016	20:27	0.20	V	10.74	36.62	+24.92	-17.12
IP7	06/06/2016	20:30	1.00	B	10.74	36.62	+24.92	-17.12
IP7	06/06/2016	20:32	0.10	R	10.74	36.62	+24.92	-17.12
IP7	06/06/2016	20:37	15.00	U	10.74	36.62	+24.92	-17.12
IP8	08/06/2016	20:39	0.10	V	10.73	36.41	+24.94	-17.02
IP8	08/06/2016	20:43	0.05	R	10.73	36.41	+24.94	-17.02
IP8	08/06/2016	20:45	0.50	B	10.73	36.41	+24.94	-17.02
IP8	08/06/2016	20:39	10.00	U	10.73	36.41	+24.94	-17.02

5.2.2 Imaging polarimetry with ToPol

Polarimetric observations of Jupiter were taken with ToPol in the U, B, V, and R filters over eight epochs during 2015 and 2016. Two epochs have data for all four filters, four epochs have data for three of the filters, with one epoch only having V and R data, and with one for just the V filter (see Table 5.1). An example of a raw CCD image of Jupiter from ToPol for dataset IP5 is shown in Fig. 5.2.

Bias and dark frames were taken as well as the science frames, and also flat field images for each filter. The flat field images were only used in datasets IP1, IP2, and IP3 to remove dust present on the filters. Standard stars were also observed to assess the instrumental polarisation and correct for it. The data reduction method is discussed in full in Section 3.3.

The imaging polarimetry data were taken over eight epochs all at different phase angles, with one of the datasets close to the maximum phase angle Jupiter is observable at from Earth, at 10.74° (the maximum is almost 12 degrees). There are some differences in the planetary parameters of Jupiter across the eight epochs: the angular diameter of the disk of Jupiter on the sky and the distance to the north pole of Jupiter from the centre of the disk. As can be seen from Table 5.1, the north pole angle of Jupiter can also be seen to vary slightly relative to that of the north celestial meridian.

The Jupiter maps are shown in Figs. 5.3, 5.4, 5.5, 5.6, 5.7, 5.8, 5.10 and 5.12. The left column shows the total flux map and the right column shows the map of P_{L}, with direction arrows superposed that show the polarisation position angle. The arrows do not have an arrowhead because the direction of polarisation only varies between 0° to 180° and angle 0 (180)° is taken to be the vertical direction. A position angle for every pixel is not indicated, as this would clutter the image, so a "rebinned" position angle is shown for sets of 10×10 pixels on the image, corresponding to an area of 5.66 square arcseconds, equating to an average area of approximately $7.74{\times}10^6\,\mathrm{km}^2$ on Jupiter (on the sky at the distance of Jupiter).

The P_{L} maps have the scale set such that it saturates at 4% to emphasise more clearly the variation in polarisation at lower latitudes in greater detail, since the polarisation drastically increases towards the polar regions in every dataset. The bottommost plots for each figure show the polarisation across the central meridian of Jupiter, taken from the polarisation images in the respective filters. This was calculated by taking the values of P_{L} for the central six longitudes and performing an average over these values.

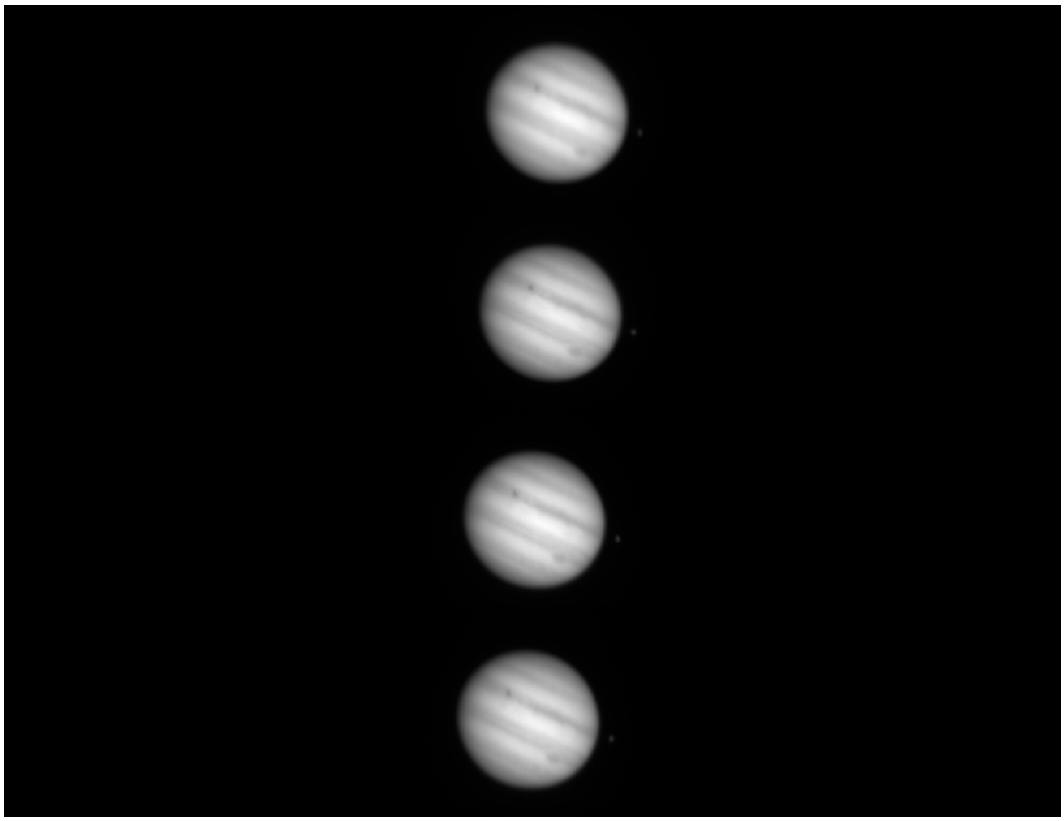

Figure 5.2: ToPol CCD image of Jupiter in the V filter. From the top down, the four beams are proportional to $F + Q$, $F - Q$, $F + U$, and $F - U$. Credit: McLean et al. [2017], reproduced with permission © ESO.

5.2.2.1 Intensity maps

The flux of the object is also usually obtained from polarimetric observations, and is presented here alongside the polarisation and position angle. The flux maps are not calibrated, so what is discussed in the following are relative differences between the filters and different datasets. In each of the total flux images (Figs. 5.3, 5.4, 5.5, 5.6, 5.7, 5.8, 5.10 and 5.12) the familiar banded structure of Jupiter can clearly be seen. The north and the south equatorial belts stand out in particular as dark stripes between latitudes of around 8 and 20 degrees on either side of the brighter equatorial zone.

North and south of the equatorial belts, Jupiter is brighter across the temperate zones. The narrow, darker belts that are commonly observed in these zones are not obvious; separate belts can only be clearly seen in dataset IP5, IP7, and IP8 (Figs. 5.7, 5.10, and 5.12; see Table 5.1), These belts are also visible in dataset IP3 and IP6, but are not as obvious. Although belts on Jupiter are known to temporarily disappear from view because of overlying hazes, their visibility in the images presented here seems related to the viewing conditions at the time of observation. The temperate zones can be seen to darken slightly towards the poles and transit at around 50 degrees into the north and south polar regions. It can be seen from a comparison along the limb of the planet that the total fluxes across the polar regions are lower than can be explained from the large local illumination and viewing angles. The hazes that are known to cover the polar regions are most likely responsible for the low total fluxes that are observed.

The U and B filter data appear to show the greater contrast between the different belts and zones of Jupiter, and this is because of greater sensitivity to different cloud altitudes at bluer wavelengths than at redder wavelengths. The clouds in the belts are known to reside at lower altitudes with more gas lying above them than for the clouds in the zones, which occupy higher altitudes. At blue wavelengths, the Rayleigh scattering optical thickness is highest, thus the cloud-top altitude should influence the contrast more. With increasing wavelength the gas scattering optical thickness decreases, and hardly affects the reflected light from the planet. In the red, differences in cloud composition are the likely cause of the subdued contrast between the belts and the zones. These influences are investigated further in Section 5.3. The photometric contrast of the belts and zones of Jupiter has been discussed in various works [West et al., 1986, 2004] showing differences in the clouds and hazes. Aside from in situ measurements that were taken with the Galileo probe [Sromovsky & Fry, 2002; Young, 2003; Vasavada & Showman, 2005], any informa-

tion on the atmosphere of Jupiter has come from remote imaging and spectroscopic study. The vertical structure of the clouds can be probed through measurement of the reflectance in parts of the spectrum where the gas absorption limits the depth that photons can penetrate to. In the visible region of the spectrum, methane is the strongest absorber, and thus methane bands between 600 nm and 1000 nm have been used extensively [West et al., 2004] to probe the cloud vertical structure.

In datasets IP3 (Fig. 5.5), IP5 (Fig. 5.7), and IP8 (Fig. 5.12) the Great Red Spot (GRS) is visible on the disk of Jupiter. In the GRS, which is located on the southern edge of the south equatorial belt, the cloud-top altitude is known to be higher than in the surrounding areas. The GRS is seen to stand out as a dark region in the U and B filter images, while it is only slightly brighter than its surroundings in the R filter. The dark dots on Jupiter in IP3 (Fig. 5.5) and IP5 (Fig. 5.7) are the shadows of Io and Europa, respectively.

5.2.2.2 Polarimetric maps

In polarised light, the images of Jupiter show clear differences between the belts and zones; in particular, the polar caps show up clearly despite the observations being taken at small phase angles where the polarisation is usually very low. The polarisation of the light scattered from the polar caps seems quite independent of the wavelength, with relatively high values in the B, V, and R bands. In the B band, the polarisation of the belts is higher than the polarisation across the zones, whilst in the V band the polarisation in the belts is smaller than in the zones. In the R band, a lot less spatial structure is noticeable, apart from in datasets IP5, IP7, and IP8, which could be due to slightly better seeing conditions at the time of observation, thus making the features much sharper.

The polarisation in the GRS stands out more clearly in the B band (in datasets IP3 (Fig. 5.5), IP5 (Fig. 5.7), and IP8 (Fig. 5.12)), showing higher polarisation than the surrounding areas. In dataset IP5, the polarisation direction in the GRS is different from that of the surrounding regions, but this difference is not as evident for dataset IP8. Additionally in dataset IP5, there is an area of relatively high polarisation present south from the GRS in the B band, with the polarisation in the GRS appearing to be lower in the V and R bands. It is clear from the polarimetric maps and the latitudinal plots that the polarisation shows considerable variation between the belts and zones, with the variations changing with filter as well. These variations are most likely connected to the particle type and the haze and cloud optical thickness and height; these differences also manifest themselves in the polar-

isation angle, and is also observed to change between the different belts and zones and between filters.

The arrows that show the position angle of the polarisation indicate changes over the disk of Jupiter, perhaps due to differing particle types, shapes, and concentrations. The position angle also appears to vary with wavelength and time; the latter possibly indicative of seasonal variations in the Jovian atmosphere. Previous studies [Lyot, 1929; Dollfus, 1957; Gehrels et al., 1969; Morozhenko & Yanovitskii, 1973; Hall & Riley, 1976; Carlson & Lutz, 1989; Starodubtseva et al., 2002; Shalygina et al., 2008; Schmid et al., 2011] have mainly indicated a polarisation around the equator parallel to the scattering plane, with the polarisation in the polar regions most often having a direction that is perpendicular to the scattering plane. Some of the data presented here is consistent with this, mostly showing a polarisation perpendicular to the scattering plane in the polar regions. This is the first study presenting a detailed evaluation of the position angle variation over the entire disk of Jupiter for eight epochs within a relatively short time period, therefore it is difficult to infer conclusions by comparing with earlier, much less spatially resolved data. The polarisation direction can be seen to change with wavelength, also appearing to vary between the belts and zones, in particular, in the B band. The direction of polarisation at the poles also has a distinct direction compared with the direction on other locations of the disk.

The bottom plots of Figs. 5.3, 5.4, 5.5, 5.6, and 5.7 show the polarisation as a function of latitude across the central meridian of Jupiter, as taken from the polarisation images. Figures 5.9, 5.11, and 5.13 show the latitudinal plots for datasets IP6, IP7, and IP8, respectively. These plots all show the variation in the polarisation that is associated with the belts and zones: the decrease and inversion of the variation up to the midlatitudes as the wavelength increases, and the sudden, steep increase in the polarisation at the poles in all four filters.

The value of the polarisation and its variation across latitude in the V filter data are similar to that detailed in other recent studies [Gorosabel et al., 2015]. Also, the difference in polarisation observed between the belts and zones is more prominent in the data presented here than that in Shalygina et al. [2008]. This is especially made more evident by the different wavelength bands used in this work, and also the better viewing conditions present in some of the datasets. The polarisation is seen to be consistently higher at the south pole than at the north pole, with this appearing to be a seasonal effect observed and described before [Shalygina et al., 2008].

Schmid et al. [2011] show a higher polarisation across the south polar region than in the north polar region from data taken in 2003, and the results presented here are consistent with this. The observations detailed by Schmid et al. [2011] were taken during a similar seasonal period on Jupiter as the ones here, namely during southern spring. While the obliquity angle of Jupiter is only 3.12°, the orbit of Jupiter has a relatively large eccentricity (of 0.048) with a perihelion coinciding with the northern summer solstice, therefore enhancing hemispherical differences in insolation. The observations presented here were carried out during the end of the southern winter season and the beginning of the southern spring, where the southern polarisation is still higher than the northern polarisation.

Latitudinal plots of P_{L} along with latitudinal cuts of the total flux for dataset IP5 are shown in Figure 5.14. These plots demonstrate that polarisation has a greater sensitivity to variations across the disk of Jupiter. Flux measurements alone can show differences in the cloud type and structure, but by including polarimetric measurements a complete description of the light scattered within the planetary atmosphere is given. This is important not just for solar system planetary atmospheres, but also for exoplanets: polarimetric measurements along with radiative transfer models are able to constrain atmospheric properties much more than flux measurements alone are able to. The greater sensitivity of polarisation data means that fitting the data is much more challenging than fitting flux data alone. Section 5.3.2 discusses this in more detail and presents models of the flux and degree of linear polarisation of light reflected by the atmospheres of exoplanets.

The imaging polarimetry datasets all show a wealth of detail, and the same trends in polarisation across the disk of Jupiter with some variations that depend on the belt and zonal cloud regions. The polarisation differences across the central part of Jupiter are more obvious in the U and B filter data, and this is likely due to an increased amount of strongly polarising Rayleigh scattering from hydrogen, helium, and methane molecules. Table 5.1 shows that, for each dataset, the time difference between the observations in each filter can be up to around 20 minutes. This corresponds to approximately 1/30th of the rotation period of Jupiter (9.9 hours) or 12 degrees of rotation, which means that a different region of the planet was sampled, possibly causing some of the differences in flux and polarisation between filters. The results presented here compare favourably with those from previous studies, such as Shalygina et al. [2008], who also found that the southern polar region of Jupiter was more highly polarised at bluer wavelengths than the northern polar region, from the average of 15 datasets taken over a timespan of 23 years. Schmid et al. [2011] also

report this from spectropolarimetric observations, with the slit positioned over the polar regions.

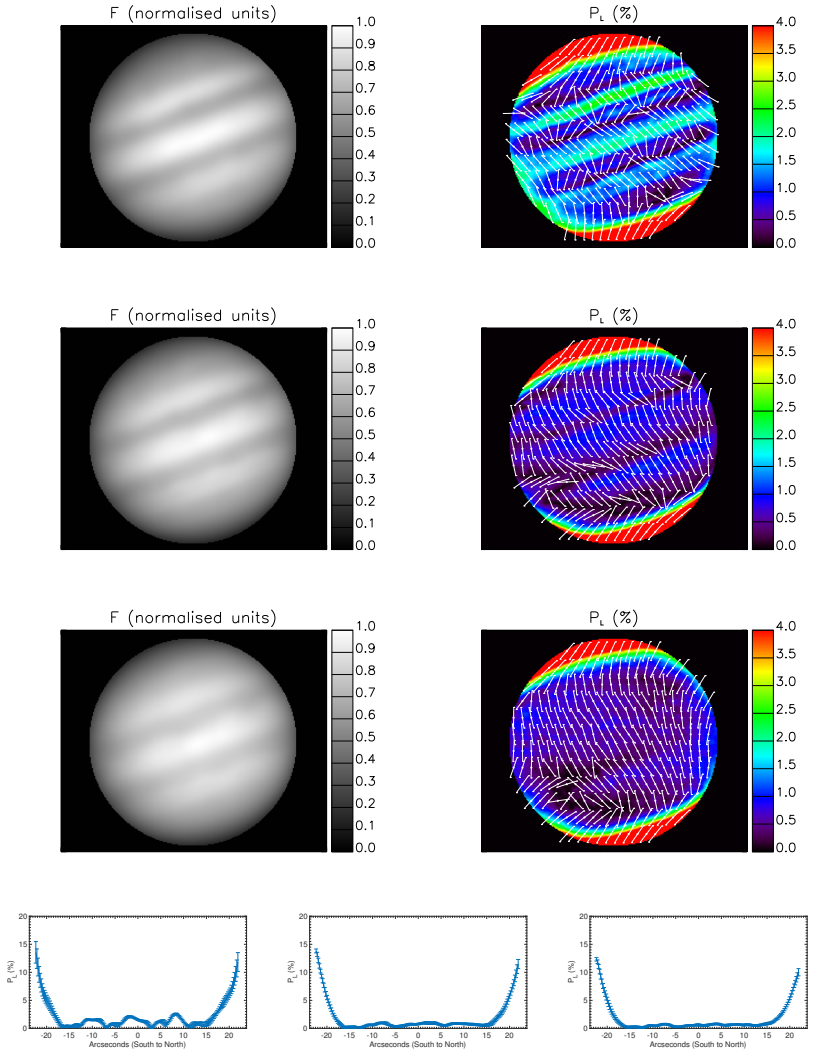

Figure 5.3: Data set IP1. From top to bottom: maps in B, V, and R, with the bottom plots showing from left to right the polarisation across Jupiter's central meridian in B, V, and R. Credit: McLean et al. [2017], reproduced with permission © ESO.

5.2.2.3 Spectropolarimetric observations with FoReRo2

Two sets of spectropolarimetric observations were taken with FoReRo2 in the wavelength range 500–850 nm (with a spectral resolution of 2 nm). Bias frames were

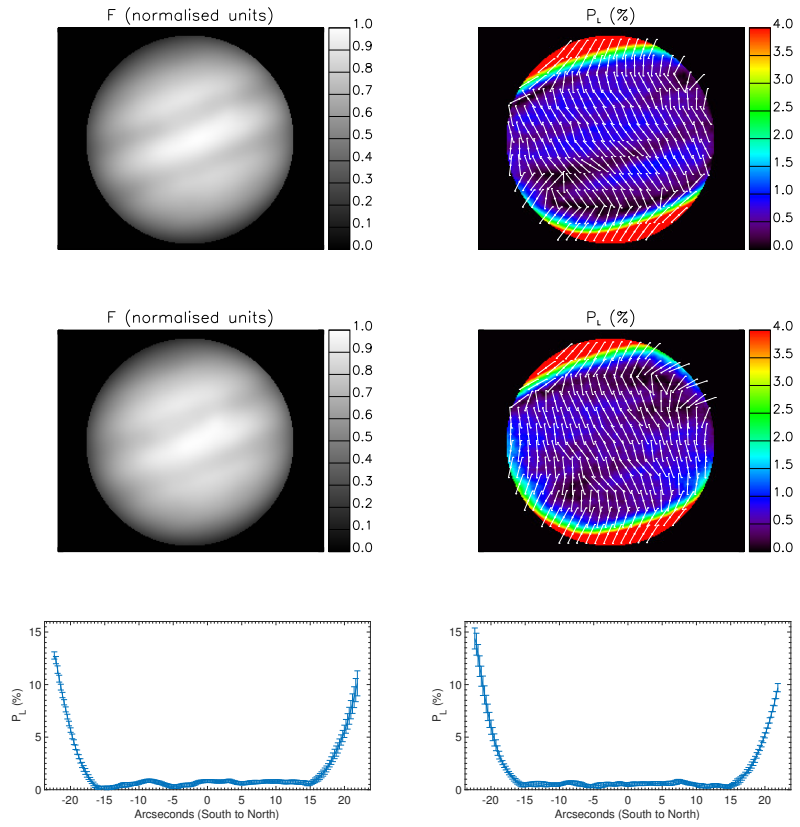

Figure 5.4: Data set IP2. From top to bottom: maps in V and R, with the bottom plots showing from left to right the polarisation across Jupiter's central meridian in V and R. Credit: McLean et al. [2017], reproduced with permission © ESO.

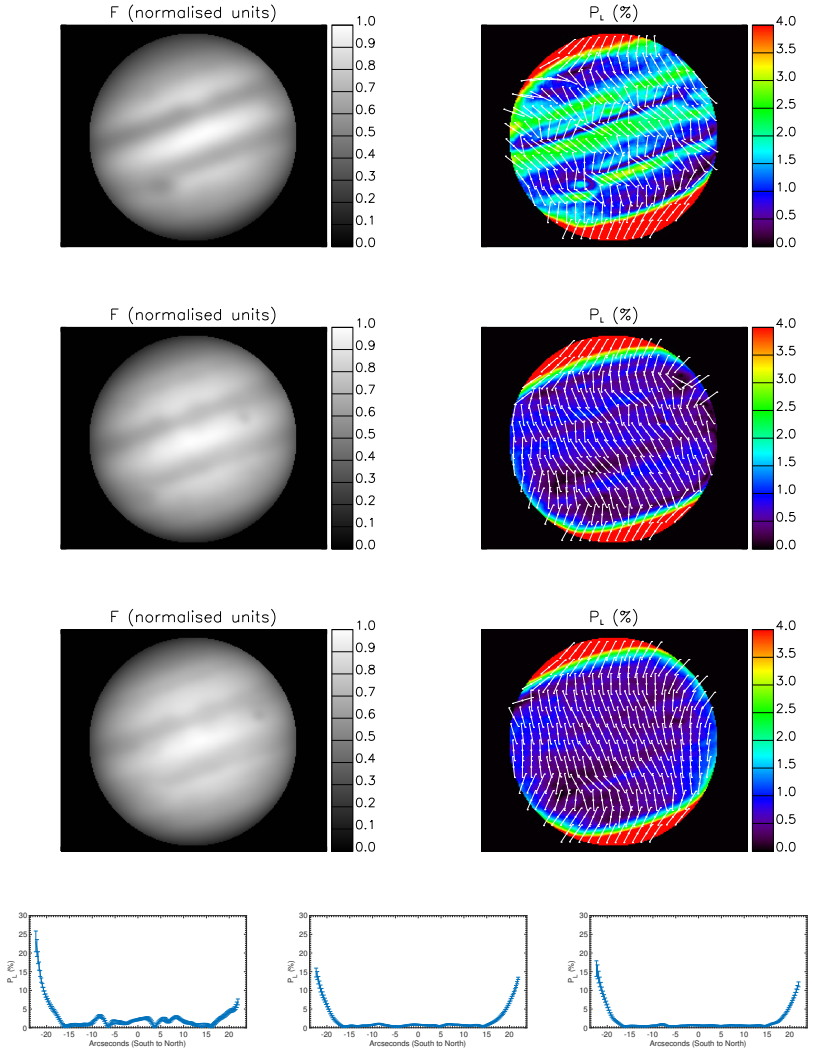

Figure 5.5: Data set IP3. From top to bottom: maps in B, V, and R, with the bottom plots showing from left to right the polarisation across Jupiter's central meridian in B, V, and R. Credit: McLean et al. [2017], reproduced with permission © ESO.

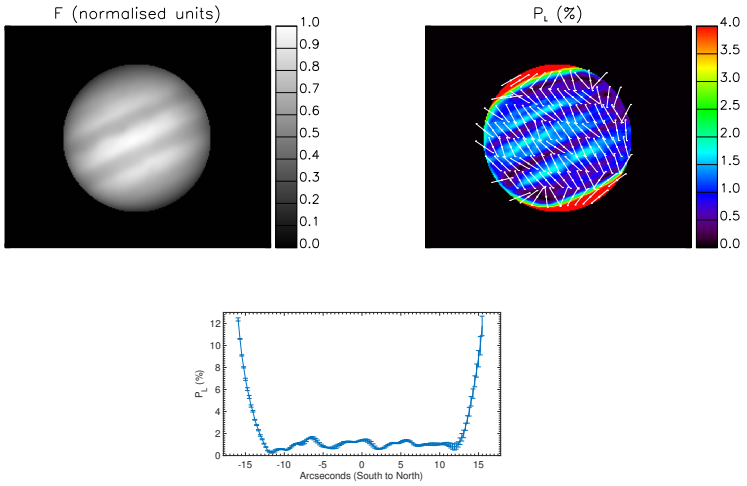

Figure 5.6: Data set IP4. Maps are shown for the V filter, with the bottom plot showing the polarisation across Jupiter's central meridian. Credit: McLean et al. [2017], reproduced with permission © ESO.

also taken, along with standard stars to assess the instrumental polarisation. The position of the slit in each set of observations is shown in Fig. 5.15.

Figure. 5.16 shows the degree of linear polarisation as a function of wavelength for each of the two spectropolarimetry datasets. For each retarder angle, the frames were collapsed with *iraf* before they were combined to compute the reduced Stokes parameters, thus these spectra represent an average across the slit (see Fig. 5.15, for the slit positions on the planet for the two measurements): not just an average across the vertical slit direction, but also over the horizontal direction (even though less of the planet is sampled in the horizontal direction than the vertical direction). The continuum polarisation decreases with increasing wavelength in both sets of spectropolarimetric data, and is mostly due to a decrease of Rayleigh scattering and, hence, the rise in contribution by scattering from cloud and haze particles. The two spectropolarimetry datasets have variations between them due to a combination in the difference in the area covered by the slit, and the differing atmospheric parameters across the regions sampled in each of the datasets. The gaseous methane absorption bands around 620 nm in the November 2015 data and a band around 720 nm in both datasets can be seen. Both of the spectropolarimetry datasets seem to be affected by fringing at wavelengths longer than 750 nm.

The degree of polarisation in the methane bands appears to be lower than in the surrounding continuum regions. It is usually expected that the degree of polarisation

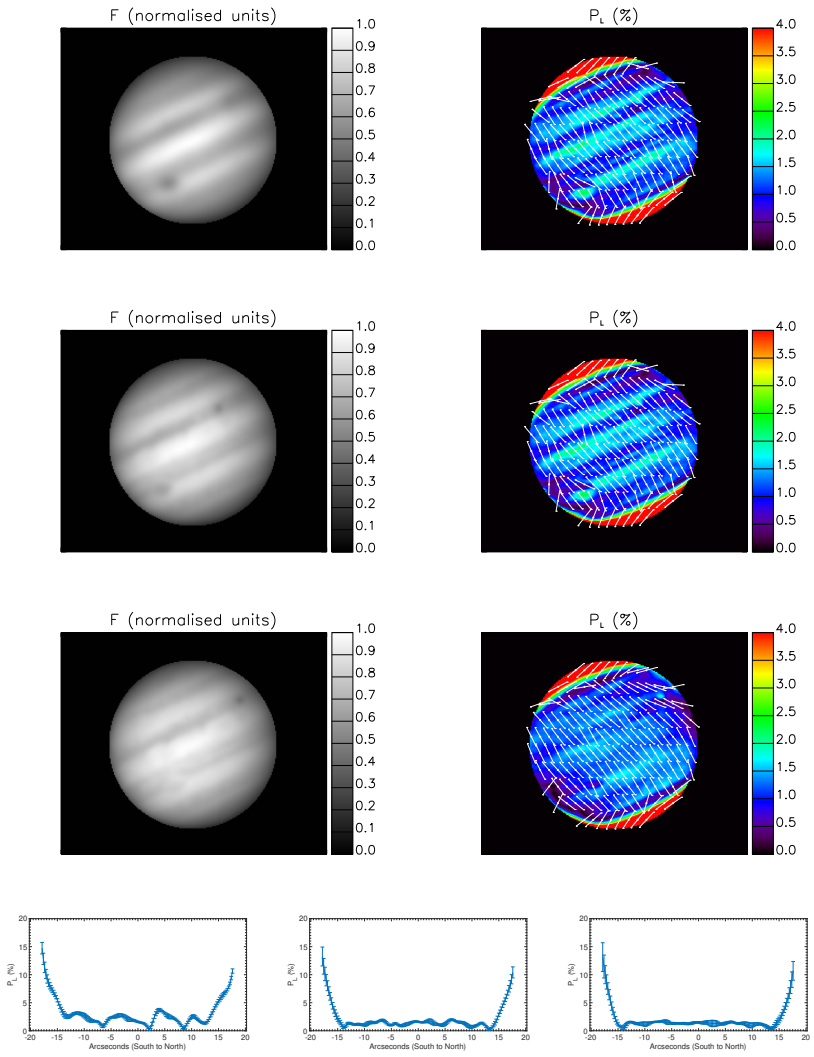

Figure 5.7: Data set IP5. From top to bottom: maps in B, V, and R, with the bottom plots showing from left to right the polarisation across Jupiter's central meridian in B, V, and R. Credit: McLean et al. [2017], reproduced with permission © ESO.

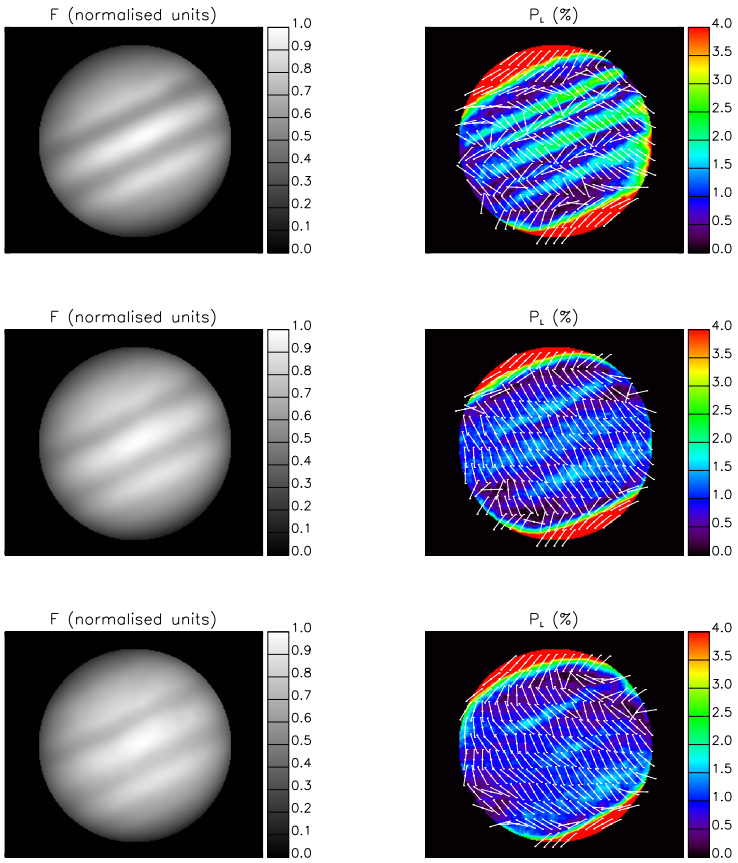

Figure 5.8: Data set IP6. From top to bottom: maps in B, V, and R.

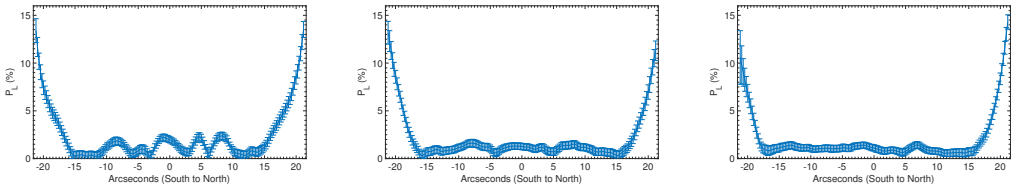

Figure 5.9: Latitudinal plots for IP6 in B, V, and R, from left to right.

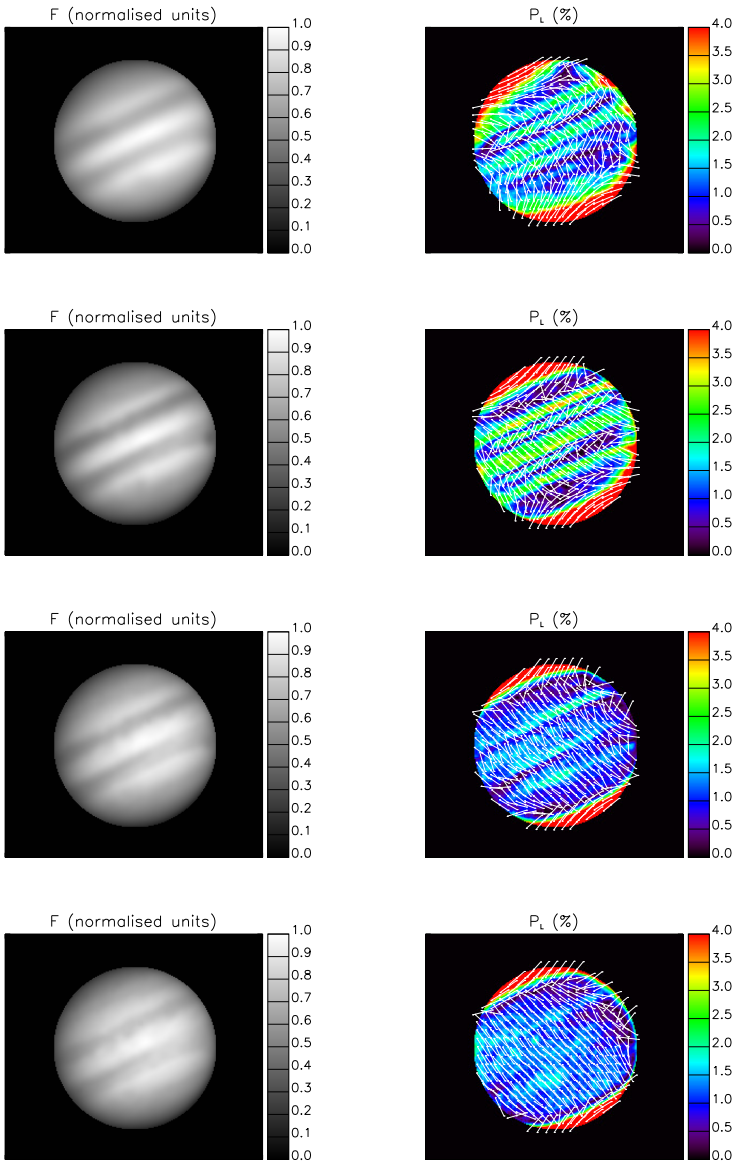

Figure 5.10: Data set IP7. From top to bottom: maps in U, B, V, and R.

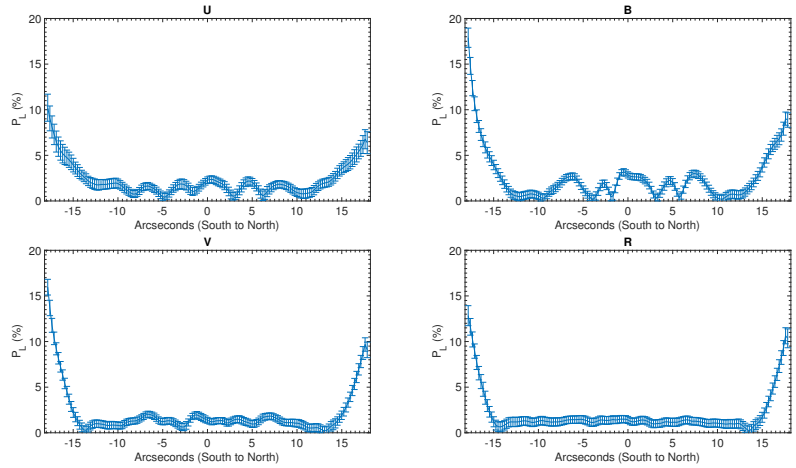

Figure 5.11: Latitudinal plots for IP7.

in an absorption band is greater than that of the continuum because with increasing absorption, the amount of multiple scattered light in the reflected light signal decreases. Since multiple scattering tends to decrease the degree of polarisation, absorption bands, such as those of methane, would therefore manifest themselves as peaks superimposed upon the continuum [Stam et al., 1999, 2004]. This effect can be seen in Fig. 4 of Schmid et al. [2011].

However, if the planetary atmosphere is vertically inhomogenous, it is possible that the degree of polarisation in absorption bands can be similar to or lower than that of the continuum [Stam et al., 1999, 2004]. This effect arises because as absorption increases, the observed reflected sunlight has been scattered in atmospheric layers at increasingly higher levels. If the degree of polarisation from scattering by gases and particles in high atmospheric layers is lower than that from (multiple) scattering by gases and particles in the lower layers at the specific phase angle, the polarisation can vanish or decrease across an absorption band, either the whole band or parts of it. Figure 3 of Schmid et al. [2011] actually shows this variation of band strength from observations of the polarisation[2] in the continuum region (at 600 nm) and in a deep methane absorption band (at 887 nm) along the central meridian of Jupiter. At latitudes near the southern polar region and at midlatitudes (the regions indicated by S- and N- in Schmid et al. [2011]), the polarisation in the methane band is greater than the continuum polarisation in an absolute sense, with the sign of the polarisation only indicating the direction of polarisation. At northern latitudes (region N+) and some southern latitudes, however, the band polarisation is lower

[2]Schmid et al. [2011] show Q/I, with I the total flux.

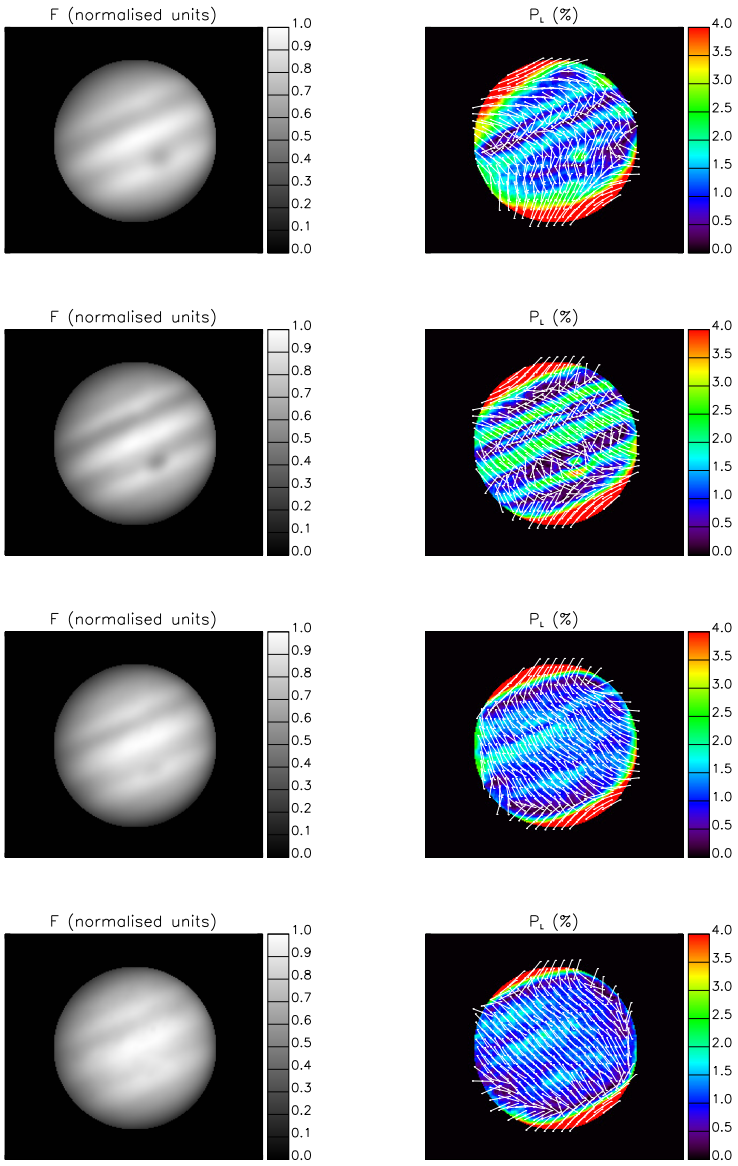

Figure 5.12: Data set IP8. From top to bottom: maps in U, B, V, and R.

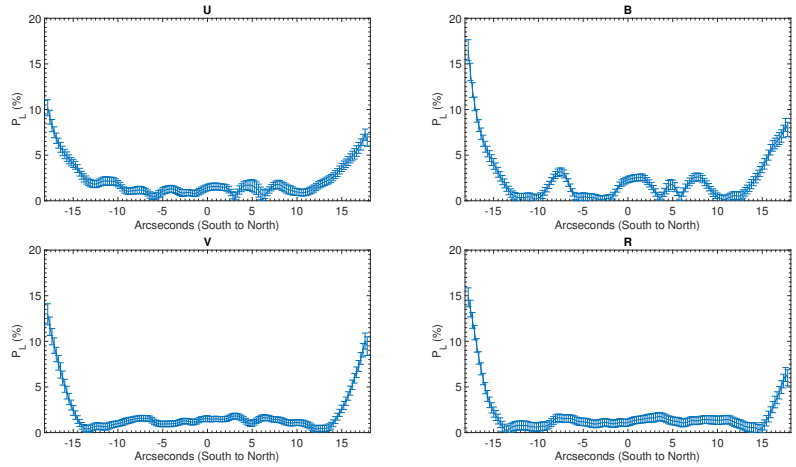

Figure 5.13: Latitudinal plots for IP8.

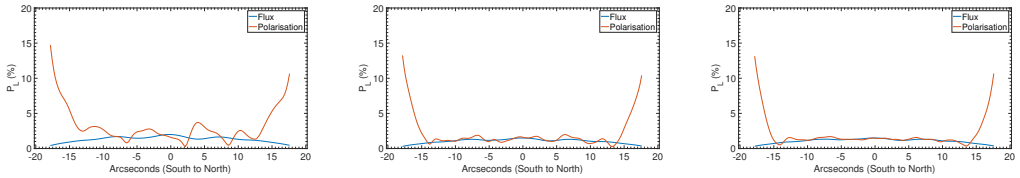

Figure 5.14: From left to right: latitudinal plots of the linear polarisation from the central meridian of IP5 in B, V, and R. The flux values are over-plotted in arbitrary units. Credit: McLean et al. [2017], reproduced with permission © ESO.

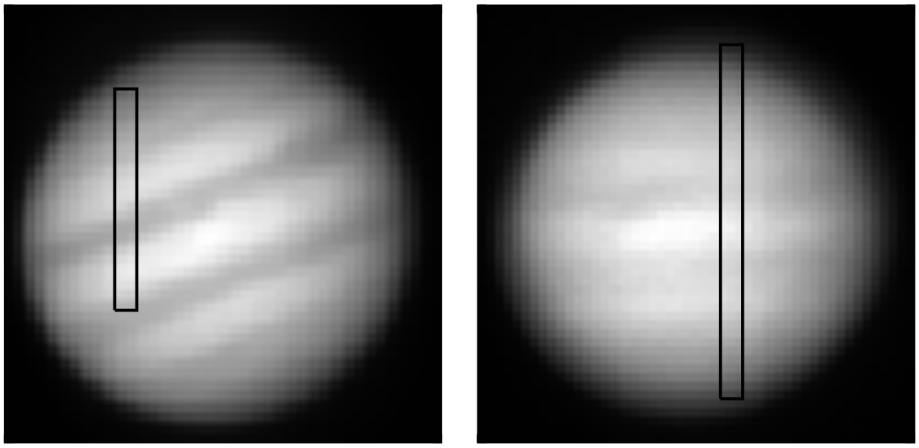

Figure 5.15: Left: the slit position on Jupiter in December 2014. Right: the slit position in November 2015. The reason for the difference in the height of the slit between each epoch is because of the smaller angular size of Jupiter in dataset SP2, thus the slit width was chosen to be narrower in SP2 so that the slit contained only the planet and not the background. Credit: McLean et al. [2017], reproduced with permission © ESO.

than that of the continuum (up to 3%) or equal to that of the continuum, and the absorption band appears as a dip in the continuum polarisation, or does not appear at all.

The reflectance spectra corresponding to both of the spectropolarimetry datasets are shown in Fig. 5.17. These were calculated by dividing the flux of Jupiter by that of a solar analogue, taken using the same instrumental setup. Correspondences between the slopes in both the flux and polarisation can be observed along with differences in the shapes and depths of the methane absorption bands. The polarisation spectra appear more sensitive to the variations in the depths of the methane absorption bands between the two epochs. The two datasets were taken almost a year apart and sampled two different regions, therefore the difference in the strength of the absorption features could be because of differences in local time, season, and the composition of the atmosphere in the sampled areas.

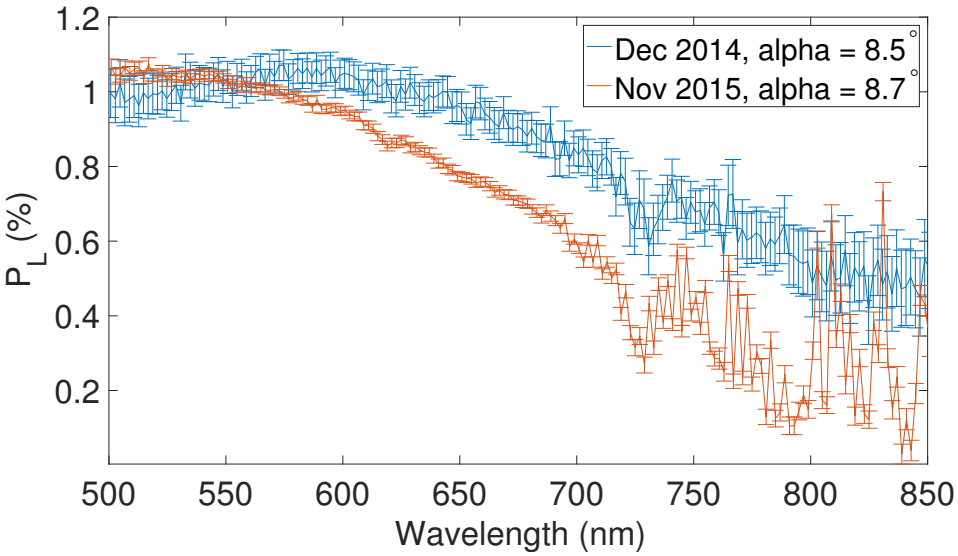

Figure 5.16: Spectropolarimetry of Jupiter for the two epochs averaged across both the vertical slit direction and across the horizontal direction. Credit: McLean et al. [2017], reproduced with permission © ESO.

5.3 Theoretical modelling

To interpret the observations, numerical models of polarised light reflected by Jupiter were carried out using the model described in Section 2.3 for the first five imaging polarimetry datasets. The atmosphere of Jupiter was considered as being composed

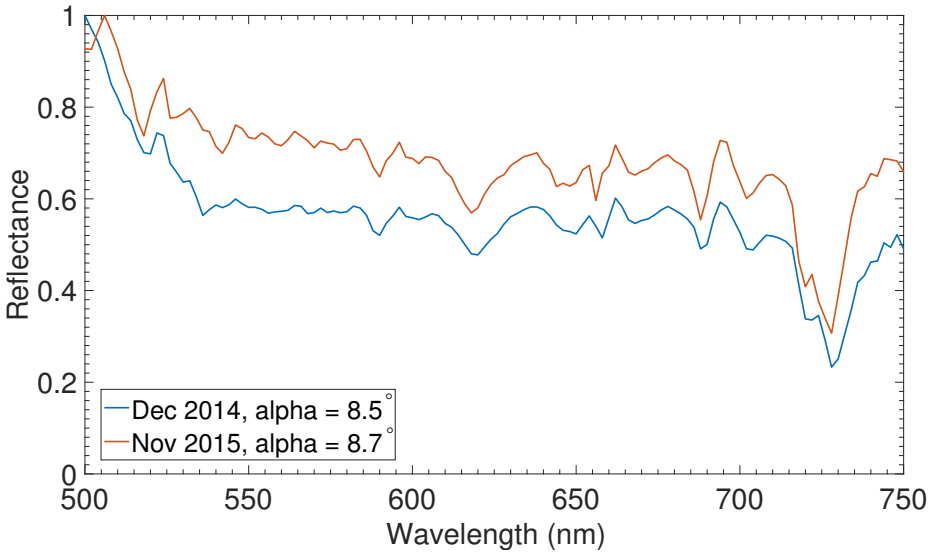

Figure 5.17: Reflectance spectra for the two spectropolarimetry datasets. Credit: McLean et al. [2017], reproduced with permission © ESO.

of locally plane parallel, horizontally homogeneous layers with a pressure profile as described by Stam et al. [2004]. Every layer in the atmosphere contained a mixture of hydrogen, helium, and methane with some of the layers additionally containing cloud and haze particle layers of varying optical thickness. Several cloud and haze particle properties were trialled, and then the height in the atmosphere of the different layers was varied to try and reproduce the variation of polarisation across the different belts and zones of Jupiter observed in the data. The cloud and haze particles considered were spherical, described by Mie theory, and with fractal aggregate particles used to model the polar haze particles, as used by Karalidi et al. [2013]. A basic representation of the model atmospheric layers is shown in Fig. 2.4a.

5.3.1 Modelling of the observations

The physical properties of the clouds and hazes of Jupiter and gas giants are known to vary with time and location on the planet. Thermodynamic models of the atmosphere of Jupiter have shown that the cloud layers in the upper troposphere should consist mainly of ammonia ice [see Sato & Hansen, 1979; Simon-Miller et al., 2001; de Pater & Lissauer, 2001]. Results from the Galileo and Cassini missions, however, have indicated that ammonia ice clouds only appear to cover small regions of Jupiter [see Baines et al., 2002; Wong et al., 2004]. Atreya et al. [2005] suggested that the

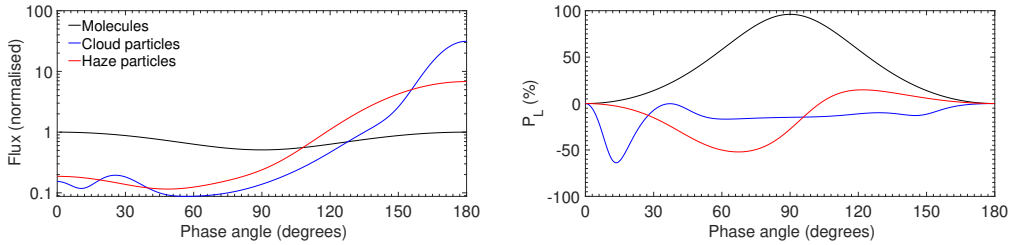

Figure 5.18: Single scattering flux and linear polarisation of the cloud and haze particles at 550 nm along with Rayleigh scattering curves. The phase angle is $180° - \Theta$, with Θ the single scattering angle. Credit: McLean et al. [2017], reproduced with permission © ESO.

ammonia ice is coated by hydrocarbon haze particles that condense from the stratosphere, therefore meaning that only the highest ammonia ice clouds would show identifiable spectral features, and would also depend on the size and shape of the ice crystals. Some recent results on the distribution of ammonia in the atmosphere of Jupiter are discussed by de Pater et al. [2016].

Various cloud particle properties were trialled in models of the Jovian atmosphere, with the best solution found being a model atmosphere containing an optically thick tropospheric cloud layer, with an overlying stratospheric haze layer. The final cloud particles chosen have effective radius $r_{\text{eff}} = 0.50\,\mu$m, and effective variance $v_{\text{eff}} = 0.05$ with a refractive index of 1.42, and an imaginary part of 0.015. The haze particles that gave the closest match to the observed polarisation in the data have $r_{\text{eff}} = 0.2\,\mu$m, with a narrow size distribution of $v_{\text{eff}} = 0.01$, with a refractive index of 1.50 and an imaginary part of 0.001. The size and refractive index of the haze is consistent with that found by Stoll [1980], who carried out models of Pioneer observations of Jupiter and attempted to constrain the properties of the cloud and haze particles. Fig. 5.18 shows plots of the single scattering flux and polarisation for the cloud and haze particles. P_{L} has some negative values because here $P_U = 0$, so P_{L} has been set equal to $-P_Q$, therefore the positive (negative) values of P_{L} in Fig. 5.18 indicate polarisation that is perpendicular (parallel) to the scattering plane.

5.3.1.1 Spectropolarimetry models

Models of the flux and degree of linear polarisation that provide the best fit to the data are shown in Figs. 5.19, 5.20, 5.21, and 5.22. The data from the observations are shown as solid lines along with the error bars, with the models plotted alongside

as dashed lines. A broad range of regions in the atmosphere of Jupiter are covered by the slit in each dataset, with contributions from the belts, zones, and polar regions. The spectropolarimetric model fits only consider a single atmosphere model, which effectively represents the atmospheric properties in the region sampled by the slit. The model of the December 2014 data contains an optically thick cloud particle layer with a cloud-top height of 1.0 bar, and a diffuse haze layer above it at a pressure level of 0.13 to 0.10 bar. The cloud layer for the November 2015 model has a higher vertical extent, going up to 0.56 bar with a haze layer slightly thicker than that of the December 2014 model, and at the same altitude. A model fit replicating both the continuum polarisation and the polarisation levels across the methane absorption bands for the November 2015 dataset was difficult to achieve, therefore the fit giving the closest approximation to the continuum polarisation is shown.

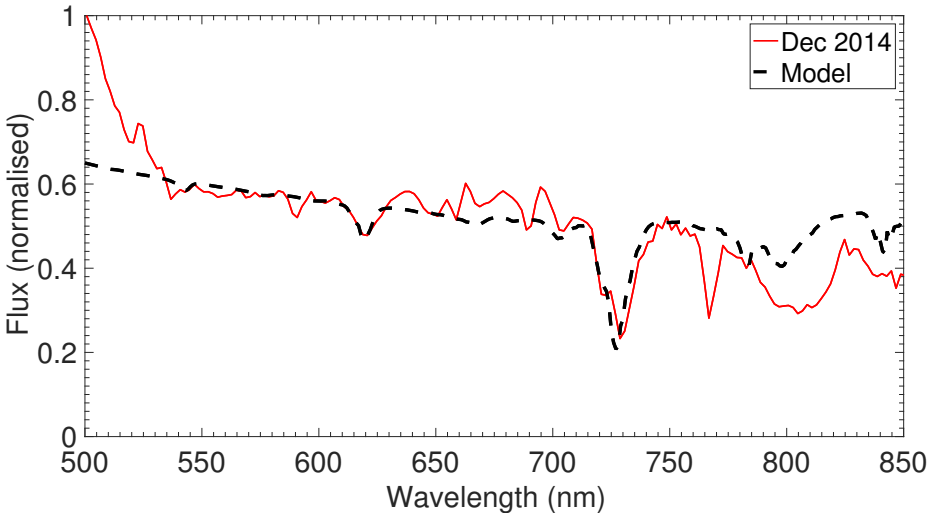

Figure 5.19: Model fit to the flux for dataset SP1.

The spectropolarimetry models closely replicate the continuum polarisation over the observed wavelength range, with no inconsistency between the blue wavelengths and longer wavelengths, although further observations at bluer wavelengths would be needed in order to investigate this further. The model fit to the November 2015 dataset (see Fig. 5.22) deviates from the observed values of P_{L} at shorter wavelengths, similar to what is shown in the models of the imaging polarimetry data (see Fig. 5.23). The spectropolarimetry data encompassed a broad range of atmospheric properties along the regions sampled in the slit (see Fig. 5.15), so it is to be expected that there are differing particle types giving the overall contribution to the total polarisation levels. The polarisation in the methane absorption bands

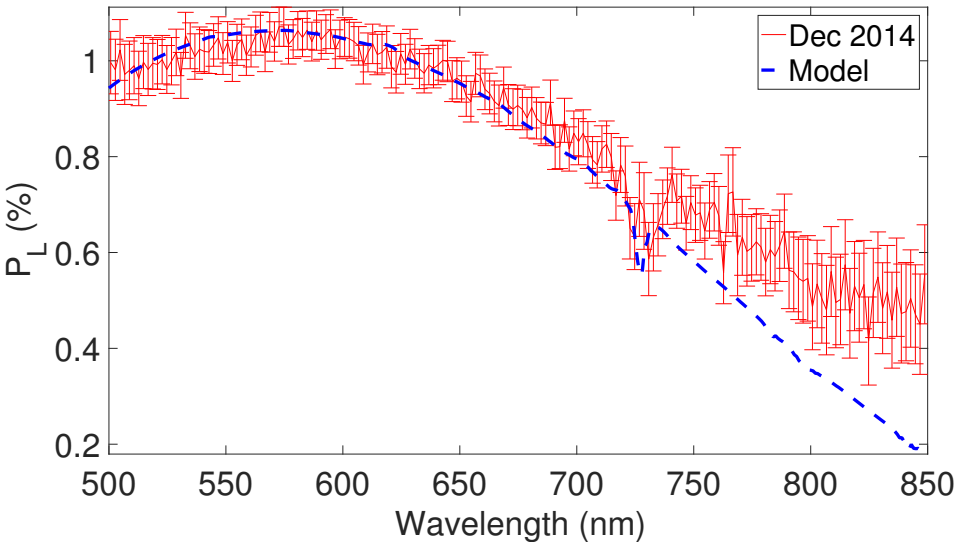

Figure 5.20: Model fit to the degree of linear polarisation for dataset SP1. Credit: McLean et al. [2017], reproduced with permission © ESO.

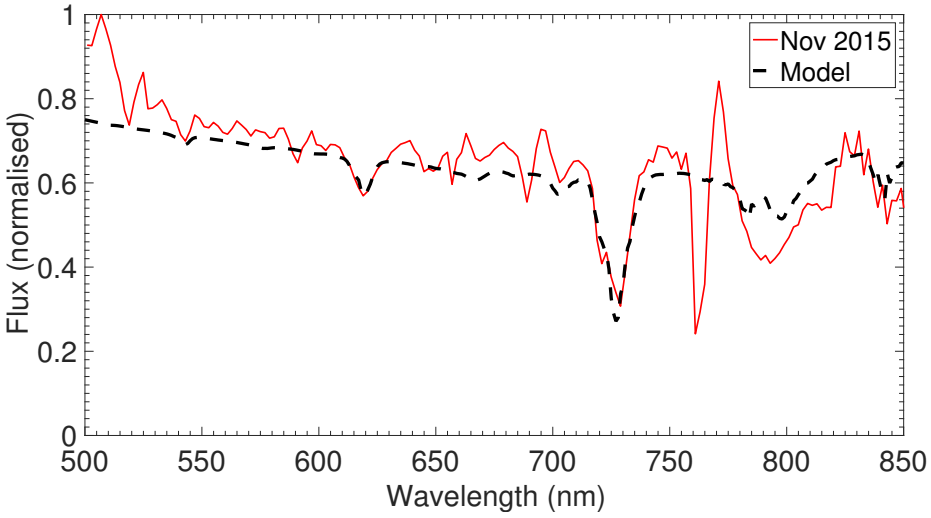

Figure 5.21: Model fit to the flux for dataset SP2.

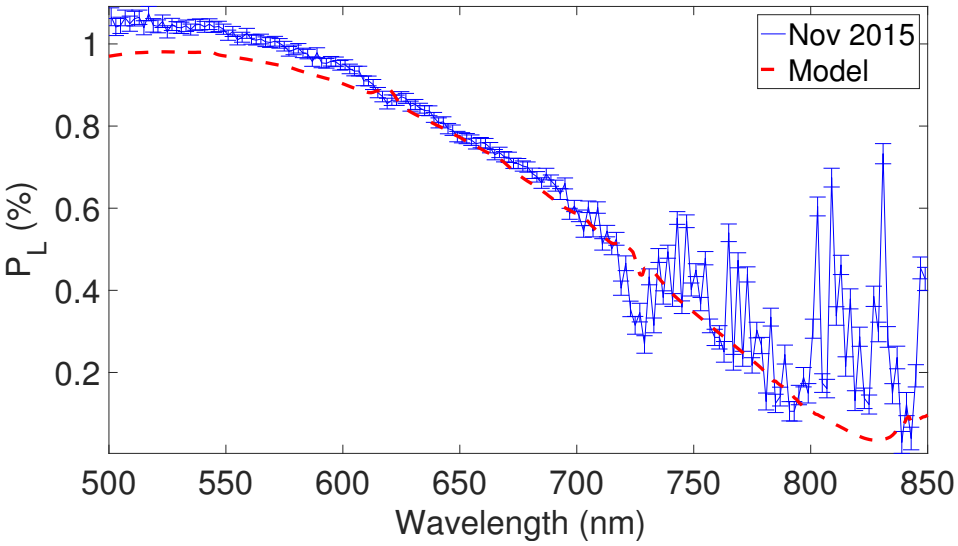

Figure 5.22: Model fit to the degree of linear polarisation for dataset SP2. Credit: McLean et al. [2017], reproduced with permission © ESO.

was modelled closely for the December 2014 dataset, although a model that was consistent with both the absorption band depth and continuum polarisation could not be found for the November 2015 dataset.

5.3.1.2 Models of the latitudinal profiles

The imaging data was modelled by fitting atmospheric models with a particle type identical to those for the spectropolarimetry models. It was found that small spherical particles scattering according to Mie theory were too depolarising and unable to model the steep increase in polarisation towards the polar regions. It was therefore decided to use fractal aggregate haze particles as an attempt to model the polarisation at the poles, the same haze particles as those used by Karalidi et al. [2013]. The particles consist of 94 spherical monomers with each of the individual monomers having a radius of approximately 0.035 μm, and the volume-equivalent sphere radius of the entire particle being 0.16 μm. A refractive index of 1.5 + 0.001i was used, corresponding to the optical properties of benzene, which Friedson et al. [2002] suggests may be present at the polar regions of Jupiter. The fractal aggregate particles were found to provide a slightly higher polarisation than individual spherical haze particles. Thick layers of smaller radius haze particles were trialled in the models, but were not found to give a sufficiently high value of polarisation to match up with the observational results. The haze and cloud optical thickness along with altitude

were varied over latitude in order to reproduce the observed values of polarisation. Table 5.2 shows the particle properties and the cloud and haze height and optical thickness of the final model used in each of the imaging polarimetry datasets.

Table 5.2: Model parameters of the Jupiter imaging polarimetry fits. The values of b^{c} and b^{h} are those defined at 550 nm. Unless otherwise indicated, the particle properties for both the cloud and haze are the same as those given in the main body of the text.

Data	Latitude (pixels)	Cloud-top pressure (bar)	Haze-top pressure (bar)	b^{c}	b^{h}
IP1	4-12	1.000	0.133 (fractals)	50.0	2.000
IP1	13-54	1.000	0.133	50.0	0.150
IP1	55-66	0.562	0.133	50.0	0.010
IP1	67-85	1.778	0.133	50.0	0.100
IP1	86-96	0.562	0.133	50.0	0.100
IP1	97-111	0.562	n/a	50.0	n/a
IP1	112-123	1.778	n/a	50.0	n/a
IP1	124-135	0.562	0.133	50.0	0.100
IP1	136-143	0.562	0.133	50.0	0.125
IP1	144-158	0.562	0.133	50.0	0.150
IP1	159-179	1.000	0.133	50.0	0.150
IP1	180-184	1.000	0.133 (fractals)	50.0	2.000
IP2	4-9	1.000	0.133 (fractals)	50.0	3.000
IP2	10-19	1.778	0.133	50.0	0.100
IP2	20-55	1.000	0.133	50.0	0.150
IP2	56-68	0.562	0.133	50.0	0.125
IP2	69-87	1.778	n/a	50.0	n/a
IP2	88-164	0.562	0.133	50.0	0.125
IP2	165-182	1.778	0.133	50.0	0.100
IP2	183-184	1.000	0.133 (fractals)	50.0	3.000
IP3	4-9	1.000	0.133 (fractals)	50.0	3.000
IP3	10-19	1.778	0.133	50.0	0.100
IP3	20-25	1.778	n/a	50.0	n/a
IP3	26-45	1.000	n/a	50.0	n/a
IP3	46-67	0.562	0.133	50.0	0.125

Data	Latitude (pixels)	Cloud-top pressure (bar)	Haze-top pressure (bar)	b^{c}	b^{h}
IP3	68-85	1.778	0.133	50.0	0.100
IP3	86-109	0.562	0.133	50.0	0.125
IP3	110-118	1.778	n/a	50.0	n/a
IP3	119-160	0.562	0.133	50.0	0.125
IP3	161-178	1.778	0.133	50.0	0.100
IP3	179-184	1.000	0.133 (fractals)	50.0	3.000
IP4	4-6	1.000	0.133 (fractals)	50.0	3.000
IP4	7-15	1.778	0.133	50.0	0.100
IP4	16-37	1.000	0.133	50.0	0.150
IP4	38-43	1.000	0.133	50.0	0.100
IP4	44-54	1.000	0.133	50.0	0.300
IP4	55-72	1.000	0.133	50.0	0.150
IP4	73-82	1.000	0.133	50.0	0.300
IP4	83-104	1.000	0.133	50.0	0.150
IP4	105-120	0.562	0.133	50.0	0.200
IP4	121-126	1.778	0.133	50.0	0.100
IP4	127-130	1.000	0.133 (fractals)	50.0	3.000
IP5	3-5	1.000	0.133 (fractals)	50.0	3.000
IP5	6-21	1.778	0.133	50.0	0.100
IP5	22-28	1.778	0.133	50.0	0.175
IP5	29-49	1.000	0.133	50.0	0.225
IP5	50-68	1.778	0.133	50.0	0.200
IP5	69-89	1.778	0.133	50.0	0.100
IP5	90-97	1.778	0.133	50.0	0.200
IP5	98-114	1.000	0.133	50.0	0.225
IP5	115-128	1.778	0.133	50.0	0.175
IP5	129-145	1.778	0.133	50.0	0.100
IP5	146-148	1.000	0.133 (fractals)	50.0	3.000

Model fits of the polarisation across the disk of Jupiter are shown in Fig. 5.23, along with the data for comparison. The general variations in polarisation observed along the central meridian of Jupiter were able to be reproduced, in particular, the higher polarisation values at the polar regions and the differences in polarisation between the belts and zones. The models used have the same cloud and haze particle types as for the spectropolarimetry data. Due to the inconsistency in the latitudinal variations between the three filters (such as an inversion of polarisation), a model reproducing the polarisation changes across the central meridian in all three bands was unable to be produced. This is likely due to the limitations in the particle types used in these models, since as mentioned before these are not fully understood. It is not only in the polar haze that non-spherical particles could be present, but the zones and/or belts may also harbour particles of different shapes, such as ice crystals. Models of the latitudinal variation could be achieved for the V and R filters, but are not consistent with the B filter data. The reason for the differing behaviour of the polarisation at blue wavelengths could be due to absorption, either by gas or a certain type of cloud or haze particle. Jupiter is known to have an as yet unknown absorber in the UV [see Karkoschka, 1994], and should be the subject of a more detailed investigation in order to achieve a closer model fit. The same challenge of finding a fit with wavelength has presented itself in the modelling of cometary data, with a potential solution of using non-spherical particles being put forward by some groups [see Kolokolova & Kimura, 2010; Kolokolova & Mackowski, 2012]. Depending on the size of such non-spherical particles, the effects of the non-sphericity may be strongest at shorter wavelengths.

The model particles used in this work are mostly spherical particles generated from Mie theory, to simulate ammonia ice particles as the predominant clouds in the troposphere of Jupiter. The type of haze particle chosen for the models at lower latitudes was quite arbitrary because not much is known about the properties of these particles, which are known to be present in the tropospheric and stratospheric regions of Jupiter's atmosphere, but was found to be consistent with the haze particle type used by Stoll [1980]. The model fits needed to be both consistent with the wavelength and phase angle variations. Polarisation of Jupiter has occasionally been observed at phase angles that are close to 90°, for example by the Cassini probe as it passed by Jupiter en route to Saturn [Vasavada & Showman, 2005], and the same trends have been shown as in this study, specifically, a relatively high value of polarisation at the poles and a lower value in the equatorial regions. However, it has been observed previously that particles of any shape appear to be insufficient for a full characterisation of the Jovian atmosphere due to the limited phase angle range

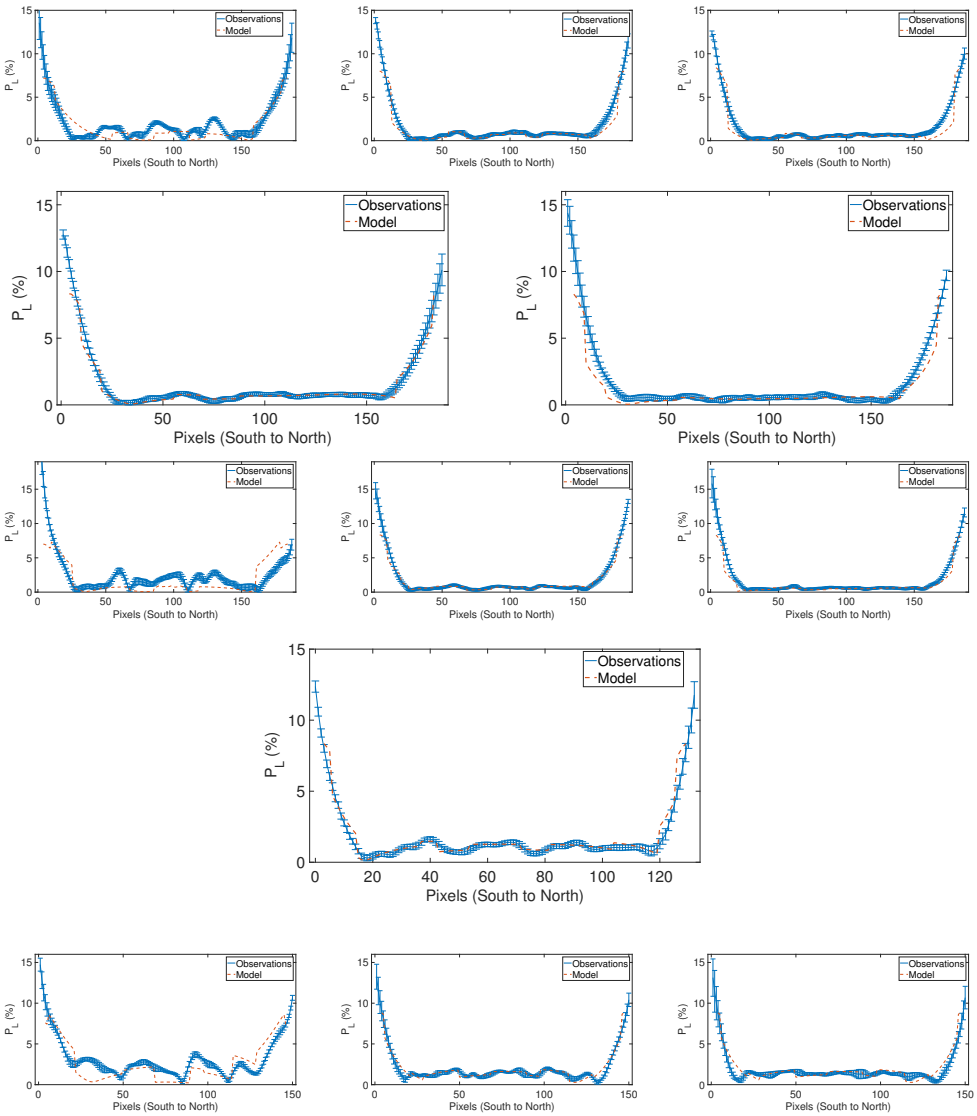

Figure 5.23: Latitudinal models of the polarisation along Jupiter's central meridian, along with the data for comparison. From top to bottom: models of IP1, IP2, IP3, IP4, and IP5. Datasets IP1, IP3, and IP5 all have models shown in B (left plot), V (middle plot), and R (right plot), IP2 has only models for V (left plot), and R (right plot), whilst IP4 has just models in the V filter shown. Credit: McLean et al. [2017], reproduced with permission © ESO.

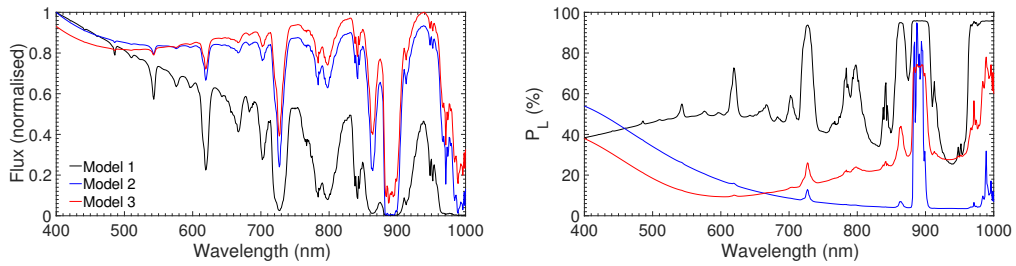

Figure 5.24: Models of the flux and degree of linear polarisation of incident starlight reflected by three Jupiter-like exoplanets, for a phase angle of 90°. Model atmosphere 1 has only molecules, model 2 is similar to model 1, but with the addition of a tropospheric cloud layer, and model 3 is similar to model 2, with the inclusion of a stratospheric haze layer. Credit: McLean et al. [2017], reproduced with permission © ESO.

that is observable from Earth [Dlugach & Mishchenko, 2005]. Observations over a wider phase angle range, and thus a higher chance of a full particle characterisation, is only completely achievable from a spacecraft orbiting Jupiter or a fly-by mission.

5.3.2 Models of signals from exoplanets

Flux and polarisation signals of Jupiter as if it were observed as an exoplanet are presented in this section. The flux and polarisation of an exoplanet would be recorded by a detector as a disk-integrated value from the visible, illuminated part of the planetary disk, depending on the locally reflected starlight across the disk and therefore on variations in atmospheric properties across the planetary disk. Models of reflected light signals from gaseous exoplanets, based on the model fits to the Jupiter observations, are shown to demonstrate both the effect of differences across the planetary disk and also to emphasise the additional information that can be gleaned from polarimetric studies.

As in Stam et al. [2004], models of the flux and polarisation of light reflected by Jupiter-like exoplanets of various configurations are presented. The models that are shown here are different to the ones shown in Stam et al. [2004] due to a slightly different atmospheric configuration used, and also the use of different cloud and haze particles. Figure 5.24 shows plots of both the flux and polarisation for three model atmospheres. The phase angle for each of the models is 90°, with the model cloud and haze particles the same as those used for the model interpretation of the observational results. Figure 5.25 shows the same models, but as a function of phase angle at a wavelength of 550 nm. The zero points in the phase angle plots are specific

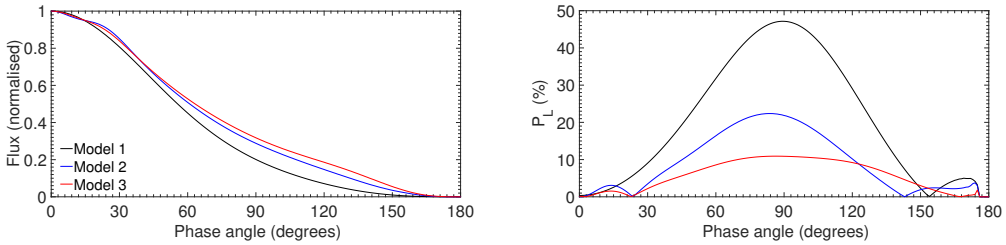

Figure 5.25: Flux and degree of linear polarisation of the three model atmospheres as a function of the planetary phase angle for a wavelength of 550 nm. Credit: McLean et al. [2017], reproduced with permission © ESO.

to the atmospheric scatterers that are present. The distance to the planetary system and the size of the planet are required in order to calculate the absolute fluxes, and these parameters can be challenging to obtain. Due to the degree of polarisation being a relative measure, it is independent of these quantities, therefore atmospheric information can be gleaned from polarimetric measurements.

Model 1 is of an atmosphere containing no cloud or haze particles, only molecular gas. The continuum flux shows a decrease as the wavelength increases, due to the decrease in the molecular scattering optical thickness towards higher wavelengths. The continuum polarisation shows a different variation with wavelength than the flux, due to a smaller Rayleigh scattering optical thickness resulting in less multiple scattering occurring, with multiple scattering tending to reduce the degree of polarisation of the reflected light. The amount of multiple scattering decreases due to increased absorption by CH_4, resulting in higher values of polarisation in the CH_4 bands [Stam et al., 1999, 2004], similar to that observed by Schmid et al. [2011].

Model 2 has the same atmospheric configuration as model 1, with the inclusion of a thick (cloud optical thickness $b^c = 50$) cloud layer in the troposphere with a cloud-top pressure of 1.0 bar. At lower wavelengths, the molecular scattering optical thickness of the gaseous atmosphere above the cloud layer is at its greatest, resulting in a lower amount of light reaching the cloud layer, and with increasing wavelength the contribution of the light scattered by the cloud particles starts to dominate for both the flux and polarisation. Increased multiple scattering within the cloud layers along with a lower degree of polarisation from light scattered by cloud particles (this can be clearly observed in Fig. 5.18) results in a decrease in the continuum polarisation. In the strong CH_4 absorption band around 890 nm, the flux and polarisation of models 1 and 2 are very similar to each other. This is due to the fact that hardly any incident stellar light penetrates deep enough into the atmosphere to reach the cloud layer, because of the high molecular absorption

optical thickness of the atmosphere that is above the cloud layer, therefore most of the light is scattered in the highest atmospheric layers.

Model 3 contains the same tropospheric cloud layer as that of model 2, with the inclusion of a haze layer in the stratosphere of optical thickness $b^{\mathrm{h}} = 0.2$, at a haze-top pressure of 0.133 bar. The polarisation values at longer wavelengths are higher for model 3 than those for model 2, and this can be attributed to a larger (absolute) degree of polarisation of light that is single scattered from the haze particle layer, which can be seen from Fig. 5.18.

Model atmosphere 3 contains a high altitude haze, therefore the light that would be observed at wavelengths where CH_4 causes absorption would not only be mainly singly scattered light, but would also contain the single scattering signature of the haze particles. Light that is singly scattered by these haze particles has a low degree of polarisation at a scattering angle of 90 degrees, therefore the polarisation in the bands is lower than that in the continuum. The polarisation at bluer wavelengths is higher than that for similar models by Stam et al. [2004] due to the use of a higher value of the complex part of the refractive index.

5.4 Discussion and summary

This chapter has presented ten polarimetric datasets from the planet Jupiter, along with some model fits to the data. Consistent trends in the polarisation for each of the imaging polarimetry datasets are observed, with higher polarisation seen in the polar regions of Jupiter, with a north-south polar asymmetry in the polarisation usually observed, which has also been found in previous studies. The two spectropolarimetric datasets show an increase in polarisation at bluer wavelengths; this is mainly due to the dominance of Rayleigh scattered light at these wavelengths, which is known to cause a higher polarisation than light scattered from larger particles. Models of the spectropolarimetric data were able to replicate the general trend of polarisation as a function of wavelength, and also reproduced the decrease in polarisation observed across the strong methane absorption band at approximately 720 nm for the December 2014 dataset.

Model fits to the imaging polarimetry data are able to reproduce the observed polarisation across latitude in the V and R filters, but these models are not consistent with those for the B filter results. The solution to this would most likely be to use different shaped particles, since spherical particles could be a relatively poor approximation to the shape of the particles that are present in the Jovian atmosphere.

Increased absorption at bluer wavelengths may also be a cause of the difference in the polarisation in the B-band data. Another limiting factor, which has been noted by previous studies, is that to fully quantify the properties of the particles in the atmosphere of Jupiter, data taken at a wider range of phase angles must be used, which was the case for the pioneering study of the clouds of Venus by Hansen & Hovenier [1974]. Observing Venus at the full phase angle range is possible for Earth-based observations of course. The study of the flux and degree of polarisation of exoplanets has, despite other challenges, the advantage that the full phase angle range is accessible, although dependent on the orbital inclination of the observed planet. Model results of Jupiter-like exoplanets have been presented that show the greater values of polarisation observed at a phase angle of 90°, and the differences arising between atmospheres that contain cloud and/or haze particles.

Recent advances in available telescope and instrument technology have presented an opportunity for polarimetric observations from ground-based telescopes to provide constraints on the scattering properties of planetary atmospheres. Data from just a 1 m telescope are able to provide sufficient signal and instrumental precision to be able to produce polarimetric maps, which match up with data that have previously been obtained from larger telescopes and more highly tested instruments. To be able to further constrain the properties of the scattering particles in the atmosphere of Jupiter, more observations at higher phase angles and in different wavelength bands are required. NASA'S JUNO mission, which achieved Jupiter orbital insertion in July 2016, does not include a polarimeter, and neither does ESA's JUICE mission to Jupiter. Polarimetric optics lead to a larger instrumental payload, and are not always considered, perhaps in part due to the lack of understanding of the full potential that polarimetry has. Ultimately, one of the goals of this chapter and thesis is hopefully to emphasise the power that polarimetry has. The study of the scattering layers of planetary atmospheres in the solar system also has an important application for the study of exoplanets, since studying the solar system should ultimately enable us to be able to further constrain models of observations of light reflected by the atmospheres of exoplanets.

Chapter 6

Saturn, its rings, and Titan

Abstract

This chapter presents several imaging polarimetry and spectropolarimetry datasets of Saturn, its rings, and Titan. The difference in polarisation and position angle between the planet and the rings is clearly seen, along with signatures in the polarisation in prominent methane bands. Model fits to the Saturn spectropolarimetry data were attempted by varying the cloud and haze height and optical thickness, and these models can give an approximate fit to the atmospheric conditions on Saturn at the time of observation. Models of Saturn-like exoplanets are also shown, investigating the potential application polarimetry has to the study of Saturn-like exoplanets.

6.1 Introduction

The polarimetric behaviour of Saturn is in many ways similar to that of Jupiter. Both of the gas giants appear to have a thick tropospheric cloud layer composed of relatively large particles, overlain with a thin stratospheric haze layer containing small particles [West et al., 2015]. However, one of the major differences between Jupiter and Saturn is that less banded structure can be seen in Saturn. Since Saturn is an outer planet, the phase angle range at which it can be observed from Earth is limited to below 6°. Several space missions have directly visited, or flown past Saturn, and have taken data in larger phase angle ranges ($\approx$ 30°-150°). Saturn is thought to have the same three main cloud decks as in Jupiter's atmosphere [Atreya et al., 1999], but since the temperature on Saturn is lower than on Jupiter these lie

at a deeper pressure level in Saturn's atmosphere [Irwin, 2003].

Lyot [1929] was the first to publish polarimetric data for Saturn, and found a variation with phase angle of the ring polarisation, and atmospheric polarisation. Saturn's disk was shown by later studies to have a strong radial limb polarisation of $> 3\%$ near 0° phase angle in the UV at 370 nm by Hall & Riley [1974], who also observed less than 1% polarisation in the visual, which was primarily in the N-S direction. Visual polarisation measurements have shown variations over time, which may be seasonal. Like for Jupiter, the poles have usually been shown to have higher polarisation than the lower latitudes, but this is not always the case [see Kemp & Murphy, 1973; Dollfus, 1996].

The most recent polarimetric study of Saturn was that of Schmid et al. [2011], who found that the south pole of Saturn showed a polarisation of 1.0 -1.5%, with the value of polarisation decreasing with wavelength, with some enhancement of the polarisation in the absorption bands. This was explained as being due to a stratospheric haze layer enshrouding the planet, which would reduce the amount of photons received from the methane in the tropospheric regions.

Pioneer 11 and Voyager 2 are both space missions to have visited Saturn. Pioneer 11 results are discussed by both Gehrels et al. [1980] and Tomasko & Doose [1984]. The polarisation data along with methane band imaging showed that the equatorial zone contains a tropospheric cloud layer around the 150 mb level. Deeper clouds were shown to be present at latitudes further away from the equatorial band. Model fits by Tomasko & Doose [1984] estimated a cloud-top height of 270 ± 80 mb.

The Cassini spacecraft is the most recent space mission to visit the Saturn system, and arrived in 2004. Cassini polarisation images show a banded structure, and the southern (summer) hemisphere was found to be, on average, weakly negatively polarising, but high southern latitudes were found to have positive polarisation [West et al., 2015]. A detailed discussion on the findings of Cassini, along with some of the polarisation results can be found in West et al. [2009]. Polarisation images of the northern polar region of Saturn obtained with Cassini in the near-infrared are shown in Figure 6.1, revealing the familiar hexagon and polar vortex, with clear structural differences inside and outside of the hexagon region.

Fitting an exact model solution to the cloud and haze particles of Saturn would require knowledge of the single scattering behaviour over the full phase angle range, which is not possible from Earth, where the viewing geometry permits phase angles of $\leq 6^\circ$ to be observed. The orbital period of Saturn is 29.48 years, so to understand the relation between seasonal changes and the physical properties of the

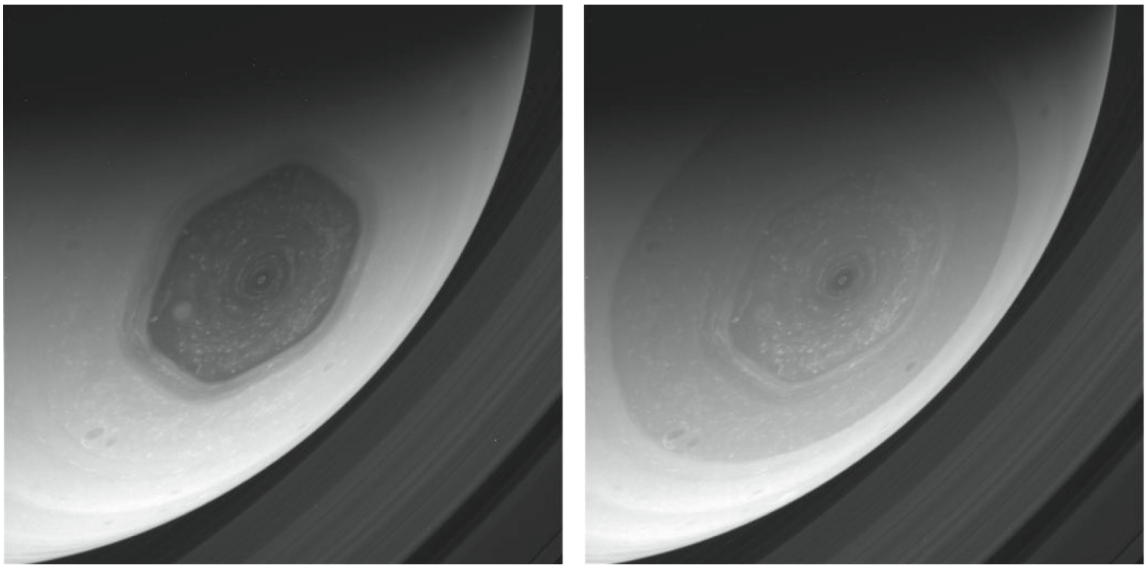

Figure 6.1: Cassini images of Saturn taken 90 s apart in a 935 nm filter, coupled with polarisers aligned with the electric field vector parallel (left image), and perpendicular (right) to the scattering plane. The hexagon and polar vortex of Saturn's northern polar region can clearly be seen, with differences in structure inside and outside the hexagonal region present. Figure from West et al. [2015].

atmospheric constituents, the atmosphere must be studied frequently over a wide phase-angle range over the course of several decades. Previous observational studies [Muñoz et al., 2004; Fletcher et al., 2011; Karkoschka & Tomasko, 2005; Roman et al., 2013; Sromovsky et al., 2013], have alluded to the presence of a cloud deck at higher pressures deep in the atmosphere, possibly made of NH_3, NH_4SH, or a mixture of both [Atreya & Wong, 2005; Barstow et al., 2016], with tropospheric and stratospheric hazes located above it. The properties of the haze particles are still unknown, and recent studies attempting model fits to Cassini data have found the problem to be highly degenerate [Fletcher et al., 2011; Barstow et al., 2016]. Stam et al. [2001] used an inversion algorithm to fit near infrared observations of Saturn, and their data were fit by two haze layers, one in the troposphere at ≈ 200 mbar, and one in the stratosphere at ≈ 20 mbar, with a deeper cloud layer below the tropospheric haze relatively free of scatterers.

Barstow et al. [2016] present four different types of model atmosphere as a fit to spectroscopic results from Cassini taken with the VIMS (Visual and Infrared Mapping Spectrometer) instrument in the 4.6–5.2 μm spectral range. Their best model has a deep cloud base made of NH_3 or NH_4SH, with a particle size of between 1-10 μm, and resides at an atmospheric height of between 1.5 and 2.7 bar. Fletcher

et al. [2011] found that a compact cloud layer in the troposphere with a finite extension provided a better model fit than an extended semi-infinite cloud deck. A tropospheric haze was also found to fit the data quite well, as was also the case for Roman et al. [2013], who fitted models to Cassini ISS data, taken in the UV to near infrared spectral range. Barstow et al. [2016] found the tropospheric haze layer to extend between 0.1 and 0.6 bar, with an effective particle radius of 2μm, which was suggested by Roman et al. [2013], and is also consistent with the findings of Karkoschka & Tomasko [2005], from fitting HST imaging data. The real part of the refractive index used for this haze is 1.43 at visible wavelengths, which is compatible with Martonchik et al. [1984] for the values of ammonia ice.

Whilst all four of the outer planets are now known to have rings systems, the rings of Saturn are the most prominent of all. Regolith much larger than the wavelength has been found through polarimetric studies, along with a small grain component that has been shown from observations at shorter wavelengths [West et al., 2015]. The degree of linear polarisation in the phase angle range 0 to 6° has a negative branch with a slope proportional to the albedo, similar to the polarimetric behaviour of asteroids and satellites [West et al., 2015].

This chapter presents three epochs of spectropolarimetric data for Saturn, two epochs of spectropolarimetric data of the rings, and three epochs of spectropolarimetry data for Titan. Imaging polarimetry in continuum and methane filters are also shown. The spectropolarimetric data were obtained with ISIS in January 2015 by Stefano Bagnulo (programme ID W/2014B/30), and in February 2015 by Alex Martin (programme ID W/2015A/28). The imaging polarimetric data were obtained with FoReRo2 by Galin Borisov in July 2016. A major aim of this work is to explore the additional information that can be gleaned from combining spectropolarimetric measurements with spectroscopy, and as well as fitting models to the data there are model computations of signals from Saturn-like exoplanets presented, showing how different particle types in the cloud and haze layers can change the signal.

This chapter is structured as follows: Section 6.2 gives details of the observations and presents the results. Section 6.3 describes and presents the atmospheric models used to interpret the observations, along with some sample results showing what could be observed from Saturn-like exoplanets. Finally, Section 6.4 summarises and concludes the findings of this study.

6.2 Observations and results

Table 6.1 shows the log of the observations of Saturn and its rings, and is organised as follows: column one assigns the name to each dataset, column two gives the dates of the observations, and column three the Universal Time (UT) in the middle of each observing block. Column four gives the exposure time of an individual frame, in seconds. Column five gives the name of the instrument, and column six lists the filter or grism used. Column seven gives the slit width, column eight the spectral resolution, and column nine the signal-to-noise ratio. Column ten then gives the phase angle, α, at the time of observation. Columns eleven through thirteen give other planetary parameters at the time of observation, namely: angular diameter at the equator in arcseconds, planetary north-pole position angle relative to the north celestial meridian in degrees, and the distance to Saturn's north pole from the centre of the disk, in arcseconds on the sky[1].

In addition to Saturn and the rings, both unpolarised and polarised standard stars were observed, along with a solar analogue. The purpose of observing the unpolarised standard star was to quantify the instrumental polarisation, which was found to be negligible, and within the error bars (see Section 3.3.3.3). The polarised standard star was observed in order to give the offset of the position angle of polarisation; details of how this correction was performed are given in Section 3.3.

[1]Planetary parameters were calculated using JPL HORIZONS: http://ssd.jpl.nasa.gov/?horizons

Table 6.1: Observing log for Saturn and the rings. Column meanings are given in the text.

Dataset	Date	UT	ET(s)	Inst.	Filter	SW(″)	SR(nm)	S/N	α (°)	AD(″)	NPA(°)	NPD(″)
Saturn SP1	07/01/2015	07:14	20	ISIS	R300B	1	2	1400	4.02	15.64	+2.23	+6.15
Saturn SP1	07/01/2015	07:12	3	ISIS	R158R	1	2	1150	4.02	15.64	+2.23	+6.15
Saturn SP2	03/02/2015	07:07	1.5	ISIS	R158R	1	2	930	5.35	16.22	+2.50	+6.36
Saturn SP2	03/02/2015	07:21	20	ISIS	R600B	1	2	2660	5.35	16.22	+2.50	+6.36
Saturn SP3	04/02/2015	06:47	1.5	ISIS	R158R	1	2	900	5.38	16.25	+2.50	+6.36
Saturn SP3	04/02/2015	06:51	20	ISIS	R600B	1	2	1760	5.38	16.25	+2.50	+6.36
Rings SP1	07/01/2015	07:22	6.0	ISIS	R158R	1	2	1380	4.02	N/A	N/A	N/A
Rings SP1	07/01/2015	07:27	20	ISIS	R300B	1	2	1670	4.02	N/A	N/A	N/A
Rings SP2	04/02/2015	07:02	1.5	ISIS	R158R	1	2	1230	5.38	N/A	N/A	N/A
Rings SP2	04/02/2015	07:05	20.0	ISIS	R600B	1	2	2830	5.38	N/A	N/A	N/A
IP1	11/07/2016	21:18	2	FoReRo2	IF590	N/A	N/A	300	3.69	18.01	+3.32	+6.97
IP1	11/07/2016	21:33	2	FoReRo2	IF620	N/A	N/A	440	3.69	18.01	+3.32	+6.97
IP1	11/07/2016	21:48	2	FoReRo2	IF642	N/A	N/A	350	3.69	18.01	+3.32	+6.97

6.2.1 ISIS Spectropolarimetry of Saturn

Spectropolarimetry was carried out with ISIS on the WHT, on three dates. The data reduction for these data are described fully in Section 3.3.3.3. A one-dimensional reduction was used for all ISIS datasets, except for dataset SP3 in both the blue and red arms. The slit position for each set is different, no set contains the entire planet in the slit.

Figures 6.2a, 6.2d, and 6.2g show the reflectance spectrum of Saturn for each dataset. The reflectance spectra all show absorption features especially prominent in the strong methane bands around 620 nm, 725 nm, and 890 nm. The absorption bands and the slope of the curves are consistent with previous measurements of the reflectance of Saturn [Karkoschka, 1998] for the entire disk, differences would be expected when sampling a specific region of the planet, and from short-term and long-term seasonal variations.

The corresponding plots of the degree of linear polarisation for each dataset are shown in Figs. 6.2b, 6.2e, and 6.2h, and the polarisation angle spectra are shown in Figs. 6.2c, 6.2f, and 6.2i. All of the spectropolarimetry plots of Saturn have a rebinned spectral resolution of 2 nm, in order to emphasise the features in the spectrum, and to reduce the noise. The spectropolarimetry datasets all show similar trends: an increase in polarisation from the UV up till around 440 nm, and then a steady decrease. The reason for the lower polarisation in the UV is due to an increase in scattering optical thickness at these wavelengths. This increased scattering optical thickness increases the multiple scattering, which lowers the degree of polarisation. However, absorption serves to increase the polarisation, since it decreases the multiple scattering, and this might explain why the polarisation increases below 500 nm.

The data presented here are similar to the results presented by Schmid et al. [2011], who reported a degree of linear polarisation of 1.0–1.5% at the south pole of Saturn, with the polarisation decreasing with wavelength, and with some enhancement of the polarisation in the methane bands. The reason put forward by Schmid et al. [2011] for the enhancement in the methane bands is the presence of a stratospheric haze layer enshrouding the planet at the time of observation, thus more singly-scattered light from the methane would be received resulting in a higher degree of polarisation at these wavelengths. This may be the case for the observations presented here: clear enhancements of polarisation in the methane bands around 620 nm, 725 nm and 890 nm are visible in dataset SP2 (Fig. 6.2e). The reason that

the methane shows up more clearly in this dataset than in the others is likely due to the local atmospheric configuration at the time of observation: a stratospheric haze layer could indeed result in a higher degree of polarisation in the methane bands.

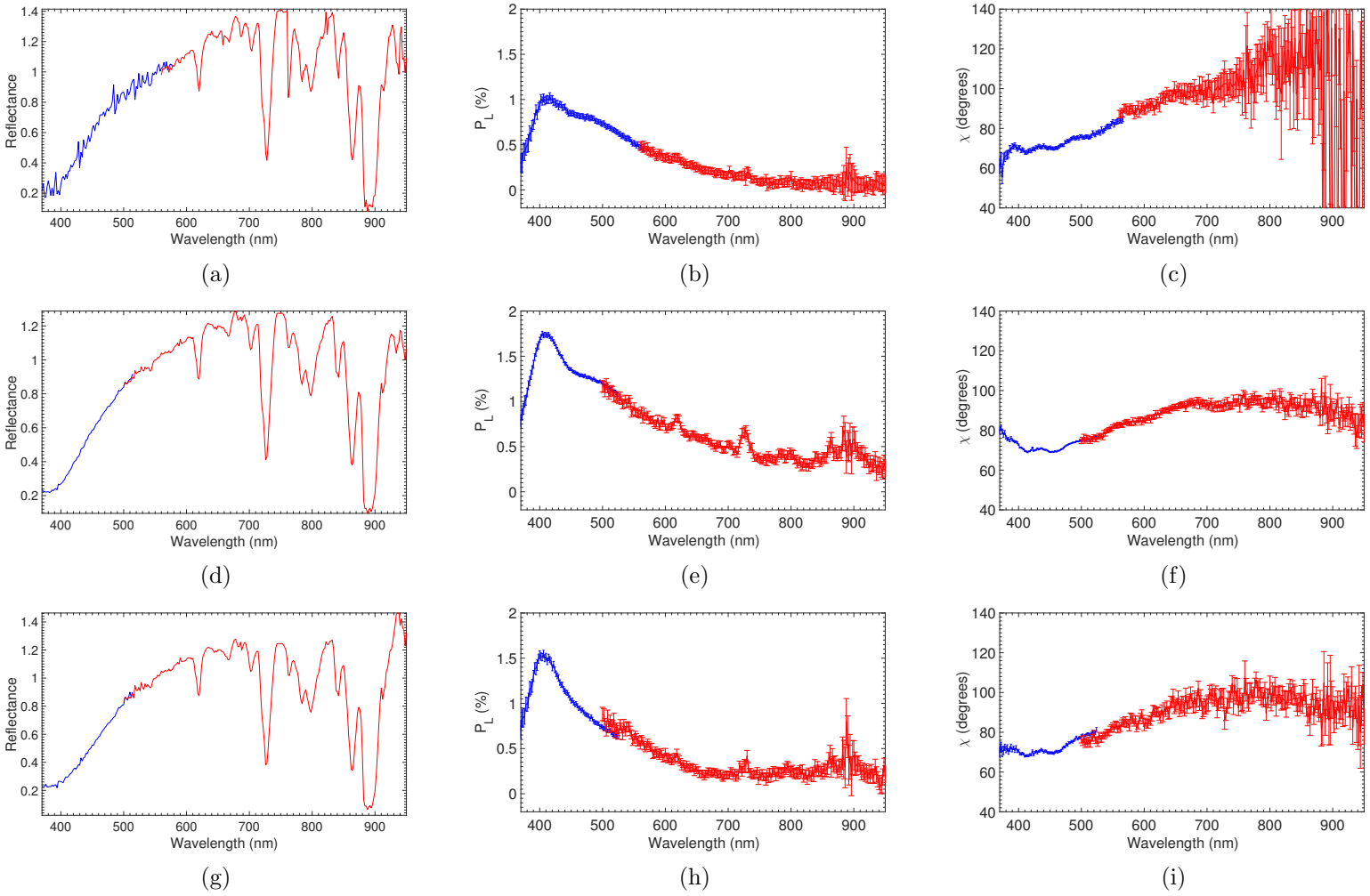

Figure 6.2: Plots of reflectance, degree of linear polarisation, and position angle for all three Saturn spectropolarimetry datasets. The top row shows the results for dataset SP1, the middle row SP2, and the bottom row SP3.

6.2.2 Imaging polarimetry with ToPol

Polarimetric observations of Saturn were taken in the U, B, V, R, and I filters for several epochs at various times throughout 2015 and 2016. An example of a raw CCD image of Saturn is shown in Fig. 6.3. Bias and dark frames were observed for each filter in addition to the science frames. Polarised and unpolarised standard stars with known values were also observed, in order to quantify the instrumental polarisation and position angle offset. The steps in the data reduction are explained in Section 3.3.5.2.

As for the Jupiter data described in Chapter 5, the ToPol data reduction proved challenging due to the misalignments and distortions present in the raw data. A great deal of time was spent trialling various methods of aligning the Jupiter images, and eventually a method was devised that involved fitting an ellipse to the individual images in order to align them. There was an attempt to account for the distortion, but as shown in Section 3.3.5.2 this proved to introduce more error. Unfortunately, the distortion proved too significant for the Saturn data, perhaps due to the combined planet+ring system being more elongated than Jupiter, and spread over more of the CCD. As for Jupiter, much time was spent attempting to align the Saturn images. As of writing, the attempt to correct for the distortion is still ongoing, and the ToPol Saturn images will hopefully be presented in a future publication.

6.2.3 ISIS spectropolarimetry of Saturn's rings

These data were obtained with ISIS on the WHT in January and February of 2015 (see Table 6.1). The data reduction for these data are described fully in Section 3.3.3.3. A one-dimensional reduction was used for each dataset. Figures 6.4 and 6.7 show the reflectance spectrum of Saturn's rings for each dataset. Each plot shows a mostly featureless curve gently increasing from the blue to the red, and are similar to previous measurements of the reflectance of the rings of Saturn [Clark, 1980] who show a sharper increase from the blue to the red. Plots of the degree of linear polarisation for each dataset are shown in Figs. 6.5 and 6.8, with the polarisation angle spectra shown in Figs. 6.6 and 6.9. All of the spectropolarimetry plots of Saturn's rings have a rebinned spectral resolution of 2 nm, in order to emphasise the features in the spectrum, and reduce the noise.

The polarisation of the rings is shown to be less than half of a percent and featureless, and is similar to what has been reported in previous studies. The position angle is

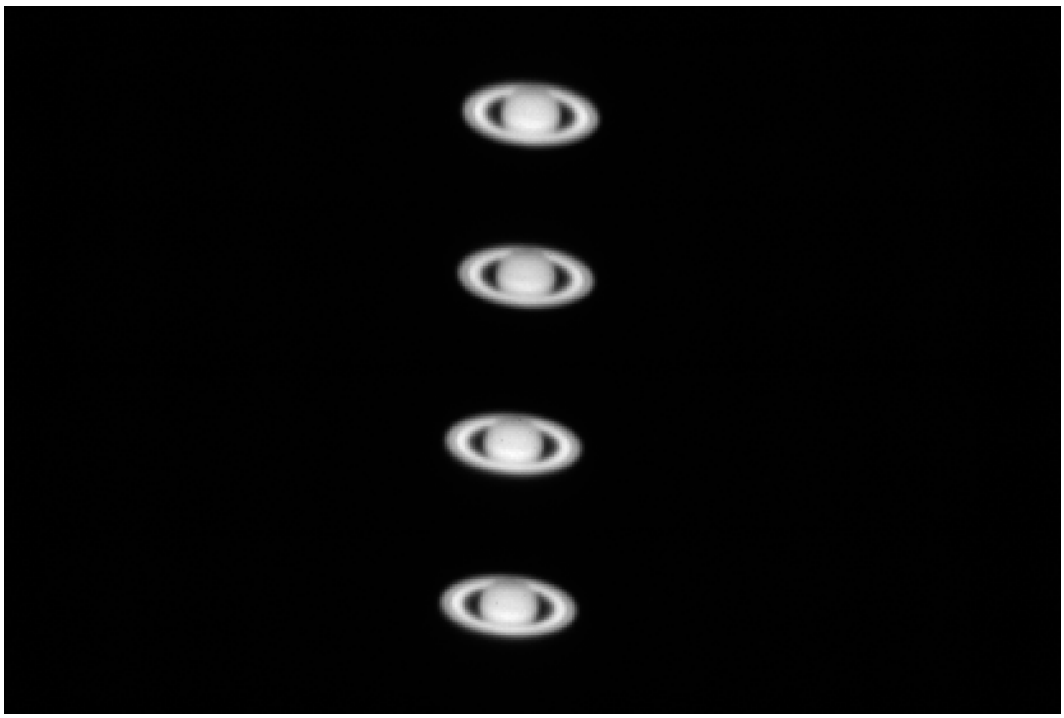

Figure 6.3: ToPol CCD image of Saturn in the V filter. From the top down, the four beams are proportional to: $F + Q$, $F - Q$, $F + U$, $F - U$.

directed parallel to the scattering plane (close to zero degrees) which is quite different to the observations of Saturn, with Figs. 6.2c, 6.2f, and 6.2i showing a position angle clearly perpendicular to the scattering plane for the planet. As mentioned in Section 6.1, previous studies of the polarisation of Saturn's rings have shown the direction of polarisation to be parallel to the scattering plane in a phase angle range from 0 to 6°, with observed properties similar to those for asteroids and planetary satellites [West et al., 2015].

6.2.4 FoReRo2 imaging polarimetry

The imaging polarimetry was carried out with FoReRo2 in three filters: the continuum 590 nm and 642 nm filters, and the 620 nm filter, which is a known wavelength of strong methane absorption. An image of Saturn on the Rozhen CCD is shown in Figure 6.10. The data reduction steps are described in Section 3.3.5.1.

Figures 6.11, 6.12, and 6.13 show the maps of flux and linear polarisation calculated from observations in the 590 nm, 620 nm, and 642 nm, respectively. The flux maps are given in normalised units, and the degree of linear polarisation is shown in units

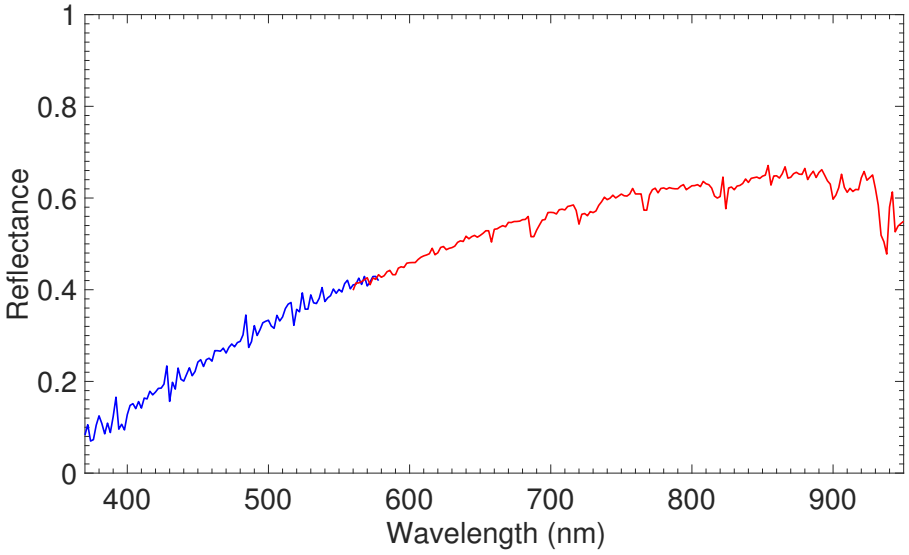

Figure 6.4: Reflectance for rings dataset SP1.

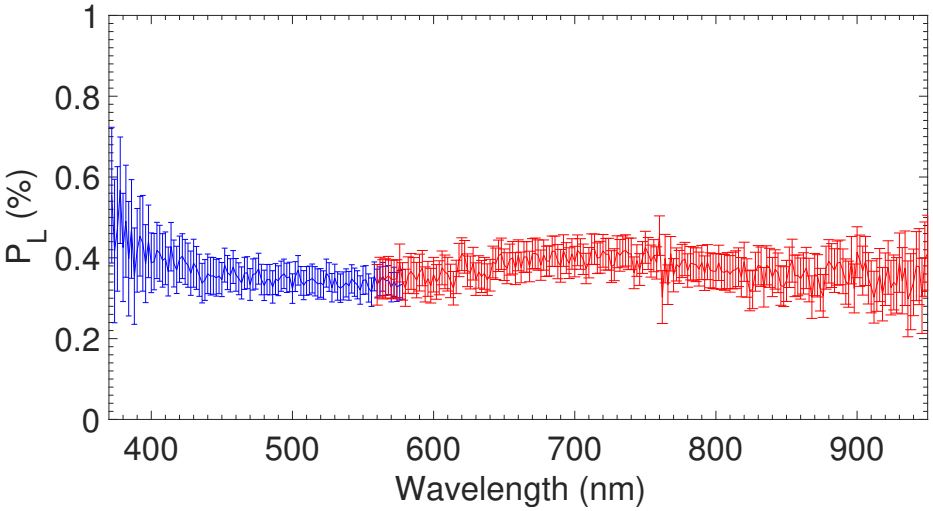

Figure 6.5: P_{L} for rings dataset SP1.

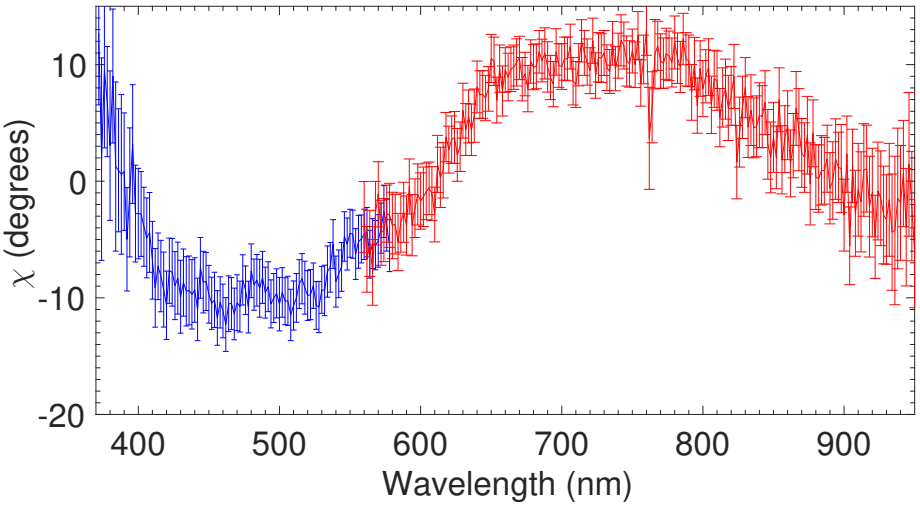

Figure 6.6: Position angle χ for rings dataset SP1.

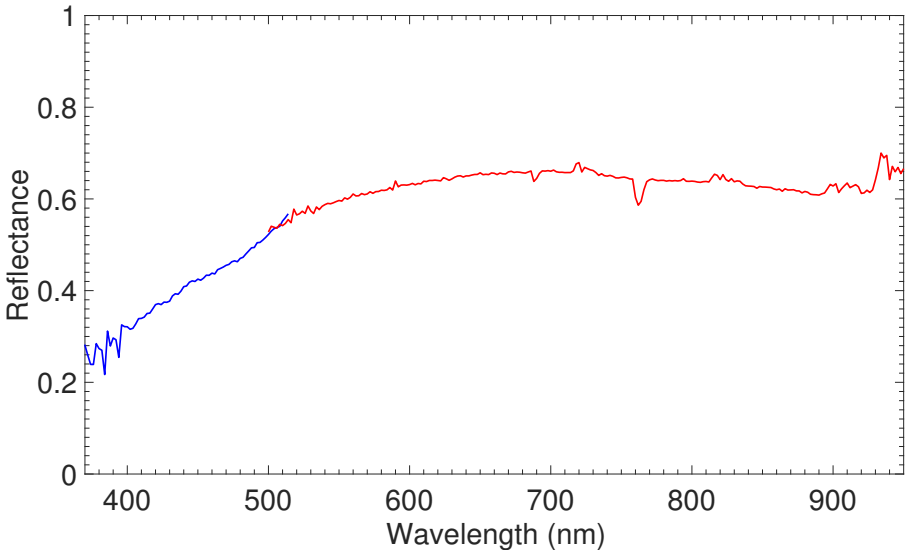

Figure 6.7: Reflectance for rings dataset SP2.

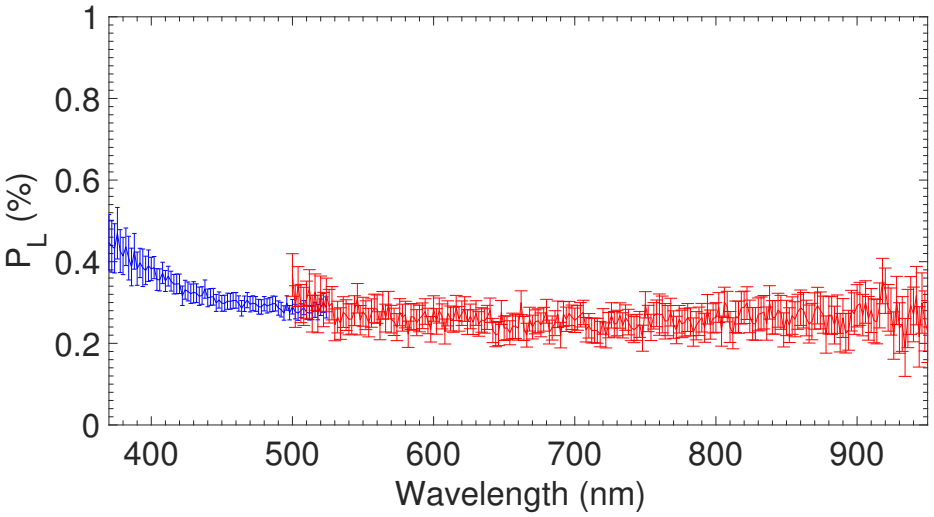

Figure 6.8: P_{L} for rings dataset SP2.

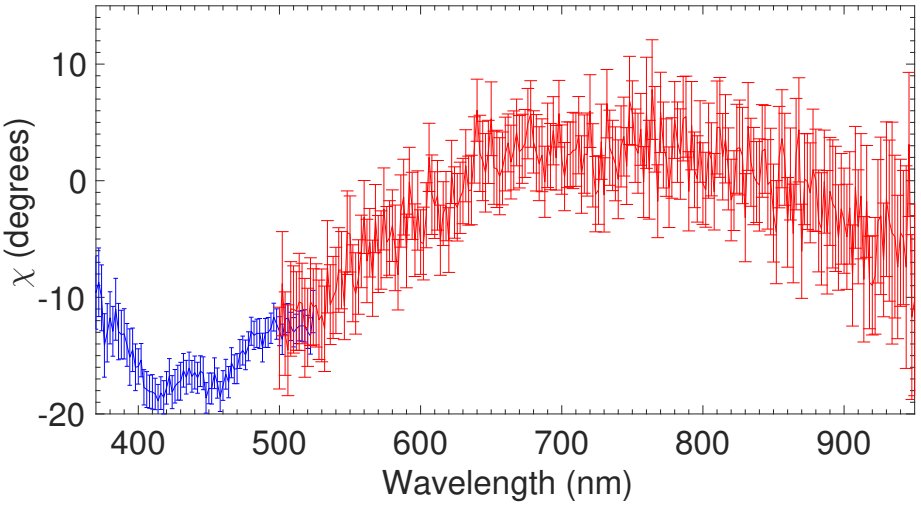

Figure 6.9: Position angle χ for rings dataset SP2.

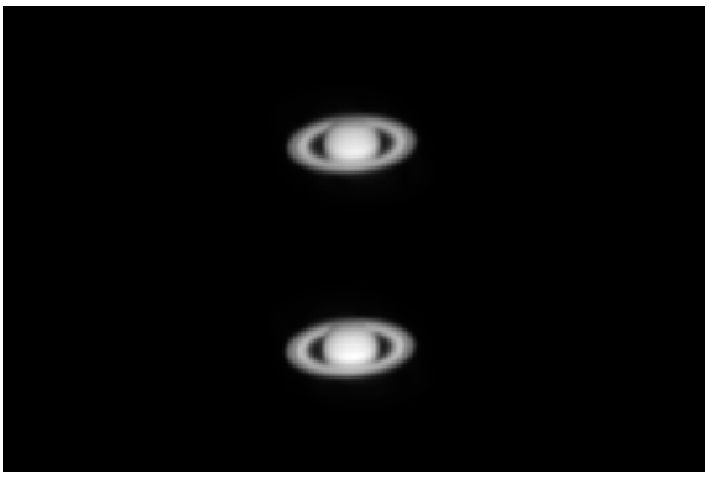

Figure 6.10: FoReRo2 CCD image of Saturn in the 620 nm filter. From the top down, the two beams are proportional to: $F + Q$, $F - Q$.

of percent, with the scale saturated at 1%. The maps of P_{L} are shown with direction arrows superposed showing the position angle of polarisation. The arrows do not have an arrowhead since the direction of polarisation only varies between 0° to 180° and angle 0 (180)° is taken to be the vertical direction. A position angle for every pixel is not indicated, as this would clutter the image, so a "rebinned" position angle is shown for clarity.

The goal of taking these data was to detect either the increase or decrease in polarisation that can often result from the presence of methane in a planetary atmosphere. There is no clear enhancement or decrease of the polarisation in the 620 nm filter compared with the continuum filters. It can be seen from the spectropolarimetric observations of Saturn though that the presence of methane is not always clear from the linear polarisation spectra (see Figs. 6.2b, 6.2e, and 6.2h). The contrast between the rings and the planet can be seen in all images, and the position angle can be clearly seen to change from near perpendicular to the scattering plane over the planet, and parallel to the scattering plane on the rings. The difference in the position angle between the planet and the rings is consistent with the spectropolarimetry data, and what has been reported in previous literature (see Section 6.2.3). These data were taken when Saturn was near opposition, and the polarisation is thus very low across both the planet and the rings.

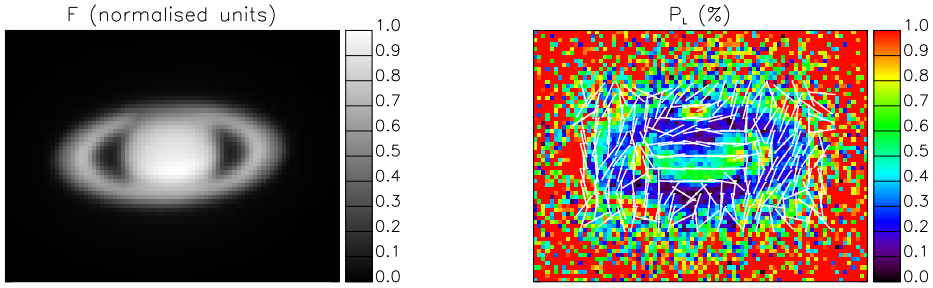

Figure 6.11: Flux, P_{L}, and χ for the 590 nm filter.

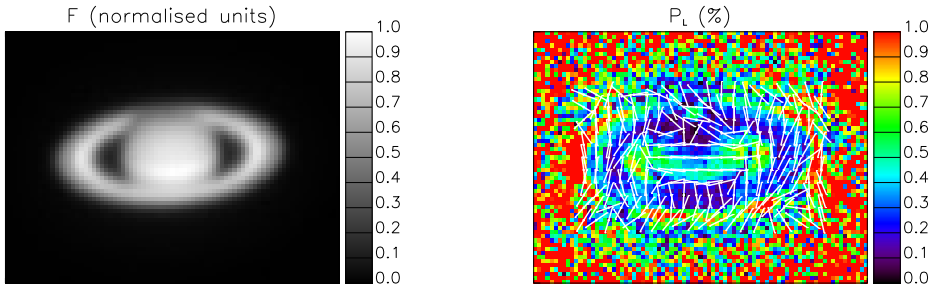

Figure 6.12: Flux, P_{L}, and χ for the 620 nm filter.

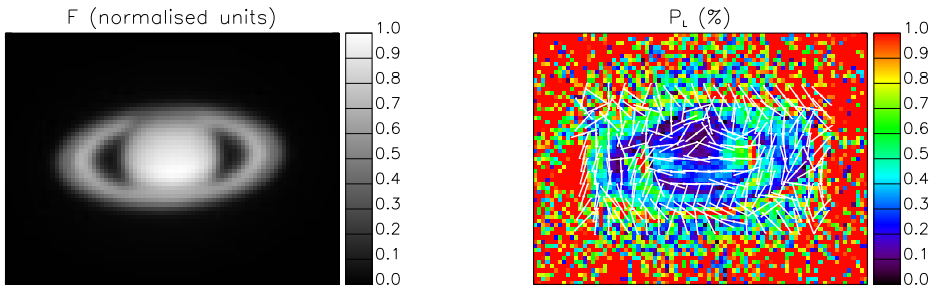

Figure 6.13: Flux, P_{L}, and χ for the 642 nm filter.

6.2.5 ISIS spectropolarimetry of Titan

Table 6.2 gives the observing log for all of the spectropolarimetry datasets of Titan. Column one assigns the name to each dataset, column two gives the dates of the observations, and column three the Universal Time (UT) in the middle of each observing block. Column four gives the exposure time of an individual frame, in seconds. Columns five lists the grism used for each of the observations. Column six then gives the phase angle, α, at the time of observation. Columns seven through nine give other planetary parameters at the time of observation, namely: angular diameter at the equator in arcseconds, planetary north-pole position angle relative to the north celestial meridian in degrees, and the distance to the planetary north pole from the centre of the disk, in arcseconds on the sky[2]. Three datasets of Titan spectropolarimetry were obtained over the course of three observing epochs, with two in both the blue and red arms of ISIS, and one set in just the red arm. The observers of dataset SP1 are Stefano Bagnulo, Will McLean, and Aaron Stinson (programme ID W/2014A/5), with SP2 observed by Stefano Bagnulo (programme ID W/2014B/30) and dataset SP3 by Alex Martin (programme ID W/2015A/28). Section 1.3.3 presents a detailed overview of previous studies of Titan.

Plots of the reflectance and degree of linear polarisation of Titan for each of the three datasets are shown in Figure 6.14, Figure 6.15, and Figure 6.16. The reflectance spectra are similar to that reported by Karkoschka [1998], with an increase from the blue to the red, showing methane absorption in the three prominent methane absorption bands, which is expected given that Titan's atmosphere is known to contain methane at concentrations of over 1% [Bézard et al., 2014]. The spectropolarimetry datasets are rather featureless, with low values of polarisation which is expected for the low phase angles, and higher polarisation towards the blue end of the spectrum. Dataset SP3 of Titan especially shows increased polarisation at bluer wavelengths, perhaps due to the predominance of Rayleigh scattering at these wavelengths.

Bazzon et al. [2014] report values between 0–0.2% for the total degree of linear polarisation in filters with effective wavelength between 448 and 762 nm. For a filter with effective wavelength 341 nm the polarisation was found by Bazzon et al. [2014] to be quite higher, at almost 1%. The phase angle for their observations was 1.8°, which is lower than for the ones presented here. Taking the phase angle difference into account, the slightly higher values obtained in this study are consistent with that found by Bazzon et al. [2014].

[2]Planetary parameters were calculated using JPL HORIZONS: http://ssd.jpl.nasa.gov/?horizons

Table 6.2: Observing log for the Titan spectropolarimetry datasets, with the column meanings explained in the text.

Dataset	Date	UT	ET (s)	Grism	α (°)	AD ($''$)	NPA (°)	NPD($''$)
SP1	12/03/2014	05:52	60	R300B	5.07	0.76	+1.38	0.35
SP1	12/03/2014	06:00	10	R158R	5.07	0.76	+1.38	0.35
SP2	06/01/2015	07:25	20	R158R	3.96	0.67	+2.38	0.30
SP3	05/02/2015	06:48	40	R158R	5.42	0.70	+2.68	0.32
SP3	05/02/2015	07:06	180	R600B	5.42	0.70	+2.68	0.32

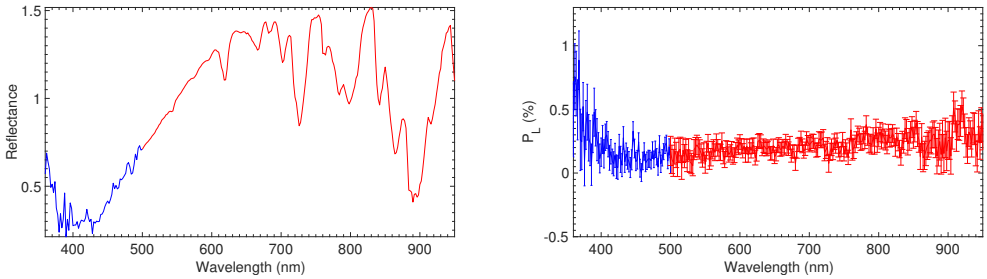

Figure 6.14: Reflectance spectrum and P_{L} of dataset Titan SP1.

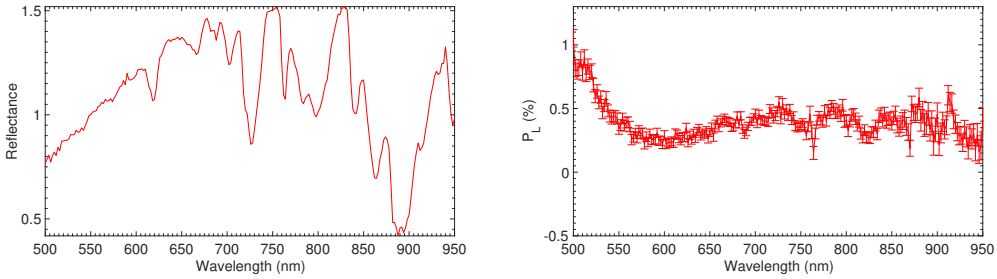

Figure 6.15: Reflectance spectrum and P_{L} of dataset Titan SP2.

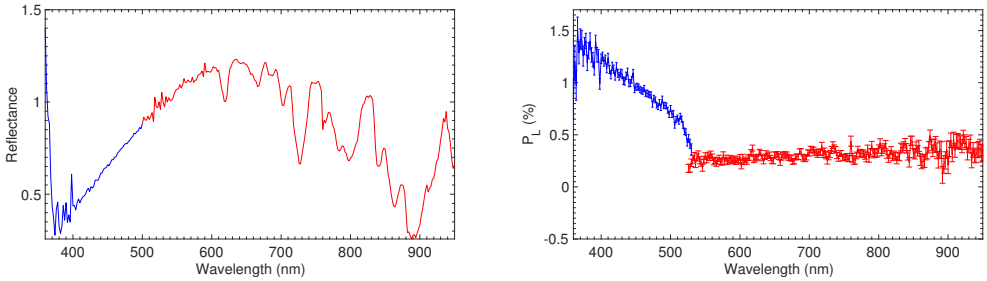

Figure 6.16: Reflectance spectrum and P_{L} of dataset Titan SP3.

6.3 Theoretical modelling

In order to interpret the Saturn data presented in the previous section, numerical models of the polarisation of the reflected light were carried out, using the adding-doubling radiative transfer code described in Section 2.3. The modelling was achieved by considering the atmosphere of Saturn as constructed from parallel, horizontally homogeneous layers, with a pressure profile as in Stam et al. [2004]. Each layer in the atmosphere contains hydrogen, helium, and methane, with some layers also containing clouds and hazes of varying thickness. The microphysical properties of the cloud and haze particles were varied, along with the height in the atmosphere of the different layers, in order to try and reproduce the observed variation of polarisation in the spectropolarimetry data. The modelling was carried out for spherical cloud and haze particles, described by Mie theory. Models of the flux and linear polarisation of Saturn-like exoplanets are also presented.

6.3.1 Spectropolarimetry models

Single scattering plots of the flux and degree of linear polarisation of the cloud and haze particles, along with Rayleigh scattering plots, are shown in Figure 6.17. Each model atmosphere used has 20 layers, and is based on the atmospheric profile of Stam et al. [2001]. All models presented have a tropospheric cloud layer, and two haze layers: one in the troposphere, and one in the stratosphere, with a schematic of the model atmosphere shown in Fig. 2.4b

The cloud model particles have $r_{\text{eff}} = 0.50\,\mu$m, and $v_{\text{eff}} = 0.05$, with a refractive index of 1.42 and an imaginary part of 0.015. The tropospheric haze particles have $r_{\text{eff}} = 0.60\,\mu$m, and $v_{\text{eff}} = 0.05$, with a refractive index of 1.50 and an imaginary part of 0.001. The stratospheric haze particles have $r_{\text{eff}} = 0.20\,\mu$m, and $v_{\text{eff}} = 0.05$, with a refractive index of 1.50 and an imaginary part of 0.001. The refractive index of the haze is that determined for Jupiter by Stoll [1980], who modelled Pioneer observations of the polarisation of Jupiter and attempted to constrain the cloud and haze particle properties. The refractive index is assumed to be non-varying with wavelength in the model fits. The mean particle size is thought to vary with latitude, but this study considers a constant size, since the slit samples a specific region of the planet. Particles with different effective radii and size distribution were trialled, with the ones used in the models giving the closest fit to the data.

When modelling the polarisation, it proved challenging to achieve the higher values at the blue end of the spectrum whilst preserving the lower values in the red. To

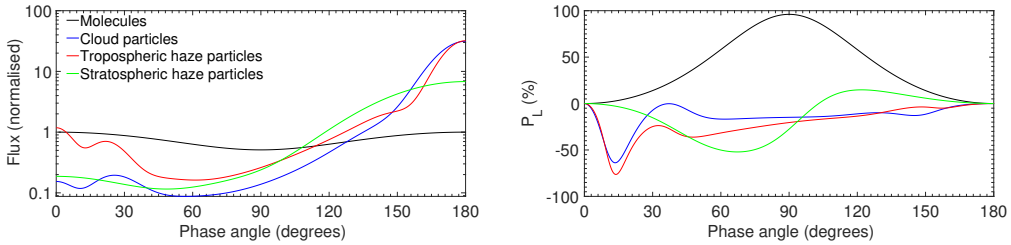

Figure 6.17: Single scattering flux and linear polarisation of the cloud and haze particles at 550 nm along with Rayleigh scattering curves. The phase angle is $180° - \Theta$, with Θ the single scattering angle.

account for this, a value of molecular absorption was added into the atmospheric model in several atmospheric layers, and can be seen in the figures presented in this section to have varying degrees of success when attempting to reproduce the observed values of reflectance and polarisation.

Models of the reflectance and degree of polarisation for dataset SP1 are shown in Figure 6.18 and Figure 6.19, respectively. The tropospheric cloud layer has cloud-top pressure 1.778 bar, and optical thickness 50. Haze type one lies at haze-top pressure 0.316 bar with optical thickness 0.15, and haze type two resides at haze-top pressure 0.100 bar with optical thickness 0.6. The reflectance model reproduces the increase in flux from the blue to the red with absorption features also present, albeit not the same shape nor as deep as those in the data. The model fit to the polarisation spectrum replicates the rise in polarisation from the UV to the blue, then the drop-off and decrease towards redder wavelengths, fitting the spectrum very closely from 550 nm to 950 nm. The slight bump in polarisation at 890 nm due to methane absorption is also reproduced in the model fit. Several values of molecular absorption were trialled in an attempt to interpret the values in the near-UV and blue, with the best result shown here.

Models of the reflectance and degree of polarisation for dataset SP2 are shown in Figure 6.20 and Figure 6.21, respectively. The tropospheric cloud layer has cloud-top pressure 1.778 bar, and optical thickness 50. Haze type one lies at haze-top pressure 0.316 bar with optical thickness 0.25, and haze type two resides at haze-top pressure 0.056 bar with optical thickness 0.6. The reflectance model shows the increase from the blue to the red seen in the data, with methane absorption features also reproduced. The model of the polarisation shows the increase from the near-UV to the blue, with the polarisation then falling towards the red. The increase in polarisation due to methane absorption is seen in the prominent methane bands, although the polarisation is lower than for the data, with the model also deviating

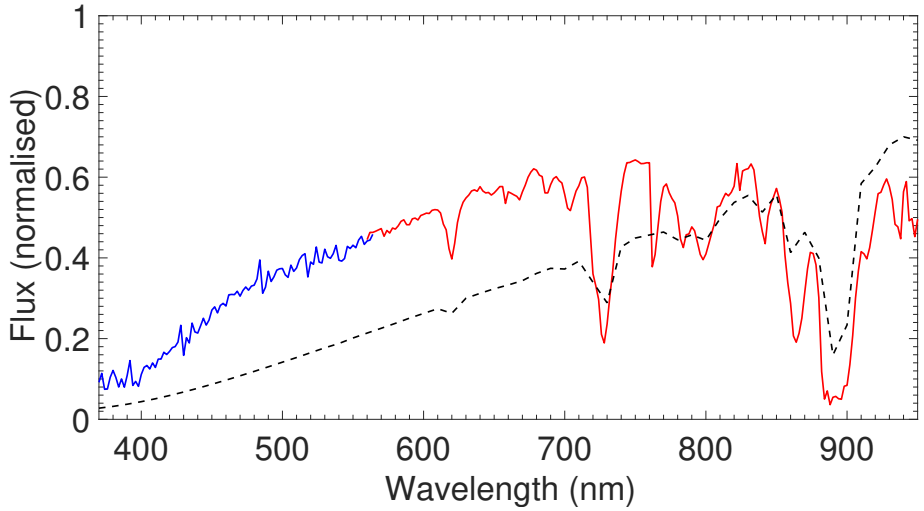

Figure 6.18: Reflectance spectrum from dataset SP1 of Saturn, with the model overlain as a black dotted line.

at both ends of the wavelength domain.

Models of the reflectance and degree of polarisation for dataset SP3 are shown in Figure 6.22 and Figure 6.23, respectively. The tropospheric cloud layer has cloud-top pressure 1.778 bar, and optical thickness 50. Haze type one lies at haze-top pressure 0.316 bar with optical thickness 0.25, and haze type two resides at haze-top pressure 0.056 bar with optical thickness 0.8. The model fit to the reflectance spectrum gives the general trend observed in the data, with methane absorption lines present. The polarisation model fits the decrease in polarisation from the blue towards the red. The model deviates in some places, but can be seen to provide a fit to the rise in polarisation due to methane absorption at 890 nm, within the error bars.

The reflectance spectra of Saturn shown in Section 6.2 show that there is increased absorption in the UV, resulting in a lower albedo at these wavelengths. The molecular species causing this absorption is presently unknown, but it can be quantified by adding in absorption in different atmospheric layers. Trial and error runs indicate that a higher molecular absorption cross section in deeper atmospheric layers gives the higher value of polarisation observed around 440 nm, whilst preserving the lower values toward redder wavelengths, which are caused by the cloud and haze particles becoming more visible as the gas optical thickness decreases with increasing wavelength.

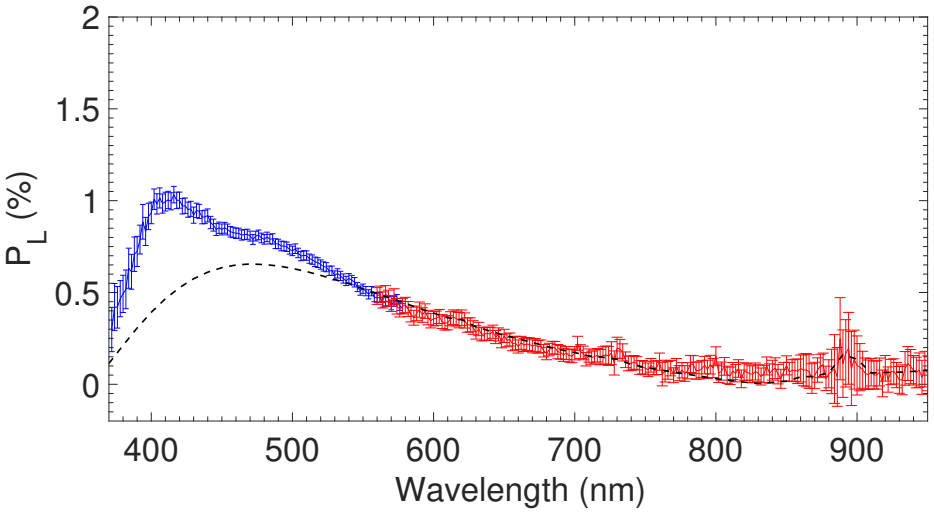

Figure 6.19: P_{L} from dataset SP1 of Saturn, with the model overlain as a black dotted line.

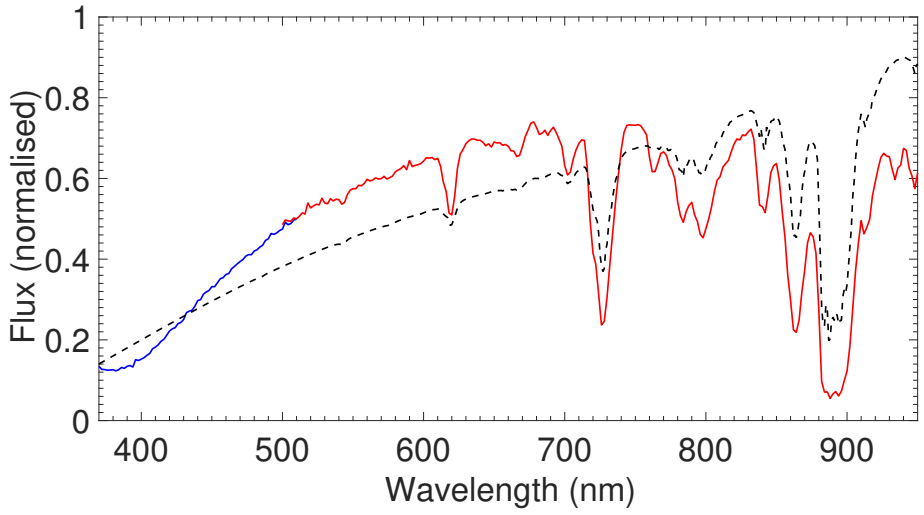

Figure 6.20: Reflectance from dataset SP2 of Saturn, with the model overlain as a black dotted line.

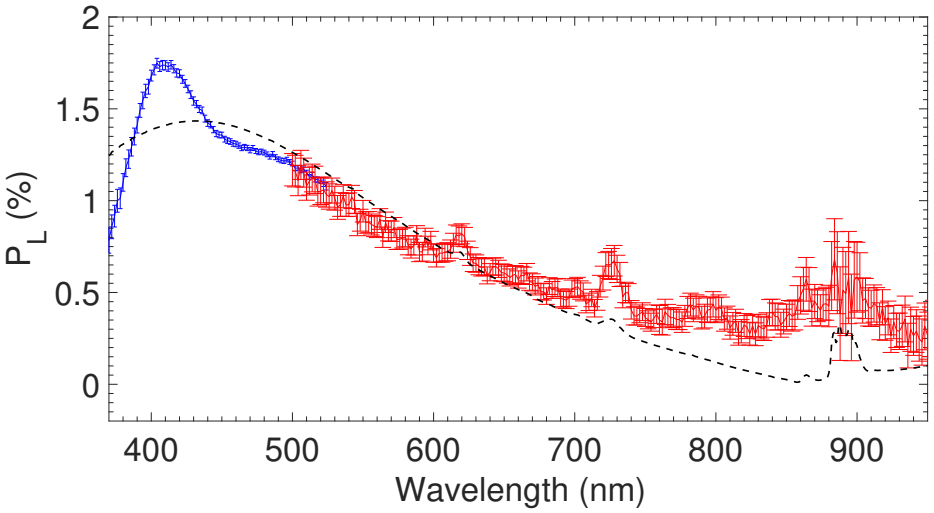

Figure 6.21: P_{L} from dataset SP2 of Saturn, with the model overlain as a black dotted line.

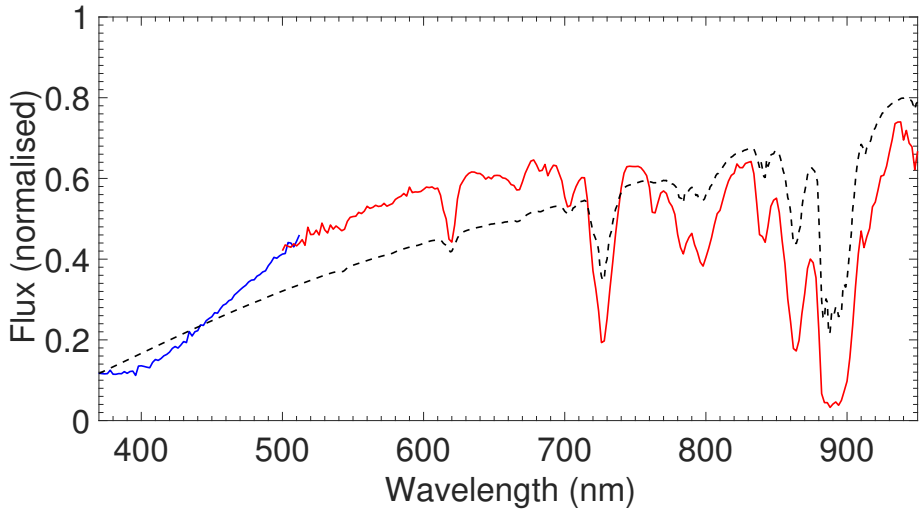

Figure 6.22: Reflectance from dataset SP3 of Saturn, with the model overlain as a black dotted line.

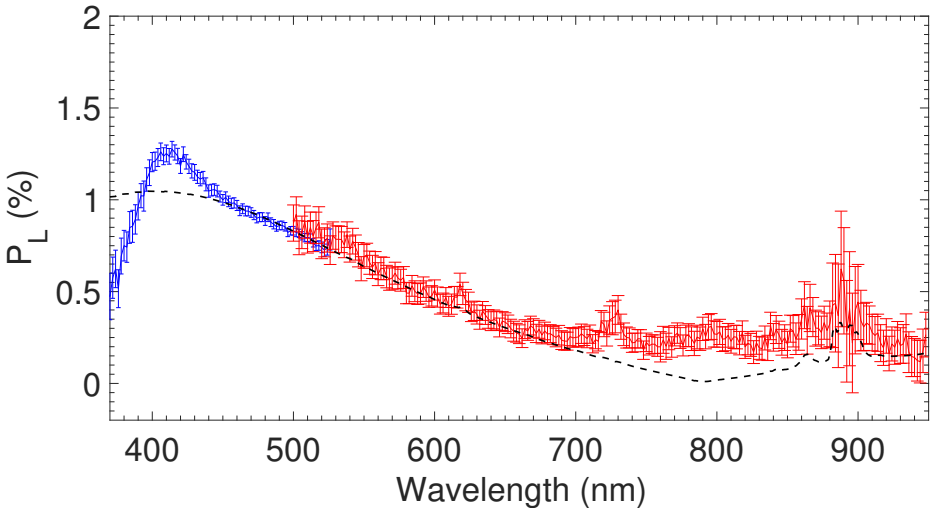

Figure 6.23: P_{L} from dataset SP3 of Saturn, with the model overlain as a black dotted line.

6.3.2 Models of signals from exoplanets

Flux and polarisation signals of Saturn as if it were observed as an exoplanet were computed, and are presented here. The photons received from an exoplanet system would be recorded by a detector as a disk-integrated value from the visible, illuminated part of the planetary disk, depending on the locally reflected starlight across the disk and therefore on variations in atmospheric properties across the planetary disk. Models of light reflected by gaseous exoplanets, based on the model fits to the Saturn spectropolarimetry observations are shown, and these demonstrate both the effect of differences across the planetary disk and also emphasise the additional information that can be inferred from polarimetric studies.

Figure 6.24 shows plots of both the flux and polarisation for three model atmospheres. The degree of linear polarisation of light reflected by an exoplanet varies with a planet's orbit around the star, and with the changing phase angle. For an unresolved giant planet close to the star, it could be $10^{-5} - 10^{-6}$ [Seager et al., 2000]. The phase angle for each of the models is 90°, with the model cloud and haze particles the same as those used for the model interpretation of the observational results. Figure 6.25 shows the same models, but as a function of phase angle at a wavelength of 550 nm. The zero points in the phase angle plots are specific to the atmospheric scatterers that are present. The distance to the planetary system and the size of the planet are required in order to calculate the absolute fluxes, and

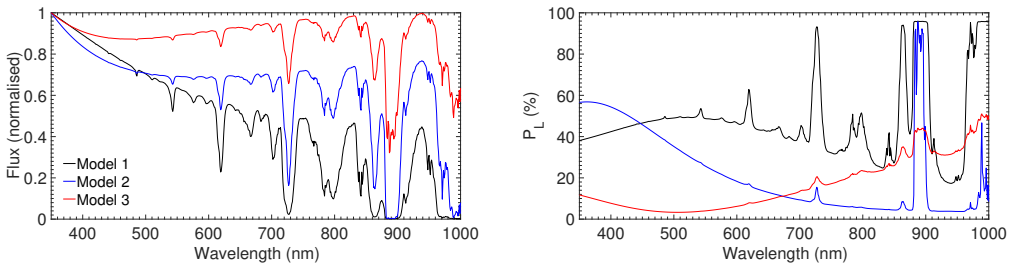

Figure 6.24: Models of the flux and degree of linear polarisation of incident starlight reflected by three Saturn-like exoplanets, for a phase angle of 90°. Model atmosphere 1 has only molecules, model 2 is similar to model 1, but with the addition of a tropospheric cloud layer, and model 3 is similar to model 2, with the inclusion of both a tropospheric and a stratospheric haze layer.

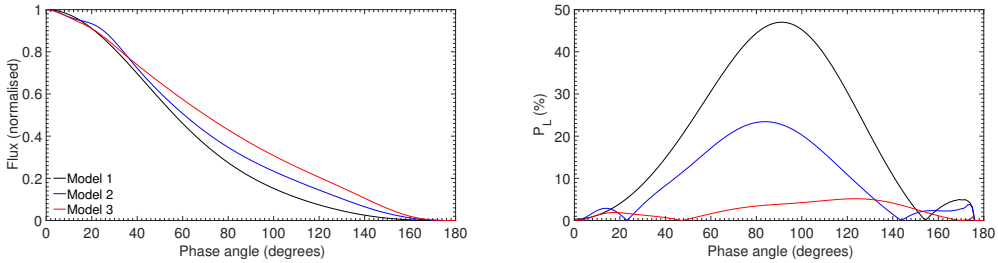

Figure 6.25: The flux and degree of linear polarisation of the three model atmospheres as a function of the planetary phase angle, for a wavelength of 550 nm.

these parameters can be challenging to obtain. Due to the degree of polarisation being a relative measure it is independent of these quantities, therefore atmospheric information can be gleaned from polarimetric measurements.

Model 1 is of an atmosphere containing no cloud or haze particles, only molecular gas. The continuum flux shows a decrease as the wavelength increases, due to the decrease in the molecular scattering optical thickness towards higher wavelengths. The continuum polarisation shows a different variation with wavelength than the flux, due to a smaller Rayleigh scattering optical thickness resulting in less multiple scattering occurring, with multiple scattering tending to reduce the degree of polarisation of the reflected light. The amount of multiple scattering decreases due to increased absorption by CH_4, resulting in higher values of polarisation in the CH_4 bands [Stam et al., 1999, 2004], similar to that observed by Schmid et al. [2011] for the haze of Jupiter.

Model 2 has the same atmospheric configuration as model 1, with the inclusion of a thick (cloud optical thickness $b^c = 50$) cloud layer in the troposphere with a cloud-top pressure of 1.78 bar. At lower wavelengths, the molecular scattering optical thickness of the gaseous atmosphere above the cloud layer is at its greatest, resulting in a lower amount of light reaching the cloud layer, and with increasing wavelength the contribution of the light scattered by the cloud particles starts to dominate for both the flux and polarisation. Increased multiple scattering within the cloud layers along with a lower degree of polarisation from light scattered by cloud particles (This can be clearly observed in Fig. 6.17) results in a decrease in the continuum polarisation. In the strong CH_4 absorption band around 890 nm, the flux and polarisation of models 1 and 2 are very similar to each other. This is due to the fact that hardly any incident stellar light penetrates deep enough into the atmosphere to reach the cloud layer, because of the high molecular absorption optical thickness of the atmosphere that is above the cloud layer, therefore most of the light is scattered in the highest atmospheric layers.

Model 3 contains the same tropospheric cloud layer as that of model 2, with the inclusion of two haze layers: a layer composed of haze particle type one with optical thickness $b^{\mathrm{h}} = 0.2$, at a haze-top pressure of 0.32 bar, and with a haze layer of particle type two at pressure of 0.06 bar with optical thickness 0.8. The polarisation values at longer wavelengths are higher for model 3 than those for model 2, and this can be attributed to a larger (absolute) degree of polarisation of light that is single scattered from the haze layer of particle type one, which can be seen from Fig. 5.18.

6.4 Discussion and summary

This chapter has presented spectropolarimetric and imaging data of Saturn, its rings, and Titan taken in several epochs. Saturn is known to have variable atmospheric properties, changing as a function of its rotation period and orbital period around the Sun. The flux and spectropolarimetric datasets show signatures of methane in the spectra, changing with phase angle and planetary location sampled in the slit. The imaging polarimetry data do not show any noticeable changes in the methane filter compared with the continuum filters, but do show the contrast between the planet and the rings, especially in the position angle.

The spectropolarimetric measurements of Saturn's rings show polarisation lower than half a percent having a direction parallel to the scattering plane, with the FoReRo2 imaging polarimetry also demonstrating the stark difference in polarisation direction between Saturn and its rings. Disk-integrated spectropolarimetry of Titan show the polarisation to be low, as expected for the phase angle, and increasing slightly towards bluer wavelengths.

A model fit to the Saturn spectropolarimetry data was able to mostly replicate the observed behaviour of polarisation, with a slight discrepancy at shorter wavelengths, possibly due to an unknown UV absorber present in Saturn's atmosphere. The model fits shown to the data are able to slightly reproduce the enhancements in the prominent methane bands, and roughly correspond to the decrease in polarisation with increasing wavelength. Ultimately, the small phase angle range in which the data has been taken precludes a full atmospheric characterisation; for this to be achieved data from space missions would be required, in a large spectral range as well. Any model which could fully replicate the observed variation in flux and polarisation would most likely not be concurrent with data taken at higher phase angles unattainable from Earth, since, as Figure 6.17 shows, the scattering properties of atmospheric particles varies greatly with the phase angle. A Saturn atmospheric probe would be the best way to maximise our knowledge of the atmospheric constituents, albeit most likely only a very localised region, as was the case for the Galileo probe in Jupiter's atmosphere. The inclusion of a polarimeter on any future visits to Saturn by space missions would certainly go a long way to ensuring we maximise the potential for the information that could be gleaned from such an undertaking.

Additionally, models of light reflected by Saturn-like exoplanets, for a phase angle of 90° have been presented, along with plots of the variation in flux and linear

polarisation with phase angle. These show that the orbital geometry is greatly important when observing planetary atmospheres, and also demonstrate the advantages presented when observing exoplanets as opposed to solar system planets. The advantage of observing exoplanets is that they orbit other stars, so are visible at larger phase angles where polarisation is highest, and thus promise to be favourable targets for Earth-based polarimetry. If, for example, we cannot disentangle the reflected flux of the planet from the overwhelming stellar signal, then any polarimetric signature would be due to reflection from the planet. If an exo-Saturn were to be observed in a wavelength band where methane is known to be prominent, then its presence can be inferred by a stark difference in polarisation between methane band wavelengths and continuum wavelengths.

Chapter 7

Uranus and Neptune

Abstract

This chapter presents several sets of imaging and spectropolarimetric data taken with FoReRo2, ISIS, and ToPol of Uranus and Neptune. The purpose of these observations was to glean further understanding of the seasonal and phase angle variation of the polarisation of light reflected by the atmospheres of these planets. Despite the low phase angle range attainable from Earth for Uranus and Neptune, some differences in polarisation that are possibly outside of the error bars are observed. It is difficult to tell whether the differences mainly arise due to seasonal or phase angle changes. Model fits were attempted for the Uranus spectropolarimetric data, reproducing some of the features due to methane absorption, and the continuum decrease in polarisation due to the lower Rayleigh scattering optical thickness towards longer wavelengths. Also investigated are the features that one may observe in light reflected by exoplanets of a similar configuration to Uranus and Neptune.

7.1 Introduction

Uranus is only observable, with Earth-based observations, up to a phase angle of 3.2°, and Neptune up to 2.0°, which corresponds to a backscattering geometry. For a phase angle of exactly 0° the reflected light is completely backscattered, and it is known that single scattered light from particles with random orientations has a degree of linear polarisation equal to zero. Light that has undergone multiple scattering can have a non-zero degree of linear polarisation, which can be observed especially near the planetary limb where photons that have undergone two scattering

events will have a polarisation with the electric field vector orientated radially when dominated by Rayleigh scattering, or tangentially if single scattered light at mid-range scattering angles has a negative polarisation [see West et al., 2015; Schmid et al., 2011]. Observed polarisation at phase angles greater than zero results from a combination of both single scattered and multiple scattered light.

Uranus and Neptune have never been visited by any dedicated space missions. Disk-integrated polarimetry of Uranus and Neptune at the low phase angles attainable from Earth can only glean very limited information on the atmospheric properties. Measurements of the limb polarisation seem the most favourable method for observing Uranus and Neptune in polarised light from Earth.

Schmid et al. [2006] performed imaging polarimetry on Uranus and Neptune, for filters in the red and near infrared regions of the spectrum. The data obtained showed that both planets exhibited limb polarisation. This is the first time imaging polarimetry had been carried out for either of these planets and produced fully resolved images. The limb polarisation shows that there is a Rayleigh scattering layer present in the atmospheres. The limb polarisation effect is observed along the entire limb for both planets, whereas for Jupiter and Saturn it is only observed at the poles. Schmid et al. [2006] investigated degradation and cancellation effects in the polarisation signal caused by the spatial resolution of the observations, which were limited due to seeing effects. Corrected values for the limb polarisation of Uranus and Neptune were obtained, and these were compared with models of Rayleigh scattering atmospheres. The comparison showed that the polarisation measured was compatible with what was theoretically expected, showing that limb polarisation measurements provide an excellent remote-sensing tool for investigating the scattering properties of particles in the upper atmospheres of Uranus and Nepune. This could be applicable to future polarimetric detections of exoplanets with similar atmospheric properties to those of Uranus and Neptune.

Joos & Schmid [2007] carried out spectropolarimetric measurements of Uranus and Neptune. Data were taken for the wavelength range between 530 nm and 930 nm, and signals from different sections of the limb and the centre of the planetary disk were compared. A strong limb polarisation was found for both planets, orientated perpendicular to the limb. The polarisation at the centre of the disk for each planet was found to be virtually zero. The limb polarisation was found to decrease towards shorter wavelengths, and was stronger in methane absorption bands. The polarisation signals for Uranus and Neptune were found to be overall very similar. The measured polarisation for Neptune was significantly lower but this was due to

the signal being averaged down by the limited spatial resolution for the obtained Neptune data.

As with the imaging polarimetry study, the measurements obtained using spectropolarimetry were consistent with results from analytic models of scattering atmospheres containing layers of particles scattering radiation similar to Rayleigh scattering processes. It is remarked by Joos & Schmid [2007] that the limb polarisation contains interesting diagnostic information, especially for the scattering properties of aerosol particles in haze layers at high altitudes.

Voyager 2 is the only spacecraft to have ever encountered Uranus and Neptune, with close and rapid encounters leaving little time for collecting data as a function of changing phase angle. Polarimetric data for Neptune are presented in Pryor et al. [1992], who showed that the observed P_Q along the central meridian of Neptune's southern hemisphere is consistent with a model that was previously derived from photometric data, with a value close to zero at a phase angle of 13 to 14°. The atmosphere was thought to contain stratospheric haze, presumably composed of hydrocarbons, with an optical thickness decreasing with wavelength, overlying a tropospheric cloud layer composed of methane or hydrogen sulphide [West et al., 2015].

Three sets of spectropolarimetry data for Uranus are presented in this chapter: two of which were taken with FoReRo2, and one with ISIS. Three sets of disk-integrated imaging polarimetry are also presented: one obtained with FoReRo2, and two with ToPol. One set of Neptune spectropolarimetry taken with ISIS is presented, along with seven sets of imaging polarimetry in various filters from both ToPol and FoReRo2. This chapter is structured as follows: Section 7.2 describes the observations, and presents the results. Section 7.3 then shows some model fits to the Uranus data, along with models of the signal that could be received from exoplanets with similar atmospheric configurations to Uranus and Neptune. Section 7.4 then discusses and summarises this chapter.

7.2 Observations and results

7.2.1 Uranus: ISIS and FoReRo2 spectropolarimetry

Table 7.1 gives the observing log for these observations. Column one assigns the name to each dataset, column two gives the dates of the observations, and column three the Universal Time (UT) in the middle of each observing block. Column four

gives the exposure time of an individual frame, in seconds. Columns five and six respectively list the instrument and the grism used for each of the observations. Column seven then gives the phase angle, α, at the time of observation. Columns eight through ten give other planetary parameters at the time of observation, namely: angular diameter at the equator in arcseconds, planetary north-pole position angle relative to the north celestial meridian in degrees, and the distance to the planetary north pole from the centre of the disk, in arcseconds on the sky[1].

[1]Planetary parameters were calculated using JPL HORIZONS: http://ssd.jpl.nasa.gov/?horizons

Table 7.1: Observing log for the Uranus spectropolarimetry datasets, with the column meanings explained in the text.

Dataset	Date	UT	Exp. Time (s)	Inst.	Grism	α (°)	Ang.Diam. (")	NP Ang (°)	NP Dist. (")
SP1	22/12/2014	18:13	120	FoReRo2	GrismW	2.76	3.56	+255.28	+1.57
SP2	06/01/2015	21:03	60	ISIS	R300B	2.81	3.52	+255.29	+1.55
SP2	06/01/2015	20:55	20	ISIS	R158R	2.81	3.52	+255.29	+1.55
SP3	14/11/2015	17:19	30	FoReRo2	GrismW	1.61	3.68	+256.02	+1.55

The observations for dataset SP2 were carried out by Stefano Bagnulo with ISIS at the WHT (programme ID W/2014B/30), and the data reduction methods are described fully in Section 3.3.3.3. The observations for the other two datasets were carried out by Galin Borisov with FoReRo2 at NAO Rozhen, with the data reduction methods described in Section 3.3.3.2. A one-dimensional data reduction was used for all of the data, except for dataset Uranus SP2, where a two-dimensional reduction was necessary due to the extent of the object in the slit.

The reflectance spectra and the degree of linear polarisation for each of the three datasets are shown in Figure 7.1, Figure 7.2, and Figure 7.3. Each of the reflectance spectra have enhancements in the polarisation in certain absorption bands of methane and ammonia, particularly at 540 nm, 580 nm (ammonia), and 620 nm and 670 nm (methane), with the reflectance comparing favourably with that in Joos & Schmid [2007] and Karkoschka [1998]. The ammonia and methane absorption features can also be seen to manifest themselves as "emission" lines in the polarisation spectra, since the polarisation is enhanced in this regions. The reason for the enhancement of the polarisation could be due to the increase of single scattered light from these particles.

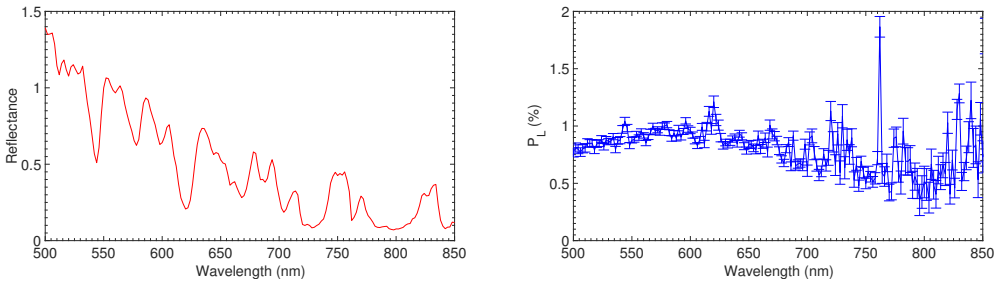

Figure 7.1: Reflectance spectrum and P_{L} for dataset Uranus SP1.

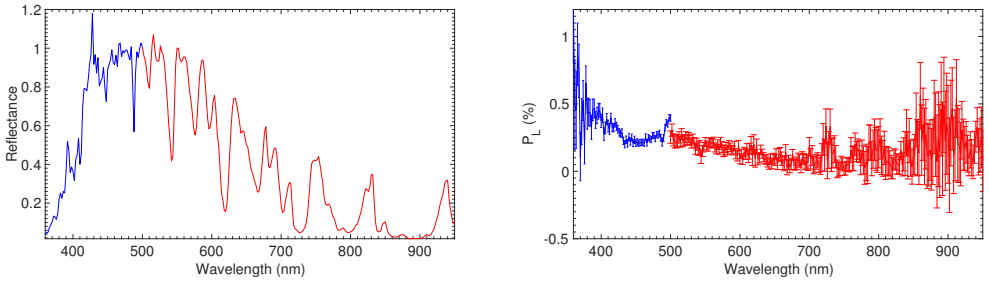

Figure 7.2: Reflectance spectrum and P_{L} for dataset Uranus SP2.

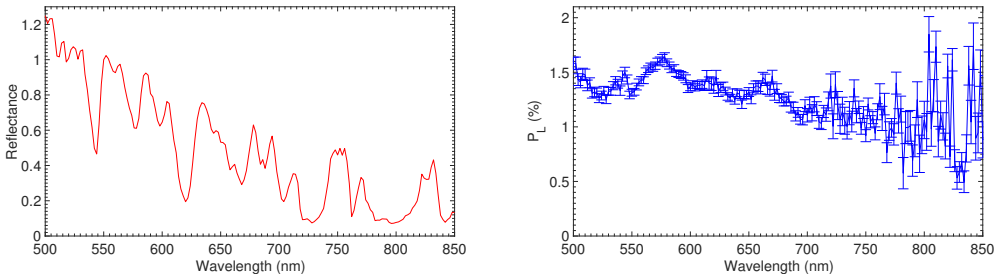

Figure 7.3: Reflectance spectrum and P_{L} for dataset Uranus SP3.

7.2.2 Uranus: FoReRo2 and ToPol imaging polarimetry

Table 7.2 shows the log of the observations and the values of polarisation of Uranus for all of the imaging polarimetry datasets. The FoReRo2 observations were carried out by Galin Borisov, and the ToPol data were obtained by Jean-Pierre Rivet and Alberto Cellino. Column one assigns a name to each dataset, with column two then giving the date of observation, and column three the Universal Time at the middle of the observing block. Column four lists the exposure time, with columns five and six respectively listing the instrument and the filter used. Column seven gives the phase angle at the time of observation, column eight the angular diameter on the sky of Uranus, with column nine giving the angle to the north pole, and column ten the distance to the north pole from the centre of the disk. Column eleven lists the degree of linear polarisation, P_{L}, and column twelve gives the position angle of polarisation.

Table 7.2: Observing log for the Uranus imaging polarimetry datasets, with the column meanings explained in the text.

Dataset	Date	UT	ET (s)	Inst.	Filter	$\alpha\,(^\circ)$	Ang. D. ($''$)	NP Ang. ($^\circ$)	NP Dist.($''$)	$P_{\rm L}$ (%)	$\theta\,(^\circ)$
IP1	22/12/2014	17:04	1	FoReRo2	V	2.76	3.56	255.28	+1.57	0.05±0.06	83.03 ±37.41
IP2	25/09/2015	22:19	2	ToPol	V	0.83	3.71	256.38	+1.53	0.23±0.03	76.49 ±3.42
IP3	09/12/2015	19:57	1	ToPol	V	2.46	3.62	255.92	+1.53	0.28±0.01	74.81 ±0.76

Table 7.3: Observing log for the Neptune spectropolarimetry datasets, with the column meanings explained in the text.

Dataset	Date	UT	ET (s)	Grism	α (°)	AD (″)	NPA (°)	NPD(″)
SP1	06/01/2015	20:21	50	R158R	1.43	2.23	+329.74	-0.97
SP1	06/01/2015	20:32	90	R300B	1.43	2.23	+329.74	-0.97

Despite IP1 being observed at the largest phase angle of the three datasets, the degree of polarisation is actually smallest. However, it is difficult to draw comparisons between datasets that have been taken months apart, due to variations in the atmosphere of Uranus that can take place on both a daily and a longer term basis. All datasets illustrate that the degree of linear polarisation of Uranus, at least disk-integrated, is virtually zero for such low phase angles. The position angle of polarisation is near the perpendicular point to the scattering plane.

7.2.3 Neptune: ISIS spectropolarimetry

Table 7.3 gives the observing log for these datasets, with column meanings the same as for Table 7.1. These observations were carried out with ISIS by Stefano Bagnulo (programme ID W/2014B/30). The reflectance and degree of linear polarisation of Neptune are shown in Figure 7.4. Absorption lines caused by the presence of ammonia can be seen in the reflectance spectrum at wavelengths close to 540 nm and 580 nm, with a slight rise in polarisation at 540 nm. Methane absorption is also seen in the reflectance spectrum, at the known methane bands of 625 nm and 725 nm, but none at the strong methane absorption band of 890 nm. The reflectance spectra has a different shape than from Karkoschka [1998], possibly due to a combination of seasonal variations and the fact that the spectra presented here is not disk-integrated. A dip in polarisation is seen at around 450 nm and 640 nm perhaps due to the various scatterers present in the atmosphere of Neptune at the time of observation. Different particle types could potentially give rise to changes in polarisation with wavelength.

7.2.4 Neptune: FoReRo2 and ToPol imaging polarimetry

Table 7.4 shows the values of polarisation of Neptune for all of the imaging polarimetry and spectropolarimetry datasets, with column meanings the same as for Table 7.2. The FoReRo2 observations were taken by Galin Borisov, and the ToPol data were taken by Maxime Devogèle and Will McLean. As would be expected for

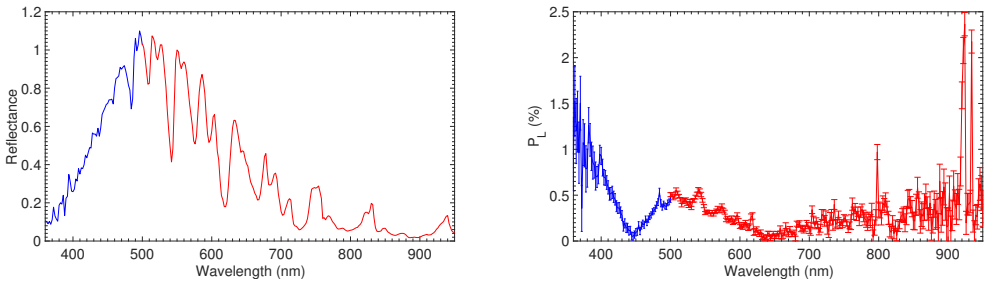

Figure 7.4: Reflectance spectrum and P_{L} for dataset Neptune SP1.

such low phase angles, the degree of linear polarisation is small.

Table 7.4: Observing log for the Neptune imaging polarimetry datasets, with the column meanings explained in the text.

Dataset	Date	UT	ET (s)	Inst.	Filter	α (°)	Ang. D. ($''$)	NP Ang. (°)	NP Dist.($''$)	$P_{\rm L}$ (%)	θ (°)
IP1	22/12/2014	16:25	5	FoReRo2	V	1.70	2.25	329.98	-0.98	0.08±0.02	129.03 ±6.45
IP2	08/12/2015	19:04	20	ToPol	B	1.86	2.27	328.70	-0.99	0.77±0.02	4.61 ±0.74
IP2	08/12/2015	18:42	5	ToPol	V	1.86	2.27	328.70	-0.99	0.39±0.02	77.97 ±1.26
IP2	08/12/2015	18:51	5	ToPol	R	1.86	2.27	328.70	-0.99	0.14±0.02	30.88 ±3.90
IP3	22/07/2016	01:04	120	ToPol	B	1.31	2.34	325.91	-1.03	0.18±0.02	161.40±2.69
IP3	22/07/2016	00:17	10	ToPol	V	1.31	2.34	325.91	-1.03	0.18±0.02	42.74 ±2.45
IP3	22/07/2016	00:34	10	ToPol	R	1.31	2.34	325.91	-1.03	0.26±0.02	48.40 ±1.84
IP3	22/07/2016	00:41	20	ToPol	I	1.31	2.34	325.91	-1.03	0.08±0.03	41.66 ±10.00
IP4	24/07/2016	23:45	10	ToPol	B	1.23	2.34	325.95	-1.03	0.29±0.08	1.67 ±7.90
IP4	24/07/2016	23:55	2	ToPol	V	1.23	2.34	325.95	-1.03	0.26±0.08	71.99 ±8.61
IP4	25/07/2016	00:00	2	ToPol	R	1.23	2.34	325.95	-1.03	0.27±0.03	46.28 ±3.07
IP5	26/07/2016	00:03	20	ToPol	B	1.18	2.34	325.97	-1.03	0.25±0.02	156.89±2.65
IP5	25/07/2016	23:31	2	ToPol	V	1.18	2.34	325.97	-1.03	0.12±0.03	33.10±6.59
IP5	25/07/2016	23:36	4	ToPol	R	1.18	2.34	325.97	-1.03	0.15±0.02	58.81±3.90
IP5	25/07/2016	23:47	20	ToPol	I	1.18	2.34	325.97	-1.03	0.17±0.02	35.07±3.38
IP6	05/08/2016	23:06	120	ToPol	U	0.90	2.35	326.10	-1.04	0.19±0.01	156.89 ±2.65
IP6	05/08/2016	22:56	60	ToPol	B	0.90	2.35	326.10	-1.04	0.62±0.01	169.99 ±0.62
IP6	05/08/2016	22:27	10	ToPol	V	0.90	2.35	326.10	-1.04	0.06±0.01	106.52 ±7.60
IP6	05/08/2016	22:34	10	ToPol	R	0.90	2.35	326.10	-1.04	0.29±0.01	39.47 ±1.44
IP6	05/08/2016	22:45	30	ToPol	I	0.90	2.35	326.10	-1.04	0.38±0.02	71.68±1.43
IP7	10/12/2016	16:53	2	ToPol	V	1.86	2.27	327.32	-1.00	0.10±0.02	166.06±6.64
IP7	10/12/2016	16:59	2	ToPol	R	1.86	2.27	327.32	-1.00	0.31±0.02	41.73 ±1.57
IP7	10/12/2016	17:12	30	ToPol	I	1.86	2.27	327.32	-1.00	0.03±0.02	120.15 ±16.92

7.3 Theoretical modelling

The radiative transfer code described in Section 2.3 was used to run models of the Uranus spectropolarimetry datasets, and to compute models of the signal from exoplanets similar to Uranus and Neptune. Since the phase angle range of the observations was limited up to 3° due to the limitations of Earth-based Uranus observations, any model cannot be known with any certainty to fully represent the atmospheric properties over the entire phase angle range. However, these models provide an approximate fit to the data at these phase angles, demonstrating the effect on polarisation of certain cloud particle parameters, and cloud and haze height and optical thickness in the atmosphere.

7.3.1 Models of the Uranus spectropolarimetry data

The model atmospheres all consist of 20 atmospheric layers, with a temperature-pressure profile similar to that used for the other models to the outer planets described in previous chapters. A cloud layer and a haze layer were added into the atmosphere, mixed with hydrogen, helium, and methane in all of the other layers. The cloud particles have $r_{\rm eff} = 0.5\,\mu$m, with $v_{\rm eff} = 0.01$, and the haze $r_{\rm eff} = 0.2\,\mu$m, with $v_{\rm eff} = 0.05$. The cloud particles have a refractive index 1.42±0.015i, and the haze particles have a refractive index 1.50±0.001i.

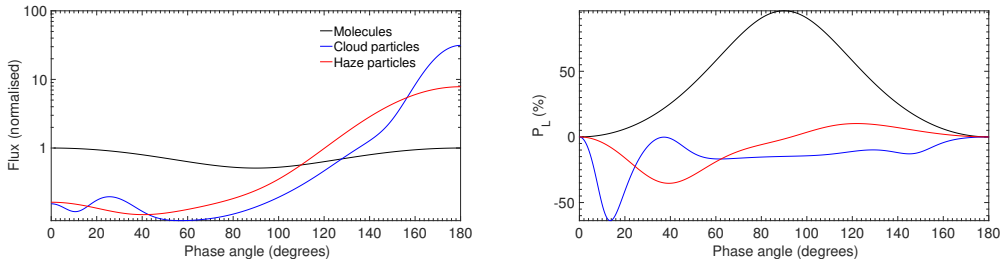

Figure 7.5: Single scattering flux and linear polarisation of the cloud and haze particles at 550 nm along with Rayleigh scattering curves.

Models of the reflectance and polarisation for dataset SP1 are presented in Figure 7.6, along with the data for comparison. The cloud was at an atmospheric pressure of 1 bar, with an optical thickness of 50, and with a diffuse haze layer at a pressure of 0.316 bar with optical thickness 0.2. The model fit to the reflectance is comparatively flatter than that of the data, but some methane absorption can still be seen. The polarisation models provide an approximate fit, but stray towards

either end of the wavelength range. Enhancements seen in the methane absorption bands in the observations are also reproduced in the polarisation model.

Model fits of the reflectance and polarisation for dataset SP2 are shown in Figure 7.7. These models have the cloud layer extending up to a pressure level of 1.778 bar, with a layer of haze at pressure level 0.316 bar of optical thickness 0.05. The reflectance model fits the general trend of a decrease towards longer wavelengths, with the presence of methane absorption, but the model deviates considerably towards the near-UV wavelengths. The polarisation model shows a slight enhancement in the 890 nm methane band, and matches closely with the value of polarisation at longer wavelengths.

The polarisation in dataset SP3 is comparatively high, and thus proved difficult to model. The higher polarisation could be due to limb effects and contributions from non-spherical particles that are not considered in this study. As mentioned previously, the models shown here are only approximations that without a full phase angle characterisation for multiple wavelengths can only serve as simple gauges of the variation in polarisation caused by the cloud and haze constituents.

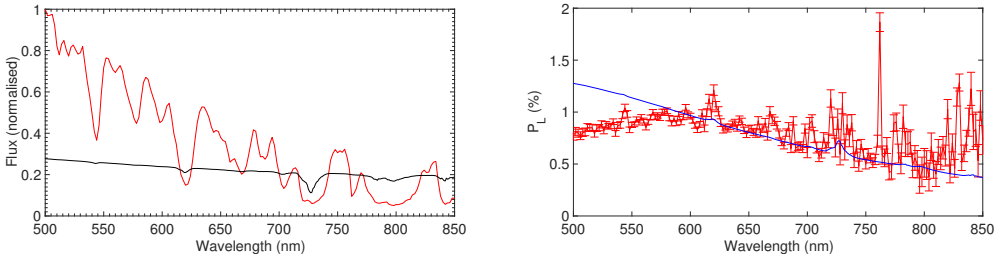

Figure 7.6: Models of the reflectance and P_{L} for dataset SP1.

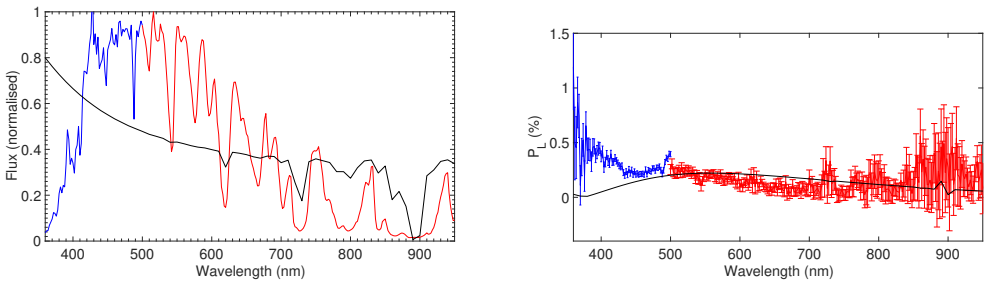

Figure 7.7: Model of the reflectance and P_{L} for dataset SP2.

7.3.2 Models of Uranus-like and Neptune-like exoplanets

Model computations for exoplanets of a similar configuration to Uranus and Neptune are presented with the same model cloud and haze particles as used for fitting the Uranus data, and are shown in Figure 7.8. Such observations of exoplanets in flux and polarised light would be received as a disk-integrated value from the illuminated and visible part of the planet's disk. This signal would thus contain imprints of the atmospheric properties on this part of the planet, at the particular phase angle. The models in Figure 7.8 were computed for a phase angle of 90°, which is close to the phase angle where the largest degree of polarisation is expected to be observed. The models shown demonstrate the differences in signal that results from the addition of cloud and haze particles in a planetary atmosphere, and also the increased diagnostic potential that polarimetry has when compared with flux measurements alone. The distance to the planetary system and the size of the planet are needed to be able to calculate absolute fluxes, and these values can be difficult to obtain. Since the degree of polarisation is a relative measure, it is independent of these parameters, therefore atmospheric information can be gleaned from polarimetry alone.

Figure 7.8 and Figure 7.10 shows plots of both the flux and polarisation for three model atmospheres of Uranus and Neptune, respectively. Figure 7.9 and Figure 7.11 shows the same models, but as a function of phase angle at a wavelength of 550 nm. Each of the zero points in the phase angle plots are specific to the scatterers in the atmosphere, and change with different model particles.

Model 1 is of an atmosphere containing no cloud or haze particles, only molecular gas. The continuum flux shows a decrease as the wavelength increases, due to the decrease in the molecular scattering optical thickness towards higher wavelengths. The continuum polarisation shows a different variation with wavelength than the flux, due to a smaller Rayleigh scattering optical thickness resulting in less multiple scattering occurring, with multiple scattering tending to reduce the degree of polarisation of the reflected light. The amount of multiple scattering decreases due to increased absorption by CH_4, resulting in higher values of polarisation in the CH_4 bands [Stam et al., 1999, 2004], similar to that observed by Schmid et al. [2011] for Jupiter.

Model 2 has the same atmospheric configuration as model 1, with the inclusion of a thick (cloud optical thickness $b^c = 50$) cloud layer in the troposphere with a cloud-top pressure of 1.0 bar. At lower wavelengths, the molecular scattering optical thickness of the gaseous atmosphere above the cloud layer is at its greatest,

resulting in a lower amount of light reaching the cloud layer, and with increasing wavelength the contribution of the light scattered by the cloud particles starts to dominate for both the flux and polarisation. Increased multiple scattering within the cloud layers along with a lower degree of polarisation from light scattered by cloud particles (this can be clearly observed in Figure 7.5) results in a decrease in the continuum polarisation. In the strong CH_4 absorption band around 890 nm, the flux and polarisation of models 1 and 2 are very similar to each other. This is due to the fact that hardly any incident stellar light penetrates deep enough into the atmosphere to reach the cloud layer, because of the high molecular absorption optical thickness of the atmosphere that is above the cloud layer, therefore most of the light is scattered in the highest atmospheric layers.

The dashed plots show the flux and degree of polarisation for a model atmosphere that is the same as model 2, but with the tropospheric cloud deck instead at a cloud top pressure of 1.78 bar. The differences between the two types of cloud-only model are mainly evident in the plots of the polarisation: methane absorption is much less evident for the atmospheres that have a higher cloud deck than for those with the lower cloud deck. This result demonstrates the effectiveness of polarimetry for determining cloud-top altitudes in planetary atmospheres.

Model 3 contains the same tropospheric cloud layer as that of model 2, with the inclusion of a haze layer in the stratosphere of optical thickness $b^{\mathrm{h}} = 0.2$, at a haze-top pressure of 0.316 bar. The polarisation values at higher wavelengths are lower for model 3 than those for model 2, and this can be attributed to a smaller (absolute) degree of polarisation of light that is single scattered from the haze particle layer, which can be seen from Figure 7.5. The light that would be observed at wavelengths where CH_4 causes absorption would not only be mainly singly scattered light, but would also contain the single scattering signature of the haze particles. Light that is singly scattered by these haze particles has a low degree of polarisation at a scattering angle of 90 degrees, therefore the polarisation in the band at around 625 nm can be seen to be lower than that in the continuum, but is still greater for the band around 890 nm due to the larger amount of methane absorption here, which is simulated by greater methane absorption coefficients used in the program.

7.4 Discussion and summary

This section has presented three sets of spectropolarimetric data of the ice giant Uranus, and one spectropolarimetry dataset for Neptune. The reflectance spectra

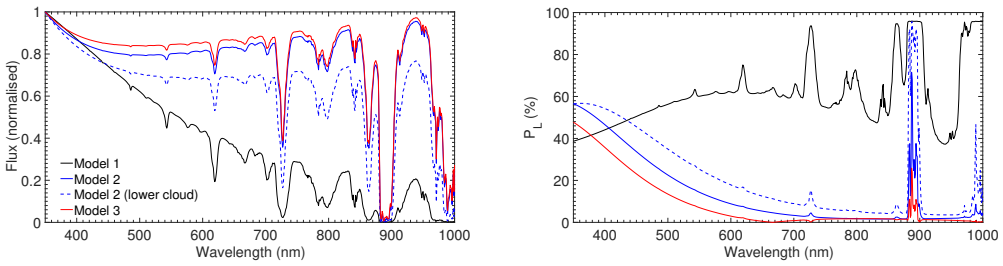

Figure 7.8: Models of the flux and degree of linear polarisation of incident starlight reflected by three Uranus-like exoplanets, for a phase angle of 90°. Model atmosphere 1 has only molecules, model 2 is similar to model 1, but with the addition of a tropospheric cloud layer, and model 3 is similar to model 2, with the inclusion of a stratospheric haze layer. Plots of model 2 with a lower cloud layer are also shown.

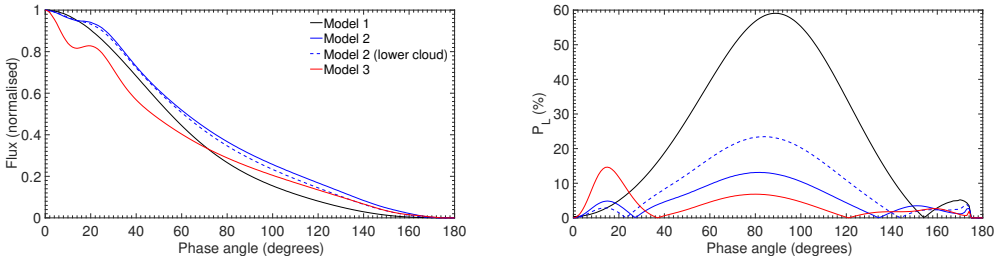

Figure 7.9: Models of the flux and degree of linear polarisation of incident starlight reflected by three Uranus-like exoplanets, as a function of phase angle for a wavelength of 550 nm.

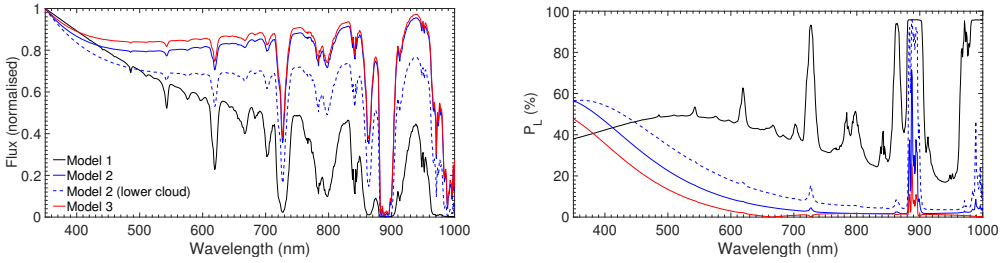

Figure 7.10: Models of the flux and degree of linear polarisation of incident starlight reflected by three Neptune-like exoplanets, for a phase angle of 90°. Model atmosphere 1 has only molecules, model 2 is similar to model 1, but with the addition of a tropospheric cloud layer, and model 3 is similar to model 2, with the inclusion of a stratospheric haze layer. Plots of model 2 with a lower cloud layer are also shown.

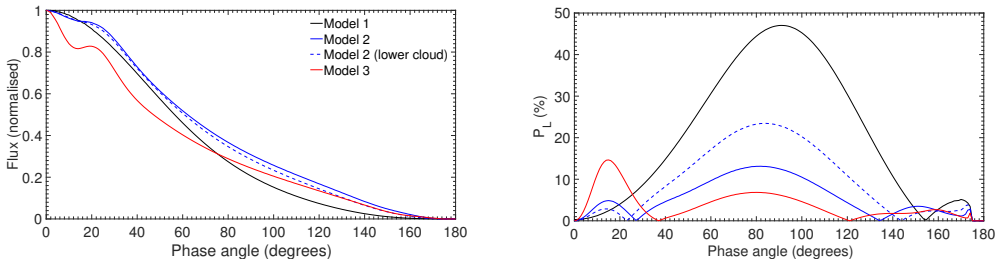

Figure 7.11: Models of the flux and degree of linear polarisation of incident starlight reflected by three Neptune-like exoplanets, as a function of phase angle for a wavelength of 550 nm.

all show signs of methane absorption in the atmospheres, alongside correspondences in the polarisation spectra with the methane bands for the planets. Ammonia absorption features are also present in the reflectance spectra. All datasets show relatively low values of polarisation, although Uranus dataset SP3 shows unusually (relatively) high polarisation for the phase angle of the observation, but could be attributed to seasonal variations or increased limb polarisation. Three sets of disk-integrated imaging polarimetry taken across three separate epochs were also presented, showing as expected the polarisation to be small at these low phase angles, along with a direction of polarisation nearly perpendicular to the scattering plane.

Model fits to two of the three Uranus spectropolarimetry datasets (all but SP3) were computed, showing some similarity to the variation in the data, but ultimately due to the limited phase angle range that Uranus is visible from Earth a full atmospheric characterisation is unachievable. Therefore, the models shown here are essentially to illustrate the signal that may be received from planets with an atmospheric configuration that is marginally similar to that of Uranus at the time periods of the observations presented here.

Models of the flux and polarisation of light reflected by Uranus-like exoplanets have also been shown, demonstrating the influence that cloud and/or haze particles in the atmosphere of such planets have on the received light. The difference in the reflected signal that can result from differing cloud heights in planetary atmospheres has also been demonstrated, showing that the degree of linear polarisation can be more sensitive to the amount of gas present above a cloud and/or haze layer.

In summary, there is not a great deal of polarimetric study of Uranus and Neptune, perhaps because of the small phase angle range accessible from Earth. The data presented here illustrate that even in such a limited phase angle range variations in

polarisation as a function of wavelength and time can still be seen, including features in strong methane absorption bands manifesting themselves in the polarisation spectra. This is an important result for exoplanet science: if the flux of a suspected Uranus or Neptune-like exoplanet proved challenging to resolve from that of the parent star, polarimetry could be used to infer the presence of methane, ammonia, or other absorbers in the planetary atmosphere.

Chapter 8

Conclusions

8.1 Summary

This thesis has presented new polarimetric data and model interpretation of large bodies of the solar system, along with a discussion of the properties of exoplanets that may be gleaned from polarimetric investigation. Ultimately, the nature of data collection in astronomy usually leads to one obtaining sporadic data points spread over time, limited by the wavelength coverage and other factors pertaining to the instrument used. Polarimetric studies of solar system objects usually require data collected over a broad time period because we need to observe under different geometrical views. For that reason, during the course of my PhD, it was possible to collect small datasets for many objects rather than complete datasets for a lower number of targets. Nevertheless, many of the data collected throughout this project could be self-consistently and successfully analysed.

The original contribution to the field that this thesis provides includes new imaging and spectropolarimetric data of the planets and one moon (Titan) of the solar system, data that corroborate and expand upon findings of previous work. A preliminary treatment of Earthshine data has been presented, along with model computations showing what may be expected from observations of exoplanets with an Earth-like atmosphere. Spectropolarimetric data of Mars all show variations that can be attributed to seasonal effects, and local variations in the atmospheric composition perhaps due to dust storms. The Jupiter, Saturn, Uranus and Neptune spectropolarimetric datasets all show features due to atmospheric absorption in both the flux and polarisation spectra, and model fits are presented showing what may be seen from gaseous exoplanets with similar atmospheric configurations.

Chapter 5 represents the largest contribution to this thesis, showing polarimetric maps and spectropolarimetry of Jupiter taken across several epochs, along with model fits to compare the data with. The data all show variations that can be from a combination of the following: differing aerosol particle properties, the atmospheric height and optical thickness of the aerosols, and the part of the Jovian disk visible in the observations. The polarimetric maps demonstrated the sharp increase of polarisation towards the polar regions of Jupiter, and also that storm systems such as the GRS show up markedly in polarised light at bluer wavelengths.

In summary, each of the four science chapters have presented new results for the six outermost planets and one moon of the solar system. Model fits to some of the data are also presented. As has been emphasised throughout this work, data taken in the limited phase angle range accessible from Earth for the outer solar system and Mars are insufficient for gaining a full understanding of the scattering properties of the atmospheric constituents, thus precluding a full model characterisation of the particles. Each chapter also presented model results for exoplanets of varying configuration, demonstrating the features that can be observed both in flux and polarised light, as a function of both wavelength and phase angle.

8.2 Future work required

To gain a more complete understanding of the polarimetric behaviour of the planets of the solar system, they must be studied frequently, and at as many wavelengths and phase angles as possible. Seasonal variations can drastically alter the behaviour of reflected light, and can cause degeneracies in the diagnosis of cloud particle type and cloud height. Future missions to planets of the solar system should include polarimetric instrumentation as part of the standard payload.

Since polarimetry is a diagnostic technique that is limited by the number of photons, it is crucial that, especially for polarimetric studies of faint objects such as exoplanets, that polarimeters are mounted on the largest telescopes available. Aside from furthering our understanding of the solar system planets, polarimetric investigation of their properties can lead us to further understand what we might expect to observe from exoplanets. As emphasised throughout this work, polarimetry has great potential to yield the detection of atmospheric constituents such as oxygen and methane on exoplanets, and thus could infer the presence of life.

Bibliography

Appenzeller, I., Fricke, K., Fürtig, W., et al. 1998, The Messenger, 94, 1

Arago, F. 1858, Popular astronomy, Vol. 2 (Longman, Brown, Green, and Longmans)

Atreya, S. K., & Wong, A.-S. 2005, Space Sci. Rev., 116, 121

Atreya, S. K., Wong, A. S., Baines, K. H., Wong, M. H., & Owen, T. C. 2005, Planet. Space Sci., 53, 498

Atreya, S. K., Wong, M. H., Owen, T. C., et al. 1999, Planet. Space Sci., 47, 1243

Bagnulo, S., Belskaya, I., Boehnhardt, H., et al. 2011, J. Quant. Spec. Radiat. Transf., 112, 2059

Bagnulo, S., Belskaya, I., Muinonen, K., et al. 2008, A&A, 491, L33

Bagnulo, S., Boehnhardt, H., Muinonen, K., et al. 2006, A&A, 450, 1239

Bagnulo, S., Cellino, A., & Sterzik, M. F. 2015, MNRAS, 446, L11

Bagnulo, S., Landolfi, M., Landstreet, J. D., et al. 2009, PASP, 121, 993

Bagnulo, S., & Landstreet, J. D. 2015, Stellar magnetic fields, ed. L. Kolokolova, J. Hough, & A.-C. Levasseur-Regourd, 224

Bailey, J. 2014, PASA, 31, e043

Bailey, J., Ulanowski, Z., Lucas, P. W., et al. 2008, MNRAS, 386, 1016

Baines, K. H., Carlson, R. W., & Kamp, L. W. 2002, Icarus, 159, 74

Bar-Nun, A., Dimitrov, V., & Tomasko, M. 2008, Planet. Space Sci., 56, 708

Bar-Nun, A., Kleinfeld, I., & Ganor, E. 1988, J. Geophys. Res., 93, 8383

Barstow, J. K., Irwin, P. G. J., Fletcher, L. N., Giles, R. S., & Merlet, C. 2016, Icarus, 271, 400

Bazzon, A., Schmid, H. M., & Buenzli, E. 2014, A&A, 572, A6

Bazzon, A., Schmid, H. M., & Gisler, D. 2013, A&A, 556, A117

Belskaya, I., & Bagnulo, S. 2015, Transneptunian objects and Centaurs, ed. L. Kolokolova, J. Hough, & A.-C. Levasseur-Regourd, 405

Belskaya, I. N., Bagnulo, S., Barucci, M. A., et al. 2010, Icarus, 210, 472

Belskaya, I. N., Fornasier, S., & Krugly, Y. N. 2009, Icarus, 201, 167

Berdyugina, S. V., Berdyugin, A. V., Fluri, D. M., & Piirola, V. 2008, ApJ, 673, L83

—. 2011a, ApJ, 728, L6

Berdyugina, S. V., Berdyugin, A. V., & Piirola, V. 2011b, ArXiv e-prints, arXiv:1109.3116

Beuzit, J.-L., Feldt, M., Dohlen, K., et al. 2008, in Proc. SPIE, Vol. 7014, Ground-based and Airborne Instrumentation for Astronomy II, 701418

Bézard, B., Yelle, R. V., & Nixon, C. A. 2014, The composition of Titan's atmosphere, ed. I. Müller-Wodarg, C. A. Griffith, E. Lellouch, & T. E. Cravens, 158

Bohren, C. F., & Huffman, D. R. 1998, Absorption and Scattering of Light by Small Particles, 544

Borucki, W. J., Koch, D. G., Lissauer, J. J., et al. 2003, in Proc. SPIE, Vol. 4854, Future EUV/UV and Visible Space Astrophysics Missions and Instrumentation., ed. J. C. Blades & O. H. W. Siegmund, 129–140

Borucki, W. J., Koch, D., Basri, G., et al. 2010, Science, 327, 977

Bouchy, F., Udry, S., Mayor, M., et al. 2005, A&A, 444, L15

Bowell, E., Dollfus, A., & Geake, J. E. 1972, in Lunar and Planetary Science Conference Proceedings, Vol. 3, Lunar and Planetary Science Conference Proceedings, ed. A. E. Metzger, J. I. Trombka, L. E. Peterson, R. C. Reedy, & J. R. Arnold, 3103

Bowell, E., & Zellner, B. 1974, in IAU Colloq. 23: Planets, Stars, and Nebulae: Studied with Photopolarimetry, ed. T. Gehrels, 381

Bozza, V., Mancini, L., & Sozzetti, A., eds. 2016, Astrophysics and Space Science Library, Vol. 428, Methods of Detecting Exoplanets

Brewster, D. 1863, Transactions of the Royal Society of Edinburgh, 23, 205

Buenzli, E., & Schmid, H. M. 2009, A&A, 504, 259

Cabane, M., Chassefiere, E., & Israel, G. 1992, Icarus, 96, 176

Cabane, M., Rannou, P., Chassefiere, E., & Israel, G. 1993, Planet. Space Sci., 41, 257

Carlson, B. E., & Lutz, B. L. 1989, NASA Special Publication, 494, 289

Cellino, A., Gil-Hutton, R., & Belskaya, I. N. 2015, Asteroids, ed. L. Kolokolova, J. Hough, & A.-C. Levasseur-Regourd, 360–378

Cellino, A., Gil-Hutton, R., Dell'Oro, A., et al. 2012, J. Quant. Spec. Radiat. Transf., 113, 2552

Chandrasekhar, S. 1950, Radiative transfer.

Charbonneau, D., Brown, T. M., Noyes, R. W., & Gilliland, R. L. 2002, ApJ, 568, 377

Cikota, A., Patat, F., Cikota, S., & Faran, T. 2017, MNRAS, 464, 4146

Clancy, R. T., Wolff, M. J., & Christensen, P. R. 2003, Journal of Geophysical Research (Planets), 108, 2

Clark, R. N. 1980, Icarus, 44, 388

Clarke, D. 2010, Stellar Polarimetry

Coffeen, D. L. 1979, Journal of the Optical Society of America (1917-1983), 69, 1051

Coffeen, D. L., & Hansen, J. E. 1974, in IAU Colloq. 23: Planets, Stars, and Nebulae: Studied with Photopolarimetry, ed. T. Gehrels, 518

Crossfield, I. J. M. 2015, PASP, 127, 941

de Haan, J. F., Bosma, P. B., & Hovenier, J. W. 1987, A&A, 183, 371

de la Provostaye, F., & Desains, P. 1850, in Annales de Chimie et de Physique, Vol. 30, 159–178

de la Provostaye, F., & Desains, P. 1852, Ann. Chim. Phys, 34, 192

de Pater, I., & Lissauer, J. J. 2001, Planetary Sciences

de Pater, I., Sault, R. J., Butler, B., DeBoer, D., & Wong, M. H. 2016, Science, 352, 1198

de Rooij, W. A., & van der Stap, C. C. A. H. 1984, A&A, 131, 237

Devogèle, M., Cellino, A., Bagnulo, S., et al. 2017, MNRAS, 465, 4335

Dlugach, J. M., & Mishchenko, M. I. 2008, MNRAS, 384, 64

Dlugach, Z. M., & Mishchenko, M. I. 2005, Solar System Research, 39, 102

Dlugach, Z. M., & Petrova, E. V. 2003, Solar System Research, 37, 87

Dollfus, A. 1957, Supplements aux Annales d'Astrophysique, 4, 3

—. 1961, Polarizations Studies of Planets, ed. G. P. Kuiper & B. M. Middlehurst, 343

—. 1962, Handbuch der Physik, 54, 180

—. 1996, Icarus, 124, 237

—. 1998, Icarus, 136, 69

—. 1999, Icarus, 140, 313

—. 2000, Icarus, 146, 420

Dollfus, A., & Auriere, M. 1974, Icarus, 23, 465

Dollfus, A., Auriere, M., & Santer, R. 1979, AJ, 84, 1419

Dollfus, A., & Bowell, E. 1971, A&A, 10, 29

Dollfus, A., Bowell, E., & Ebisawa, S. 1984, A&A, 134, 343

Dollfus, A., Bowell, E., & Titulaer, C. 1971, A&A, 10, 450

Dollfus, A., Deschamps, M., & Ksanfomaliti, L. V. 1983, A&A, 123, 225

Dollfus, A., Ebisawa, S., & Crussaire, D. 1996, J. Geophys. Res., 101, 9207

Dollfus, A., & Focas, J. 1969, A&A, 2, 63

Dougherty, L. M., & Dollfus, A. 1989, Journal of the British Astronomical Association, 99, 183

Draine, B. T. 1988, ApJ, 333, 848

Dzhapiashvili, V. P., & Korol', A. N. 1982, Polarimetric atlas of the moon.

Ebisawa, S., & Dollfus, A. 1993, A&A, 272, 671

Ejeta, C., Boehnhardt, H., Bagnulo, S., & Tozzi, G. P. 2012, A&A, 537, A23

Fletcher, L. N., Baines, K. H., Momary, T. W., et al. 2011, Icarus, 214, 510

Fossati, L., Bagnulo, S., Haswell, C. A., et al. 2012, ApJ, 757, L15

Fox, G. K. 1997, MNRAS, 286, 963

Fox, G. K., Code, A. D., Anderson, C. M., et al. 1997, AJ, 113, 1152

Fresnel, A. 1819, Memoire sur la diffraction de la lumiere, 339

Friedson, A. J., Wong, A.-S., & Yung, Y. L. 2002, Icarus, 158, 389

Gehrels, T., Gradie, J. C., Howes, M. L., & Vrba, F. J. 1979, AJ, 84, 671

Gehrels, T., Herman, B. M., & Owen, T. 1969, AJ, 74, 190

Gehrels, T., Baker, L. R., Beshore, E., et al. 1980, Science, 207, 434

Goloub, P., Herman, M., Chepfer, H., et al. 2000, J. Geophys. Res., 105, 14

Gorosabel, J., García Muñoz, A., Sánchez-Lavega, A., Hueso, R., & Pérez Hoyos, S. 2015, in Highlights of Spanish Astrophysics VIII, ed. A. J. Cenarro, F. Figueras, C. Hernández-Monteagudo, J. Trujillo Bueno, & L. Valdivielso, 868–868

Greenler, R. 1980, Rainbows, halos and glories

Grinspoon, D. H., Pollack, J. B., Sitton, B. R., et al. 1993, Planet. Space Sci., 41, 515

Hall, J. S., & Riley, L. A. 1974, Icarus, 23, 144

—. 1976, Icarus, 29, 231

Hansen, J. E. 1971a, Journal of Atmospheric Sciences, 28, 1400

—. 1971b, Journal of Atmospheric Sciences, 28, 1400

Hansen, J. E., & Arking, A. 1971, Science, 171, 669

Hansen, J. E., & Hovenier, J. W. 1974, Journal of Atmospheric Sciences, 31, 1137

Hansen, J. E., & Travis, L. D. 1974, Space Sci. Rev., 16, 527

Hapke, B. 2005, Theory of Reflectance and Emittance Spectroscopy, 469

Hough, J. H., Lucas, P. W., Bailey, J. A., et al. 2006, PASP, 118, 1302

Hovenier, J. W., Van Der Mee, C., & Domke, H., eds. 2004, Astrophysics and Space Science Library, Vol. 318, Transfer of polarized light in planetary atmospheres : basic concepts and practical methods

Hovenier, J. W., & van der Mee, C. V. M. 1983, A&A, 128, 1

Howell, S. B. 2000, Handbook of CCD Astronomy

Ingersoll, A. P. 1976, Icarus, 29, 245

Ingersoll, A. P., Dowling, T. E., Gierasch, P. J., et al. 2004, Dynamics of Jupiter's atmosphere, ed. F. Bagenal, T. E. Dowling, & W. B. McKinnon, 105–128

Irwin, P. G. J. 2003, in Giant planets of our solar system : atmospheres, compositions, and structure, by P.G.J. Irwin. Springer Praxis books in geophysical sciences. Berlin: Springer, 2003, 112

Jockers, K., Credner, T., Bonev, T., et al. 2000, Kinematika i Fizika Nebesnykh Tel Supplement, 3, 13

Jones, R. C. 1941, Journal of the Optical Society of America (1917-1983), 31, 488

Joos, F., & Schmid, H. M. 2007, A&A, 463, 1201

Karalidi, T., & Stam, D. M. 2012, A&A, 546, A56

Karalidi, T., Stam, D. M., & Guirado, D. 2013, A&A, 555, A127

Karalidi, T., Stam, D. M., & Hovenier, J. W. 2011, A&A, 530, A69

—. 2012a, A&A, 548, A90

Karalidi, T., Stam, D. M., Snik, F., et al. 2012b, Planet. Space Sci., 74, 202

Karkoschka, E. 1994, Icarus, 111, 174

—. 1998, Icarus, 133, 134

Karkoschka, E., & Tomasko, M. 2005, Icarus, 179, 195

Kawabata, K., Coffeen, D. L., Hansen, J. E., et al. 1980, J. Geophys. Res., 85, 8129

Kawabata, K., & Hansen, J. E. 1975, Journal of Atmospheric Sciences, 32, 1133

Kaydash, V., Shkuratov, Y., Wolff, M., & Videen, G. 2015, Terrestrial planets, ed. L. Kolokolova, J. Hough, & A.-C. Levasseur-Regourd, 289

Kaydash, V. G., Kreslavsky, M. A., Shkuratov, Y. G., et al. 2006, Icarus, 185, 97

Keller, C. U. 2002, in Astrophysical Spectropolarimetry, ed. J. Trujillo-Bueno, F. Moreno-Insertis, & F. Sánchez, 303–354

Kemp, J. C., Henson, G. D., Steiner, C. T., & Powell, E. R. 1987, Nature, 326, 270

Kemp, J. C., & Murphy, R. E. 1973, ApJ, 186, 679

Kiselev, N., Rosenbush, V., Levasseur-Regourd, A.-C., & Kolokolova, L. 2015, Comets, ed. L. Kolokolova, J. Hough, & A.-C. Levasseur-Regourd, 379

Kiselev, N. N., & Lupishko, D. F. 2004, Solar System Research, 38, 85

Knibbe, W. J. J., de Haan, J. F., Hovenier, J. W., & Travis, L. D. 1997, J. Geophys. Res., 102, 10945

Kolokolova, L., & Kimura, H. 2010, Earth, Planets, and Space, 62, 17

Kolokolova, L., & Mackowski, D. 2012, J. Quant. Spec. Radiat. Transf., 113, 2567

Konnen, G. P., Schoenmaker, A. A., & Tinbergen, J. 1993, Icarus, 102, 62

Korablev, O., Fedorova, A., Bertaux, J.-L., et al. 2012, Planet. Space Sci., 65, 38

Ksanfomality, L., Harmon, J., Petrova, E., et al. 2007, Space Sci. Rev., 132, 351

Kuiper, G. P. 1944, ApJ, 100, 378

Kvaratskhelia, O. I. 1988, Soobshcheniya Byurakanskoj Observatorii Akademiya Nauk Armyanskoj SSR Erevan, 64, 3

Landi Degl'Innocenti, E., & Landolfi, M., eds. 2004, Astrophysics and Space Science Library, Vol. 307, Polarization in Spectral Lines

Laven, P. 2004, J. Quant. Spec. Radiat. Transf., 89, 257

Lavvas, P., Yelle, R. V., & Vuitton, V. 2009, Icarus, 201, 626

Lee, P., Ebisawa, S., & Dollfus, A. 1990, A&A, 240, 520

Limaye, S. S. 1984, Icarus, 57, 362

López Ariste, A., Leblanc, F., Casini, R., et al. 2012, Icarus, 220, 1104

Lucas, P. W., Hough, J. H., Bailey, J. A., et al. 2009, MNRAS, 393, 229

Lyot, B. 1929, Annales de l'Observatoire de Paris, Section de Meudon, 8, 1

—. 1934, Bull. Astron, 67

Macintosh, B., Graham, J., Palmer, D., et al. 2006, in Proc. SPIE, Vol. 6272, Society of Photo-Optical Instrumentation Engineers (SPIE) Conference Series, 62720L

Macintosh, B., Graham, J. R., Ingraham, P., et al. 2014, Proceedings of the National Academy of Science, 111, 12661

Malus, É.-L. 1809, Mémoires de physique et de chimie de la Société dArcueil, 2, 143

Martonchik, J. V., Orton, G. S., & Appleby, J. F. 1984, Appl. Opt., 23, 541

Mayor, M., & Queloz, D. 1995, Nature, 378, 355

McLean, W., Stam, D. M., Bagnulo, S., et al. 2017, A&A, 601, A142

Miles-Páez, P. A., Pallé, E., & Zapatero Osorio, M. R. 2014, A&A, 562, L5

Minnis, P., Heck, P. W., Young, D. F., Fairall, C. W., & Snider, J. B. 1992, Journal of Applied Meteorology, 31, 317

Mishchenko, M. I. 1990, Icarus, 84, 296

Mishchenko, M. I., Lacis, A. A., Carlson, B. E., & Travis, L. D. 1995, Geophys. Res. Lett., 22, 1077

Morozhenko, A. V., & Yanovitskii, E. G. 1973, Icarus, 18, 583

Muñoz, O., Moreno, F., Molina, A., et al. 2004, Icarus, 169, 413

Muinonen, K., Mishchenko, M. I., Dlugach, J. M., et al. 2012, ApJ, 760, 118

Muinonen, K., Piironen, J., Shkuratov, Y. G., Ovcharenko, A., & Clark, B. E. 2002, Asteroid Photometric and Polarimetric Phase Effects, ed. W. F. Bottke, Jr., A. Cellino, P. Paolicchi, & R. P. Binzel, 123–138

Mustard, J. F., & Bell, J. F. 1994, Geophys. Res. Lett., 21, 353

Oliva, E. 1997, A&AS, 123, doi:10.1051/aas:1997175

Opanasenko, N. V., & Shkuratov, Y. G. 1994, Astronomicheskii Vestnik, 28, 133

Pernechele, C., Abe, L., Bendjoya, P., et al. 2012, in Society of Photo-Optical Instrumentation Engineers (SPIE) Conference Series, Vol. 8446, Society of Photo-Optical Instrumentation Engineers (SPIE) Conference Series, 84462H

Petrova, E., Shalygina, O., Markiewicz, W. J., & Almeida, M. 2013, in EGU General Assembly Conference Abstracts, Vol. 15, EGU General Assembly Conference Abstracts, EGU2013–7839

Petrova, E. V. 1999, J. Quant. Spec. Radiat. Transf., 63, 667

Pont, F., Knutson, H., Gilliland, R. L., Moutou, C., & Charbonneau, D. 2008, MNRAS, 385, 109

Pont, F., Sing, D. K., Gibson, N. P., et al. 2013, MNRAS, 432, 2917

Pryor, W. R., West, R. A., Simmons, K. E., & Delitsky, M. 1992, Icarus, 99, 302

Queloz, D., Eggenberger, A., Mayor, M., et al. 2000, A&A, 359, L13

Ragent, B., & Blamont, J. 1980, J. Geophys. Res., 85, 8089

Ragent, B., Esposito, L. W., Tomasko, M. G., Marov, M. I., & Shari, V. P. 1985, Advances in Space Research, 5, 85

Rages, K. A., & Pollack, J. B. 1981, in BAAS, Vol. 13, Bulletin of the American Astronomical Society, 703

Rannou, P., McKay, C. P., & Lorenz, R. D. 2003, Planet. Space Sci., 51, 963

Roman, M. T., Banfield, D., & Gierasch, P. J. 2013, Icarus, 225, 93

Rosenbush, V., Kiselev, N., & Afanasiev, V. 2015, Icy Moons of the Outer Planets, ed. L. Kolokolova, J. Hough, & A.-C. Levasseur-Regourd, 340

Rosenbush, V. K., & Kiselev, N. N. 2005, Icarus, 179, 490

Rossi, L., Marcq, E., Montmessin, F., et al. 2015, Planet. Space Sci., 113, 159

Rossi, L., Montmessin, F., Fedorova, A., & Korablev, O. 2013, European Planetary Science Congress 2013, held 8-13 September in London, UK., 8, EPSC2013

Sato, M., & Hansen, J. E. 1979, Journal of Atmospheric Sciences, 36, 1133

Sato, M., Travis, L. D., & Kawabata, K. 1996, Icarus, 124, 569

Schmid, H. M., Joos, F., Buenzli, E., & Gisler, D. 2011, Icarus, 212, 701

Schmid, H. M., Joos, F., & Tschan, D. 2006, A&A, 452, 657

Schmidt, G. D., Elston, R., & Lupie, O. L. 1992, AJ, 104, 1563

Seager, S., Turner, E. L., Schafer, J., & Ford, E. B. 2005, Astrobiology, 5, 372

Seager, S., Whitney, B. A., & Sasselov, D. D. 2000, ApJ, 540, 504

Shalygina, O. S., Korokhin, V. V., Starukhina, L. V., et al. 2008, Solar System Research, 42, 8

Shkuratov, I. G., & Opanasenko, N. V. 1992, Icarus, 99, 468

Shkuratov, I. G., Opanasenko, N. V., & Kreslavskii, M. A. 1992, Icarus, 95, 283

Shkuratov, Y., Opanasenko, N., Korokhin, V., & Videen, G. 2015, The Moon, ed. L. Kolokolova, J. Hough, & A.-C. Levasseur-Regourd, 303

Shkuratov, Y., Ovcharenko, A., Zubko, E., et al. 2002, Icarus, 159, 396

Shkuratov, Y., Kreslavsky, M., Kaydash, V., et al. 2005, Icarus, 176, 1

Shkuratov, Y. G. 1987, Soviet Astronomy Letters, 13, 182

Shurcliff, W. 1962, Polarized Light: Production and Use (Harvard University Press)

Simon-Miller, A. A., Banfield, D., & Gierasch, P. J. 2001, Icarus, 154, 459

Smith, P. H., & Tomasko, M. G. 1984, Icarus, 58, 35

Snik, F., & Keller, C. U. 2013, Astronomical Polarimetry: Polarized Views of Stars and Planets, ed. T. D. Oswalt & H. E. Bond, 175

Sparks, W., Hough, J., & Kolokolova, L. 2015, Astrobiology, ed. L. Kolokolova, J. Hough, & A.-C. Levasseur-Regourd, 462

Sparks, W. B., Hough, J. H., & Bergeron, L. E. 2005, Astrobiology, 5, 737

Spencer, J. R., & Denk, T. 2010, Science, 327, 432

Spencer, J. R., Pearl, J. C., Segura, M., et al. 2006, Science, 311, 1401

Sromovsky, L. A., Baines, K. H., & Fry, P. M. 2013, Icarus, 226, 402

Sromovsky, L. A., & Fry, P. M. 2002, Icarus, 157, 373

Stam, D. M. 2008, A&A, 482, 989

Stam, D. M., Banfield, D., Gierasch, P. J., Nicholson, P. D., & Matthews, K. 2001, Icarus, 152, 407

Stam, D. M., De Haan, J. F., Hovenier, J. W., & Stammes, P. 1999, J. Geophys. Res., 104, 16843

Stam, D. M., & Hovenier, J. W. 2005, A&A, 444, 275

Stam, D. M., Hovenier, J. W., & Waters, L. B. F. M. 2004, A&A, 428, 663

Starodubtseva, O. M. 1987, Astronomicheskij Tsirkulyar, 1511, 3

Starodubtseva, O. M. 1991, in Lunar and Planetary Inst. Technical Report, Vol. 22, Lunar and Planetary Science Conference

Starodubtseva, O. M., Akimov, L. A., & Korokhin, V. V. 2002, Icarus, 157, 419

Sterzik, M., Bagnulo, S., Azua, A., et al. 2010, The Messenger, 142, 25

Sterzik, M. F., Bagnulo, S., & Palle, E. 2012, Nature, 483, 64

Stokes, G. G. 1852, Royal Society of London Philosophical Transactions Series I, 142, 463

Stoll, C. P. 1980, PhD thesis, Arizona Univ., Tucson.

Takahashi, J., Itoh, Y., Akitaya, H., et al. 2013, PASJ, 65, 38

Taylor, F. W. 2006, Planet. Space Sci., 54, 1249

Tishkovets, V. P., & Shkuratov, Y. G. 1982, Soviet Ast., 26, 599

Tomasko, M. G. 1980, J. Geophys. Res., 85, 5937

Tomasko, M. G., & Doose, L. R. 1984, Icarus, 58, 1

Tomasko, M. G., Doose, L. R., Dafoe, L. E., & See, C. 2009, Icarus, 204, 271

Tomasko, M. G., & Smith, P. H. 1982, Icarus, 51, 65

Torres, G., Winn, J. N., & Holman, M. J. 2008, ApJ, 677, 1324

Travis, L. D., Coffeen, D. L., Hansen, J. E., et al. 1979, Science, 203, 781

Umov, N. 1905, Physik. Z, 6, 674

Vasavada, A. R., & Showman, A. P. 2005, Reports on Progress in Physics, 68, 1935

Veverka, J. 1973, Icarus, 18, 657

Veverka, J. 1977, in IAU Colloq. 28: Planetary Satellites, ed. J. A. Burns, 210–230

West, R. A., Baines, K. H., Friedson, A. J., et al. 2004, Jovian clouds and haze, ed. F. Bagenal, T. E. Dowling, & W. B. McKinnon, 79–104

West, R. A., Baines, K. H., Karkoschka, E., & Sánchez-Lavega, A. 2009, Clouds and Aerosols in Saturn's Atmosphere, ed. M. K. Dougherty, L. W. Esposito, & S. M. Krimigis, 161

West, R. A., & Smith, P. H. 1991, Icarus, 90, 330

West, R. A., Strobel, D. F., & Tomasko, M. G. 1986, Icarus, 65, 161

West, R. A., Yanamandra-Fisher, P. A., & Korokhin, V. 2015, in Polarimetry of Stars and Planetary Systems, ed. L. Kolokolova, J. Hough, & A.-C. Levasseur-Regourd (Cambridge University Press), 320

West, R. A., Hart, H., Simmons, K. E., et al. 1983, J. Geophys. Res., 88, 8699

Wiktorowicz, S. J. 2009, ApJ, 696, 1116

Wiktorowicz, S. J., & Stam, D. M. 2015, Exoplanets, ed. L. Kolokolova, J. Hough, & A.-C. Levasseur-Regourd, 439

Wolff, M. J., & Clancy, R. T. 2003, Journal of Geophysical Research (Planets), 108, 1

Wolstencroft, R. D., & Breon, F.-M. 2005, in Astronomical Society of the Pacific Conference Series, Vol. 343, Astronomical Polarimetry: Current Status and Future Directions, ed. A. Adamson, C. Aspin, C. Davis, & T. Fujiyoshi, 211

Wolszczan, A., & Frail, D. A. 1992, Nature, 355, 145

Wong, M. H., Bjoraker, G. L., Smith, M. D., Flasar, F. M., & Nixon, C. A. 2004, Planet. Space Sci., 52, 385

Woolf, N. J., Smith, P. S., Traub, W. A., & Jucks, K. W. 2002, ApJ, 574, 430

Woszczyk, A., Iwaniszewska, C., & Union, I. A. 1974, Exploration of the Planetary System: International Astronomical Union Symposium No 65 (Copernicus Symposium IV) Held in Torún, Poland, 5-8 September, 1973, Copernicus symposium (D. Reidel Publishing Company)

Young, A. T. 1973, Icarus, 18, 564

Young, R. E. 2003, New A Rev., 47, 1